Michał Basista

MICROMECHANICAL AND LATTICE MODELING OF BRITTLE DAMAGE

(PRACA HABILITACYJNA)

3/2001

WARSZAWA 2001

ISSN 0208-5658

Praca wpłynęła do Redakcji dnia 21 grudnia 2000 r.

recenzent – Prof. dr hab. Jacek Skrzypek

IPPT
PAN

Praca habilitacyjna

Instytut Podstawowych Problemów Techniki PAN
Nakład 100 egz. Ark. wyd. 12,0 Ark. druk 15,0
Oddano do drukarni w maju 2001 r.

I wish to thank Professor Dietmar Gross and Professor Dusan Krajcinovic for stimulating cooperation which gave rise to many of the results presented in this study.

I am also indebted to late Professor Antoni Sawczuk for his scientific guidance and Professor Jakub Mames for his encouragement in research over the years.

Summary

This thesis is a multi-aspect study concerned with theoretical modeling of damage in brittle solids with special emphasis on rocks and plain concrete. Motivated by the complex and diverse nature of damage processes in these materials, an integrated approach involving micromechanical, phenomenological and lattice modeling is pursued. It is shown that these seemingly disparate classes of models turn to be complementary in their objectives and utility. The bulk of the work is devoted to the local description of damage problems in rock-like materials under quasi-static mechanical loading (tensile or compressive) at isothermal conditions. Slightly off the mainstream but well in tune with the micromechanical damage modeling promoted in this thesis, a type of environmental damage of concrete due to chemically aggressive ambient is also investigated. Application of the methods of physics of critical phenomena to brittle damage and fracture problems constitutes an important part of this study. It is suggested that the percolation and other disorder models be used at large microdefects densities where the traditional methods of micromechanical and continuum damage mechanics cease to be valid. The individual chapters of the thesis can be summarized as follows.

Chapter 1 presents in a concise way the basic definitions and assumptions of the damage mechanics. Main differences (and similarities, if any) between damage and fracture, damage and plasticity are pointed out. It is stressed that the presently used name of damage mechanics (shortly DM) shall not be identified with the early phenomenological damage theories (CDM) which were chronologically the first to deal with the damage problems in the framework of continuum mechanics. The former is much a wider class comprising micromechanical damage models, statistical damage models, and the CDM models themselves. In Chapter 1, these three classes of models are briefly characterized and critically evaluated in the context of brittle deformation.

Chapter 2 provides experimental background for the analytical models proposed in this thesis. Mechanisms of tensile and compressive microcracking in rocks inducing inelastic macroscopic stress–strain behavior, microcrack related anisotropy, positive dilatancy, pressure dependence, hysteresis, etc. are discussed in considerable detail. Additionally, some basic facts

about the subcritical microcrack growth as well as the acoustic emission application to rock microcracking and fracture are reviewed. It seems that accoustic emission (AE) is gaining a steadily growing reputation as a reliable, non-destructive technique capable of unraveling focal mechanisms and locating, both temporary and spatially, the evolving microcracks within the material volume. The important point is that AE allows for continuous screening of the microcrack nucleation, growth and localization into a dominant fault.

Chapters 3, 4, 5, 6, 7, 8 constitute the original research part of the thesis. Chapter 3 is concerned with a relatively straightforward case of damage development in brittle materials subjected to displacement-controlled (homogeneous) tensile loading. On the example of plain concrete and using a general internal-variable thermodynamic framework, it is shown in a systematic manner how a workable micromechanical damage model can be constructed starting with the behavior of a single tensile microcrack in the unit cell. A new microcrack growth condition (3.5)–(3.6) is proposed based on an experimentally supported dependence of the fracture toughness on the microcrack length. The model is formulated for the uniaxial tension and then generalized for two-dimensional case. Typical configurations of interacting microcracks having analytical solutions for the K_I factors are incorporated into the model to illustrate how the stress amplification effects might influence the overall σ–ε behavior in tension.

Chapter 4 deals with the compressive damage in rocks. Of several possible micromechanism of inelastic rock deformation in brittle regime, the sliding microcrack model is selected for modeling purposes owing to its remarkable versatility in replicating the macroscopically observed effects of rock response in compression. The original contribution of this chapter includes application of the Rice thermodynamic formalism with microstructural variables to the sliding microcrack deformational mechanism, detailed analysis of all phases of sliding microcrack behavior in loading and unloading, derivation of the ensuing incremental stress–strain equations, their numerical implementation and comparison of the computed results with the available test data on granite to show the model at work.

Chapter 5 is devoted to estimation of the stress intensity factors for interacting slits endowed with frictional and cohesive resistance and for sliding microcracks with developed tension wings under overall compression. The very effective analytical-numerical method of Kachanov (1987) is extended and modified to account for friction and cohesion on the crack faces. Also, the case of point-force loading on interacting cracks is considered. Using a developed FORTRAN code, a number of test problems of crack interaction is solved and compared with the corresponding "exact" *BEM* results.

In Chapter 6, a micromechanical model is formulated for the deformation of hardened concrete exposed to chemical corrosion by sulphate ions migrating into the concrete structure from ground water. The model is quite complex involving several coupled physico-chemical processes such as non-steady diffusion, heterogeneous chemical reactions, expansion of reaction products, microcracking of heterogeneous matrix (hardened cement paste with ettringite inclusions), and percolation. These processes are modeled on the microscale and the resulting equations are volume-averaged leading to the macroscopic expansions which closely match the test data of Ouyang et al. (1988) on ASTM recommended specimens.

Chapter 7 suggests a micromechanically-based phenomenological damage model for brittle response of solids. For deformation processes dominated by Mode I microcracking, the inelastic change of the compliance tensor is identified as the flux, and the fourth-order tensor $\mathbf{Q} = \frac{1}{2}(\boldsymbol{\sigma} \otimes \boldsymbol{\sigma})$ as the affinity. The conditions under which a damage potential exists are indicated. Illustrative examples are worked out.

Chapter 8 is devoted to modeling brittle damage and fracture using methods of statistical physics of the critical phenomena – an alternative modeling methodology which is entirely different from the conventional (micromechanical or phenomenological) damage mechanics models. In the search for possible interrelations between damage mechanics and statistical lattice models, two classes of disordered systems are given particular attention: percolation model and central-force model. It is found that the percolation theory can be quite useful when verifying the accuracy of the effective-continua methods in predicting the effective elastic constants of a damaged solid. Furthermore, results of the numerical simulations on central-force triangular lattices in Hansen, et al. (1989) are compared with the corresponding analytical estimates yielded by the parallel bar model (widely used in damage mechanics). To this end, a number of original results is obtained in this chapter including accuracy assessment of the effective-media methods, selection of the secant effective compliance tensor as the damage variable, microcrack interactions in tension, etc.

Contents

Chapter 1

Introduction, objectives and scope

Engineering materials commonly classified as *brittle* (e.g. rocks, concrete, ceramics, some metallic materials) contain numerous microstructural flaws such as microcracks, pores, inclusions, grain boundaries and other stress inhomogeneities even in the virgin unstressed state. Under the action of externally applied loads these microdefects grow and interact with each other influencing the macroscopic material properties. For example, the observed nonlinearity of the stress–strain curves in unconfined compression and tension tests on rock specimens is unanimously attributed by rock mechanicians to irreversible processes of internal microcracking.

It is rather difficult to offer a precise definition of **damage** as a phenomenon. Talreja (1985), for instance, defines damage as "a collection of permanent microstructural changes brought about in material by a set of irreversible physical (or chemical) processes resulting from the application of thermomechanical loadings." Somewhat descriptively, damage can be defined as the effect that an ensemble of randomly distributed microdefects (microcracks, microvoids, etc.) of random sizes, orientation and geometry have on the deformation and mechanical performance of a structure. In the literature, the damage is typically understood as a continuum concept (characterized by a damage variable) that is intrinsically related to microscale processes of the nucleation, growth, and interaction of a large number of microdefects within the material volume. It is essential to recognize that damage can be measured only indirectly through the cumulative effect of these microdefects on the macroscopic response, e.g. the material compliance and ultimate strength.

One should distinguish between brittle damage and brittle fracture. The former is intentionally referred to gradual reduction of the load bearing capacity of a structural element due to progressive material deterioration, whereas the latter generally means the structural element's disability to carry loads. In this sense damage is a preceding phase of the final fracture. It should be emphasized that brittle damage is generated by a large number of microcracks within the material. In contrast, the fracture is usually associated with a single dominant macrocrack growing in a homogeneous isotropic or anisotropic material of a specimen or structure.

Evidently, these two phenomena differ in scale: damage develops at the material mesoscale, i.e. at the level of grains in polycrystalline rocks or aggregates in concrete, while the fracture is identified with a macroscopic crack growing in the specimen. A material defect can be regarded as a microdefect in the damage mechanics sense if its size does not exceed some characteristic distance of the material microstructure. In polycrystalline brittle solids such distance encompasses several grain sizes. Larger cracks must be dealt with using the fracture mechanics methods of analysis. For example, in compact rocks (e.g. granite) the average length of the pre-load microcracks is of the order of 1 mm (Tapponier and Brace, 1976; Scholz, 1968) while at the onset of the overall failure it usually falls within the range of 3–7 mm (Costin, 1983). In plain concrete, the average size of the pre-load microcracks is determined by the average aggregate size being of the order of 10 mm (Zaitsev, 1982). For hot-pressed ceramics like Si_3N_4 the size in question is of the order of 1 μm (Tsai and Raj, 1982). The size of a microcrack should be discussed in the context of the linear size of the Representative Volume Element. For more elaborate discussion of the RVE concept — see Section 3.2.

Strictly speaking, the materials considered in this study (i.e. rocks and concrete) are not brittle per se. Their response in compression tests strongly depends on the testing conditions such as the lateral pressure, temperature and rate of loading. For example, it is known from experimental rock mechanics that a sufficiently high lateral confinement applied to an axially compressed rock specimen makes this specimen behave in a typically ductile manner showing no tendency to fail in brittle mode. Therefore, it is more appropriate to speak of a brittle deformation rather than of a brittle material. Nevertheless, if the confinement is kept low, the temperature remains at room level, the loading process is quasi-static, then the brittle-to-ductile transition point will not yet be reached and it is legitimate to speak of brittle materials in a conventional sense. It is in this sense that the term *brittle materials* is used throughout this thesis. To be more specific, the actual concern of this thesis is with materials and deformation processes characterized by a nonlinear segment in the stress–strain curve preceding the final failure. Physically, this nonlinearity is not to be traced back to plastic flow but to the degradation of material elastic properties induced by a progressive deterioration of the material bonds with increasing loading.

Due to microstructural heterogeneity, the final fracture in these materials is not abrupt but is preceded by distributed microcracking. On the other hand, the advance of fracture is to be seen as a process of localization of distributed microcracks into a major continuous macrocrack. The mathematical description of the failure process in such materials and structures is much more complicated than for ductile materials described by the theory of plasticity, or for perfectly brittle materials for which the fracture is abrupt. To distinguish this specific class of materials from the other two (perfectly brittle or ductile), a term *quasi-brittle*[1] has been coined and is often used for rocks, concretes, mortars, toughened ceramics, certain fiber composites, ice, wood, paper, and even some advanced tough metallic alloys (Bazant et al., 1994). In the literature the name "brittle" is probably as often and interchangeably used as "quasi-brittle" when describing rock-like materials (e.g. Willam and Iordache, 1994; Horii and Nemat-Nasser, 1985a, to mention only a few). Merely for convenience, we shall drop the prefix "quasi" and consistently use "brittle" for the materials in question.

Another issue in the open literature that may lead to misunderstandings is the usage of adjectives *micromechanical* vs. *mesomechanical* in the context of damage mechanics. According to a simplified physical classification of the volume scales, the microscale encompasses atoms and molecule chains with typical material defects being those of vacancies and dislocations. The mesoscale refers to an ensemble of grains containing very small cracks, voids, etc. The macroscale refers to laboratory specimens or structural elements with macrocracks and shear bands being typical defects. Clearly, in terms of this classification damage processes develop at the material mesoscale. Consequently, *mesomechanical* (or *mesoscale*) would be more appropriate to use, and are in fact used by some authors. However, such a systematic assignment of the volume scales to characteristic material defects is not shared by the majority of applied mechanicians. Most of them persist to stick a label *micromechanical* to processes and models dealing with defects whose sizes are of the order of grain size. This situation seems to be rooted in the terminology used in the theory of elasticity when addressing the problems of inclusions and inhomogeneities in elastic matrices (cf. Mura, 1987; Nemat-Nasser and Hori, 1993; Aboudi, 1991; Kachanov, 1993, and many

---

[1] *quasi-brittle* materials should not be confused with *semi-brittle* ones. The latter refers to a class of materials, (e.g. MgO ceramics, ionic crystals, glassy polymers, most b.c.c. metals) which is characterized by limited plastic flow prior to the growth of a brittle crack (Lawn and Wilshaw, 1975).

others). In order to establish links with these basic works the terms *micromechanical* and *micromechanics* in the above sense will be adopted and used throughout this thesis.

As has already been noted, the damage essentially depends on the material, type of applied loading, stress state, temperature, and environmental conditions. Different types of damage encountered in the literature include: brittle (or elastic-brittle) damage, ductile (or elastic-plastic) damage, creep damage, fatigue damage, spall damage (i.e. dynamic damage due to impulsive loading of high intensity and short duration), etc. From the purely geometrical point of view, the class of damage-related microdefects can be divided into two groups:

- microcracks – roughly planar in shape, growing mostly on grain boundaries, typical of brittle solids like rocks, concrete, ceramics, some metals at certain temperature levels;
- microvoids (or cavities) – volumetric defects growing within grains or on grain boundaries, observed mainly in ductile materials (majority of metals and alloys).

Unlike very ductile metals manifesting dilute and random distributions of almost sphereoidal voids, the nucleation and, especially, evolution of microdefects in most brittle materials exhibit pronounced anisotropy.

The literature pertinent to constitutive modeling of brittle solids is quite extensive. Generally, three main groups of solid mechanics models have been used for this purpose: hypoelastic models (e.g. Coon and Evans, 1972), plasticity models (e.g. Chen, 1982), and damage models (e.g. Lemaitre and Chaboche, 1985; Krajcinovic, 1996).

The hypoelastic models, once quite popular among analysts dealing with the nonlinear response of plain concrete, favor an incremental formulation relating the total increment of stress to the total increment of strain with no diagonal-symmetry requirements imposed on the tangent compliance matrix. In these models, no reference is made to the mechanisms responsible for the macroscopic nonlinear response of concrete. They seem not to have been pursued further in the context of brittle damage.

The theory of plasticity is probably one of the few theories in solid mechanics that offer a sound mathematical framework to deal with nonlinear problems. An appealing idea of a direct extension of plasticity models to the description of brittle deformation processes is based on a somewhat artificial argument that any nonlinear, time-independent material response, irrespective of the underlying physics of the inelasticity, can be modeled on the macroscale using the concepts of classical plasticity. However, the presence of positive dilatancy, frictional sliding and progressive degradation of the elastic constants makes the constitutive relations for brittle materials quite different from those of plasticity. In particular, residual strains observed in experiments after complete unloading are predominantly due to imperfect crack closure and not to plastic flow (as long as the lateral pressure remains low). The nonlinear behavior of brittle materials is directly related to the breaking process of atomic bonds. Obviously, this kind of microstructural rearrangement is not a major micromechanism in plastic flow. The plastic flow can be understood as a motion of the matter through the crystalline lattice with the number of atomic bonds remaining practically unchanged.

The above comment points to different physical backgrounds of damage in brittle rock-like materials vs. plastic flow in metals. Consequently, it is suggested that direct application of methods of the classical theory of plasticity may turn out inadequate when modeling damage in brittle materials. This, however, has nothing to do with the damage-plasticity coupling in ductile metallic materials for which plasticity models with damage and plastic potentials are well suited (cf. Hayakawa and Murakami, 1998).

The third group of models, namely the damage models of brittle deformation, may be arranged in three subgroups:

- continuum damage mechanics models,
- micromechanical damage models,
- lattice damage models.

The continuum damage mechanics (CDM) models are phenomenological models that relate the nonlinear macroscopic material behavior to the process of internal microcracking. The modeling philosophy behind the CDM, which started with a pioneering work by Kachanov (1958), is the following. By its very nature, the damage is a discrete and stochastic phenomenon induced by a large number of interacting microdefects. An exact analysis of the behavior of these microdefects is a formidable task well beyond our present computing capabilities. On the other hand, the whole problem can alternatively be seen as a collective effect of all microdefects on the overall material response without going into local stress and strain fields of each microdefect. Hence a damaged material may be treated as a fictitious continuum with microdefects uniformly smeared within its volume. Consequently, and this constitutes the basic concept of the CDM, it is conceivable that an instantaneous state of material deterioration in every point of the body can be represented in an average sense by a specific field variable called *damage variable*. The damage variable so introduced is nothing else but a macroscopic internal variable. Therefore, any CDM model can suitably be formulated within the well-established framework of irreversible thermodynamics with internal variables. The effect of a large number of microcracks can be described mathematically by a single damage variable provided that the material sample is statistically homogeneous. A majority of the CDM models start by introducing the damage variable of either scalar, vector, or tensor type. Since damage is to be modeled as a process, the damage variable has to be endowed with an evolution law. It should be stressed that early CDM models were plagued by too many unidentifiable constants or even lead to contradictory predictions (Krajcinovic, 1984). That was a direct consequence of ignoring the underlying micromechanisms of damage. The accomplishments and deficiencies of various phenomenological CDM models are discussed at length in comprehensive review studies by Chaboche (1988) and Krajcinovic (1996).

The outburst of micromechanical damage models in the past two decades can, to some extent, be explained as the search for a remedy for the shortcomings of the CDM models (e.g. Mura, 1982; Nemat-Nasser and Hori, 1993; Krajcinovic, 1996). The attribute *micromechanical* is commonly attached to the class of models relating macroproperties and macroresponse of a material to its microstructure. As such, these models span two different scales, one of which is typically inhomogeneous (microscale) while the other (macroscale) is, for computational expedience, approximated by a homogeneous effective continuum. An unquestionable merit of micromechanical damage models resides in their ability to explain the physics of damage processes with a minimum of ambiguity and arbitrariness. All the constants appearing in a micromechanical model have clear physical interpretations. This is not to say, though, that their numerical values can always be measured using available experimental techniques.

Since the micromechanical damage models inherently deal with average stress and strain fields (thus with effective material properties), it seems appropriate to comment on that in the context of the homogenization theory. The macrofields in damage mechanics models are provided by volume averages of spatial variations of the corresponding microfields using the averaging theorems of micromechanics. This micromechanics theory is grounded on "the physics and experimental definition of the overall properties of microscopically heterogeneous solids" (Nemat-Nasser and Hori, 1999). For example, the fundamental formula (4.34) describing the microcrack-induced strain is derived in a relatively straightforward manner using simple volume averaging of the strain and stress fields for a two-phase composite (damaged body) consisting of a linear-elastic, homogeneous matrix (phase 1) and microcracks (phase 2). This derivation further involves the equilibrium and stress boundary conditions, relations between strain and displacement fields, and the Gauss theorem.

Alternatively, the effective material properties may be determined within the framework of the homogenization theory — a branch of applied mathematics dealing with relations between micro and macrofields without any reference to specific physical measurements (e.g. Bensoussan et al., 1978; Sanchez-Palencia, 1981; Ponte-Castañeda and Suquet, 1998; Lewiński and Telega, 2000). The homogenization theory is usually applied to periodic microstructures (composites) for which it proved most powerful. Extensions to random microstructures, although feasible are not as efficient. In brittle solids, the interplay of the material microstructure, microcrack interaction and coalescence changes the initial microcrack distribution as the deformation proceeds. Hence, the assumption of a regular microcrack pattern, although admissible when studying the basic effects of damage on the material response, needs to be relaxed when modeling the evolving damage in real rocks or concrete.

The response of a brittle solid in the ascending part of the stress–strain curve depends predominantly on the volume averages of defects. The influence of microcracks is felt by the material in a smoothed sense involving orientation-weighed volume averages of microcracks. Consequently, as the current modeling practice shows, the pre-peak response can accurately be represented using micromechanical models based on the representative volume element (RVE) and the effective continuum concept (cf. self-consistent method, differential scheme, etc.). Also, carefully constructed, i.e. inspired by micromechanics, phenomenological damage models have a good chance for success in the pre-peak regime. As the external loading increases, the evolving defects reach a certain threshold density at which their hithertodilute concentration (disordered state) is replaced by a large defect cluster (ordered state). The emergence of a single dominant cluster (in terms of damage mechanics – a crack band or a macrocrack) is preceded by intensive cooperative action of defects involving their own interactions and the interplay between the hot spots (stress concentrations) and weak links (cleavage planes, interfaces, etc.). The transition from a disordered state to an ordered state is a non-deterministic, non-local, nonlinear and non-equilibrium process which requires quite different methods than those of continuum mechanics (cf. Krajcinovic, 1996). Such methods are offered by the physics of critical phenomena, a branch of modern statistical physics dealing with the behavior of disordered systems. The most known and probably the most appealing theory of that kind is the percolation theory (e.g. Stauffer, 1985). Originally applied to transport phenomena like conduction and diffusion, the percolation theory turned out to be a powerful tool when applied to brittle damage-fracture problems. The aim of the percolation studies is twofold: (1) determination of the percolation threshold, i.e. a critical density of defects at which an infinite cluster is formed, and (2) determination of the scaling laws for the transport properties in the vicinity of the percolation threshold. On the credit side, no simplifying assumptions with regard to crack shapes and sizes, distributions of weak spots, etc., are necessary for the percolation theory to be applicable. On the debit side, percolation theory relies heavily on large-scale numerical simulations burdened by considerable computational efforts necessary when determining the percolation thresholds and the universal parameters needed in applications.

The generic name of *damage mechanics* (DM) is now being used to embrace all three classes of models i.e. CDM-, micromechanical- and lattice models dealing with the response and reliability of materials and structures weakened by many distributed microdefects. In fact, the label DM has deliberately been introduced (Krajcinovic, 1996, 2000) to distinguish it from the CDM. The rationale behind that was to stress the fact that DM addresses a much wider spectrum of problems and solution algorithms than CDM which postulates that damage be quantified by a single deterministic damage parameter.

Objectives and scope

The present study summarizes the author's 15 years of research in theoretical modeling of damage processes in rocks and concrete within brittle deformation regime. The primary objective here is to formulate micromechanical damage models capable of reproducing the salient features of the rock-like materials' response to tensile and compressive loadings. Secondly, the micromechanical modeling framework will be employed to tackle the problem of environmental brittle damage brought about by chemically aggressive ambient. Thirdly, the limits of micromechanical modeling being known, the attention will be shifted to lattice models of brittle damage which provide valuable solutions beyond the micromechanics domain of applicability. Finally, inspired by the underlying micromechanics, certain aspects of phenomenological damage description in rock-like materials will also be investigated. It will be shown that these seemingly disparate classes of models (micromechanical, phenomenological, lattice) are in fact complementary in their goals and utility.

The main theme spanning all the chapters of this thesis is the formulation of workable constitutive models for brittle solids based on the physics of the underlying microcracking phenomena. The scope of the thesis includes:

- experimental background of various damage processes (Chapter 2),
- micromechanical damage model for brittle solids in tension (Chapter 3),
- micromechanical damage model for brittle solids in compression based on the sliding crack mechanism (Chapter 4),
- analysis of microcrack interaction in compression (Chapter 5),
- investigation of chemically-assisted damage of concrete exposed to aggressive ambient (Chapter 6),
- formulation of a phenomenological damage model suitable for brittle solids in tensile and compressive stress states (Chapter 7),
- application of the percolation theory to assess accuracy of the effective continua techniques when predicting the effective elastic constants of heterogeneous solids; analysis of disordered lattices in modeling brittle fracture processes in elastic solids (Chapter 8).

Throughout the thesis it will tacitly be assumed that the brittle deformation processes investigated are quasi-static and isothermal, the total strains remain small and plastic strains are neglected. Consequently, the considered nonlinear behavior of rocks and concrete is entirely due to damage of various types and not to plastic flow.

The following chapters contain the author's original research results obtained during his employment at the Institute of Fundamental Technological Research in Warsaw or when on leave at the Darmstadt University of Technology (Germany), University of Illinois at Chicago, and Arizona State University at Tempe (USA). The thesis as a whole is a synthetic recapitulation of the author's contributions to brittle damage mechanics. It contains published and unpublished considerations, results and views that have been formed over the years of research and finally become matured enough to be expressed within this study.

Chapter 2

Damage and fracture in polycrystalline rocks: experimental background

Abstract. Consistently with the scope of the thesis, this chapter is a cursory review of the most essential experimental observations on damage phenomena in brittle polycrystalline rocks at diverse loading conditions. Microcracking and corrosion in plain concrete are addressed separately in Chapter 3 and Chapter 7.

2.1. Introduction

Even a superficial review (cf. Basista, 1984; 1988; 1997) of the available experimental data concerning damage processes in engineering materials reveals their complexity and diverse nature. One general conclusion comes out quite clearly, though: damage develops practically in all materials and loading régimes.

The aim of this section is to give a synthetic account of the experimental evidence acquired over the years of laboratory testing and *in situ* observations on brittle materials stressed to failure. The specific damage mechanisms pertinent to the problems considered in the next chapters will be discussed in detail at the beginning of these chapters. The primary concern here is with damage and fracture in brittle polycrystalline rocks. Additionally, the microcracking and corrosion in plain concrete will be addressed in Chapter 3 and Chapter 7.

The quasi-brittle behavior of rocks has a number of features in common with the processes of microcracking, fracture and failure in other quasi-brittle materials such as concrete and ceramics. Most of these similarities result from the intrinsic, heterogeneous, polycrystalline microstructure of these materials. As for crustal rocks, there exists, however, a number of substantial differences in rock fracturing which result from rock burial in the crust. The most important among them are: (1) rocks are subjected to triaxial compressive stresses in the crust, (2) preexisting microcracks, pores and voids are filled with fluids which are typically under pressure, (3) average rate of natural deformation of a crustal rock is very slow. Since crack growth is necessarily a dilatant process involving volume increase, it is thus pressure dependent. Consequently, compressive stresses stabilize the microcrack growth and toughen the material. Conversely, pressurized fluids present in the microstructure tend to weaken the rocks by reducing the confining effect of lateral pressure and by promoting fluid–rock chemical reactions that are conducive to *subcritical* microcrack growth processes (e.g. stress corrosion). It should be underlined that subcritical microcrack growth is an important deformation mode in rocks because the inferred rate of natural tectonic deformation in the crust (strain rates of the order of 10^{-14} 1/s) is much lower than typical engineering rates of strain. For example, the compressive fracture strength of unconfined rock can decrease by a factor of 2 or 3 as the strain rate is reduced form those ordinarily used in laboratory tests (10^{-4}–10^{-6} 1/s) to that associated with natural tectonic deformation (Meredith et al., 1991). Also, since the size of rock masses in engineering problems are many orders of magnitude larger than the sizes of rock laboratory specimens, the scale effect must be considered when modeling and analyzing rock fracture problems *in situ* using the laboratory acquired data. But even under compressive loading, rock deformation proceeds by the growth, interaction and coalescence of numerous tensile microcracks.

2.2. Tension

The tensile damage in polycrystalline rocks deformed in displacement-controlled tests consists in gradual activation of the most favorably oriented and longest preexisting microcracks located at the grain boundaries or within the grains of inferior strength. A destabilized microcrack grows unstably until it is forced to stop by the superior toughness of an adjacent grain on its path. As the external load is further increased, more and more preexisting microcracks become activated causing a nonlinear overall rock response. On the other hand, the tensile fracture of a brittle rock is relatively simple and thoroughly understood. At a certain load level, one of the previously activated and arrested microcracks becomes critical again when K_I at its tip exceeds locally the fracture toughness K_{Ic} of the surrounding material. In all probability, the rock inhomogeneity is unable to trap the crack again for the much longer crack sees the surrounding material as almost homogeneous. The final rupture may thus be seen as an unstable growth of a single macroscopic crack.

The fracture toughness of a polycrystalline rock is generally much higher than that of any of the rock's constituent minerals. On the other hand, for rocks of similar mineralogical composition, K_{Ic} tends to increase with increasing grain size (Meredith et al., 1991). When large variation of grain sizes is present, it is the largest size that has the controlling influence since large grains act as microcrack stoppers. This should not be confused with the ordinary (sample) size effect observed in brittle solids, according to which the fracture strength decreases as the sample size increases. Interestingly, the rising R-curve behavior in function of crack length is typical of many rocks and is being linked directly to inelastic processes taking place ahead and behind the crack tip (microplastic deformations, microvoid formation, frictional interlocking of rough crack surfaces, ligamentary bridging between crack walls, etc.), e.g. Ingraffea (1987).

2.3. Compression

The polycrystalline rocks exhibit a very complex nonlinear response when exposed to compressive loading. The following effects are usually observed in the confined and unconfined compression tests (cf. Jaeger and Cook, 1976; Brace et al., 1966; Peng and Johnson, 1972; Zoback and Byerlee, 1975, Basista and Gross, 1998a):

- threshold-type deviation from linear elastic behavior,
- gradual degradation of elastic constants,
- strong influence of confining pressures on the ultimate strength and failure modes,
- positive dilatancy, i.e. nonlinear volume increase due to opening of axial cracks,
- load-induced anisotropy ensuing from directional process of microcrack evolution,
- hysteresis loops in the stress–strain curves in loading–unloading–reloading cycles,
- pronounced permanent volumetric strain after complete unloading,
- softening regime in strain-controlled tests.

Most of these features are intimately related to the processes of compressive damage and fracture in rocks. Generally speaking, the compressive damage in rocks is much more complex than the tensile one since it is not just an instability of a single, most favorably oriented crack but it generally involves a cooperative action of a distributed array of the microcracks. The cooperative damage process by which these microcracks produce macroscopic failure has remained one of the most elusive problems of modern fracture mechanics. There is no doubt, however, that final failure occurs at a stress which can be much larger than that at which individual microcracks become active. Hence microcrack interactions must play a vital role in compressive fracture of rocks. As already mentioned, direct observations of stress induced microcracks (Peng and Johnson, 1972; Tapponier and Brace, 1976) revealed that microcracks nucleate from the preexisting flaws and grow in a direction subparallel to the maximum principal compressive stress. The confining (compressive) stress plays a stabilizing role in the microcrack growth. If there is no confinement, the final failure is typically unstable and is brought about by the propagation of a few axial cracks forming a vertical splitting surface. By contrast, even a small amount of lateral compressive stress makes individual microcracks extend in a stable manner. A microcrack will extend once the fracture toughness K_{Ic} is exceeded locally to relieve the local stress concentrations, and will then arrest. However, under compression the stress intensity factor is a decreasing function of the microcrack length and individual microcracks only extend until equilibrium $K_I = K_{Ic}$ is reached. An increase in stress difference is needed for further growth of the arrested microcracks and to activate other as yet dormant microcracks. Once a microcrack has grown relaxing the stress locally in a high stress zone, it becomes a relatively low stress zone. It is very likely that the next stress relief will be accommodated by growth of a different microcrack rather than by further extension of the same microcrack since the latter is embedded in a low stress zone. Under the conditions of increasing stress, the population of activated microcracks reaches eventually a density at which microcrack interactions start to play a crucial role. When this has happened, the simple scenario of stress relief (negative feedback) is no more valid since the cooperative action of interacting microcracks may induce stress amplification effects (positive feedback) on other microcracks leading ultimately to overall instability and failure. In stress–strain diagrams this situation corresponds to a flip from strain hardening to strain softening.

Volume changes of both elastic and permanent type are typically observed during rock deformation under compression. At low stresses, the volume first decreases sharply as a result of closure of some initial microcracks and pores. Then it decreases linearly reaching a minimum at an axial stress called C' in the rock mechanics nomenclature. For many rocks, the axial stress C' at which the stress–volumetric strain curve leaves the linear region is about $\frac{1}{2}C$, with C being the rock fracture strength. As the stress further increases, the volume of the specimen increases relative to elastic changes leading to a positive permanent volumetric strain after complete unloading. The positive volumetric changes (dilatancy) are due to the formation of open axial microcracks growing parallel to the maximum principal compression. The magnitude of the dilatancy ranges from $1/5$ to 2 times the elastic volume changes that would have occurred if the rock was simple elastic (Brace et al., 1966).

As far as the overall failure is concerned, brittle rocks in compression may fail in a bewildering variety of modes. In unconfined compression tests specimens tend to fail by vertical splitting (slabbing), Figure 2.1a. At low and intermediate confining pressures failure occurs by localization of deformation on a shear band (or cone fracture), Figure 2.1b. At high confining

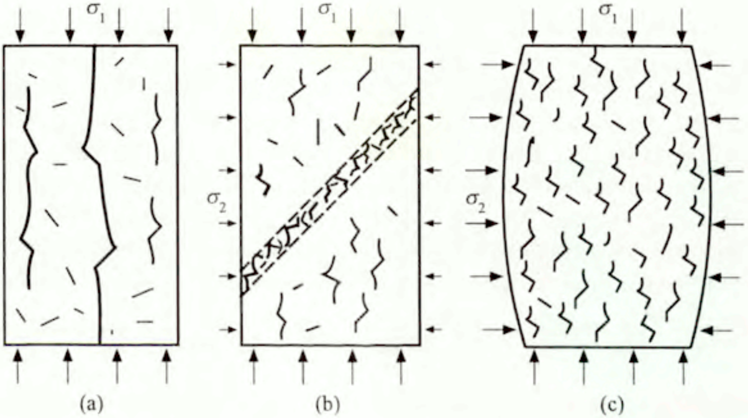

Figure 2.1. Failure modes in brittle rock specimens under compression: (a) vertical splitting in unconfined compression, (b) shear fracture at moderate confinement, (c) pseudo-ductile mode at large confinement.

pressures a single failure surface does not form but the specimen deforms in a pseudo-ductile mode (cataclastic flow) with large scale deformations and many short, homogeneously distributed microcracks, Figure 2.1c. In this case, the material may flow at constant stress or manifest strain hardening.

The deformation and failure mode in rocks tested in compression are highly dependent on the end-boundary conditions. During compressive loading a frictional constraint develops at the interface between the specimen and loading device. A cylindrical geometry when placed in direct contact with rigid platens takes on a barrel shape and a nonuniform stress state develops throughout the cylinder. The specimens of Chelmsford granite examined in Peng and Johnson (1972) subjected to direct contact end conditions failed by faulting. The type of faulting was commensurate with frictional properties of the platens. In material testing the occurrence of a nonuniform stress state is a serious hindrance since the observed response may then be due to unknown boundary conditions – an undesirable effect. Hence, much effort in the laboratory work goes into achievement of a homogeneous deformation by finding an appropriate friction reducer. This is usually done by using thin neoprene or teflon inserts placed between the specimen and the loading platens. Also, steel disks are used for this purpose as well as some specific lubricants such as greases, mineral oils, graphite, stearid acid, and alike (Labuz and Bridell, 1993).

Incidentally, the compressive strength (a constant critical stress for failure), which is a very useful failure parameter for ductile materials, becomes of rather limited utility for rock-like materials. Here, the fracture strength varies with lateral pressure, specimen size and geometry. Instead, the fracture toughness is found to be the fundamental property dictating compressive failure. This fact has long been recognized in materials science where the fracture toughness is a commonly used parameter. In contrast, it is not the case yet with rock mechanics where the fracture strength persists in analyses despite its obvious lack of universality (Peng and Johnson, 1972; Kendall, 1978).

2.4. Shear

The microcracking in brittle rocks under shear loading can formally be viewed as induced by a combined action of tension and compression. Thus the pertinent microcrack growth mechanisms will be those already elucidated in the preceding subsections. A microcrack under pure shear conditions tends to leave its original plane by kinking in the direction of the maximum energy release rate. This is in accordance with the Erdogan and Sih (1963) criterion which postulates that crack growth will occur in a direction perpendicular to the maximum principal (hoop) stress. Incidentally, the Erdogan and Sih criterion proved very accurate in experiments and is now widely used in fracture mechanics (cf. Broek, 1974; Gross, 1996).

Likewise, when the shear mode (Mode II) is superposed onto the tensile mode (Mode I), a common tendency for a brittle crack is to seek a trajectory which minimizes the shear loading. Consequently, under combined loading the shear stresses deflect the microcrack away from its own plane causing the so-called microcrack "directional instability" (Lawn and Wilshaw, 1975). This deflection always tends towards the orientation of minimum shear. It may be concluded that the shear stresses play a "corrective role" restoring the kinked microcracks to a stable path perpendicular to the greatest principal tensile stress (pure Mode I). In contrast to Mode II, a Mode I microcrack is said to have "directional stability" since it is favored to extend in its original plane.

Genuine shear fractures (no kinking) do occur in rock masses when large geological pressures suppress the tensile mode. This is usually accompanied by plastic deformations of individual crystals (Jaeger and Cook, 1976).

2.5. Temperature effects

The influence of temperature on the fracture of rocks, although beyond the scope of this thesis, will now be briefly addressed. In essence, the fracture toughness (K_{Ic}) and the brittle-ductile transition are two (interrelated) material characteristics that are most sensitive to the temperature effects.

Generally, low temperatures induce lower values of the fracture toughness emphasizing the brittle type of fracture. High temperatures lead to higher values of the fracture toughness and thus to ductile fracture (Kanninen et Popelar, 1985).

The transition from a typical brittle behavior to fully ductile behavior is governed by rather ill-defined, material-dependent values of the confining pressure and temperature. It has been observed in laboratory tests that elevated temperatures may drastically reduce the brittle-ductile transition pressure. For example, a granite specimen manifesting brittle response in a confined compression test at room temperature becomes almost fully ductile if the temperature is raised to 800°C (Griggs et al., 1960).

The temperature effects and the brittle-ductile transition are increasingly significant in geology and geophysics of the lower crust where they are readily observed. They are also of primary practical importance in mine engineering and tunneling where elevated temperatures must be taken into account due to enhanced fire risk. These effects, however, are not of "great interest in rocks mechanics since the necessary pressures and temperatures rarely occur" (Jaeger and Cook, 1976). Similarly, rock degradation effects due to cyclic temperature changes, ice build-up in pores, detrimental chemical reactions (rock weathering) are interdisciplinary topics pursued in geophysics and structural geology for their importance in geological engineering projects.

2.6. Acoustic emission

Acoustic emission (AE) is a powerful experimental tool in the study of rock damage and fracture. An acoustic emission is defined as an elastically radiated wave generated by the rapid release of mechanical energy within a material. The energy release is caused by irregular microstructural movements like microcracking, dislocation slip, or phase transition. The acoustic signals that are spontaneously generated from the microcracking provide information about the size, location and deformation mechanisms of the events. According to Zhang et al., (1996), the first AE study in materials science was concerned with a phase transition in steel (Forster and Scheil, 1936) while in geological sciences it was first employed to predict rock bursts in mines (Obert, 1941). The acoustic emission studies in rocks utilize hypocenter mapping, event statistics and focal mechanisms to investigate damage evolution, crack formation and failure modes. There exists a certain overlap between AE and seismology (e.g. Mogi, 1962). Both fields are concerned with the generation and propagation of elastic waves although at different scales and frequency ranges. Development of AE research is thus strongly motivated by earth sciences since rock microfracturing and the formation of earthquake ruptures seem to be operated by similar processes. It has been found that brittle fracturing obeys similar statistics over source dimensions spanning more than eight orders of magnitude from large crustal earthquakes to laboratory subgrain-size microcracks. To this end, the well known Gutenberg–Richter relation for earthquake events seems also to hold in laboratory AE studies.

The literature pertinent to AE applications in rock deformation is quite rich. Recently, Scott (1991) and Lockner (1993) published exhaustive state-of-the-art articles providing detailed accounts of the accomplishments and drawbacks of acoustic emission.

Laboratory AE studies can be classified as follows: (a) simple counting of AE events, (b) location of hypocenters of AE events, (c) analysis of full waveform data to determine fault plane solutions from first motion. Recent laboratory studies concentrate on (b) and (c) categories, i.e. on spatial and temporal determination of AE hypocenters with complete focal mechanism solution. This requires precise arrival time data of AE signals recorded by a set of AE sensors. The AE positions are then calculated numerically using existing algorithms and the location errors are estimated. For example, the Lockner's numerical algorithm modified in Zhang et al. (1996) and used for dry sandstone yielded the hypocenters locations with an error less than ±3 mm.

The results in Zhang et al. (1996) are quite illuminating and consequential for the modeling purposes of the present thesis. These authors have found that in dry sandstone specimens under compression two distinct classes of AE signals can be distinguished: "blue AE" being short-pulse, high-energy events, and "red AE" with long duration times and low energies. It has been further identified that red signals are attributable to shear couples whereas high-energy blue signals are due to tensile microcrack growth (pore crushing occurring in hydrostatic stress states may also fall into blue category). From the time evolution of the red and blue AE, the authors concluded that both shear and tensile events occurred simultaneously throughout the experiment. This might suggest that the sliding microcrack mechanism of brittle deformation, involving coupling of frictional shearing and tensile wing opening, was indeed operative in that experiment. Similar observation was also made by Lockner (1993). Before failure, the red AE dominated over the blue ones indicating localized failure mode in form of a shear-band.

Another important aspect of the compressive damage in rocks is the so-called *Kaiser effect*, a well known phenomenon in metallurgy and laboratory AE studies. Kaiser (1950) was the first to notice that for cyclic loading of metals, AE is observed in the first cycle of a given stress path but during subsequent cycles there is an absence of acoustic emissions at stresses below the previous maximum stress, with an abrupt increase in AE when that stress level is exceeded. More that a decade later, a similar effect was reported in rocks under compressive loading (Goodman, 1963). Kaiser effect can be a very important source of information about irreversible damage in rocks since appreciable new microcracking will occur only when the previous (damage-producing) stress state is exceeded. This essentially was the motivation of Holcomb and Costin (1986) to use Kaiser effect as an indicator in determining the magnitude and shape of the damage surface for rocks. It should be stressed that Kaiser effect does not reliably occur in all rocks and at all stress levels. For example, while it occurred as a rule in coarse-grained granite up to the failure stress, fine-grained leptite samples produced AE at stress levels significantly below previous peak stress, what rules out the Kaiser effect in that particular rock.

2.7. Subcritical microcrack growth

At elevated temperatures and in presence of reactive environments microcracks may grow in a stable quasi-static manner at stress intensities considerably below the fracture toughness. This phenomenon of subcritical microcrack growth has been observed in various quasi-brittle materials including glass, ceramics and rocks. It is concluded from a vast body of experimental evidence that subcritical microcrack growth in rocks at low temperatures is governed by stress corrosion, with water being the most active reagent. The overall trend is that the more complex the rock microstructure, the lower is its susceptibility to subcritical microcrack growth. In other words, the more heterogeneous rocks behave in more brittle manner (Atkinson and Meredith, 1987). This observation is at variance with the conclusion of Cox and Paterson (1990) that heterogeneous rocks with large initial flaw distribution behave in a less brittle manner than more homogeneous rocks.

2.8. Dynamic damage

For the sake of completeness, consider the problem of damage produced by impulsive loads of high intensity and short duration such as projectile impact, air-shock loading, explosion and alike. Dynamic loading of this kind induces the so-called spall damage which has some characteristic features as compared with damages caused by quasi-static loads (Davison and

Stevens, 1973; Perzyna, 1986). Spall damage is a process of gradual internal degradation of a material implied by the rarefaction waves that follow the compressive waves caused by the impact. In general, it consists of the same basic phases as static damage, i.e. nucleation, growth and coalescence of microcracks or voids, while the overall failure is realized by a complete separation of a target into disjoint elements. Ductile spall damage takes form of roughly spherical voids (Davison and Stevens, 1973), brittle spall is associated with the development of planar microcracks (Seaman et al., 1976; Shockey et al., 1974). In one-dimensional wave propagation problems, the spall damage usually occupies a major part of the target volume. However, the concentration of both voids and microcracks reaches a maximum value in narrow zones perpendicular to the impact direction and localized near the center of the target where intersection of several rarefaction tensile waves occurs.

In brittle spalling, a process of fragmentation occurs as the microcracks begin to interact and link up. Fragments of various sizes are produced by the intersections of microcracks having different lengths. Since the fragmentation necessarily involves some voided spaces among the separated parts, the stress in the effective cross section must increase in order to sustain the external load. This in turn leads to the nucleation of more and more microcracks that form new fragments, and the whole process reaches a self-accelerating cataclysmic stadium which ends up by a complete disintegration of the sample (Seaman et al., 1976).

Chapter 3

Micromechanical damage model for brittle materials in tension

Abstract. In this chapter, a simple constitutive model is proposed to predict nonlinear response of brittle solids loaded in tension. Motivated by experimental evidence for concrete specimens stretched in displacement-controlled rigid loading devices, a two-dimensional process model is formulated based on the micromechanics of a tensile microcrack. Reminiscent of the R-curve in fracture mechanics, a functional dependence of the stress intensity factor on the microcrack length increment is introduced leading to an evolution law for microcrack growth. A nonlinear incremental stress–strain relationship is derived for the uniaxial case and then generalized for two-dimensional stress states. The present formulation combines linear elastic fracture mechanics and thermodynamic framework with microstructural internal parameters. A single microcrack as well as analytically solvable systems of interacting microcracks are considered.

3.1. Physical evidence

In plain concrete, the initial (pre-load) microdefects are located most frequently at the aggregate-matrix interfaces since these are the weakest links of concrete microstructure (cf. Table 3.1).

Table 3.1. Typical values of fracture toughness for constituents of plain concrete (cf. Zaitsev, 1982).

	Cement matrix	Aggregate	Aggregate-matrix interface
Fracture toughness K_{Ic}/K_{Ic}^{M}	1	>1	0.5

One possible source of these (bond) microcracks is the mix water migration due to bleeding during the forming process. Water lenses may get trapped at the undersides of coarse aggregates while migrating towards free surfaces. When drying up these lenses transform into bond microcracks at

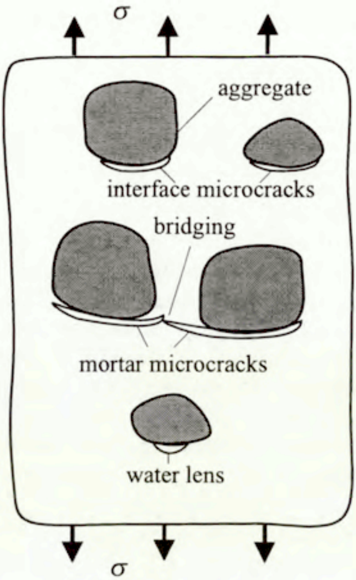

Figure 3.1. Damage mechanism for concrete in tension.

the interfaces as sketched in Figure 3.1. Another source of the pre-load microcracks are volume changes due to shrinkage during the hardening of fresh concrete. It is observed that shrinkage microcracks emanate radially from the aggregate particles in contrast to bond microcracks which grow mainly along the aggregate facets.

Under the action of macroscopic tensile stress, microcracking commences at those aggregate-matrix interfaces that are oriented almost perpendicularly to the load axis. The destabilized microcrack grows along the aggregate facet until it comes to the facet edge where it is forced to stop by a superior toughness of the mortar. Adjacent interface microcracks bridge among themselves forming continuous microcracks patterns. When the fracture toughness of the mortar is exceeded, bond microcracks branch into the mortar, coalesce and form a transverse macrocrack. The macrocrack, if not stopped by an obstacle on its path, grows in an unstable manner and the final rupture is imminent.

If a direct tension test is stress-controlled, the final rupture is abrupt and takes place at the highest recorded stress, i.e. at the peak stress f_t (tensile strength). However, if the uniaxial tension test is strain-controlled and the loading device is very stiff, then the strain–stress curve shows three distinct phases of linear elastic, hardening, and softening behavior, Figure 3.2. In other words, the macroscopic response of concrete to direct tension is qualitatively quite similar to that of the uniaxial compression revealing also a rounded apex (Evans and Marathe, 1968). The major difference is the magnitude of sustainable stresses. For concrete, the average tensile to compressive strength ratio (f_t/f_c) varies form 1:8 to 1:12.

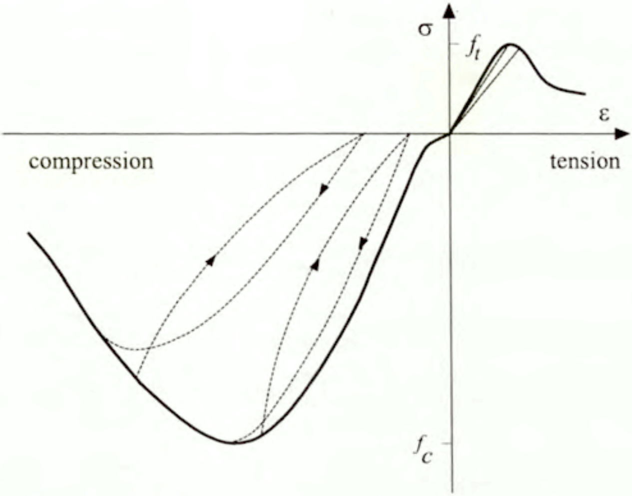

Figure 3.2. Illustration of complete stress–strain curves for concrete in uniaxial strain-controlled tests in stiff loading machine.

3.2. Theoretical setting

The primary objective of this chapter is to propose a workable two-dimensional constitutive model for predicting the time-independent stress–strain relation for concrete-like materials subjected to tension, (cf. the right hand part of Figure 3.2). The model will be based on the micromechanics of brittle damage under tensile stresses. In order to better understand the underlying micromechanics and to make the model tractable, we shall start with the simplest case of uniaxial constant loading and generalize it subsequently to biaxial loading states.

In detail, the proposed model is organized as follows. First, the growth of a single microcrack in a unit cell under homogeneous uniaxial tension is considered (Section 3.2). Then, microcrack interactions under uniaxial tension are studied for their possible effect on the stress–strain curves (Section 3.3). Finally, the one-dimensional model of Section 3.3 is extended to two dimensions by considering an elastic plate with N non-interacting randomly distributed microcracks under plane stress (strain) conditions (Section 3.4). Evidently, Section 3.2 could have been handled as a special case of Section 3.4 but the chosen sequence seemed more didactic.

In micromechanical damage models aimed at computing overall constitutive laws the concept of representative volume element (RVE) is usually employed (e.g. Aboudi, 1991; Ostoja-Starzewski, 1994; Krajcinovic, 1996; Nemat-Nasser and Hori, 1999). The minimum prescription for the RVE is that (a) it must be large enough to be structurally entirely typical of the whole body, i.e. the material within the RVE must be statistically homogeneous, and (b) it must at the same time be small enough compared to the whole body since on the macroscopic level it plays the role of a material point (satisfying the postulate of the local state). In terms of computational micromechanics, the size of a finite element must not be smaller than the size of the RVE if the discretization is to be objective. On the other hand, if the stress field within the material is inhomogeneous, the finite elements should be as small as possible to ensure their statistically homogeneous response. Evidently, these two conditions impose contradictory requirements on the size of the RVE and the finite elements (cf. Krajcinovic, 1996). The properties of the RVE should be insensitive to the boundary conditions (traction vs. displacement) as long as these conditions are macroscopically uniform. Rigorously speaking, for randomly damaging bodies the RVE concept is an approximation. According to the homogenization theory (e.g. Gambin and Telega, 2000), an RVE is of finite size only for deterministically periodic distributions of microcracks. Consequently, in real brittle solids, inherently exhibiting some randomness in microcrack nucleation and evolution, the finite size of an RVE is based on experimental observations rather than on a mathematical proof. Nevertheless, as numerous workable RVE-based micromechanical damage models show, the RVE approximation proved sufficiently accurate for modeling brittle material response preceding the softening regime.

The stress $\boldsymbol{\sigma}^{\Gamma}$ acting on the outer boundary Γ of the RVE necessitates a separate comment. In general $\boldsymbol{\sigma}^{\Gamma}$ may fluctuate along Γ. However, it is a common modeling assumption that $\boldsymbol{\sigma}^{\Gamma}$ be replaced by its volume average $\bar{\boldsymbol{\sigma}}$. It is argued that putting $\boldsymbol{\sigma}^{\Gamma} = \bar{\boldsymbol{\sigma}}$ will affect only a boundary layer of the RVE. If the remotely applied stress $\boldsymbol{\sigma}^{\infty}$ is such that the stress field in the virgin material would be homogeneous, then it approximately holds $\boldsymbol{\sigma}^{\Gamma} \approx \boldsymbol{\sigma}^{\infty}$ (cf. Kachanov, 1993). In the analysis to follow, the remote stress boundary conditions are homogeneous and the matrix material is homogeneous as well. Consequently, the approximation $\boldsymbol{\sigma}^{\Gamma} = \bar{\boldsymbol{\sigma}} = \boldsymbol{\sigma}^{\infty}$ is justified. In the sequel, the overbar for stresses and strains will be dropped and it will tacitly be assumed that $\boldsymbol{\sigma} = \bar{\boldsymbol{\sigma}} = \boldsymbol{\sigma}^{\infty}$ and $\boldsymbol{\varepsilon} = \bar{\boldsymbol{\varepsilon}}$.

Consider now an infinite, isotropic, elastic plate subjected to uniaxial tension. As has been stressed in the preceding section, in uniaxial tensile tests only those microcracks that are oriented perpendicularly to the load axis experience substantial growth while all other ones are inconsequential for the material response. Therefore, it is assumed that the damaged plate contains only parallel (noninteracting) microcracks of the average length $2a$. For studying purposes, instead of an RVE with statistically homogeneous distribution of open microcracks (cf. Section 3.4), a representative unit cell with a single microcrack under uniaxial stress $\sigma = \sigma^{\infty}$ will be considered, Figure 3.3. The unit cell is meant here to be a microcrack-attached characteristic area whose size ΔA will be limited by the condition that no interaction is admissible between the adjacent microcracks. It is further assumed that the microcrack growth is self-similar for the whole deformation process to be modeled.

The complementary energy density stored in the damaged plate consists of two terms, namely that of the energy density ψ^0 of the virgin elastic material being solely a function of stresses, and that of the change $\Delta\psi$ due to appearance of a microcrack, depending both on the stresses and the microcrack length:

$$\psi(\boldsymbol{\sigma}, a) = \psi^0(\boldsymbol{\sigma}) + \Delta\psi(\boldsymbol{\sigma}, a). \tag{3.1}$$

The complementary energy density (3.1) is supposed to be the Gibbs potential, i.e. a scalar function of the stress tensor whose derivative with

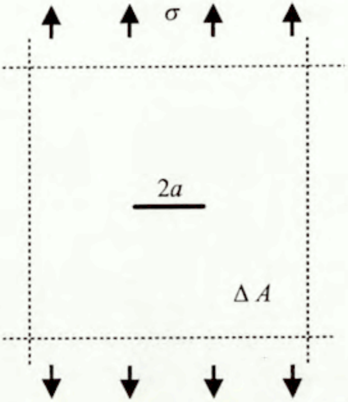

Figure 3.3. Unit cell containing single microcrack under uniaxial tension.

respect to a stress component furnishes the corresponding strain component

$$\varepsilon_{ij} = \left.\frac{\partial \psi}{\partial \sigma_{ij}}\right|_{a=\text{const.}} = f(\sigma_{ij}\,,\, a). \tag{3.2}$$

The microcrack length may be considered here as a microstructural internal variable reflecting locally the current state of material deterioration. Note that Equation (3.2) holds if the microcrack length is held fixed. This is nothing else but a basic premise of the formalism of the themodynamics with internal variables (cf. Rice, 1971, 1975; Kestin, 1992, etc.). According to that formalism, an irreversible thermodynamic process can be approximated by a sequence of fictitious constrained equilibrium states with the internal variables somehow frozen at their current values. Equilibrium is thus induced by the thermodynamic forces conjugate to the internal variables. To make the constitutive framework complete, it is necessary to endow the internal variables with kinetic equations (evolution laws) relating them to their conjugate thermodynamic forces. In the next chapter, the formalism of internal variables will be addressed in more detail in the context of brittle damage processes.

In terms of Equation (3.2), the thermodynamic force conjugate to the internal variable a is the corresponding elastic energy release rate G. Therefore, the simplest choice when formulating a kinetic equation for a is to assume that the microcrack begins to grow if the corresponding stress intensity factor at the microcrack tip reaches some critical level (Griffith criterion)

$$K_I = K_{Ic}\,, \tag{3.3}$$

where K_I is the Mode I stress intensity factor and K_{Ic} is the fracture toughness. Routinely, Equation (3.3) is considered as a fracture condition. It may also be seen, though, as the integrated form of a kinetic equation (evolution law) for the microcrack length. The stress intensity factor describes the loading of a crack and depends on the stress state and the configuration of microcracks in the unit cell. It can always be expressed in the following form no matter how complex the geometry of the microcrack system might be

$$K_I = \sigma\sqrt{\pi a}\,\tilde{f}(a, b, c, \ldots), \tag{3.4}$$

where b, c, …, stand for some geometrical parameters; if there is no crack interaction then $\tilde{f} = 1$. Usually, it is assumed that K_{Ic} is a material constant characterizing the material resistance to crack growth. However, in real brittle materials the energy required for the crack growth is larger than the pure surface energy needed to create new surfaces since the process of crack evolution is accompanied by certain inelastic, energy consuming phenomena occurring in front of the crack tip. These are, for instance, microplastic deformations observed even in brittle materials, nucleation of microvoids, etc. These phenomena depend on the history of deformation, thus on the crack growth. Once K_{Ic} is to be a measure for the material resistance to crack growth, it should depend on the crack length. This conclusion, experimentally well supported for macrocracks, is the central point of the R-curve analyses (Broek, 1974). Here, it is postulated that the same mechanism is relevant for microcracks at the level of grains. This assumption is also shared by some other authors (cf. Costin, 1983; Zaitsev, 1982). Consequently, in contrast to the Griffith fracture criterion (3.3), K_{Ic} is no more a material constant but a material function depending on the change of the microcrack length Δa:

$$K_I = K_{Ic}(\Delta a). \tag{3.5}$$

A more precise form of (3.5) can be deduced on examining the available experimental data pertinent to the crack resistance curves ($K_{Ic}(\Delta a)$ or R-curves) for rocks, concrete, or mortars (e.g. Schmidt and Lutz, 1979; Ingraffea, 1987; Mai and Cotterell, 1982; Meredith, 1989; Mai, 1990; Ouyang et al., 1990, Steinbrech et al., 1990). These data suggest that a $K_{Ic}(\Delta a)$ curve is initially very steep and keeps rising (with continuously changing tangent) as the crack extends until a steady state (plateau) is reached where the curve becomes flat. Even though this shape is on average typical of the brittle materials considered, the specific slope of the $K_{Ic}(\Delta a)$ curve depends on the material, the stress state at the microcrack tip and the fracture mechanism. The slope of the $K_{Ic}(\Delta a)$ curve may also vary with specimen's size and geometry — an undesirable effect. However, for small cracks in an infinite plate (cf. present model) the assumption of a size and geometry independent crack resistance curve is correct (Mai, 1991; Ouyang et al., 1990; Broek, 1974).

Based on the above experimental evidence, the following exponential form for the material function $K_{Ic}(\Delta a)$ is proposed (Basista and Gross, 1985)

$$K_{Ic}(\Delta a) = K_{cu} - (K_{cu} - K_{cl})\, e^{-\eta\, \Delta a / a_0}\,, \tag{3.6}$$

where K_{cu}, K_{cl}, η are material constants and a_0 is the initial microcrack half-length. The expression (3.6) depicted in Figure 3.4 meets the requirements imposed by the experimental observations and is relatively simple to handle analytically. In fact, it introduces two additional material constants (K_{cl}, η) as compared with the Griffith criterion (3.3). It should be stressed that the specific choice of the material function (3.6) is not crucial for the present model. Other possible expressions for K_{Ic}, accounting for the energy barriers distribution within the material, can be incorporated if required. For example, a periodic form of $K_{Ic}(\Delta a)$ could be used when modeling the microcrack growth in a periodically inhomogeneous solid (cf. Kasperkiewicz, 1983), Figure 3.4.

Having specified the $K_{Ic}(\Delta a)$ in Equation (3.6), the next step consists in substituting it into (3.5) and solving the latter for the microcrack length, namely

$$a = F^{*}(\sigma). \tag{3.7}$$

However, this leads to a transcendental equation which is undesirable in the present analytical approach. The situation gets exacerbated when more complex microcrack configurations are considered. To bypass this problem, the following algorithm is proposed. Reciprocally to (3.7), it holds

$$\sigma = F(a), \tag{3.8}$$

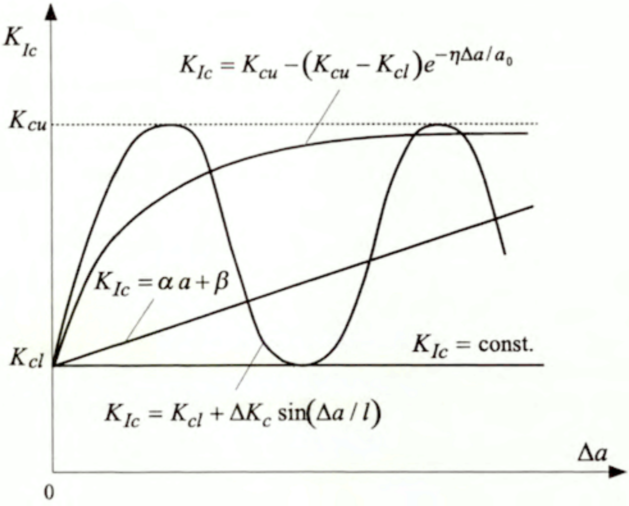

Figure 3.4. Various shapes of critical stress intensity function $K_{Ic}(\Delta a)$ (Basista and Gross, 1985).

which is straightforward on account of the algebraic structure of Equations (3.4), (3.5), (3.6).

At this stage of model development it proved convenient to switch to incremental formulation by computing da from (3.8). Unlike the microcrack length a, its increment da can always be extracted from Equation (3.8). With the notation used in (3.2) and (3.8), it follows that (Basista and Gross, 1985)

$$\mathrm{d}\varepsilon = \frac{\partial f}{\partial \sigma}\,\mathrm{d}\sigma + \frac{\partial f}{\partial a}\,\mathrm{d}a, \qquad \mathrm{d}\sigma = \frac{\partial F}{\partial a}\,\mathrm{d}a. \tag{3.9}$$

Hence,

$$\mathrm{d}\varepsilon = \left[\frac{\partial f}{\partial \sigma} + \frac{\partial f}{\partial a}\left(\frac{\partial F}{\partial a}\right)^{-1}\right]\mathrm{d}\sigma. \tag{3.10}$$

It is advantageous to proceed henceforth with dimensionless variables defined as follows

$$\tilde{\sigma} = \sigma/\sigma_0\,, \qquad \tilde{\varepsilon} = \varepsilon/\varepsilon_0\,, \qquad \tilde{a} = a/a_0\,, \tag{3.11}$$

where σ_0 , ε_0 , are the values of stress and strain at which the microcrack of initial length $2a_0$ starts to grow.

To obtain a particular constitutive equation it is necessary to determine the functions f and F. The first task is commensurate with derivation of the Gibbs energy density ψ for a particular microcrack configuration in the unit cell. For a single microcrack in the unit cell under uniaxial tension (Figure 3.3) ψ can rigorously be expressed as

$$\psi(\sigma, a) = \frac{\sigma^2}{2E_0} + 2\int_0^a \frac{K_I^2}{E_0\,\Delta A}\,\mathrm{d}a = \frac{\sigma^2}{2E_0}\left(1 + \frac{2\pi a^2}{\Delta A}\right), \tag{3.12}$$

where E_0 , ν_0 are the Young modulus and the Poisson ratio of the virgin (microcrack-free) material. The function F follows from Equations (3.5) and (3.6) governing the microcrack growth, and is given by (Basista and Gross, 1985)

$$\sigma = F(a) = \frac{1}{\sqrt{\pi a}}\left[K_{cu} - (K_{cu} - K_{cl})\,e^{-\eta\,\Delta a/a_0}\right]. \tag{3.13}$$

Finally, the strain–stress relation follows from (3.10)–(3.13) as (Basista and Gross, 1985)

$$\mathrm{d}\tilde{\varepsilon} = \frac{1}{1+\kappa}\left[1 + \kappa\tilde{a}^2 + 4\kappa\tilde{a}^2\,\frac{\gamma^* - (\gamma^* - 1)\,e^{\eta(1-\tilde{a})}}{(\gamma^* - 1)\,e^{\eta(1-\tilde{a})}(2\eta\tilde{a} + 1) - \gamma^*}\right]\mathrm{d}\tilde{\sigma}, \tag{3.14}$$

with

$$\tilde{\sigma} = \frac{1}{\sqrt{\tilde{a}}}\left[\gamma^* - (\gamma^* - 1)\,e^{\eta(1-\tilde{a})}\right]. \tag{3.15}$$

The dimensionless constants κ and γ^* are defined as follows

$$\kappa = \frac{2\pi\,a_0^2}{\Delta A}, \qquad \gamma^* = \frac{K_{cu}}{K_{cl}} \geq 1. \tag{3.16}$$

Note that κ can be interpreted as a microcrack density parameter. It can be deduced that for non-interacting microcracks κ should not exceed 0.1 (cf. Gross, 1982).

The stress–strain curves in the integrated form obtained form (3.14), (3.15) are depicted in Figure 3.5 for a few exemplary values of material parameters η, γ^*. Qualitatively, these curves are, indeed, quite similar to

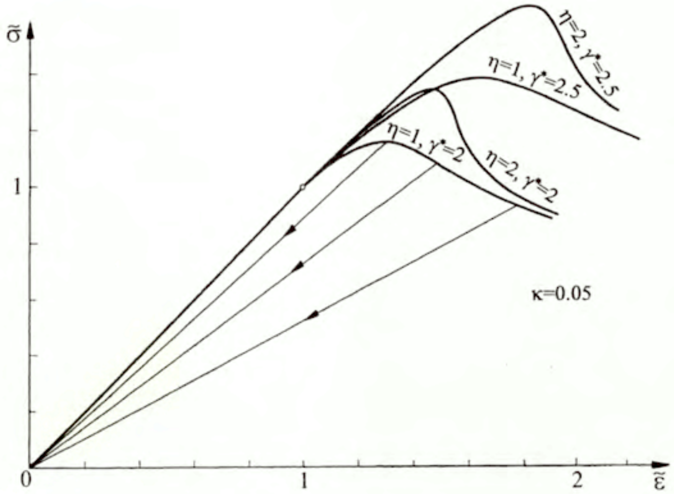

Figure 3.5. Normalized stress–strain curves predicted by present model (Basista and Gross, 1985).

the experimental ones for concrete in direct tension (Evans and Marathe, 1968; see also Figure 3.2). They properly reflect the linear and the hardening regimes. Apparently, the model is also capable of describing the softening regime and the asymptotic behavior of concrete at the advanced stage of straining. However, the last two properties are to be taken with a bit of caution since they are nothing more but a numerical outcome of the assumed evolution law (3.6). This law, in turn, ceases to be valid if a dominant macrocrack appears, i.e. beyond the peak in σ–ε curve.

A more general comment seems in order at this point. This and other micromechanical or phenomenological damage models aimed at formulation of constitutive equations in terms of average stresses and strains should not be over-interpreted and freely extended to the regimes where the averages are meaningless. In terms of the present model this is the case when the interacting microcracks link to form a dominant cluster (macrocrack). In fact, in such a situation it is the macrocrack that contributes most to the inelastic strain (or more correctly – displacement) while the remaining parts of the material volume may respond elastically or even experience elastic unloading. The formation of a macrocrack usually violates the necessary conditions for statistical homogeneity. Since the qualitative change of the material behavior observed at the peak of σ–ε curve must be related to the appearance of a macrocrack, any extension of a continuum damage model beyond the peak, even if formally possible (e.g. Figure 3.5), seems to be of dubious merit.

In unloading, the present model predicts that all deformation paths tend to the origin 0 and no permanent strain remains after complete unloading. On the other hand, there will be no recovery within the damaged material during unloading (no microcrack healing) which seems to be a reasonable assumption for concrete in tension.

It is instructive to re-examine the case when the classical Griffith condition (3.3) is assumed to rule the microcrack growth. From (3.2), (3.3) and (3.12) it follows that (Basista and Gross, 1985)

$$\bar{\varepsilon} = \frac{1}{1+\kappa}\left(\bar{\sigma} + \kappa\frac{1}{\bar{\sigma}^3}\right). \tag{3.17}$$

Some illustrative numerical results furnished by (3.17) are shown in Figure 3.6. The material exhibits linear elastic behavior up to the point where the K_I reaches its critical level. At this point the microcrack starts to grow making the overall material response nonlinear. However, for physically admissible values of κ the curves $\bar{\sigma}$–$\bar{\varepsilon}$ go backwards. This means that the material would manifest an unstable behavior as a sudden jump in stresses down to the point from which the microcrack would continue to grow in a stable manner. Obviously, the reason for such an unstable material response is hidden in the nature of Griffith cracks, i.e. once a Griffith crack starts to grow in a homogeneous, linear elastic body, its growth cannot be arrested. In other words, when the classical Griffith criterion (3.3) is used in the constitutive model for an elastic microcracked solid under tension, a direct consequence of that is the unstable material behavior (Equation (3.17), Figure 3.6) that contradicts the experimental observations, Figure 3.2. Apparently, the model based on (3.3) is insufficient to capture the salient features of the damage growth in a heterogeneous brittle material under tension. Equations (3.5)–(3.16) have shown that to get closer to the real material response, a more sophisticated description of the microcrack growth is necessary.

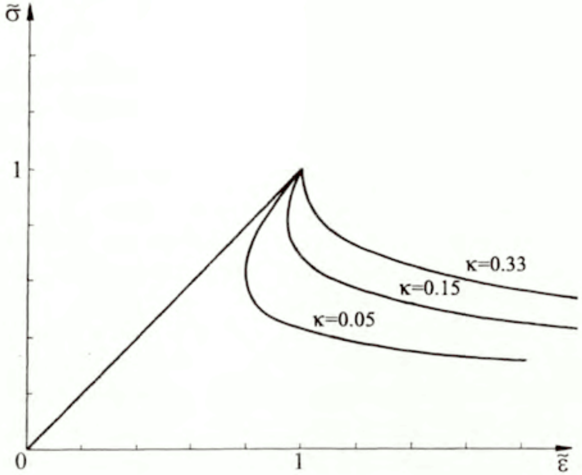

Figure 3.6. Unstable $\tilde{\sigma}$–$\tilde{\varepsilon}$ response induced by Griffith microcracks in homogeneous matrix (Basista and Gross, 1985).

3.3. Microcrack interaction in tension

The microcracks distributed within the material volume are in fact not isolated objects but they necessarily exert some influence on each other. The interaction effects may amplify or shield the growth of individual microcracks. As was mentioned in Section 2.1, in brittle materials loaded in tension the microcrack interaction is less consequential for the overall fracture than in compression because, as the experiments show, it is the largest and most favorably oriented microcrack that triggers the overall rupture of the specimen. However, in certain microcrack configurations, like collinear crack arrays, the interaction effects might be quite important for the overall material response under tension.

The objective of this section is to investigate the simplest possible cases of interaction of open microcracks in order to show how the interaction effects can be incorporated in the developed constitutive framework and how they affect the σ–ε response of the unit cell. Two specific cases will be examined in detail: (a) a pair of collinear microcracks under uniaxial tension, (b) an infinite row of collinear microcracks under uniaxial tension.

Both problems have analytical solutions what makes the analysis traceable but is not mandatory for the present framework.

Consider two collinear microcracks in the unit cell of area ΔA subjected to the uniaxial tension, Figure 3.7. To avoid microcrack overlapping, the ratio $\chi_0 = a_0/c_0$ should be smaller than $1/4$, a_0 being initial microcrack length; the distance c_0 is fixed. It is assumed that these microcracks influence each other but there is no interaction between the adjacent unit cells. It is intuitively obvious that the most dangerous zone for this elementary microcrack system is the surrounding of the inner tips denoted by the plus signs in Figure 3.7.

The problem at hand is symmetric and K_I^+ is always larger than K_I^- meaning that the microcrack growth condition (3.5) is always satisfied for the inner tips first. Consequently, it is legitimate to assume that the microcracks will extend by moving their inner tips towards each other along the line of the initial microcracks while leaving the positions of the outer tips unchanged. This complicates significantly the computations since the middle points distance b varies with increasing microcrack length. The corresponding K_I factor accounting for the microcrack interaction reads (Tada et al., 1974)

$$K_I = \sigma\sqrt{\pi a}\, g(\lambda), \tag{3.18}$$

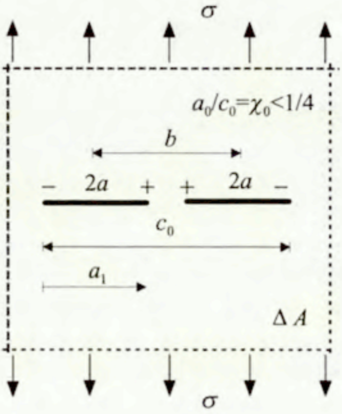

Figure 3.7. Two collinear microcracks in unit cell under uniaxial tension.

with

$$g(\lambda) = \frac{b_2^2 \, \frac{E_1(l_2)}{E_2(l_2)} - a_2^2}{a_2 \sqrt{b_2^2 - a_2^2}} = 1 + \frac{1}{2}\lambda^2 + \frac{1}{2}\lambda^3 + \frac{11}{8}\lambda^4 + \cdots , \tag{3.19}$$

where $a_2 = \frac{1}{2}(b-a)$, $b_2 = \frac{1}{2}c_0$, $l_2 = \sqrt{1-(a_2/b_2)^2}$ and $E_1(l_2)$, $E_2(l_2)$ are the elliptic integrals of the first and second order, respectively. The parameter λ is defined as

$$\lambda = \frac{a}{b} = \frac{a_1}{2b} = \frac{a_1}{2(c_0 - a_1)} , \tag{3.20}$$

where a_1 has been introduced for computational expedience since the microcracks extend unilaterally by moving the inner tips only.

The Gibbs energy density of the representative unit cell containing two collinear interacting microcracks is given by (Basista and Gross, 1985)

$$\begin{aligned} \psi &= \frac{\sigma^2}{2E_0} + 2\int_0^{2a} \frac{[K^+(a_1)]^2}{\Delta A \, E_0} \, \mathrm{d}a_1 \\ &= \frac{\sigma^2}{2E_0} + \int_0^{2a} \frac{\sigma^2 \pi a_1}{\Delta A \, E_0} \, [g(\lambda)]^2 \mathrm{d}a_1 . \end{aligned} \tag{3.21}$$

In the extreme case of two microcracks placed far apart from each other, i.e. for $b \to \infty$, it follows that $g(\lambda) \to 1$ and (3.21) reduces to (3.12), the latter expressed for two non-interacting microcracks.

The microcrack growth condition (3.5)–(3.6) takes now the form

$$\sigma\sqrt{\pi a}\, g(\lambda) = K_{cu} - (K_{cu} - K_{cl})\, e^{-\eta\, \Delta a / a_0} . \tag{3.22}$$

Equations (3.18)–(3.22) constitute the basic set of equations from which the stress–strain relation can be derived along the lines of the preceding section. The incremental and the integrated forms of this relation are algebraically too involved to be presented here and are relegated to Appendix 3.1. The ensuing $\bar{\sigma}$–$\bar{\varepsilon}$ curves are shown in Figure 3.8. Up to the point A, the material exhibits a linear elastic behavior. Then comes a slightly nonlinear (hardening) portion AB, apparently due to small changes of the internal energy as limited by the geometry of the microcrack configuration. Finally, the axial stress drops (BC) to the softening portion of the curve. A possible interpretation of this response under the overall strain-controlled conditions is that the two microcracks presumably have

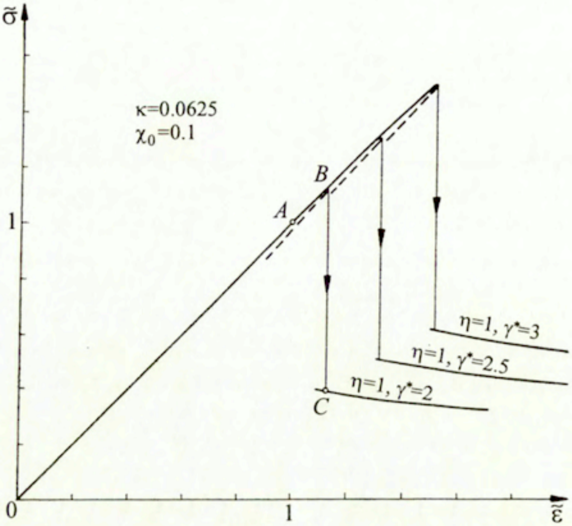

Figure 3.8. Stress–strain curves for unit cell with two collinear microcracks (Basista and Gross, 1985).

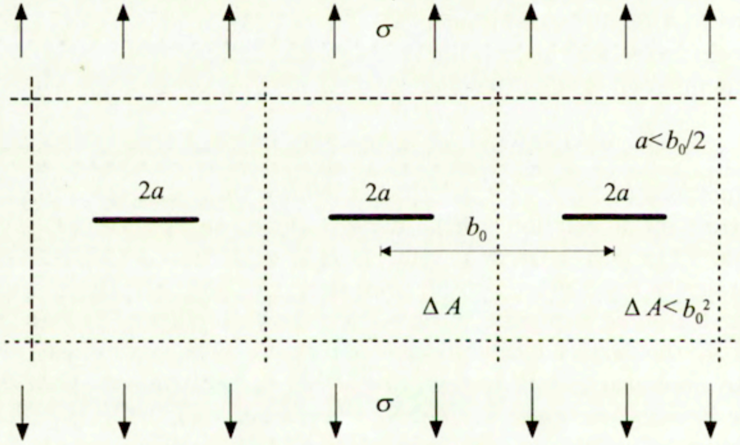

Figure 3.9. Infinite row of interacting microcracks under uniaxial tension.

joined each other forming a single crack which continues to grow in a stable manner heading for the specimen's rupture.

Consider now an infinite row of equally spaced microcracks, Figure 3.9. Suppose that there is one microcrack per unit cell and each microcrack influences the adjoining ones.

The condition for microcrack growth (3.5)–(3.6) takes the following closed form

$$K_I = \sigma \sqrt{b \tan \frac{\pi a}{b_0}} = K_{cu} - (K_{cu} - K_{cl})\, e^{-\eta\, \Delta a / a_0}, \tag{3.23}$$

since the corresponding K_I factor is exact in this case (Sih, 1973). Skipping routine integration, the final outcome for the Gibbs energy density is

$$\psi = \frac{\sigma^2}{2E_0} - \frac{2\sigma^2 b_0^2}{\pi\, E_0 \Delta A} \ln[\cos(\pi a / b_0)]. \tag{3.24}$$

Hence, the constitutive equation expressed in the incremental and non-dimensional form is (Basista and Gross, 1985)

$$\begin{aligned} \mathrm{d}\tilde{\varepsilon} = & \left\{ 1 - \frac{2\kappa}{\pi^2 \lambda_0^2} \ln[\cos(\pi\lambda_0)] \right\}^{-1} \left\{ 1 - \frac{2\kappa}{\pi^2 \lambda_0^2} \ln[\cos(\pi\lambda_0 \tilde{a})] \right. \\ & \left. + \frac{4\kappa}{\pi\lambda_0} \frac{\sin^2(\pi\lambda_0\tilde{a})\, [\gamma^* - (\gamma^* - 1) e^{\eta(1-\tilde{a})}]}{\eta(\gamma^* - 1) e^{\eta(1-\tilde{a})} \sin(2\pi\lambda_0\tilde{a}) - \pi\lambda_0 [\gamma^* - (\gamma^* - 1) e^{\eta(1-\tilde{a})}]} \right\} \mathrm{d}\tilde{\sigma}. \end{aligned} \tag{3.25}$$

In view of (3.23) the stress is related to the microcrack length as

$$\tilde{\sigma} = \left[\gamma^* - (\gamma^* - 1) e^{\eta(1-\tilde{a})} \right] \sqrt{\frac{\tan(\pi\lambda_0)}{\tan(\pi\lambda_0\tilde{a})}}. \tag{3.26}$$

Recall that the non-dimensional stress, strain and microcrack length $\tilde{\sigma}, \tilde{\varepsilon}, \tilde{a}$ have already been introduced in (3.11) while the material constants κ, γ^*, η in (3.16) and (3.6). The parameter λ_0 is defined as $\lambda_0 = a_0 / b_0$ with $2a_0$ being the initial microcrack length and b_0 the microcrack spacing (Figure 3.9). In the limit as $b_0 \to \infty$, Equations (3.14) and (3.15) valid for an isolated microcrack (no interaction) are recovered from Equations (3.25) and (3.26) as shown in Appendix 3.2.

Once (3.25) and (3.26) are established, it is fairly straightforward to compute numerically the corresponding stress–strain curves. The final plot is shown in Figure 3.10. The curves for $\lambda_0 \to 0$ and $\lambda_0 = 0.0891$ bound an admissible region satisfying the assumed geometrical requirements marked in Figure 3.9.

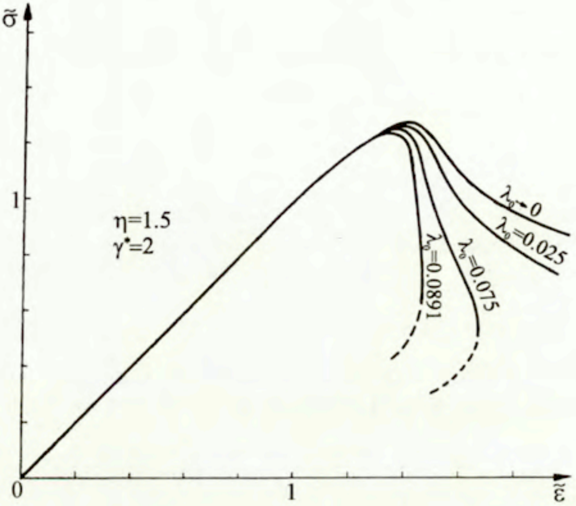

Figure 3.10. Model predictions of $\tilde{\sigma}$–$\tilde{\varepsilon}$ curves for microcrack configuration in Figure 3.9 (Basista and Gross, 1985).

3.4. Generalization to two-dimensional stress states

An extension of the introduced damage model to two-dimensional tension stress states will now be outlined. Since the following analysis is of more general nature, an RVE with N randomly distributed and oriented microcracks will be considered rather than a unit cell with a single preexisting microcrack. For simplicity, consider the case of plane stress shown in Figure 3.11. Let an isolated L-th microcrack of the length $2a^L$ have a unit normal vector $\mathbf{n}^L$. The normal and tangential components of the stress vector acting on the microcrack midpoint are denoted by $\boldsymbol{\sigma}^L$ and $\boldsymbol{\tau}^L$. The angle φ^L specifies the microcrack orientation with respect to the x-axis. The principal directions I, II of the stress tensor are inclined to the x, y coordinate axes by the angle α.

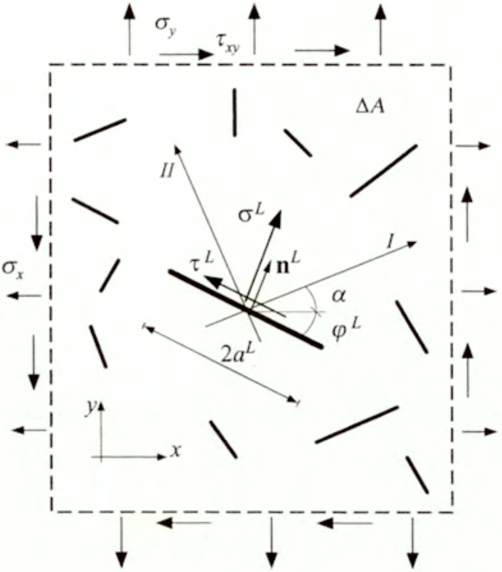

Figure 3.11. RVE with N microcracks under plane stress.

The Gibbs energy density for a two-dimensional RVE containing N rectilinear (interacting or non-interacting) microcracks is given by

$$\psi = \frac{1}{2}\, S^0_{ijkl}\, \sigma_{ij}\, \sigma_{kl} + \sum_L 2 \int_0^{a^L} \frac{(K_I^L)^2 + (K_{II}^L)^2}{E_0'\, \Delta A}\, \mathrm{d}a^L, \tag{3.27}$$

where S^0_{ijkl} is the elastic compliance tensor of the matrix material, $E_0' = E_0$ in plane stress, $E_0' = E_0/(1-\nu_0^2)$ in plane strain, K_I^L and K_{II}^L are the Mode I and the Mode II stress intensity factors at the tip of L-th microcrack, ΔA denotes now the surface area of the RVE. In (3.27) the upper index L stands for the microcrack label and the summation operator refers to all $L = 1, \ldots, N$ microcracks. The lower indices when repeated are subject to the Einstein summation convention.

To keep the current analysis self-contained, the integrand in expression (3.27) should perhaps be commented upon. It incorporates the fundamental equivalence relation between the strain energy release rate G and the stress intensity factors for a straight crack under mixed mode (I+II) conditions, i.e. $G = (K_I^2 + K_{II}^2)/E_0'$. The general and detailed derivation of this formula based on the principle of virtual work and definition of G as a "limiting form of strain energy comparison of a crack of length a with one of length $(a + \Delta a)$" is presented in Rice (1968).[1] Making the appropriate substitutions of the near crack tip stress field and the corresponding crack opening displacements, and proceeding to the limit $\Delta a \to 0$ in the expression for the strain energy increment, the above equivalence relation (involving no mixed terms $K_I K_{II}$) is obtained. Note that this relation holds unconditionally for the self-similar crack growth. Any deviation of the crack path from the original crack plane makes the above relation more complicated, as shown in Lawn and Wilshaw (1975).

In the plane case and non-interacting straight microcracks, K_I^L and K_{II}^L can be expressed as

$$K_I^L = \sigma^L \sqrt{\pi a^L}, \qquad K_{II}^L = \tau^L \sqrt{\pi a^L}, \tag{3.28}$$

where σ^L and τ^L denote normal and shear tractions on the line of L-th microcrack. Employing the elementary relations between the tractions and the stress tensor, we get

$$(K_I^L)^2 + (K_{II}^L)^2 = \pi a^L \sigma_{ij} \sigma_{jk} n_k^L n_i^L \,. \tag{3.29}$$

Equation (3.27) can now be integrated by use of (3.29) leading to

$$\begin{aligned} \psi &= \frac{1}{2} S^0_{ijkl} \sigma_{ij} \sigma_{kl} + \frac{\pi}{E_0'} \frac{1}{\Delta A} \sum_L \left(a^2 n_i n_k\right)^L \sigma_{ij} \sigma_{jk} \\ &= \frac{1}{2} S^0_{ijkl} \sigma_{ij} \sigma_{kl} + \frac{\pi}{E_0'} \omega_{ik} \sigma_{ij} \sigma_{jk} \,. \end{aligned} \tag{3.30}$$

Incidentally, the second order symmetric tensor

$$\boldsymbol{\omega} = \frac{1}{\Delta A} \sum_L (a^2 \mathbf{n} \otimes \mathbf{n})^L$$

---

[1] This key result was first established by Irwin (1957) for Mode I cracks (i.e. $G = K_I^2/E'$) using the so-called crack-closure operation to compute the strain energy loss as the crack extends under fixed grip conditions. Remarkably, some other important notions of the contemporary fracture mechanics should also be credited to Irwin and his associates, e.g. the three basic modes of crack extension (opening, sliding, and tearing) and the stress intensity factors K_I, K_{II}, K_{III} (K for J.A. Kies, one of G.R. Irwin's collaborators).

is the so-called crack density tensor well-known in the damage mechanics literature (cf. Vakulenko and Kachanov, 1971; Kachanov, 1980; Murakami and Ohno, 1981; Lubarda and Krajcinovic, 1993). A dual derivation to that of (3.30) was presented in Kachanov (1993) where the elastic potential of a microcracked body was expressed via the crack opening displacements. The final result (Equation (6.15) in Kachanov, 1993) is identical to Equation (3.30) of this study (originally derived in Basista and Gross, 1989).

Making use of (3.2), (3.9) and (3.30), the incremental form of strain–stress relation reads (Basista and Gross, 1989)

$$\mathrm{d}\varepsilon_{ij} = -\frac{\nu_0}{E_0'}\,\mathrm{d}\sigma_{kk}\delta_{ij} + \frac{1+\nu_0}{E_0'}\,\mathrm{d}\sigma_{ij} + \frac{2\pi}{E_0'}(\omega_{ik}\,\mathrm{d}\sigma_{kj} + \mathrm{d}\omega_{ik}\,\sigma_{kj}) \tag{3.31}$$

where the increment of the microcrack density tensor is given by

$$\mathrm{d}\omega_{ik} = \sum_L \left(\mathrm{d}N_{ik}a^2\right)^L + 2\sum_L \left(N_{ik}a\,\mathrm{d}a\right)^L. \tag{3.32}$$

In (3.32), the dyad $N_{ik} = n_i n_k$ characterizes the microcrack orientation. Note that $\mathrm{d}N_{ik} = 0$ if the microcrack growth is self-similar, in all other cases $\mathrm{d}N_{ik} \neq 0$.

Even though the orientation of the pre-load microcracks is in all probability a random variable, in tensile stress fields only those microcracks which are perpendicular or nearly perpendicular to the maximum tensile stress direction will experience substantial growth. Consequently, the microcrack pattern will be dominated by microcracks that are normal to the greatest principal stress direction. This conclusion is firmly supported by the published data (e.g. Costin, 1983; Lawn and Wilshaw, 1975). Moreover, motivated by the linear fracture mechanics solution, it is assumed that the microcracks that are not perpendicular to the direction of maximum tension will grow along that direction. In other words, an inclined microcrack evolves by sprouting kinked (curvilinear) wings from the tips of the original microcrack. However, as the deformation goes on the wings promptly align themselves with the paths normal to σ_{II}, Figure 3.12. Since the SIFs for the kinked microcrack are not available in closed analytical form, the following simplifications are made with regard to the microcrack kinetics (Basista and Gross, 1989):

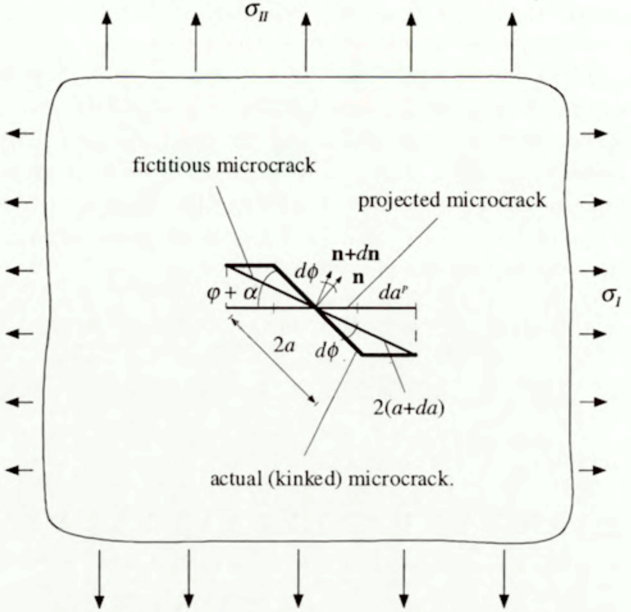

Figure 3.12. Simplified model of microcrack growth under biaxial tension (Basista and Gross, 1989).

1. The actual kinked microcrack is replaced by a fictitious straight microcrack of the length $2(a + \mathrm{d}a)$, as shown in Figure 3.12.

2. The microcrack starts to grow if the stress and the microcrack length projected on the plane normal to the maximum tensile stress direction attain the threshold values yielded by the microcrack growth condition.

In view of the simplification 2, the microcrack growth condition (3.5)–(3.6) takes the form (Basista and Gross, 1989)

$$\sigma_{ij} n_i^P n_j^P \sqrt{\pi a^P} = K_{cu} - (K_{cu} - K_{cl})\, e^{-\eta\, \Delta a^P / a_0^P}\ , \tag{3.33}$$

where the superscript P stands for "projected".

After simple manipulations on (3.33), the incremental relationship between the stress tensor and the microcrack length is (Basista and Gross, 1989)

$$\mathrm{d}\sigma_{ij}N^P_{ij} = \frac{1}{\sqrt{\pi(a^P)^3}}\left[(K_{cu}-K_{cl})e^{\eta(1-a^P/a^P_0)}\left(\eta+\frac{1}{2}\right)-\frac{1}{2}K_{cu}\right]\mathrm{d}a^P, \tag{3.34}$$

where $N^P_{ij}=n^P_i n^P_j$; the material constants K_{cl} , K_{cu} , η are as introduced in (3.6).

The simplifying assumption 1 involves a change in the microcrack orientation represented by the tensor $\mathrm{d}N_{ik}$. Omitting the laborious derivation, the final output reads (Basista and Gross, 1989)

$$\mathrm{d}N_{ik}=\mathrm{d}\phi\,(N_{il}\nu_{lk}+\nu_{kl}N_{li}), \qquad \nu_{lk}=\begin{bmatrix}0 & 1\\ -1 & 0\end{bmatrix}. \tag{3.35}$$

Finally, the present model is completed by geometrical relations:

$$\mathrm{d}a^P=\frac{\mathrm{d}a}{\cos(\varphi+\alpha)}, \qquad \mathrm{d}\phi=\frac{\mathrm{d}a}{a}\tan(\varphi+\alpha). \tag{3.36}$$

The model of microcrack evolution under biaxial tension (Figure 3.12) was proposed in Basista and Gross (1989) for proportional loading. It is based on two experimentally confirmed facts that: (1) among many comparable in size and isotropically distributed microcracks, those oriented perpendicularly to the greatest principal stress direction will be activated first and their growth may be assumed self-similar, (2) inclined microcracks will grow next by sprouting curvilinear kinks that promptly align themselves with the direction normal to the greatest principal stress direction. The material inhomogeneity may somewhat disturb this picture since the microcracks may temporarily become arrested by the higher energy barriers (hard particles, inclined grain boundaries, etc.) and forced to change their path. Nevertheless, when zoomed out, a tortuous microcrack path generally follows the direction normal to the greatest principal stress.

Under non-proportional loading, observations (1, 2) remain valid but the actual microcrack path may become quite complex when the principal stress axes rotate. In such a situation, if a material sample contained only a single microcrack, the rotating microcrack model (Figure 3.12) could lead to inconsistencies. On the other hand, real brittle materials contain a fairly dense population of microcracks which are activated gradually depending on their orientation relative to the principal stress axes. Once a microcrack has grown, some amount of stress has been released caused by the new free surface creation. Consequently, this microcrack becomes a low stress microcrack and it is rather improbable that this particular microcrack will grow again when the principal stress directions change. Usually, it is another, more favorably oriented, microcrack that becomes critical next. This issue, however, needs further studies.

3.5. Concluding remarks

In this chapter, a simple micromechanical damage model has been proposed for concrete-like materials subjected to quasi-static tensile loading. The cases of uniaxial tension and plane stress (plane strain) have been given particular attention. The basic assumption of the model is that the observed inelastic response in strain-controlled tensile tests be solely attributed to irreversible process of internal microcracking. A continuum description of the material behavior is accomplished by introducing a damaging RVE. The incremental stress–strain relationships have been derived using the framework of irreversible thermodynamics with internal variables (Rice, 1975). As a necessary prerequisite for that, the complementary (Gibbs) energy density has been determined for the representative unit cell containing an open microcrack or a system of interacting open microcracks. In order to show how the microcrack interaction influences the constitutive description, two simplest arrays of collinear microcracks (having analytical solutions for the SIFs) have been considered in detail. Unlike the familiar Griffith criterion, the microcrack growth condition postulated in this chapter assumes that K_{Ic} is not a material constant but a raising function of the microcrack length, as suggested by the experimental data (Broek, 1974; Costin, 1983, and many others). The developed model is capable of reproducing the salient features of the behavior of concrete-like materials under tensile loading. However, for the reasons stated in Section 3.2, the model does not aspire to handle the softening regime, even though the curves depicted in Figures 3.5, 3.6, 3.10 might suggest the opposite.

The microcrack growth criterion (3.5)–(3.6), originally proposed in Basista and Gross (1985), has been extensively used by Feng and Yu (1995) in their formulation of a complete constitutive model for brittle materials subjected to tensile loads. A similar approach employing the R-curve concept was later promoted in Gambarotta and Lagomarsino (1993). Also, an idea resembling that of the equivalent rotating microcrack in Figure 3.12 was independently introduced in a recent paper by Swoboda and Yang (1999).

The specific expression (3.6) for the fracture toughness function $K_{Ic}(\Delta a)$ emphasizes the role of material inhomogeneity and inelastic processes in the neighborhood of the microcrack tip. The microcrack growth equation, when incorporated in the adopted constitutive framework, leads eventually to nonlinear stress–strain curves closely matching the shape of the experimental curves. Note, however, that an alternative microcracking scenario is often invoked when modeling nonlinear response of brittle materials in tension. It assumes that the fracture toughness is a material constant and the observed nonlinear σ–ε behavior is due to sequential activations and arrests of more and more of the preexisting microcracks as the external loading increases. In fact, such damage evolution mechanism was used by several authors (e.g. Krajcinovic and Fanella, 1986; Sumarac, 1987; Gross, Becker and Basista, 1990) to model inelastic deformation of brittle materials in tension.

Appendix 3.1.

To preserve clarity of the body text, the detailed derivation of the incremental stress-strain relation for the unit cell with two collinear interacting microcracks has been omitted in Section 3.3. For the sake of completeness, though, it might be of interest to highlight the main steps of that derivation now.

Let $\Delta\psi$ denote the change of the Gibbs energy density (3.21) due to the presence of two collinear microcracks, i.e.

$$\Delta\psi = \frac{2}{\Delta A\, E_0}\int_0^{a_1}\left[\sigma\sqrt{\frac{\pi a_1}{2}}\left(1+\frac{\lambda^2}{2}+\frac{\lambda^3}{2}+\frac{11}{8}\lambda^4\right)\right]^2 \mathrm{d}a_1\,, \qquad \text{(A3.1)}$$

where a_1 and λ are defined in (3.20) and the series (3.19) has been truncated to the first 4 terms. Performing the necessary integrations, the final outcome reads

$$
\begin{aligned}
\Delta\psi \;=\; & \frac{\pi\sigma^2 a^2}{\Delta A E_0}\left\{2.6380 + 1.8662\,(\tilde{a}\chi_0)^{-1} + 2.1389(\tilde{a}\chi_0)^{-2}\ln(1-2\tilde{a}\chi_0)\right.\\
& + (\tilde{a}\chi_0)^{-2}\big[2.220\,(1-2\tilde{a}\chi_0)^{-1} - 0.8227\,(1-2\tilde{a}\chi_0)^{-2}\big]\\
& + 0.3168(1-2\tilde{a}\chi_0)^{-3} - 0.1204(1-2\tilde{a}\chi_0)^{-4}\\
& + 0.04106(1-2\tilde{a}\chi_0)^{-5} - 0.00929(1-2\tilde{a}\chi_0)^{-6}\\
& \left. + 0.001065(1-2\tilde{a}\chi_0)^{-7} - 1.6265\right\}, \qquad \text{(A3.2)}
\end{aligned}
$$

where $\chi_0 = a_0/c_0$, $\tilde{a} = a/a_0$ (cf. Figure 3.7). When the microcracks are far apart form each other (i.e. $c_0, b \to \infty$), Equation (A3.2) correctly reduces to the known solution for two non-interacting microcracks in the unit cell,

$$
\Delta\psi = \frac{2\pi\sigma^2 a^2}{\Delta A E_0}\,.
$$

The incremental form of the axial stress vs. axial strain relation is obtained combining (3.10), (3.2) and (A3.2), namely

$$
\begin{aligned}
\mathrm{d}\tilde{\varepsilon} \;=\; & \Big\{1 + \kappa\Big[2.638 + 1.8662\chi_0^{-1} + 2.1389\chi_0^{-2}\ln(1-2\chi_0)\\
& + \lambda_0^{-2}\Big(2.22(1-2\chi_0)^{-1} - 0.8227(1-2\chi_0)^{-2} + 0.3168(1-2\chi_0)^{-3}\\
& - 0.1204(1-2\chi_0)^{-4} + 0.04106(1-2\chi_0)^{-5} - 0.00929(1-2\chi_0)^{-6}\\
& + 0.001055(1-2\chi_0)^{-7} - 1.6265\Big)\Big]\Big\}^{-1}\\
\times & \Big\{\Big[1 + \kappa\tilde{a}^2\Big[2.638 + 1.8662(\chi_0\tilde{a})^{-1} + 2.1389(\chi_0\tilde{a})^{-2}\ln(1-2\chi_0\tilde{a})\\
& + (\chi_0\tilde{a})^{-2}\Big(2.22(1-2\chi_0\tilde{a})^{-1} - 0.8227(1-2\chi_0\tilde{a})^{-2}\\
& + 0.3168(1-2\chi_0\tilde{a})^{-3} - 0.1204(1-2\chi_0\tilde{a})^{-4} + 0.04105(1-2\chi_0\tilde{a})^{-5}\\
& - 0.00929(1-2\chi_0\tilde{a})^{-6} + 0.001055(1-2\chi_0\tilde{a})^{-7} - 1.6265\Big)\Big]\Big]\\
& + \kappa\tilde{a}\Big[5.276 + 1.8662(\chi_0\tilde{a})^{-1} - 2(\chi_0\tilde{a})^{-1}\Big(2.1389(1-2\chi_0\tilde{a})^{-1}\\
& - 2.22(1-2\chi_0\tilde{a})^{-2} + 1.6454(1-2\chi_0\tilde{a})^{-3} - 0.9504(1-2\chi_0\tilde{a})^{-4}\\
& + 0.4816(1-2\chi_0\tilde{a})^{-5} - 0.2053(1-2\chi_0\tilde{a})^{-6} + 0.05574(1-2\chi_0\tilde{a})^{-7}\\
& - 0.007385(1-2\chi_0\tilde{a})^{-8}\Big)\Big]\cdot\left(\frac{\partial F}{\partial a}\right)^{-1}\Big\}\mathrm{d}\tilde{\sigma}, \qquad \text{(A3.3)}
\end{aligned}
$$

with

$$\frac{\partial F}{\partial a} = \frac{\eta(\gamma^{*}-1)\, e^{\eta(1-\tilde{a})}}{\gamma^{*}-(\gamma^{*}-1)\, e^{\eta(1-\tilde{a})}} - \frac{1 + (\frac{5}{2}\tilde{c}-1)\hat{c}^{-3} + (\frac{7}{2}\tilde{c}-1)\hat{c}^{-4} + \frac{11}{4}(\frac{9}{2}\tilde{c}-1)\hat{c}^{-5}}{\tilde{a}\left(2 + \hat{c}^{-2} + \hat{c}^{-3} + \frac{11}{4}\hat{c}^{-4}\right)}$$

where $\tilde{c} = (\chi_0 \tilde{a})^{-1}$ and $\hat{c} = \tilde{c} - 2$. In (A3.3), $\tilde{\sigma}$, $\tilde{\varepsilon}$ are the normalized stress and strain as in (3.11); η, γ^{*}, κ are defined in (3.6) and (3.16).

The normalized stress $\tilde{\sigma}$ is related to the normalized microcrack length $\tilde{a}$ through the microcrack growth condition (3.22), which can finally be expressed as

$$\tilde{\sigma} = \frac{\left(2 + \hat{\chi}_0^{-2} + \hat{\chi}_0^{-3} + \frac{11}{4}\hat{\chi}_0^{-4}\right)\left[\gamma^{*} - (\gamma^{*} - 1)\, e^{\eta(1-\tilde{a})}\right]}{\sqrt{\tilde{a}}\left(2 + \hat{c}^{-2} + \hat{c}^{-3} + \frac{11}{4}\hat{c}^{-4}\right)}\,, \tag{A3.4}$$

where $\hat{\chi}_0 = \chi_0^{-1} - 2$.

The $\tilde{\sigma}$–$\tilde{\varepsilon}$ curves depicted in Figure 3.8 were computed numerically from the coupled equations (A3.3) and (A3.4) for a set of plausible values of the material constants: $\chi_0 = 0.1$, $\kappa = 0.0625$, $\eta = 1$, $\gamma^{*} = 2;\ 2.5;\ 3$.

Appendix 3.2.

The correctness of Equations (3.25) and (3.26) can be verified by checking whether they reduce to Equations (3.14) and (3.15), respectively, when the microcrack spacing b_0 tends to infinity (i.e. $\lambda_0 \to 0$).

Transition (3.25) → (3.14) *as* $\lambda_0 \to 0$.

Since the expression (3.25) is algebraically rather complex, the limits of individual terms in (3.25) will be computed separately. The key element of this operation is the development of the logarithmic terms into Taylor series. This is feasible upon noting that the arguments of both functions are less than $\pi/2$ due to geometric restriction $a/b_0 < \frac{1}{2}$, Figure 3.9. Therefore,

$$\begin{aligned} &\lim_{\lambda_0 \to 0}\left\{1 - \frac{2\kappa}{\pi^2\lambda_0^2}\,\ln\left[\cos(\pi\lambda_0)\right]\right\}^{-1} \\ &\quad = \lim_{\lambda_0 \to 0}\left\{1 - \frac{2\kappa}{\pi^2\lambda_0^2}\left(-\frac{\pi^2\lambda_0^2}{2}\right)\left(1 + \frac{\lambda_0^2}{6} + \frac{2\lambda_0^4}{45} + \frac{54\lambda_0^6}{2520} + \cdots\right)\right\}^{-1} \\ &\quad = \frac{1}{1+\kappa}\,, \end{aligned} \tag{A3.5a}$$

$$\lim_{\lambda_0\to 0}\left\{1-\frac{2\kappa}{\pi^2\lambda_0^2}\,\ln\left[\cos(\pi\lambda_0\tilde{a})\right]\right\}=1+\kappa\,\tilde{a}^2, \tag{A3.5b}$$

$$\begin{aligned}
&\lim_{\lambda_0\to 0}\left\{\frac{4\kappa}{\pi\lambda_0}\cdot\frac{\sin^2(\pi\lambda_0\tilde{a})\left[\gamma^*-(\gamma^*-1)\,e^{\eta(1-\tilde{a})}\right]}{\eta(\gamma^*-1)\,e^{\eta(1-\tilde{a})}\sin(2\pi\lambda_0\tilde{a})-\pi\lambda_0[\gamma^*-(\gamma^*-1)\,e^{\eta(1-\tilde{a})}]}\right\}\\
&\quad=\lim_{\lambda_0\to 0}\left\{\left[\frac{\sin(\pi\lambda_0\tilde{a})}{\pi\lambda_0\tilde{a}}\right]^2 4\kappa\tilde{a}^2\right.\\
&\qquad\left.\times\frac{\left[\gamma^*-(\gamma^*-1)\,e^{\eta(1-\tilde{a})}\right]}{2\eta\,\tilde{a}\,(\gamma^*-1)\,e^{\eta(1-\tilde{a})}\frac{\sin(2\pi\lambda_0\tilde{a})}{2\pi\lambda_0\tilde{a}}-\left[\gamma^*-(\gamma^*-1)\,e^{\eta(1-\tilde{a})}\right]}\right\}\\
&\quad=4\kappa\,\tilde{a}^2\frac{\gamma^*-(\gamma^*-1)\,e^{\eta(1-\tilde{a})}}{(\gamma^*-1)\,e^{\eta(1-\tilde{a})}(2\eta\tilde{a}+1)-\gamma^*}\,.
\end{aligned} \tag{A3.5c}$$

Assembling the partial results (A3.5a)–(A3.5c) as in (3.25), we finally get

$$\mathrm{d}\tilde{\varepsilon}=\frac{1}{1+\kappa}\left[1+\kappa\tilde{a}^2+4\kappa\,\tilde{a}^2\frac{\gamma^*-(\gamma^*-1)\,e^{\eta(1-\tilde{a})}}{(\gamma^*-1)\,e^{\eta(1-\tilde{a})}(2\eta\,\tilde{a}+1)-\gamma^*}\right]\mathrm{d}\tilde{\sigma}$$

which is exactly Equation (3.14).

Transition (3.26) → (3.15) *as* $\lambda_0\to 0$.

In this case, the algebraic manipulations are rather elementary and can concisely be expressed as follows:

$$\begin{aligned}
&\lim_{\lambda_0\to 0}\left\{\left[\gamma^*-(\gamma^*-1)\,e^{\eta(1-\tilde{a})}\right]\sqrt{\frac{\tan(\pi\lambda_0)}{\tan(\pi\lambda_0\tilde{a})}}\right\}\\
&\quad=\lim_{\lambda_0\to 0}\left\{\left[\gamma^*-(\gamma^*-1)\,e^{\eta(1-\tilde{a})}\right]\sqrt{\frac{\sin(\pi\lambda_0)}{\sin(\pi\lambda_0\tilde{a})}\,\frac{\pi\lambda_0\tilde{a}}{\pi\lambda_0}\,\frac{\cos(\pi\lambda_0\tilde{a})}{\cos(\pi\lambda_0)}\,\frac{1}{\tilde{a}}}\right\}\\
&\quad=\frac{1}{\sqrt{\tilde{a}}}\left[\gamma^*-(\gamma^*-1)\,e^{\eta(1-\tilde{a})}\right].
\end{aligned} \tag{A3.6}$$

The final expression in (A3.6) is identical to (3.15) what makes the proof complete.

Chapter 4

Micromechanical damage model for brittle materials in compression

Abstract. This chapter is concerned with mathematical modeling of the inelastic behavior of brittle materials loaded in compression. Special emphasis is given to damage modeling of reservoir rocks although application to concrete, ceramics and some brittle composites is also conceivable provided that they exhibit low porosity. The basic building block of the proposed micromechanical model is the so-called sliding microcrack mechanism of brittle deformation. The Rice internal variable theory including a micro-to-macro transition relation is employed as constitutive framework. Within the proposed approach, the potential functions are not just postulated but are derived from the micromechanics of the sliding microcrack. The microfluxes and conjugated thermodynamic forces are unambiguously identified. Incremental stress–strain relations are derived in loading and unloading and compared with the kinematic model of Nemat-Nasser and Obata (1988). An illustrative example is worked out showing the capability of the present model in predicting experimentally observed response of Westerly granite.

4.1. Problem formulation

The microcrack growth under compression at low-to-moderate lateral pressures may occur according to several distinct mechanisms. Some of these mechanisms such as frictional sliding on initial flaws inducing secondary tension wings, tension cracking from isolated pores, and pore collapse have been extensively studied both experimentally and analytically (e.g. Brace and Bombolakis, 1963; Bieniawski, 1967; Walsh, 1965; Scholz and Kranz, 1974; Peng and Johnson, 1976; Nemat-Nasser and Horii, 1982; Wang and Kemeny, 1993; Zhao et al., 1993).

For porous brittle materials, the pore-squeezing mechanism (Figure 4.1a) is often employed to account for the appearance and growth of tension microcracks parallel to the direction of maximum compressive stress (e.g. Sammis and Ashby, 1986). Other idealizations, based on K_I-solutions, identify bending of elongated inclusions (Figure 4.1b) or mismatch in the elastic constants of material constituents (Figure 4.1c) as potential sources of brittle microcracking (Kemeny and Cook, 1991). Also, the mechanism shown in Figure 4.1d is invoked when studying compressive damage in concrete (e.g. Ortiz, 1985; Gross, Becker and Basista, 1990). Under uniaxial compressive stresses, aggregate is squeezed out sideways inducing high splitting stresses in mortar. This, in turn, may cause microcracking parallel to the axis of loading.

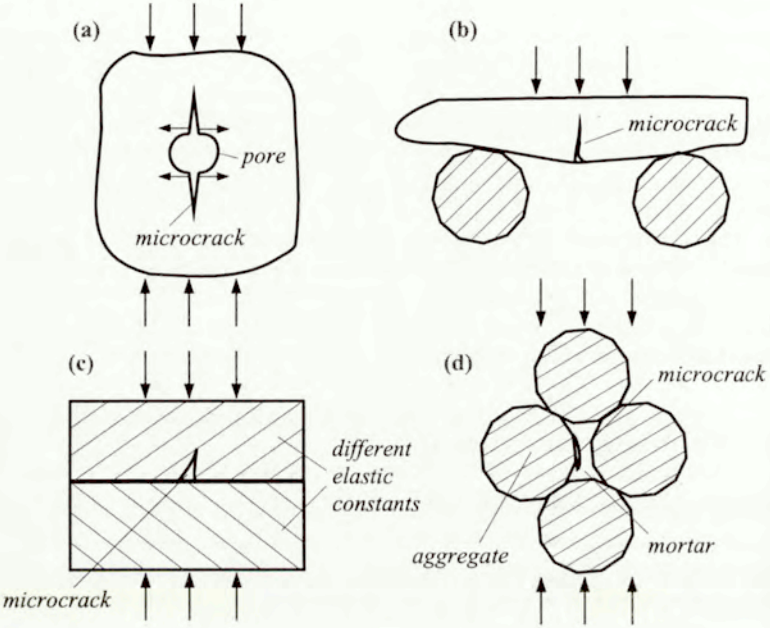

Figure 4.1. Mechanisms of microcrack nucleation and growth under compression: (a) pore-squeezing, (b) bending of elongated inclusion, (c) mismatch in elastic constants, (d) squeezing out of aggregate in concrete.

In the case of low-porosity rocks, the **sliding microcrack** mechanism originated in Brace and Bombolakis (1963) and pursued thereafter in a series of papers (Rudnicki and Rice, 1975; Horii and Nemat-Nasser, 1985a, 1986; Nemat-Nasser and Obata, 1988; Deng and Nemat-Nasser, 1992, 1994; Kachanov, 1982; Moss and Gupta, 1982; Steif, 1984; Zaitsev, 1985; Sammis and Ashby, 1986; Ashby and Hallam, 1986; Fanella and Krajcinovic, 1988; Kemeny and Cook, 1991; Ju, 1991; Dyskin et al., 1995; Sadowski, 1994; Lehner and Kachanov, 1996; Basista, 1993, 1999; Basista and Gross, 1997, 1998a, 1998b; Lauterbach and Gross, 1998; Lawn and Marshall, 1998) is one of the major sources of rock inelasticity. It involves a complex sequence of events starting with frictional sliding along the faces of preexisting closed flaws, followed by out-of-crack plane curvilinear kinking from the microcrack tips, and completed by the pure Mode I growth of the kinked wings in planes roughly parallel to the direction of maximum compression. Depending on the sign of the lateral stress the wings may grow either in stable (lateral compression) or unstable manner (lateral tension).

The principal objective of this chapter is to explore the issue whether the internal variable thermodynamic framework in the spirit of Rice (1971, 1975) can be useful for damage mechanics modeling of brittle deformation when the sliding microcrack mechanism constitutes the basic building block of the model. In contrast to common use of macroscopic internal variables in the continuum damage mechanics, *microstructural internal variables* have scarcely been employed to model brittle damage processes. And yet, an unquestionable advantage of a microstructural internal variable is that its physical meaning is straightforward. On the other hand, the Rice framework was intentionally devised to link the microstructural rearrangements within a material to its inelastic macroscopic response. Therefore, Rice's framework seemed to be perfectly suited for micromechanically based constitutive modeling of brittle deformation. Quite surprisingly, it has not been applied yet in the context of sliding microcracks, although applications to open cracks are known (e.g. Rice, 1975; Basista and Gross, 1985, 1989; Krajcinovic and Sumarac, 1989). The considerations presented in this chapter are aimed at filling up this gap.

4.2. Sliding microcrack mechanism

Consider an isothermal deformation process of an elastic solid such as low porosity rock weakened by an ensemble of dilutely distributed initial microcracks. Admit infinitesimal strains and low-to-moderate confining pressures so that plastic effects, typically observed in rocks under high confining pressures, be neglected. Suppose that damage develops from the preexisting defects and no new microcrack nucleation is allowed in the course of deformation. These assumptions are pertinent to *cleavage 1* type of deformation in the Ashby (1979) classification.[1] Microcrack interactions are not being examined at the moment and will be addressed in the following chapter. To make the analysis tractable, select a representative initial microcrack as a single, closed, rectilinear slit PP' of the length $2c$ oriented at an angle φ, as depicted in Figure 4.2. This microcrack is embedded in a two-dimensional, elastic, isotropic, homogeneous, unbounded matrix loaded under plane strain conditions. The sign convention is that of continuum me-

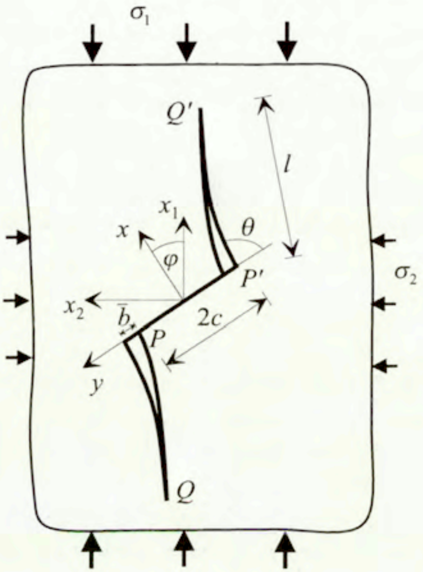

Figure 4.2. Sliding microcrack model of brittle deformation under biaxial compression.

---

[1] Ashby (1979) distinguishes "cleavage 1", "cleavage 2", "cleavage 3" within the grains as well as "brittle intergranular damage". Cleavage 1 means a purely brittle damage with no general plasticity for the stresses are below the yield point. Nevertheless, some microplasticity is admissible at microcrack tips. Cleavage 1 microcracks always develop from preexisting flaws. Cleavage 2 microcracking appears when the preexisting microcracks are very small or absent, so that the stress can reach a level at which slips or twins may be initiated. Both slips and twins can produce internal stresses that can in turn nucleate microcracks. Cleavage 3 mode is induced by the stresses above the yield point. It requires higher temperatures and large plastic strains present.

chanics, i.e. compressive stresses are viewed negative. Moreover, it is chosen that $|\sigma_1| > |\sigma_2|$. Two Cartesian coordinate systems will be used throughout: a fixed global frame of reference $(x_1\ ,\ x_2)$ and a local one (x, y). They are chosen as shown in Figure 4.2 so as to enable comparison with the results of Nemat-Nasser and Obata (1988). The symbols l and $\bar{b}$ in Figure 4.2 denote the wing length and the averaged slip of the preexisting microcrack, respectively.

Neglecting the initial closure of pores, the actual onset of macroscopic nonlinear deformation in compact rocks is routinely attributed to the activation of frictional sliding over the faces of preexisting microcracks. During this phase, called *phase 1* in the sequel, the microcracks retain their length $2c$, thus no new internal surfaces are created (no wings yet). Hence, sliding in the shearing mode is the only source of free energy change. It is also assumed that preexisting microcracks remain closed during the whole deformation process. Phase 1 is characterized by a trigger-like kinetics, i.e. sliding commences when the actual shear stress acting on the microcrack faces exceeds the combined resistance of friction, cohesion, and that of the elastic crack-closing forces. Once sliding is activated, the representative microcrack is in Mode II loading for which only K_{II} stress intensity factor is nonzero. At some point, the elastic energy release rate $G(\theta)$ of an infinitesimal kink tip will reach a critical value in a plane at an angle θ_c to the original microcrack. The critical value of G corresponds to the critical value of the tensile hoop stress $\sigma_{\theta\theta}$ in the vicinity of the microcrack tip. Regardless of interpretation, the original microcrack will abruptly sprout a curvilinear wing (kink) microcrack at each tip at $\theta_c = 70.5°$, Figure 4.2. According to the linear fracture mechanics solution, the microcrack tip will follow a path for which $K_I = \max$, or equivalently, $K_{II} = 0$. After a short initial curving, the wings will align themselves with the direction of maximum principal compression σ_1 and become rather straight. The exact trajectory of the wing tip can be determined by maximizing $\sigma_{\theta\theta}$ with respect to θ. In this phase, called *phase 2*, the inelastic strains result from coupled effects of frictional sliding along PP' and opening of the wing cracks PQ and $P'Q'$.

The sliding microcrack model with cohesive and frictional resistance seems to capture most of the characteristics of the pre-peak response of rocks under compressive stresses. Apparently, it is for this versatility that the sliding crack mechanism, originated by Brace and Bombolakis (1963), is so widely used in rock mechanics. However, until recently it has been a matter of debate in the rock mechanics journals whether the sliding microcrack mechanism actually occurs in *real* brittle materials. Some authors argued that SEM observations do not support the existence of winged microcracks but seem to favor complex configurations of tensile microcracks growing form different sources. On the other hand, recent data from the acoustic emission tests do indicate that both tensile and shear events occur during brittle rock deformation (Lockner, 1993; Zhang et al., 1996; Labuz and Carvalho, 1998). Also, sliding cracks have been directly observed in ice (Cannon et al., 1990) and in model experiments on photoelastic materials (Horii and Nemat-Nasser, 1985, 1986; Germanovich et al., 1996). It seems that for compact and relatively homogeneous rocks such as granite, the sliding microcrack mechanism should be considered as one of the major micromechanisms of inelastic deformation. It is clear, though, that more sophisticated experimental techniques and problem-oriented experimental programs are still necessary to give a definite answer to that question.

The sliding microcrack mechanism may also be applied to model the compression damage in concrete. However, due to relatively high porosity and weak aggregate-mortar interfaces in plain concrete other microcracking mechanisms (e.g. Figure 4.1a,d) should probably be the first choice of an analyst.

4.3. Rice's thermodynamic framework with microstructural internal variables

In the next sections, the stress–strain relations will be derived for each phase separately. In preparation for that, it is advisable to recall the basics of Rice's thermodynamic framework with internal variables and to interpret it in the context of sliding microcrack mechanism.

A key hypothesis of the internal variable theory developed in Kestin and Rice (1970), Rice (1971, 1975), Hill and Rice (1973) is that every irreversible process of quasi-static deformation over a statistically homogeneous material sample under macroscopically homogeneous strain and temperature may be viewed as a sequence of (fictitious) constrained equilibrium states at which internal variables are somehow *frozen* so as to have the same values as in the actual (non-equilibrium) state. Each internal (or hidden) variable represents a particular dissipative mechanism of microstructural rearrangement. Equilibrium is maintained by a set of fictitious thermodynamic forces conjugate to the selected internal variables. Following the notation of Rice

(1975), let H denote symbolically the current collection of values of (scalar) internal variables $\xi_1, \xi_2, \ldots, \xi_n$ which characterize the current microstructural state of arrangement of the material constituents within the volume V_0 of an RVE. Hence, if the internal variables are frozen at their instantaneous values (H fixed), the standard formalism of the equilibrium thermodynamics applies. Consequently, one can derive the volume averaged strain (or stress) from the thermodynamic potentials much in the same way as for elastic solids, with internal variables as parameters, i.e.

$$\varepsilon_{ij} = \left.\frac{\partial\psi(\boldsymbol{\sigma}, H)}{\partial\sigma_{ij}}\right|_{H \text{ fixed}} ; \qquad \sigma_{ij} = \left.\frac{\partial\phi(\boldsymbol{\varepsilon}, H)}{\partial\varepsilon_{ij}}\right|_{H \text{ fixed}} , \tag{4.1}$$

where $\phi = \Phi/V_0$ is the density of the (Helmholtz) free energy, and $\psi = \Psi/V_0$ the density of the (Gibbs) complementary energy. Since fracture and sliding criteria are intrinsically stress-controlled, it proved more convenient to proceed with the Gibbs energy within the framework of Rice formalism.

The inelastic part of an increment of the Gibbs energy density under isothermal loading conditions is defined as the change in ψ when H changes to $H + \mathrm{d}H$ while $\boldsymbol{\sigma}$ is assigned the same value (Rice, 1975):

$$\mathrm{d}^i\psi = \psi(\boldsymbol{\sigma}, H + \mathrm{d}H) - \psi(\boldsymbol{\sigma}, H) . \tag{4.2}$$

Similarly, the inelastic part of the strain increment is defined as

$$\mathrm{d}^i\boldsymbol{\varepsilon} = \boldsymbol{\varepsilon}(\boldsymbol{\sigma}, H + \mathrm{d}H) - \boldsymbol{\varepsilon}(\boldsymbol{\sigma}, H) . \tag{4.3}$$

Take now two neighboring inelastic states characterized by H and $H + \mathrm{d}H$. Suppose that these two states are the constrained equilibrium states. Then, from Equations (4.1), (4.2), (4.3) it follows for fixed H and fixed $H + \mathrm{d}H$ that (Rice, 1975)

$$\mathrm{d}^i\varepsilon_{ij} = \frac{\partial\left(\mathrm{d}^i\psi(\boldsymbol{\sigma}, H)\right)}{\partial\sigma_{ij}} . \tag{4.4}$$

The inelastic change in ψ can alternatively be represented as

$$\mathrm{d}^i\psi = \frac{1}{V_0}\sum_{\alpha} f_\alpha \, \mathrm{d}\xi_\alpha , \tag{4.5}$$

where $f_\alpha = f_\alpha(\boldsymbol{\sigma}, H)$ is the set of thermodynamic forces conjugate to the internal variables ξ_α. Combining (4.5) and (4.4), a fundamental expression

(Rice, 1971, 1975) follows relating the increments of internal variables at the microscale to inelastic portions of the macroscopic strain increments:

$$\mathrm{d}^i\varepsilon_{ij} = \frac{1}{V_0}\sum_\alpha \frac{\partial f_\alpha(\boldsymbol{\sigma}, H)}{\partial\sigma_{ij}}\,\mathrm{d}\xi_\alpha\,. \tag{4.6}$$

Note that the only assumption underlying (4.6) was that of pure elastic material response, admitting the existence of thermodynamic potentials, if the internal variables were held fixed.

In order to make the above theory complete, the micro-to-macro transition relation (4.6) should be endowed with kinetic (evolution) equations for the rates of change of internal variables (fluxes)

$$\dot{\xi}_\alpha = \dot{\xi}_\alpha(\mathbf{f}, H)\,, \tag{4.7}$$

where dot denotes time differentiation, $\mathbf{f}$ is a set (collectively a vector) of all thermodynamic forces on which an individual flux depends at a given level of the microstructural rearrangement H. It can be shown that if $\dot{\xi}_\alpha$ is fully determined by its *own* conjugated thermodynamic force f_α, then a normality structure emerges in respective macroscopic constitutive equations (Rice, 1971).

The kinetic equations are restricted by the second law of thermodynamics which requires that the sum of work-rates of the conjugated forces on internal variables be non-negative:

$$\sum_\alpha f_\alpha\dot{\xi}_\alpha \geq 0\,. \tag{4.8}$$

4.4. Application of Rice's formalism to sliding microcrack mechanism

In view of the present modeling purposes, Basista and Gross (1998a) have interpreted Rice's formalism in the context of sliding cracks. The basic premise of Rice's approach, requiring that material response be purely elastic when internal variables are held constant, is satisfied for frictional microcracks as well. No energy is dissipated if the slip displacements and the wing microcrack lengths are fixed through appropriate constraints. Hence, if the total strain increment is decomposed as

$$\mathrm{d}\boldsymbol{\varepsilon} = \mathrm{d}^e\boldsymbol{\varepsilon} + \mathrm{d}^i\boldsymbol{\varepsilon} = \mathbf{M} : \mathrm{d}\boldsymbol{\sigma} + \mathrm{d}^i\boldsymbol{\varepsilon}\,, \tag{4.9}$$

then its inelastic part is derivable from (4.4). The instantaneous compliance tensor M_{ijkl} is given by

$$M_{ijkl} = \left. \frac{\partial^2 \psi(\boldsymbol{\sigma}, H)}{\partial \sigma_{ij} \partial \sigma_{kl}} \right|_{H \text{ fixed}} , \tag{4.10}$$

so that M_{ijkl} is symmetric on interchange of ij and kl (diagonal symmetry).

For *open microcracks*, the instantaneous compliance **M** coincides with the secant (effective) compliance **S** which is symmetric and anisotropic (Horii and Nemat-Nasser, 1983). It should be stressed that at fixed microcrack lengths **M** is nothing else but the unloading compliance. This is so because open cracks are usually assumed to close perfectly (but not heal) upon unloading. Consequently, the specific Gibbs energy in this case reads

$$\psi_{(\text{open cracks})} = \frac{1}{2} \boldsymbol{\sigma} : \mathbf{S} : \boldsymbol{\sigma} . \tag{4.11}$$

However, for Mode II *frictional sliding* on closed microcrack faces, the secant compliance matrix **S** is non-symmetric (e.g. Ju, 1991; Kachanov, 1993). The elastic potential defined in (4.11) does not exist. The secant effective

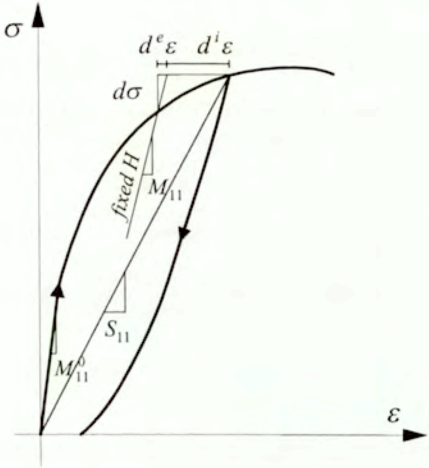

Figure 4.3. Strain increment partition, instantaneous compliance **M**, effective secant compliance **S**, and actual unloading path for typical rock specimen in uniaxial compression (Basista and Gross, 1998a).

compliance is not the unloading compliance due to frictional effects. To illustrate these statements, the initial elastic compliance M_{11}^0, the secant (non-symmetric) compliance S_{11}, the actual unloading path with backsliding, and the instantaneous (symmetric) compliance M_{11} given by (4.10) are illustrated in Figure 4.3 for the uniaxial case. In conclusion, all basic relations of the Rice thermodynamic framework remain valid for an elastic body with frictional cracks with the only difference that the instantaneous compliance $\mathbf{M}$ is not the secant compliance anymore (Basista and Gross, 1998a). It is just an auxiliary concept ensuing from the adopted theory. As will be shown later, $\mathbf{M}$ is expressible in terms of $\mathbf{M}^0$ and the wing microcrack length l.

4.5. Constitutive model

The outlined thermodynamic framework with microstructural internal variables will now be used to model brittle deformation in the case of: (a) frictional microcracks (*phase 1*, no wings yet), and (b) winged microcracks (*phase 2*, full mechanism active). The balance of this chapter comprises the original results of Basista and Gross (1997, 1998a), Basista (1993, 1999) unless stated otherwise.

Phase 1 (frictional sliding along closed microcrack faces). Initially, the preexisting microcracks are closed by the compressive loading and their presence is not felt by the material. At some point the driving shear force exceeds the resistive action of friction and cohesion and the points on the microcrack faces start to move in the sliding mode with the microcrack tips remaining fixed. Elementary equilibrium along the microcrack line and the superposition principle (Figure 4.4) yield

$$\tau_{\mathit{eff}}\, 2c + 2F_{el} = 0 \qquad \text{and} \qquad \sigma_x = \sigma_x^\infty , \tag{4.12}$$

where

$$\tau_{\mathit{eff}} = \tau_{xy} - \tau_{xy}^\infty \tag{4.13}$$

will be called the effective shear stress. In Equations (4.12) and (4.13), $2c$ is the length of the preexisting slit PP', σ_x and τ_{xy} are the unknown normal and shear stresses *actually* acting on PP' expressed in the local coordinate system (x, y); σ_x^∞ and τ_{xy}^∞ are the normal and shear stresses due to remote loading resolved in the cross section PP', F_{el} is (as yet undetermined) elastic

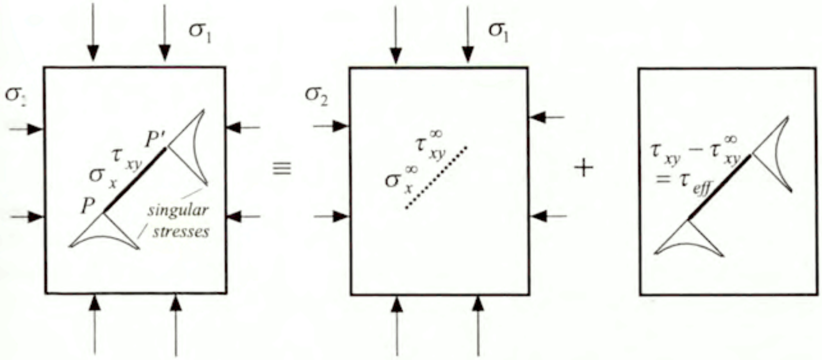

Figure 4.4. Superposition of stresses in phase 1.

crack-closing force acting as to reverse the slip displacement. Note that the crack-closing forces result from the singular stress distributions in the material surrounding the crack tips, as sketched in Figure 4.4.

The Gibbs complementary energy density for the RVE containing a microcrack can formally be decomposed as

$$\psi(\boldsymbol{\sigma}, H) = \psi^0(\boldsymbol{\sigma}) + \Delta\psi(\boldsymbol{\sigma}, H)\,, \tag{4.14}$$

where $\psi^0(\boldsymbol{\sigma}) = \frac{1}{2}\sigma_{ij} M^0_{ijkl} \sigma_{kl}$ with M^0_{ijkl} being the elastic compliance tensor of the matrix material. The term $\Delta\psi(\boldsymbol{\sigma}, H)$ stands for the part of ψ ($\mathrm{d}H \neq 0$) induced by inelastic changes in the microstructural rearrangement, e.g. microcrack growth. In the considered plane case, the presence of a Mode II microcrack in the RVE leads to the following expression for $\Delta\psi$ (Basista and Gross, 1998a)

$$\Delta\psi(\boldsymbol{\sigma}, H) = \frac{1}{A_0} \int_{-c}^{c} \int_{0}^{b(y)} \tau_{xy}(\boldsymbol{\sigma}, b)\, \mathrm{d}b\, \mathrm{d}y\,, \tag{4.15}$$

where A_0 is the surface area of the RVE. The expression (4.15) is the area average of the work done by the actual (shear) tractions τ_{xy} on the corresponding relative (slip) displacements $\mathrm{d}b$ which vary along PP'. In order to facilitate further analysis, introduce the average slip as

$$\bar{b} = \frac{1}{2c} \int_{-c}^{c} b(y)\, \mathrm{d}y\,. \tag{4.16}$$

According to the linear fracture mechanics solution, the average slip (crack opening displacement in Mode II) is related to the net shear stress (4.13) in plane strain as

$$\bar{b} = \frac{1}{2c}\int_{-c}^{c} \frac{-4\tau_{\mathit{eff}}(1-\nu_0^2)}{E_0}\sqrt{c^2-y^2}\,\mathrm{d}y = -\frac{\pi c\tau_{\mathit{eff}}(1-\nu_0^2)}{E_0}\,, \quad (4.17)$$

where E_0 and ν_0 are Young's modulus and Poisson's ratio of the matrix material. Making use of (4.13), (4.16) and (4.17), $\Delta\psi$ given by (4.15) becomes (Basista and Gross, 1998a)

$$\Delta\psi(\boldsymbol{\sigma},\bar{b}) = \frac{2c}{A_0}\int_0^{\bar{b}} \tau_{xy}(\boldsymbol{\sigma},\bar{b})\,\mathrm{d}\bar{b} = \frac{1}{A_0}\left[\tau_{xy}^{\infty}\bar{b}\,2c - \frac{\bar{b}^2E_0}{\pi(1-\nu_0^2)}\right]. \quad (4.18)$$

The correctness of (4.18) can be verified in the following way (Basista, 1999). Consider an intact RVE loaded in biaxial compression. The stresses along the (non-existent) microcrack line take the resolved values σ_x^{∞} , τ_{xy}^{∞} and the effective shear stress as defined in (4.13) is zero. Now, introduce a frictional rectilinear slit of the length $2c$ into the RVE and admit sliding along its faces. This would correspond to a slow release of stresses from the resolved values σ_x^{∞} , τ_{xy}^{∞} down to the actual values σ_x , τ_{xy} currently acting on the microcrack faces. The linear dependence $\tau_{xy}(\bar{b})$ is schematically shown in Figure 4.5.

The microcrack-related part of the Gibbs energy density $\Delta\psi$ is computed from the area below the bold line marked in Figure 4.5 and normalized with respect to A_0 :

$$\begin{aligned}\Delta\psi &= \frac{1}{A_0}\left[\tau_{xy}^{\infty}\bar{b}\,2c - \frac{1}{2}\bar{b}\underbrace{(\tau_{xy}^{\infty}-\tau_{xy})}_{-\tau_{\mathit{eff}}}2c\right] \\ &= \frac{1}{A_0}\left[\tau_{xy}^{\infty}\bar{b}\,2c - \frac{\bar{b}^2E_0}{\pi(1-\nu_0^2)}\right]. \quad (4.19)\end{aligned}$$

The formula (4.19) is identical to (4.18) what makes the checking complete. For a non-frictional microcrack, the microcrack faces are shear stress-free ($\tau_{xy}=0$) as visualized in Figure 4.5 by the dashed line. Accordingly, the formula (4.19) reduces to the familiar form $\Delta\psi = (1/2A_0)\tau_{xy}^{\infty}\,\bar{b}\,2c$.

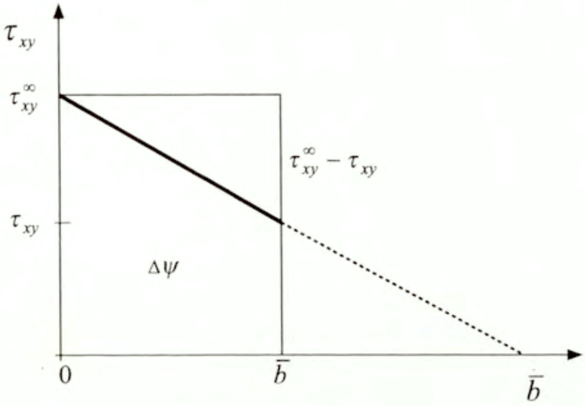

Figure 4.5. Graphical interpretation of $\Delta\psi$ computed in (4.18) (Basista, 1999)

Having determined $\Delta\psi$ in (4.18), it is now possible to compute its inelastic change $\mathrm{d}^i\psi$:

$$\mathrm{d}^i\psi = \left.\frac{\partial(\Delta\psi(\boldsymbol{\sigma},\bar{b}))}{\partial\bar{b}}\right|_{\boldsymbol{\sigma}\text{ fixed}} \mathrm{d}\bar{b} = \frac{1}{A_0}\tau_{xy}2c\,\mathrm{d}\bar{b}\,, \tag{4.20}$$

from which it is straightforward to identify the incremental internal variable and its conjugated thermodynamic force in phase 1 (Basista and Gross, 1998a):

$$\mathrm{d}\xi_1 = \mathrm{d}\bar{b}\,, \qquad f_1 = \tau_{xy}2c = 2c\left[\tau_{xy}^{\infty} - \frac{\bar{b}E_0}{\pi c(1-\nu_0^2)}\right]. \tag{4.21}$$

In view of (4.17), the increment of the frictional slip $\mathrm{d}\bar{b}$ is driven by the increment of the net shear stress τ_{eff} which is different from the conjugated thermodynamic stress τ_{xy}, (4.21). Rice (1971) proved that if the rate of change of each internal variable depends on the external stresses only via its own conjugated thermodynamic force then the normality rule holds in the corresponding macroscopic constitutive law. Since this condition is violated in the considered case, the normality property will not emerge in the macroscopic constitutive law. This observation (cf. Basista and Gross, 1998a) provides a simple micromechanical explanation of the well-known fact that the normality rule does not hold for frictional materials (e.g. Rudnicki and Rice, 1975).

By inserting the conjugate force (4.21) into the fundamental relation (4.6) and performing the required differentiation, the increment of inelastic strain in phase 1 takes the following explicit form (Basista and Gross, 1998a)

$$\mathrm{d}^i\varepsilon_{ij} = \omega_0 \begin{bmatrix} -\sin 2\varphi & \cos 2\varphi \\ \cos 2\varphi & \sin 2\varphi \end{bmatrix} \mathrm{d}\tilde{b} \tag{4.22}$$

where $\omega_0 = Nc^2/A_0$ is the microcrack density parameter in 2D case, N is the number of (non-interacting) microcracks having the same orientation φ and equal length $2c$. Also, the following normalized slip and normalized microcrack length will be used from now on:

$$\tilde{b} = \bar{b}/c\,, \qquad \tilde{l} = l/c\,. \tag{4.23}$$

Depending on the context, both the averaged slip $\bar{b}$ (not normalized) and its normalized counterpart $\tilde{b}$ will appear in the sequel. It is rewarding to see that (4.22), derived strictly within the Rice thermodynamic framework, is exactly the same as the expression (A.4) in Nemat-Nasser and Obata (1988) obtained on kinematic grounds.

The next step of analysis consists in specification of a physical law for the frictional contact on the preexisting microcrack faces. A simple Coulomb–Mohr law of dry friction is assumed to relate the actual shear stress τ_{xy} to the normal stress σ_x along PP':

$$\tau_{xy} = \tau_c - \mu\sigma_x^\infty\,, \tag{4.24}$$

where τ_c is the cohesion and μ the coefficient of dry friction. Both quantities are in fact not constants but some functions of the slip displacement $b(y)$ depending on the loading program. However, it is assumed for simplicity that τ_c and μ are positive constants throughout. If appropriate relations determining τ_c and μ are available they can easily be incorporated in the present framework. In phase 1, the actual normal stress coincides with the resolved normal stress as dictated by the equilibrium condition $(4.12)_2$. Consequently, σ_x^∞ enters the friction law (4.24) instead of σ_x. To keep the analysis self-contained, we recall the elementary expressions for the resolved stresses on PP' in a general 2D case:

$$\begin{aligned} \sigma_x^\infty &= \sigma_{11}\cos^2\varphi + \sigma_{22}\sin^2\varphi + \tau_{12}\sin 2\varphi\,, \\ \tau_{xy}^\infty &= -\frac{1}{2}(\sigma_{11} - \sigma_{22})\sin 2\varphi + \tau_{12}\cos 2\varphi\,, \end{aligned} \tag{4.25}$$

where σ_{11} , σ_{22} , τ_{12} are the applied remote stresses. Under the axial and lateral compression σ_1 and σ_2 , the effective shear stress driving the frictional slip on PP' can now be expressed as

$$\tau_{eff} = \tau_c - \mu(\sigma_1 \cos^2\varphi + \sigma_2 \sin^2\varphi) + \frac{1}{2}\sin 2\varphi(\sigma_1 - \sigma_2)\,. \tag{4.26}$$

From (4.12) and (4.17), the as yet undetermined elastic crack-closing force takes the form

$$F_{el} = \frac{\bar{b}E_0}{\pi(1-\nu_0^2)}\,. \tag{4.27}$$

Combining the equilibrium equation (4.12) with the Coulomb–Mohr condition (4.24) and making use of the expressions (4.26) and (4.27), the *sliding activation equation* is obtained (Basista and Gross, 1998a)

$$\begin{aligned}\Omega_1^s \;=\; & \underbrace{\tau_c - \mu(\sigma_1 \cos^2\varphi + \sigma_2 \sin^2\varphi) + \tfrac{1}{2}\sin 2\varphi(\sigma_1 - \sigma_2)}_{\tau_{eff}} \\ & + \frac{\bar{b}E_0}{\pi c(1-\nu_0^2)} = 0\,. \end{aligned} \tag{4.28}$$

Similar equation has already been used in Moss and Gupta (1982) for a particular representation of the winged microcrack configuration. In their analysis, however, phase 1 has not been considered. It can easily be seen that (4.28) predicts the onset of sliding when $\tau_{eff} = 0$.

To make the constitutive model complete, it is necessary to relate the increment of slip displacement to the increment of stress. This is done by imposing the consistency condition $\dot{\Omega}_1^s = 0$ on (4.28). Note that the consistency condition assures continuous forward sliding.

Phase 2 (full mechanism operative). In this phase curvilinear tension wings are nucleated from the tips of preexisting mirocracks, Figure 4.2. The nucleation and growth of tension wings are induced by the wedging action of the frictional sliding on the surrounding material. In order to make the analytical model tractable, the curvilinear wings will be represented by equivalent straight ones whose orientation θ is to be determined by maximizing K_I at a given straight wing length l. Consequently, the curved trajectory of the wing tip will be modeled as a sequence of positions of the straight wing microcracks rotating around the corner points P or P' by the angle for which K_I reaches a maximum.

The microcrack-induced part of the Gibbs complementary energy density for the RVE containing N winged microcracks of the same orientation is (Basista and Gross, 1997, 1998a)

$$\begin{aligned}\Delta\psi(\boldsymbol{\sigma},H) &= \frac{N}{A_0}\left[\int_{-c}^{c}\int_{0}^{b(y)}\tau_{xy}(\boldsymbol{\sigma},b)\,\mathrm{d}b\,\mathrm{d}y + 2\int_0^l G(\boldsymbol{\sigma},l,\theta)\,\mathrm{d}l\right]\\ &= \frac{N}{A_0}\left[\int_0^{\bar{b}}\tau_{xy}(\boldsymbol{\sigma},\bar{b})\,\mathrm{d}\bar{b} + \frac{1}{E_0'}\,2\int_0^l (K_I^2+K_{II}^2)\,\mathrm{d}l\right],\end{aligned} \tag{4.29}$$

where G is the elastic energy release rate and E_0' has been already defined in (3.27). The integrated form of (4.29), although analytic, is rather lengthy and is not displayed here. The inelastic change of ψ reads

$$\begin{aligned}\mathrm{d}^i\psi &= \frac{\partial\psi}{\partial\bar{b}}\,\mathrm{d}\bar{b} + \frac{\partial\psi}{\partial l}\,\mathrm{d}l + \frac{\partial\psi}{\partial\theta}\,\mathrm{d}\theta\\ &= \frac{N}{A_0}\left[\tau_{xy}2c\,\mathrm{d}\bar{b} + 2G\,\mathrm{d}l + \frac{\partial}{\partial\theta}\left(2\int_0^l G\,\mathrm{d}l\right)\mathrm{d}\theta\right]\\ &= \frac{N}{A_0}\sum_{\alpha=1}^{3} f_\alpha\,\mathrm{d}\xi_\alpha\,.\end{aligned} \tag{4.30}$$

From (4.30), the incremental internal variables and the conjugated thermodynamic forces for a single microcrack are (Basista and Gross, 1997)

$$\begin{aligned} f_1 &= \tau_{xy}2c\,, & \mathrm{d}\xi_1 &= \mathrm{d}\bar{b}\,;\\ f_2 &= G, & \mathrm{d}\xi_2 &= \mathrm{d}l\,;\\ f_3 &= \int_0^l \frac{\partial G}{\partial\theta}\,\mathrm{d}l\,, & \mathrm{d}\xi_3 &= \mathrm{d}\theta\,.\end{aligned} \tag{4.31}$$

The explicit expressions for f_1, f_2, f_3 are contingent on the actual shear stress τ_{xy} on PP' and the stress intensity factors K_I and K_{II} at the wing tips.

Using stress superposition and balancing the forces projected on the line PP' in the cross section $QPP'Q'$ (Figure 4.2), it follows that

$$\tau_{eff}\, 2c - \left[\sigma_{11}\, \cos^2(\theta+\varphi) + \sigma_{22}\, \sin^2(\theta+\varphi) + \tau_{12}\, \sin 2(\theta+\varphi)\right] 2l \sin\theta$$
$$+ \left[\frac{1}{2}(\sigma_{11} - \sigma_{22}) \sin 2(\theta+\varphi) - \tau_{12} \cos 2(\theta+\varphi)\right] 2l \cos\theta + 2\hat{F}_{el}(\bar{b}, l) = 0\,, \tag{4.32}$$

where the term $\hat{F}_{el}(\bar{b}, l) = F^{I}_{el} \sin\theta + F^{II}_{el} \cos\theta$ is the sum of the projections on PP' of the appropriate elastic crack-closing forces F^{I}_{el}, F^{II}_{el} in Mode I and Mode II, respectively. Recall that F^{I}_{el}, F^{II}_{el} are the forces in elastic material due to stress singularities at the crack tip. These forces tend to reverse the crack opening displacements. In view of (4.31) and (4.32), the thermodynamic force conjugated to $\mathrm{d}\bar{b}$ becomes

$$\begin{aligned} f_1 \;=\; & \tau^{\infty}_{xy} 2c - \sigma_{11}\, 2l\, \sin\varphi\, \cos(\theta+\varphi) + \sigma_{22}\, 2l\, \cos\varphi\, \sin(\theta+\varphi) \\ & - \tau_{12}\, 2l\, \cos(\theta + 2\varphi) - 2\hat{F}_{el}(\bar{b}, l). \end{aligned} \tag{4.33}$$

The exact solution for the SIFs at the tips of curvilinear wings can be obtained only numerically (Horii and Nemat-Nasser, 1985a; Lauterbach and Gross, 1998). However, numerous closed-form approximations of K_I and K_{II} are available in the literature. They can be arranged in two classes: displacement-driven models (e.g. Steif, 1984; Nemat-Nasser and Obata, 1988) and force-driven models (e.g. Moss and Gupta, 1982; Zaitsev 1985; Horii and Nemat-Nasser, 1986; Kemeny and Cook, 1991). The displacement-driven and the force-driven models of the basic mechanism are depicted in Figure 4.6a,b. In both models, the curvilinear wings of the sliding microcrack (Figure 4.2) are replaced by the straight ones whose orientation θ is determined by maximizing $K_I(\theta)$, while the length l follows from the Griffith condition (see Equations (4.47)). Recently, Lehner and Kachanov (1996) published a critical and exhaustive review of all available approximations of the SIFs for the sliding crack.

In the displacement-driven model (Figure 4.6a), the rectilinear wings are pushed sideways by a rigid wedge whose dimensions are determined by the preexisting microcrack length $2c$ and the varying slip displacement $\bar{b}$. Here, the SIFs involve complete elliptic integrals of the first and second kind, $K(k)$ and $E(k)$, with the modulus $k = \sqrt{l^2 + 2lc\cos\theta}/(l + c\cos\theta)$, cf. Tada et al. (1985). These SIFs are not expressible by means of analytic functions except for the special case of a *semi-infinite wedge* which would correspond to a pair of separate straight wing microcracks not interacting with each other. This might be a realistic approximation only for the initial phase

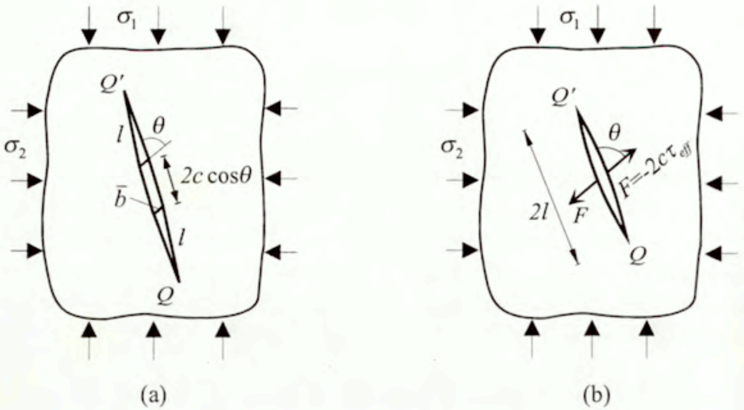

Figure 4.6. Two simplified models of sliding microcrack mechanism: (a) displacement-driven, (b) force-driven.

of kinking when the wings are very small ($l \ll c$). Incidentally, such an approximation has been used as a basis in Nemat-Nasser and Obata (1988) for an alternative analytical derivation of the inelastic strains, according to the well-known kinematic formula

$$\boldsymbol{\varepsilon}^i = \frac{1}{2V_0} \sum_k \int_{A^{(k)}} (\mathbf{n} \otimes [\mathbf{u}] + [\mathbf{u}] \otimes \mathbf{n}) \, \mathrm{d}A \,, \tag{4.34}$$

where $[\mathbf{u}]$ is the COD vector, $\mathbf{n}$ is the unit vector normal to the microcrack surface, $A^{(k)}$ is the surface area of the k-th microcrack and V_0 the volume of the RVE. For separate wings, there is no wing–wing interaction thus the modulus k equals zero. Consequently, the SIFs at the tips Q and Q' are expressible in the following form (e.g. Tada et al., 1985)

$$\begin{aligned} K_I(\bar{b}, l, \boldsymbol{\sigma}) &= \frac{E_0' \bar{b} \sin\theta}{2\sqrt{2\pi(l + l^{**})}} + \sqrt{\frac{\pi l}{2}} \left[\sigma_{11} \cos^2(\theta + \varphi) \right. \\ &\qquad \left. + \sigma_{22} \sin^2(\theta + \varphi) + \tau_{12} \sin 2(\theta + \varphi)\right], \\ K_{II}(\bar{b}, l, \boldsymbol{\sigma}) &= \frac{-E_0' \bar{b} \cos\theta}{2\sqrt{2\pi(l + l^{**})}} - \sqrt{\frac{\pi l}{2}} \left[\tau_{12} \cos 2(\theta + \varphi) \right. \\ &\qquad \left. - \tfrac{1}{2}(\sigma_{11} - \sigma_{22}) \sin 2(\theta + \varphi)\right], \end{aligned} \tag{4.35}$$

where $l^{**} = 0.27\,c\pi^2/32$ is the nucleus wing length introduced in Nemat-Nasser and Obata (1988) to get the correct asymptotic behavior of (4.35) in the short wing limit (Cotterell and Rice, 1980).

Strictly speaking, the original sliding microcrack $QPP'Q'$ (Figure 4.2) is displacement-driven. The SIFs at the wing tips are directly proportional to the relative slip of the slanted microcrack faces. However, when the preexisting microcrack undergoes forward- or backsliding, its wedging action upon the wings may equivalently be considered as force-driven (Nemat-Nasser and Obata, 1988). Then, the wedging effect can be represented by two collinear splitting forces $F = -2c\tau_{\mathit{eff}}$, Figure 4.6b. If the curvilinear wing microcracks are further approximated by the equivalent straight microcracks whose orientation θ_c satisfies the condition $K_I(\theta_c) \to \max$, the estimates of the SIFs are (Horii and Nemat-Nasser, 1986):

$$\begin{aligned} K_I(F,l,\boldsymbol{\sigma}) &= \frac{F\sin\theta}{\sqrt{\pi(l+l^*)}} + \sqrt{\pi l}\,\big[\sigma_{11}\,\cos^2(\theta+\varphi) \\ &\qquad + \sigma_{22}\,\sin^2(\theta+\varphi) + \tau_{12}\,\sin 2(\theta+\varphi)\big]\,, \\ K_{II}(F,l,\boldsymbol{\sigma}) &= \frac{-F\cos\theta}{\sqrt{\pi(l+l^*)}} - \sqrt{\pi l}\,\big[\tau_{12}\,\cos 2(\theta+\varphi) \\ &\qquad - \tfrac{1}{2}(\sigma_{11}-\sigma_{22})\sin 2(\theta+\varphi)\big]\,, \end{aligned} \tag{4.36}$$

where $l^* = 0.27\,c$ plays the same role as l^{**} in the displacement-driven model. Examination of the structure of (4.35) and (4.36) reveals an interplay between the first term that drives the wing microcrack growth and the second one which suppresses (if compressive) or aggravates (if tensile) the wing growth. The microcrack driving terms are proportional to $1/\sqrt{l}$ while the suppressive (aggravating) ones to $\sqrt{l}$.

The inelastic strains induced by the coupled effects of frictional sliding along preexisting flaw, wing extension, and its simultaneous rotation can now be computed. It should be kept in mind that the wing rotation is just a by-product of the adopted model of the curvilinear wing tip trajectory. The wing length itself is calculated from the $K_I = K_{Ic}$ condition. The inelastic strain increments are obtained from the fundamental relation (4.6) using the derived microstructural thermodynamic forces (4.31), (4.33) and the approximate expressions for the SIFs (4.35), (4.36). It is essential that the conjugate forces f_α be symmetrized in the components of $\boldsymbol{\sigma}$ and all three components of the stress applied at infinity be included when performing differentiation in (4.6). Also, due caution should be exercised when differentiating the conjugate forces with respect to the macroscopic stress tensor as prescribed by Equation (4.6). This differentiation is to be carried out at fixed H, i.e. at $\tilde{b}$ and $\tilde{l}$ held constant. In the present model, the effect of frictional sliding along PP' is represented by the action of two collinear splitting forces F. Once the internal variables $\tilde{b}$ and $\tilde{l}$ are held frozen, so are the splitting forces F. Therefore, the physical law (4.24) or its extended version (4.26), defining the effective shear stress in terms of the applied stresses, should not be substituted in the expressions for the SIFs (4.36) prior to the differentiation operation in (4.6) (cf. Basista and Gross, 1998a). Otherwise, an incorrect solution for the inelastic strains may follow, as in Kemeny and Cook (1991). This issue is further elaborated in Appendix 4.1.

After some computational effort, the final outcome in the global coordinates $(x_1\,,\,x_2)$ reads (Basista and Gross, 1997):

Strain increment due to frictional sliding ($\tilde{b}$-driven and F-driven model alike)[1]

$$\begin{aligned} \mathrm{d}\varepsilon^s_{ij} \;&=\; \omega_0 \begin{bmatrix} -\sin 2\varphi & \cos 2\varphi \\ \cos 2\varphi & \sin 2\varphi \end{bmatrix} \mathrm{d}\tilde{b} \\ &+ \omega_0 \begin{bmatrix} -2\sin\varphi\,\cos(\theta+\varphi) & \cos(\theta+2\varphi) \\ \cos(\theta+2\varphi) & 2\cos\varphi\,\sin(\theta+\varphi) \end{bmatrix} \mathrm{d}\tilde{b}\,\tilde{l}. \end{aligned} \tag{4.37}$$

The parameter $\omega_0 = Nc^2/A_0$, which arises here in a natural manner from the structure of the potential $\Delta\psi$, is identical to the damage parameter introduced in Walsh (1965). In the literature, a similar parameter is also often referred to as the Budiansky–O'Connell (1976) crack density parameter.

---

[1] Abbreviations ***$\tilde{b}$-driven*** and ***F-driven*** used in Equations (4.37)–(4.43) refer to the displacement-driven model (Figure 4.6a) and the force-driven model (Figure 4.6b) of the sliding microcrack mechanism (Figure 4.2).

Strain increment due to wing microcrack extension ($\tilde{b}$-driven)

$$
\begin{aligned}
\mathrm{d}\varepsilon^c_{ij} = {} & \frac{\omega_0}{2}\, g_1(\tilde{l}) \begin{bmatrix} -2\sin\varphi\cos(\theta+\varphi) & \cos(\theta+2\varphi) \\ \cos(\theta+2\varphi) & 2\cos\varphi\sin(\theta+\varphi) \end{bmatrix} \tilde{b}\,\mathrm{d}\tilde{l} \\
& + \frac{\pi\omega_0}{2E_0'} \Bigg\{ \left[4\sigma_1\cos^2(\theta{+}\varphi) + 4\sigma_2\sin^2(\theta{+}\varphi)\right] \\
& \qquad \times \begin{bmatrix} \cos^2(\theta{+}\varphi) & \frac{1}{2}\sin 2(\theta{+}\varphi) \\ \frac{1}{2}\sin 2(\theta{+}\varphi) & \sin^2(\theta{+}\varphi) \end{bmatrix} \\
& \qquad - (\sigma_1-\sigma_2)\sin 2(\theta{+}\varphi) \begin{bmatrix} -\sin 2(\theta{+}\varphi) & \cos 2(\theta{+}\varphi) \\ \cos 2(\theta{+}\varphi) & \sin 2(\theta{+}\varphi) \end{bmatrix} \Bigg\} \tilde{l}\,\mathrm{d}\tilde{l}
\end{aligned}
\tag{4.38}
$$

where $g_1(\tilde{l}) = \sqrt{\tilde{l}/(\tilde{l}+\tilde{l}^{**})}$.

Strain increment due to wing microcrack rotation ($\tilde{b}$-driven)

$$
\begin{aligned}
\mathrm{d}\varepsilon^\theta_{ij} = {} & \omega_0 \begin{bmatrix} \sin\varphi\sin(\theta+\varphi) & -\frac{1}{2}\sin(2\varphi+\theta) \\ -\frac{1}{2}\sin(2\varphi+\theta) & \cos\varphi\cos(\theta+\varphi) \end{bmatrix} \tilde{b}\, h_1(\tilde{l})\,\mathrm{d}\theta \\
& + \omega_0\,\frac{\pi\tilde{l}^2}{E_0'} \begin{bmatrix} -\sin 2(\theta+\varphi)\,\sigma_1 & \begin{gathered}\frac{1}{2}\cos 2(\theta+\varphi) \\ \times(\sigma_1+\sigma_2)\end{gathered} \\ \begin{gathered}\frac{1}{2}\cos 2(\theta+\varphi) \\ \times(\sigma_1+\sigma_2)\end{gathered} & \sin 2(\theta+\varphi)\,\sigma_2 \end{bmatrix} \mathrm{d}\theta,
\end{aligned}
\tag{4.39}
$$

where

$$
h_1(\tilde{l}) = \sqrt{\tilde{l}(\tilde{l}+\tilde{l}^{**})} - \frac{\tilde{l}^{**}}{2}\,\ln\left[\frac{2\tilde{l}}{\tilde{l}^{**}} + 2\sqrt{\frac{\tilde{l}}{\tilde{l}^{**}}\left(\frac{\tilde{l}}{\tilde{l}^{**}}+1\right)} + 1\right].
$$

Strain increment due to wing microcrack extension (F-driven)

$$
\begin{aligned}
\mathrm{d}\varepsilon_{ij}^{c} = {} & \frac{-4\omega_0\tau_{\mathit{eff}}}{E_0'}\, g_2(\tilde{l}) \\
& \times \begin{bmatrix} -2\sin\varphi\cos(\theta+\varphi) & \cos(\theta+2\varphi) \\ \cos(\theta+2\varphi) & 2\cos\varphi\sin(\theta+\varphi) \end{bmatrix} \mathrm{d}\tilde{l} \\
& + \frac{\pi\omega_0}{E_0'} \left\{ \left[4\sigma_1\cos^2(\theta+\varphi) + 4\sigma_2\sin^2(\theta+\varphi)\right] \right. \\
& \qquad \times \begin{bmatrix} \cos^2(\theta+\varphi) & \frac{1}{2}\sin 2(\theta+\varphi) \\ \frac{1}{2}\sin 2(\theta+\varphi) & \sin^2(\theta+\varphi) \end{bmatrix} \\
& \quad - (\sigma_1-\sigma_2)\sin 2(\theta+\varphi) \\
& \qquad \left. \times \begin{bmatrix} -\sin 2(\theta+\varphi) & \cos 2(\theta+\varphi) \\ \cos 2(\theta+\varphi) & \sin 2(\theta+\varphi) \end{bmatrix} \right\} \tilde{l}\,\mathrm{d}\tilde{l}
\end{aligned}
\tag{4.40}
$$

where $g_2(\tilde{l}) = \sqrt{\tilde{l}(\tilde{l}+\tilde{l}^{*})}$.

Strain increment due to wing microcrack rotation (F-driven)

$$
\begin{aligned}
\mathrm{d}\varepsilon_{ij}^{\theta} = {} & \omega_0\,\frac{-8\tau_{\mathit{eff}}}{E_0'} \begin{bmatrix} \sin\varphi\sin(\theta+\varphi) & -\frac{1}{2}\sin(2\varphi+\theta) \\ -\frac{1}{2}\sin(2\varphi+\theta) & \cos\varphi\cos(\theta+\varphi) \end{bmatrix} h_2(\tilde{l})\,\mathrm{d}\theta \\
& + \omega_0\,\frac{2\pi\,\tilde{l}^2}{E_0'} \begin{bmatrix} -\sin 2(\theta+\varphi)\,\sigma_1 & \begin{matrix}\frac{1}{2}\cos 2(\theta+\varphi) \\ \times(\sigma_1+\sigma_2)\end{matrix} \\ \begin{matrix}\frac{1}{2}\cos 2(\theta+\varphi) \\ \times(\sigma_1+\sigma_2)\end{matrix} & \sin 2(\theta+\varphi)\,\sigma_2 \end{bmatrix} \mathrm{d}\theta,
\end{aligned}
\tag{4.41}
$$

where

$$
h_2(\tilde{l}) = \sqrt{\tilde{l}(\tilde{l}+\tilde{l}^{*})} - \frac{\tilde{l}^{*}}{2}\,\ln\left[\frac{2\tilde{l}}{\tilde{l}^{*}} + 2\sqrt{\frac{\tilde{l}}{\tilde{l}^{*}}\left(\frac{\tilde{l}}{\tilde{l}^{*}}+1\right)} + 1\right].
$$

The elastic part of the strain increment is computed from the relations (4.9) and (4.10) with the Gibbs potential given by (4.29). The final form of the elastic part of strain tensor increment in the global coordinates $(x_1\,,\,x_2)$ reads (Basista and Gross, 1997)

Elastic part of strain increment ($\tilde{b}$-driven)

$$\begin{aligned} \mathrm{d}^e\varepsilon_{ij} &= M^0_{ijkl}\,\mathrm{d}\sigma_{kl} \\ &\quad + \omega_0\,\frac{\pi\,\tilde{l}^2}{E'_0}\begin{bmatrix} \mathrm{d}\sigma_1\ \cos^2(\theta+\varphi) & \begin{array}{c}\frac{1}{4}(\mathrm{d}\sigma_1+\mathrm{d}\sigma_2)\\ \times\sin 2(\theta+\varphi)\end{array} \\ \begin{array}{c}\frac{1}{4}(\mathrm{d}\sigma_1+\mathrm{d}\sigma_2)\\ \times\sin 2(\theta+\varphi)\end{array} & \mathrm{d}\sigma_2\ \sin^2(\theta+\varphi) \end{bmatrix}. \end{aligned} \tag{4.42}$$

Elastic part of strain increment (F-driven)

$$\mathrm{d}^e\varepsilon_{ij} = 2\,\mathrm{d}^e\varepsilon_{ij}^{\tilde{b}\text{-}driven}. \tag{4.43}$$

The total strain increment comprises all the individual terms, namely

$$\mathrm{d}\varepsilon_{ij} = \mathrm{d}^e\varepsilon_{ij} + \mathrm{d}\varepsilon^s_{ij} + \mathrm{d}\varepsilon^c_{ij} + \mathrm{d}\varepsilon^\theta_{ij}\,. \tag{4.44}$$

The constitutive framework for phase 2 is now completed by specifying the kinetic equations for the rates $\mathrm{d}\xi_i/\mathrm{d}t$. Since no microcrack–microcrack interaction is yet included, it suffices to consider kinetic equations for the three microstructural internal variables $\tilde{b}$, $\tilde{l}$, θ pertinent to a single winged microcrack. Consequently, the overall strains may be estimated afterwards using a simple averaging procedure that sums up the individual contributions of all active microcracks while accounting for the assumed spatial distribution of the preexisting flaws.

In general, the slip displacement $\tilde{b}$ is to be computed from the forward- or backsliding activation condition, the wing length $\tilde{l}$ from the winged microcrack growth condition, the orientation angle θ of the equivalent straight microcrack from the maximization of K_I with respect to θ. The rates $\dot{\tilde{b}}$, $\dot{\tilde{l}}$, $\dot{\theta}$ expressed in terms of the applied stress rates $\dot{\sigma}_{ij}$ are obtained imposing the consistency requirements upon the above conditions.

The sliding activation condition for phase 2 is obtained by combining the equilibrium Equation (4.32) and the Mohr–Coulomb condition (4.24) for frictional glide (Basista and Gross, 1997):

$$\begin{aligned}\Omega_2^s = \sigma_{11}&\left[\cos\varphi(\sin\varphi-\mu\cos\varphi)+\tilde{l}\cos(\theta+\varphi)\sin\varphi\right]\\ &-\sigma_{22}\left[\sin\varphi(\cos\varphi+\mu\sin\varphi)+\tilde{l}\sin(\theta+\varphi)\cos\varphi\right]\\ &+\tau_{12}\left[\cos 2\varphi+\mu\sin 2\varphi-\tilde{l}\cos(\theta+2\varphi)\right]+\tau_c+c^{-1}\hat{F}_{el}=0\,.\end{aligned} \tag{4.45}$$

As noticed by Moss and Gupta (1982), it is difficult to determine $\hat{F}_{el}$ because the stress-COD relation for the entire kinked microcrack is not available. Consequently, some approximate solutions were sought. For example, Moss and Gupta (1982) neglected the initial slit ($c \to 0$) and considered two limiting cases: $\theta \to 90°$ (locally Mode I microcrack) and $\theta \to 0°$ (Mode II microcrack). Upon introducing a simplification that the wings grow parallel to the direction of the dominant principal compressive stress σ_1 (i.e. $\theta+\varphi = \pi/2$), these authors obtained from (4.45) that

$$\hat{F}_{el} = \frac{\tilde{b}E_0'}{4}\,. \tag{4.46}$$

Incidentally, Basista and Gross (1998a) obtained the same result while the derivation algorithm itself was based on a somewhat different reasoning. Estimation of the elastic restoring forces makes the computation of $\tilde{b}$ (normalized average slip) straightforward. Furthermore, the kinetic equation for $\dot{\tilde{b}}$ can now be derived from the sliding activation Equation (4.45) by time differentiation. For the sake of completeness, we recall also an alternative algorithm for computing $\tilde{b}$ proposed by Nemat-Nasser and Obata (1988), see also Deng and Nemat-Nasser (1992). Nemat-Nasser and Obata (1988) did not analyze the equilibrium of the slanted microcrack but stated that $\tilde{b}$ can be derived from a duality of K_I factors upon requiring that K_I of the displacement-driven model (4.35) be equal to that of the force-driven model (4.36) when the sliding mechanism is active.

The remaining kinematic variables $\tilde{l}$ and θ are obtained as functions of σ_{ij} from the following conditions:

$$\begin{cases} K_I = K_{Ic}, \\ \dfrac{\partial K_I}{\partial\theta} = 0, \end{cases} \tag{4.47}$$

where K_I is given by (4.35) or (4.36) depending on the considered model. Kinetic relations for $\dot{\tilde{l}}(\dot{\sigma}_{ij})$ and $\dot{\theta}(\dot{\sigma}_{ij})$ follow from (4.47) by time differentiation. The resulting equations are algebraically quite involved thus have been solved numerically using the symbolic algebra softwares. In the long-wing limit, these equations take much simpler forms and for uniaxial compression are even solvable analytically.

It is interesting to compare the expressions for inelastic strains derived in this section using the microstructural internal variable framework and the force-driven model of the sliding microcrack (Figure 4.6b) with the corresponding ones in Nemat-Nasser and Obata (1988) derived using the kinematic algorithm (Equation (4.34)) and the displacement-driven model (Figure 4.6a). To make the comparison tractable, consider the specific case of long-wing limit for which the following relations hold: $\theta + \varphi = \pi/2$, $\mathrm{d}\theta = 0, \tilde{l} \gg 1$. The Nemat-Nasser and Obata result $(2.15)^1$, when specified for long wings and rewritten in a comparable form, reads

$$\begin{aligned}\mathrm{d}^i\varepsilon_{ij} \;=\; & \omega_0 \begin{bmatrix} -\sin 2\varphi & \cos 2\varphi \\ \cos 2\varphi & \sin 2\varphi \end{bmatrix} \mathrm{d}\tilde{b} \\ & + \omega_0 \begin{bmatrix} 0 & -\sin\varphi \\ -\sin\varphi & 2\cos\varphi \end{bmatrix} \frac{1}{2}(\tilde{l}\,\mathrm{d}\tilde{b} + \tilde{b}\,\mathrm{d}\tilde{l}) \\ & + \frac{2\pi\omega_0(1-\nu_0^2)}{E_0} \begin{bmatrix} 0 & 0 \\ 0 & \sigma_2 \end{bmatrix} \tilde{l}\,\mathrm{d}\tilde{l}. \end{aligned} \tag{4.48}$$

Its counterpart in this study are expressions (4.37) and (4.40) which in the long-wing limit reduce to

$$\begin{aligned}\mathrm{d}^i\varepsilon_{ij} \;=\; & \omega_0 \begin{bmatrix} -\sin 2\varphi & \cos 2\varphi \\ \cos 2\varphi & \sin 2\varphi \end{bmatrix} \mathrm{d}\tilde{b} \\ & + \omega_0 \begin{bmatrix} 0 & -\sin\varphi \\ -\sin\varphi & 2\cos\varphi \end{bmatrix} \left(\tilde{l}\,\mathrm{d}\tilde{b} - \frac{4(1-\nu_0^2)}{E_0}\,\tau_{\mathit{eff}}\,\mathrm{d}\tilde{l}\right) \\ & + \frac{4\pi\omega_0(1-\nu_0^2)}{E_0} \begin{bmatrix} 0 & 0 \\ 0 & \sigma_2 \end{bmatrix} \tilde{l}\,\mathrm{d}\tilde{l}. \end{aligned} \tag{4.49}$$

At the glance, the general structure of either solution is very similar. However, a closer look reveals certain differences. The first terms in (4.48) and (4.49) are identical. The last term in (4.49) is twice as large as that in

---

[1] numbering of Nemat-Nasser and Obata (1988).

(4.48). This difference can easily be explained if one notices that a single microcrack of the total length $2\tilde{l}$ (present model) responds differently to the applied load than two separate wing microcracks each of the length $\tilde{l}$ (Nemat-Nasser and Obata's model), see Appendix 4.2. Although the proof in Appendix 4.2 refers to elastic strains, the factor of 2 appears in the elastic and inelastic strains alike. Comparison of the second term in (4.49) with the corresponding term in (4.48) needs a somewhat extended comment. First, it is necessary to express τ_{eff} in function of $\tilde{b}$. As already stated in this chapter, it can be done in two ways. The relation $\tau_{eff}(\tilde{b})$ can be either extracted from (4.45), (4.46), or computed upon demanding that $(4.35)_1$ and $(4.36)_1$, be equal when the sliding microcrack is growing (cf. Nemat-Nasser and Obata, 1988; Basista, 1993). If the latter option is selected, the term in question becomes

$$\left[\frac{1}{2}\left(2\tilde{l}\,\mathrm{d}\tilde{b}+\sqrt{2}\tilde{b}\,\mathrm{d}\tilde{l}\right)-\frac{16\pi(1-\nu_0^2)}{E_0\cos\varphi}\left(1-\sqrt{\frac{1}{2}}\right)\sigma_2\tilde{l}\,\mathrm{d}\tilde{l}\right]. \qquad (4.50)$$

It is seen that in comparison with (4.48), the expression (4.50) contains an extra term that is proportional to $\sigma_2\tilde{l}\,\mathrm{d}\tilde{l}$. Its appearance can be explained if we look more closely into what happens with the two models if a microcrack is allowed to grow by $\mathrm{d}\tilde{l}$. The reasoning to follow is based on a thought experiment (*Gedankenexperiment*) rather than on a real physical realization. If the microcrack length changes by $\mathrm{d}\tilde{l}$ (while $\tilde{b}$ is held constant) then in the kinematic model of Nemat-Nasser and Obata (Figure 4.7a) the inelastic part of strain increment is simply proportional to $\tilde{b}\mathrm{d}\tilde{l}$. However, in the present force-driven model, the incremental cut $\mathrm{d}\tilde{l}$ induces some additional (normal and shear) incremental displacements, as depicted in Figure 4.7b. These displacements are then reflected as additional inelastic strain increments in (4.50). The first term in the first parenthesis of (4.50) accounts for the influence of wings on the amount of strain induced by frictional sliding along preexisting microcracks. It differs by a factor of 2 from the corresponding term in (4.48). However, Nemat-Nasser and Obata's result obtained for two separate, displacement-driven, wing microcracks is strictly valid only in the short wing limit, and will be larger as the wings keep growing. In the present analysis, the examined term was obtained from the winged microcrack equilibrium and the fundamental relation (4.6). No reference has been made yet to a particular model for the computation of the sliding related strains. Finally, the factor $\sqrt{2}$ accompanying $\tilde{b}\,\mathrm{d}\tilde{l}$ in (4.50) is

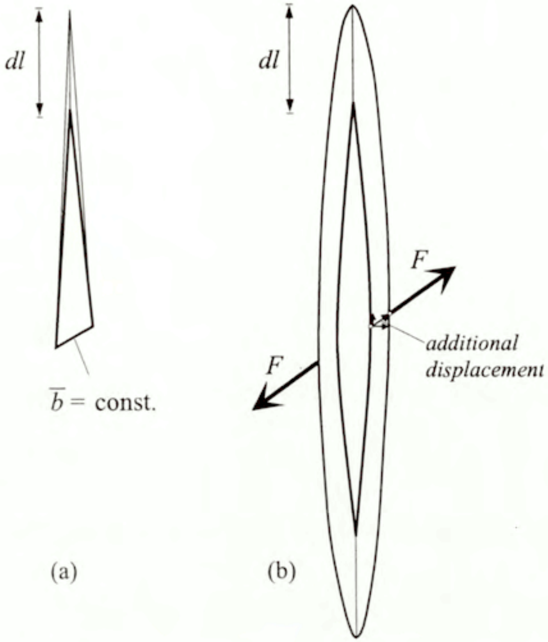

Figure 4.7. (a) Graphic representation of inelastic strain increment in Nemat-Nasser and Obata's model. (b) Additional normal and tangential displacement increments produced by force-driven model (Basista and Gross, 1998a).

due to different predictions furnished by F-driven vs. $\bar{b}$-driven model. This issue is discussed in detail in Appendices 4.2 and 4.3.

4.6. Unloading of sliding microcrack

So far the present analysis has been concerned with loading regime. Consider now unloading by *reducing* the applied stresses. It should be emphasized that for sliding microcracks, any reduction of applied stresses does not necessarily mean elastic unloading. The energy may locally be dissipated on backsliding or wing growth of some microcracks despite the fact that the overall stress is actually decreasing. Also, unloading on some sliding microcracks may happen if the load path is changed, the load itself being not necessarily reduced. In the present model, similarly as in Nemat-Nasser and Obata (1988), a winged microcrack is considered 'unloaded' if its effective shear stress changes, for whatever reason, such that $\mathrm{d}|\tau_{\mathit{eff}}| < 0$. Depending on the load path, various situations may take place (Basista and Gross, 1998a; Nemat-Nasser and Obata, 1988):

- *sliding microcrack mechanism is locked*; such situation may happen when axial stress has dropped but insufficiently to initiate backsliding (or wing growth, if wings are curvilinear) while lateral confinement remains constant,
- *backsliding occurs without wing microcrack closure*; this is expected when axial stress is reduced far enough to initiate reverse sliding on a preexisting microcrack; backsliding is driven by the maximum effective shear stress accumulated within the system at the end of loading regime,
- *wing microcrack partially closes without backsliding*; this may happen, for instance, when axial stress is held constant while lateral confinement grows but not enough to initiate backsliding (this example shows that a sliding microcrack may become unloaded by merely changing the load path in loading),
- *wing microcrack partially closes with backsliding, wing microcrack grows without forward sliding*; this is observed when σ_1 is held constant while lateral confinement is reduced but not sufficiently to trigger forward sliding; it may also happen when a real winged microcrack with curved wings is locked at σ_2 held constant while axial stress is reduced.

These cases will now be systematically interpreted within the present framework for the long-wing approximation.

Locked microcrack ($\mathrm{d}\tilde{b} = 0$, $\mathrm{d}\tilde{l} = 0$) There is no energy dissipation when the sliding microcrack mechanism is locked. Hence, unloading in this case is a purely elastic process. However, in comparison with the initial (unstressed) state, the material is now slightly more compliant in the lateral direction, as predicted by the second term in (4.42). This behavior is to be traced back to the growth of axial wing microcracks during the loading regime. In the long-wing approximation, the axial compliance remains unaffected.

Backsliding without wing microcrack closure ($\mathrm{d}\tilde{b} < 0,\ \mathrm{d}\tilde{l} = 0$) As soon as the applied axial stress is reduced, the opposing forces of friction and cohesion change sign. The maximum effective shear stress attained at the end of the loading regime is accumulated as a spring force in the locked microcrack. At some instant in unloading, this force overcomes the cooperative resistance of friction, cohesion, and the actual shear stress on PP' so that backsliding may commence. The backsliding activation equation has the same form as the forward sliding activation equation (4.45), except for the signs of the cohesive and frictional stresses. The maximum microcrack restoring force $\hat{F}_{el}^{M}$ is to be computed from the forward sliding activation equation (4.45) at the end of the loading process. As a consequence, the onset of backsliding takes place when (Basista and Gross, 1998a)

$$\begin{aligned}&\left(\tau_{xy}^{\infty M} - \tau_{xy}^{\infty}\right) + \mu\left(\sigma_{x}^{\infty M} + \sigma_{x}^{\infty}\right)\\&\qquad + \left(\sigma_{22}^{M} - \sigma_{22}\right)\tilde{l}^{M}\cos\varphi - \left(\tau_{12}^{M} - \tau_{12}\right)\tilde{l}^{M}\sin\varphi - 2\tau_c = 0, \quad (4.51)\end{aligned}$$

where σ_{22}, τ_{12} are the lateral and shear components of the macroscopic stress tensor, the resolved stresses τ_{xy}^{∞}, $\tau_{xy}^{\infty M}$, σ_{x}^{∞}, $\sigma_{x}^{\infty M}$ are given by (4.25), whereas $\tilde{l}^{M} = \text{const.}$ follows from the Griffith condition $(4.47)_1$. The superscript M when assigned to a variable denotes its maximum value recorded in the loading process.

The inelastic part of the strain increment comprises only two first terms of the expression (4.49) (cf. Basista and Gross, 1998a):

$$\begin{aligned}\mathrm{d}^{i}\varepsilon_{ij} \;=\; &\omega_0 \begin{bmatrix} -\sin 2\varphi & \cos 2\varphi \\ \cos 2\varphi & \sin 2\varphi \end{bmatrix} \mathrm{d}\tilde{b}\\ &+ \omega_0 \begin{bmatrix} 0 & -\sin\varphi \\ -\sin\varphi & 2\cos\varphi \end{bmatrix} \tilde{l}^{M}\,\mathrm{d}\tilde{b}, \qquad (4.52)\end{aligned}$$

where $\mathrm{d}\tilde{b} < 0$ is obtained from (4.45) and (4.46) rephrased for backsliding in the long-wing limit. It can be inferred from the structure of (4.52) that a permanent set remains after complete unloading both in the axial and lateral direction, with the latter prevailing.

Partial microcrack closure without backsliding ($\mathrm{d}\tilde{b} = 0,\ \mathrm{d}\tilde{l} < 0$) In general, the condition for crack closure is $K_I = 0$. In the present case, the initial microcrack remains locked, thus the force driven stress intensity factors (4.36) cannot be used. It is necessary to express the SIFs in terms of $\tilde{b}$, $\tilde{l}$, and the applied stress. This has been done in (4.35) where the sliding microcrack mechanism was modeled as displacement-driven. Thus, the condition for microcrack closure becomes

$$K_I = \frac{E_0}{1-\nu_0^2}\,\frac{\tilde{b}\sqrt{c}\,\cos\varphi}{2\sqrt{2\pi\tilde{l}}} + \sigma_{22}\sqrt{\frac{\pi c\tilde{l}}{2}} = 0. \tag{4.53}$$

Using the maximum values for the slip and the wing length $\tilde{b}^M$, $\tilde{l}^M$ attained in the loading regime, it is possible to compute the lateral confinement necessary to initiate wing closure. If the microcrack closure process is to continue, the consistency relation $\dot{K}_I = 0$ must be satisfied. Hence, as the lateral pressure increases the wing length decreases according to (Basista and Gross, 1998a)

$$\mathrm{d}\tilde{l} = \frac{E_0\tilde{b}^M\,\cos\varphi}{2\pi(1-\nu_0^2)(\sigma_{22})^2}\,\mathrm{d}\sigma_{22} < 0. \tag{4.54}$$

The microcrack closure is a non-dissipative process (microcrack healing is here excluded). The ensuing elastic compliance tensor **M** is obtained from (4.9), (4.10), (4.29) with the only difference that K_I and K_{II} are now given by (4.35), in which $\bar{b} = \bar{b}^M$. Hence, putting $\tau_{12} = \mathrm{d}\tau_{12} = 0$, and using (4.54), the strain increment in this phase becomes (Basista and Gross, 1998a)

$$\begin{aligned}\mathrm{d}\varepsilon_{ij} = \mathrm{d}^e\varepsilon_{ij} \;=\; & M^0_{ijkl}\mathrm{d}\sigma_{kl} \\ & + \omega_0\frac{E_0}{4\pi(1-\nu_0^2)}\left(\frac{\tilde{b}^M}{\sigma_2}\right)^2\cos^2\varphi\,\delta_{i2}\delta_{j2}\,\mathrm{d}\sigma_2\,.\end{aligned} \tag{4.55}$$

This result coincides with the Nemat-Nasser and Obata (1988) result (2.28)[1] obtained from the kinematic model.

Partial microcrack closure with backsliding ($\mathrm{d}\tilde{b} < 0$, $\mathrm{d}\tilde{l} < 0$) In this case, the backsliding activation condition (4.51) and the microcrack closure condition (4.53) must simultaneously be met. The strains resulting from backsliding are inelastic, while those from wing microcrack closure are elastic. Both strain increments have already been computed separately in (4.52) and

---

[1] to within a simplification introduced in their (E.4) and commented thereafter.

(4.55). However, the superscript M at $\tilde{b}^M$ in (4.55) must be dropped now since backsliding has been activated, i.e. $\tilde{b}$ is not constant anymore. The reverse slip $\tilde{b}$ and its increment $\mathrm{d}\tilde{b}$ can be computed from (4.45) and (4.46) modified for the backsliding. The microcrack length $\tilde{l}$ and its negative increment $\mathrm{d}\tilde{l}$ are derivable from the microcrack closure condition (4.53).

Wing microcrack growth without forward sliding ($\mathrm{d}\tilde{b} = 0$, $\mathrm{d}\tilde{l} > 0$) This is also a macroscopic unloading case, since $|\sigma_{22}|$ decreases. If the winged microcrack is locked, the displacement-driven SIFs (4.35) are relevant. The derivation of $\mathrm{d}^i\varepsilon_{ij}$ is similar to that of phase 2 without forward sliding (cf. (4.38) specified for the long-wing case). Omitting fine details, the final outcome reads (Basista and Gross, 1998a)

$$\begin{aligned}\mathrm{d}^i\varepsilon_{ij} = \frac{N}{A_0}\,2\frac{\partial G}{\partial \sigma_{ij}}\,\mathrm{d}l = {} & \frac{\omega_0}{2}\begin{bmatrix} 0 & -\sin\varphi \\ -\sin\varphi & 2\cos\varphi \end{bmatrix}\tilde{b}^M\,\mathrm{d}\tilde{l} \\ & + \frac{1-\nu_0^2}{E_0}\,2\pi\omega_0\begin{bmatrix} 0 & 0 \\ 0 & \sigma_2 \end{bmatrix}\tilde{l}\,\mathrm{d}\tilde{l},\end{aligned} \tag{4.56}$$

where $\tilde{l}$ and $\mathrm{d}\tilde{l}$ are to be computed from the microcrack growth condition $(4.47)_1$.

4.7. Application

The capability of the developed theoretical model has been confronted (cf. Basista and Gross, 1998a) with the test data of Zoback and Byerlee (1975) on Westerly granite under unconfined compression. Westerly granite is a relatively homogeneous and nearly brittle compact rock whose properties and mechanical behavior are thoroughly known in rock mechanics. For these reasons it has been selected for the verification of the present analytical model.

For distributed damage, the overall stresses and strains may fairly well be approximated by simple area averages of the contributions of individual sliding microcracks. Assuming a finite number of specific orientations of the preexisting microcracks, the average strain increment may be computed as

$$\mathrm{d}\bar{\varepsilon}_{ij} = \frac{1}{R}\sum_{r=1}^{R}\mathrm{d}\varepsilon_{ij}(\varphi_r\,,\,\omega_0(\varphi_r)), \tag{4.57}$$

where R is the number of considered orientations φ_r. The strain increments under the summation sign in (4.57) have been derived in two preceding sections. In the example to follow, an isotropic distribution of preexisting microcracks is assumed, i.e. all microcrack orientations are likely to appear. From symmetry arguments, the shear strains in the global coordinate system $(x_1\,,\,x_2)$ disappear.

The following material constants have been used in computations:

$$\begin{aligned} &E_0 = 58000\,\mathrm{MPa}, && \nu_0 = 0.23, && \sigma_{uc} = -204\,\mathrm{MPa}, \\ &\mu = 0.65, && c = 5\cdot 10^{-4}\,\mathrm{m}, && K_{Ic} = 0.7\,\mathrm{MPa}\sqrt{\mathrm{m}}, \\ &\tau_c = 12\,\mathrm{MPa}, && \omega_0 = 0.375, && R = 90. \end{aligned} \tag{4.58}$$

The numerical values for E_0, ν_0, σ_{uc} have been read off from the test curves in Zoback and Byerlee (1975); see also Costin (1983); σ_{uc} denotes the highest compressive stress recorded in loading. The friction coefficient μ, the average initial microcrack half-length c, and the fracture toughness K_{Ic} have been estimated using the values for Westerly granite reported in Moss and Gupta (1982), Costin (1983), Jaeger and Cook (1979), Nemat-Nasser and Obata (1988). No data were available for Westerly granite with regard to the initial microcrack density parameter $\omega_0 = Nc^2/A_0$. The selected value provided the best fit with the data, and is rather consistent with those assumed in Moss and Gupta (1982), Nemat-Nasser and Obata (1988).

The solid curves depicted in Figure 4.8a,b represent $(\sigma–\varepsilon)$ equations predicted by the present model, while dots are the data measured by Zoback and Byerlee (1975) on cylindrical specimens in uniaxial compression. The theoretical curves have been obtained integrating the incremental formulas for strain derived in Sections 4.5 and 4.6 by means of a symbolic algebra software. Since the initial closure of voids is not accounted for in the model, the computed $(\sigma–\varepsilon)$ curve has been shifted from the origin 0 by the strain obtained from the intercept of the linear portion of the experimental curve with the ε-axis. To facilitate drawing, the stress sign convention in Figures 4.8 and 4.9 has been reversed, i.e. compression is viewed positive. The agreement between the theoretical and the experimental results in Figure 4.8 is fairly good both in loading and unloading regime. However, a word of caution is advisable since the tests were carried out on (3D) cylindrical specimens whereas the computational model is two-dimensional. In any case, the present model does predict several typical features of the brittle response of granite. For example, the overall shapes of loading and

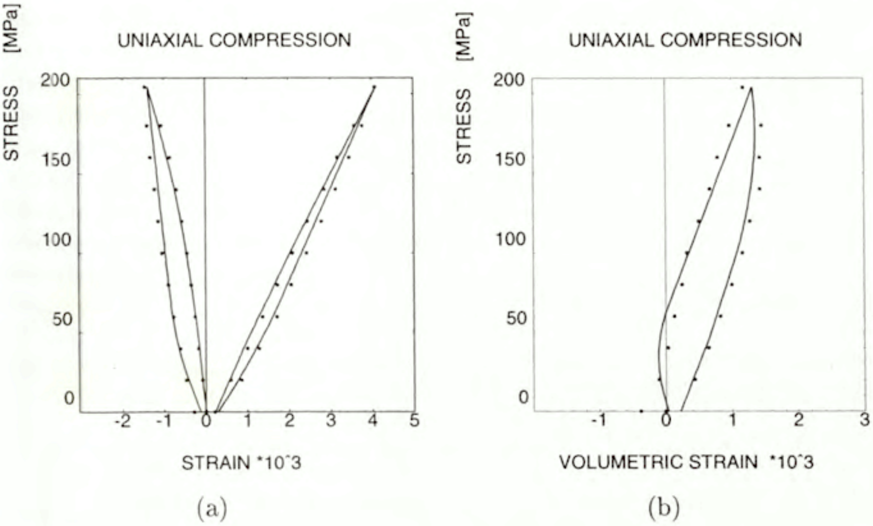

Figure 4.8. Theoretical predictions of stress–strain curves (solid lines) vs. test data on Westerly granite (Zoback and Byerlee, 1975). Loading–unloading cycle in unconfined compression: (a) axial and lateral strains, (b) volumetric strains (Basista and Gross, 1998a).

unloading curves are well reflected, the lateral inelastic strain is substantially larger than its axial counterpart, the permanent set and hysteresis loops are accounted for. Note that material parameters (4.58) used in computations are well documented in the referenced literature. Typically of all micromechanical models, the present formulation contains no fitting parameters. The involved parameters have clear physical meanings, although their measured values may not always be available.

In a very recent study, Lauterbach (2001) implemented the theoretical model presented in this chapter into a FEM code (FEAP) for a complete loading-unloading cycle in plane case. In parallel, that author performed an extensive analytical and numerical 2D analysis of a curvilinear sliding microcrack using the complex variable method, the boundary integral method, and the Boundary Element Method (BEM) to compute the stress-strain curves assuming the least possible number of model-induced simplifications. The results furnished by the two models are shown in Figure 4.9a,b. Note that "diskret" refers to the BEM computations, "mikromechanisch" to the FEAP implementation of the present model, "experimentell" to the test data of Zoback and Byerlee (1975) on Westerly granite. The fair agreement of the theoretical predictions with the experimental data although pleasing was, for the reasons named in the preceding paragraph, not the main motivation of reproducing these diagrams here. The most interesting observation made from Figure 4.9a,b is that the present approximate model (dotted line) and the "exact" BEM solution (solid line) actually coincide. That seems to further warrant the compression damage model proposed in this chapter.

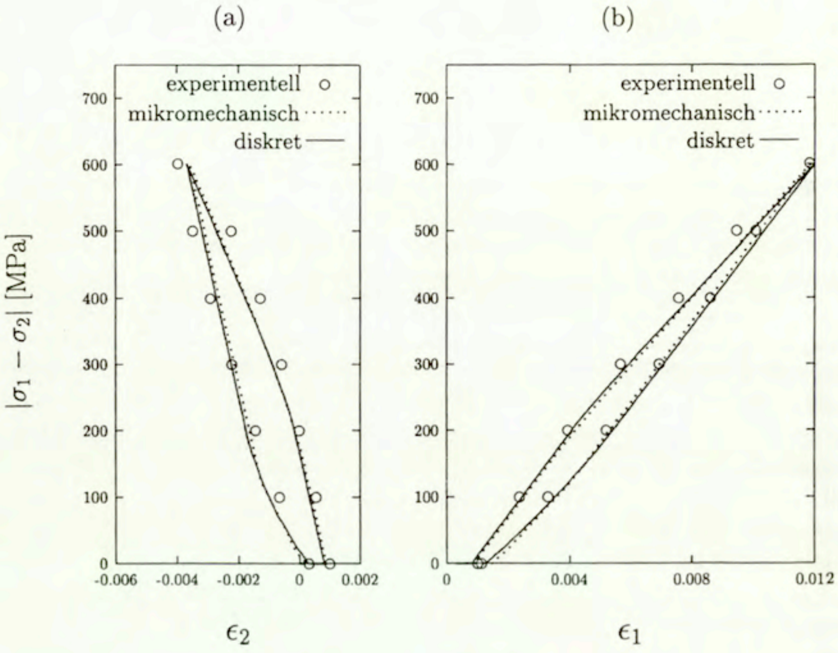

Figure 4.9. Stress–strain diagram for two-dimensional load cycle (confined compression): (a) lateral strain, (b) axial strain. Reproduced with permission from Lauterbach (2001).

Appendix 4.1.

Kemeny and Cook (1991) derived nonlinear stress–strain relations for an elastic body containing a single sliding microcrack, neglecting the energy loss on friction. These authors considered the long-wing approximation with the $K_I = K_{Ic}$ condition for microcrack growth. Their equation (15) for K_I is identical to $(4.36)_1$ of this chapter with $\theta + \varphi = \pi/2$, $\tau_{12} = 0$. Furthermore, they used the Castigliano theorem, i.e. essentially the same numerical operation, to compute inelastic strains due to Mode I microcrack extension.

Equation (39) in Kemeny and Cook (1991) gives the inelastic strain in the *axial* direction as

$$\begin{aligned}\varepsilon_1^i &= \frac{8\omega_0 \cos\varphi(\sin\varphi\cos\varphi - \mu\cos^2\varphi)}{E_0} \\ &\quad\times\left[\frac{2\tau_{\mathit{eff}}\cos\varphi}{\pi}\ln\tilde{l} - \sigma_2(\tilde{l}-1)\right].\end{aligned} \tag{A4.1}$$

However, for a straight microcrack growing in pure Mode I parallel to the direction of σ_1 it holds that $\varepsilon_1^i = 0$ and the only non-zero inelastic strain is that of ε_2^i. A closer look at Kemeny and Cook's computations revealed the following sequence of events that had led to (A4.1). In the expression $(4.36)_1$ of this chapter, the physical law specifying the concentrated force F was introduced leading to

$$\begin{aligned}F = -2c\tau_{\mathit{eff}} &= 2c\left[\mu(\sigma_1\cos^2\varphi + \sigma_2\sin^2\varphi) - \frac{1}{2}\sin 2\varphi(\sigma_1 - \sigma_2)\right],\\ \tau_c &= 0.\end{aligned} \tag{A4.2}$$

The Gibbs potential was next built as

$$\begin{aligned}\Delta\psi &= \frac{\omega_0}{E_0}\, 2\int_1^{\tilde{l}} K_I^2(\sigma_1\,,\,\sigma_2\,,\,\tilde{l})\,\mathrm{d}\tilde{l} \\ &= \frac{\omega_0}{E_0}\left[\frac{8\tau_{\mathit{eff}}^2\cos^2\varphi}{\pi}\ln\tilde{l} - 8\tau_{\mathit{eff}}\sigma_2\cos\varphi(\tilde{l}-1) + \sigma_2^2\pi(\tilde{l}^2-1)\right]\end{aligned} \tag{A4.3}$$

where $\omega_0 = Nc^2/A_0$, $\tilde{l} = l/c$. Finally, after expressing τ_{eff} in terms of σ_1 and σ_2 as in (A4.2), axial inelastic strain (A4.1) was obtained by differentiating (A4.3) with respect to σ_1. Apparently, the expression (A4.2), being the physical law for τ_{eff} based on the Coulomb–Mohr friction law, should not be inserted into (A4.3) before the differentiation or, equivalently, τ_{eff} in (A4.3) should be taken as parameter when computing $\partial(\Delta\psi)/\partial\sigma_1$ (Basista and Gross, 1998a).

Appendix 4.2.

Consider the crack configurations shown in Figure A4.1. Assume no interaction between the two cracks in Figure A.4.1b.

Problem: compute M_{22} component (Voigt notation) of the instantaneous compliance tensor $\mathbf{M}$ for the RVEs depicted in Figure A4.1a and Figure A4.1b. From (4.10) we have

$$\begin{aligned} M_{22}^{(a)} &= \frac{1-\nu_0^2}{A_0E_0}\,2\int_0^l 2\pi l\,\mathrm{d}l = \frac{1-\nu_0^2}{A_0E_0}\,2\pi l^2, \\ M_{22}^{(b)} &= 2\frac{1-\nu_0^2}{A_0E_0}\,2\int_0^{l/2} 2\pi l'\,\mathrm{d}l' = \frac{1-\nu_0^2}{A_0E_0}\,\pi l^2. \end{aligned} \tag{A4.4}$$

It can be seen that $M_{22}^{(a)}$ is twice as much as $M_{22}^{(b)}$ (Basista and Gross, 1998a).

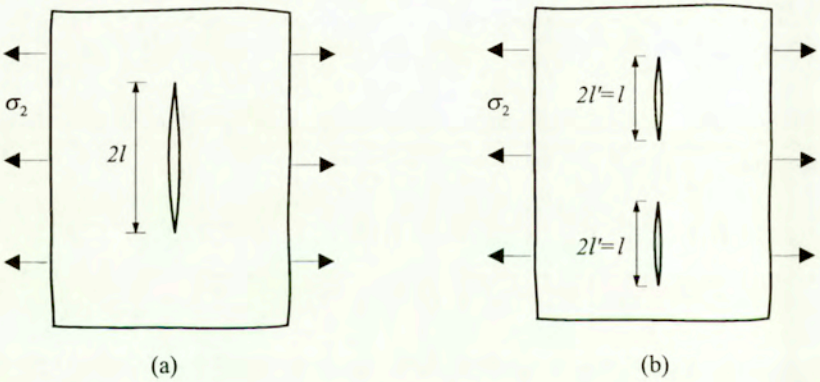

Figure A4.1. Crack configurations used for computation of elastic compliances in (A4.4).

Appendix 4.3.

It is instructive to compare the F-driven and $\bar{b}$-driven model of wing crack growth in the context of resulting strains. The comparison will be done in the simplest, yet relevant for the present study, cases of crack geometry and applied loads.

Consider a Mode I crack loaded by a pair of collinear concentrated forces shown in Figure A4.2a. Consider next a Mode I crack whose faces are pushed away by a very long, thin, rigid wedge (Figure A4.2b) so that the interaction between the crack tips is negligible. The force-loaded crack in Figure A4.2a has the total length $2l$. The displacement-loaded crack in Figure A4.2b consists of two cracks, each having the total length l.

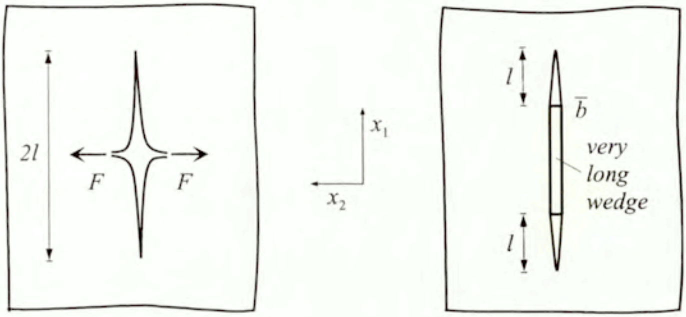

(a) (b)

Figure A4.2. (a) Mode I crack loaded by two collinear concentrated forces. (b) Mode I crack induced by semi-infinite rigid wedge.

Problem: assuming that $K_I(F) = K_I(\bar{b}) = K_I$ compute the *inelastic* strain ε_2^i in each configuration under plane strain conditions. The solution to this problem is exact and follows from the Westergaard stress functions given, for example, in Tada et al. (1985, pages 4.9, 3.11):

$$\begin{aligned} \varepsilon_2^i(F) &= \frac{1-\nu_0^2}{A_0 E_0}\, 4K_I l\sqrt{\pi l}\,, \\ \varepsilon_2^i(\bar{b}) &= \frac{1-\nu_0^2}{A_0 E_0}\, 2\sqrt{2}K_I l\sqrt{\pi l}\,. \end{aligned} \tag{A4.5}$$

Evidently, it holds that $\varepsilon_2^i(F) = \sqrt{2}\,\varepsilon_2^i(\bar{b})$ (Basista and Gross, 1998a).

Chapter 5

Microcrack interactions in compression

Abstract. The bulk of this chapter is devoted to estimation of the stress intensity factors for interacting cracks under overall compression. Motivated by the two-dimensional sliding crack model, interaction of frictional Mode II cracks is considered first. Then, interaction of straight cracks loaded by a pair of splitting point-forces under remote compression is studied. The crack interaction effects are examined via the Kachanov method (1987) which is extended here to account for frictional-cohesive resistance on crack faces, and adopted to deal with point-force loading. The obtained approximate solutions are compared with "exact" numerical ones yielded by a boundary element method (*BEM*).

5.1. Introduction

The problem of a linear elastic solid with a multitude of interacting, arbitrarily located, *open* cracks under uniform remote loading $\boldsymbol{\sigma}^{\infty}$ has been considered by many authors over the past 20 years. A general algorithm of solving such a problem is as follows. Using the superposition principle, a multiple crack problem is reduced to a subproblem of a single crack but loaded by unknown tractions that are induced by the other cracks. The unknown tractions are then interrelated through singular integral equations which, except for a handful of special cases, do not lend themselves to rigorous analytical methods of solution. Consequently, one has to solve the problem numerically or resort to approximate techniques. As for numerical approach, a boundary element method (*BEM*) proved quite effective in solving 2D multiple crack problems when formulated in terms of the complex variable method and the dislocation distribution along crack contours (cf. Horii and Nemat-Nasser, 1985; Bettin and Gross, 1990). A rather obvious reason behind the popularity of the *BEM* vs. *FEM* in crack problems is that in the *BEM* approach only the boundary of the problem geometry requires discretization. For multiple cracks, where a large number of model runs are necessary, this feature is of primary importance. However, at large crack concentrations in 3D problems, the exact solution is practically still out of our reach. Consequently, an alternative approach furnished by the so called *approximate direct meth-*

ods of crack–crack interactions is often used as a way out. In these methods, the tractions on interacting cracks are accurately approximated using Legendre or Chebyshev orthogonal polynomials (e.g. Gross, 1982; Chen, 1984; Horii and Nemat-Nasser, 1985b; Kachanov, 1987; Benveniste et al., 1989). Recently, Ju and Tseng (1995) have presented a comprehensive appraisal of these asymptotic polynomial techniques for crack interaction problems in plane elasticity. Of several approximate direct methods the one proposed in Kachanov (1987) deserves particular attention for its simplicity and remarkable accuracy and will be used in what follows. Some other methods employing the path-independent integrals when deriving the crack interaction forces were discussed in Matczyński and Sokołowski (1982).

For completeness, we recall that crack interactions may also be analyzed *indirectly* through one of the effective continua techniques (e.g. self-consistent method, differential method) and mean-field techniques (e.g. Mori–Tanaka method). A comprehensive account of the effective continua and mean field techniques can be found for example in Aboudi (1991), Nemat-Nasser and Hori (1993), Kachanov (1993).

Motivated by the sequence of events in the sliding crack model, the present chapter is focused on an extension of the Kachanov method to 2D crack interaction problems under overall *compression*. The main objective here is to compute the stress intensity factors for:

(a) straight closed cracks undergoing frictional sliding (phase 1),

(b) straight open cracks loaded by splitting forces and remote compression (phase 2).

A number of test examples will be solved and the results confronted with the solutions obtained using the *BEM*. Since somewhat different algorithms are necessary in phase 1 and phase 2, the two phases will be considered separately.

5.2. Interactions of frictional cracks

Consider two closed cracks in an infinite, linear elastic plate (Figure 5.1) with the local (crack-attached) coordinate systems (x^L, y^L) and the global coordinate system (x_1 , x_2). Note that these coordinate systems are different from those used in Chapter 4. To facilitate drawing, only two cracks are shown but the ensuing equations are formulated for an arbitrary 2D crack

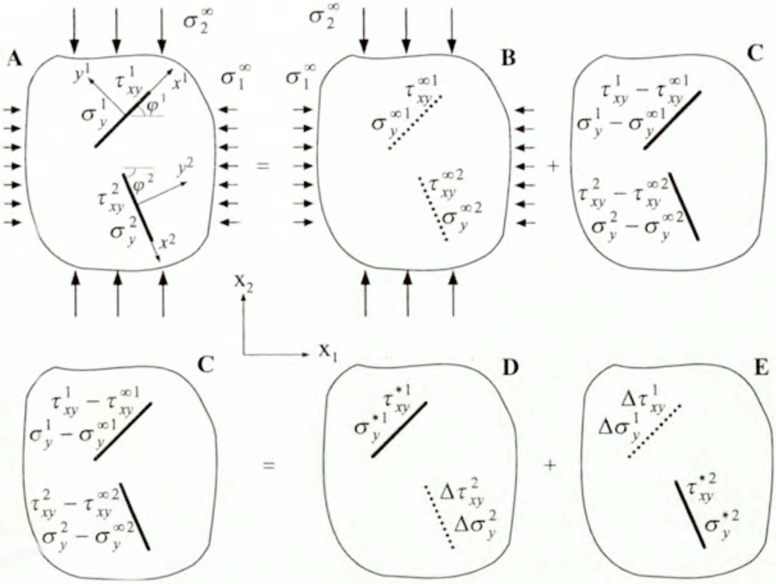

Figure 5.1. Superposition of stresses for interacting frictional cracks in infinite, linear elastic plate under compression (Basista, 2000).

array ($L = 1, 2, \ldots, N$). The actual (contact) shear and normal stresses existing on the faces of L-th crack are denoted by τ_{xy}^L, σ_y^L. The boundary-value problem A can trivially be decomposed into two subproblems B, C. On the other hand, the problem C can be represented as a superposition of N subproblems, each involving only a single crack but subjected to *unknown* shear and normal stresses τ_{xy}^{*L}, σ_y^{*L}. For open cracks considered in Kachanov (1987), the sign convention for stresses was inconsequential. In contrast, the signs of the superimposed stresses in compression (Figure 5.1A–E) are strictly observed. Consistently with the preceding chapters, the adopted sign convention is that of continuum mechanics, i.e. compression is viewed negative. Consequently, for closed frictional cracks it follows from Figure 5.1 that (Basista, 2000)

$$\tau_{xy}^{*L} = \tau_{xy}^L - (\tau_{xy}^{\infty L} + \Delta\tau_{xy}^L), \tag{5.1}$$

$$\sigma_y^{*L} = \sigma_y^L - (\sigma_y^{\infty L} + \Delta\sigma_y^L), \tag{5.2}$$

where $\tau_{xy}^{\infty L}$, $\sigma_y^{\infty L}$ are the resolved (due to remote loading $\boldsymbol{\sigma}^\infty$) shear and normal stresses in the continuous material along the line of L-th crack; $\Delta\tau_{xy}^L$, $\Delta\sigma_y^L$ are the interaction terms, i.e. shear and normal stresses generated by all other cracks along the line of L-th crack in the continuous material. As long as the crack remains closed, it holds $\sigma_y^{*L} = 0$. Otherwise, $\sigma_y^{*L} = -(\sigma_y^{\infty L} + \Delta\sigma_y^L)$.

A necessary prerequisite for computation of the SIFs is determination of the loading of crack faces (τ_{xy}^{*L}, σ_y^{*L}). Once τ_{xy}^{*L}, σ_y^{*L} are known, the SIFs can be computed according to the well-known formulas, Tada et al. (1985):

$$K_I^L(\pm c^L) = \frac{1}{\sqrt{\pi c^L}} \int_{-c^L}^{c^L} \sqrt{\frac{c^L \pm \zeta}{c^L \mp \zeta}}\, p^{*L}(\zeta)\, \mathrm{d}\zeta, \tag{5.3}$$

$$K_{II}^L(\pm c^L) = \frac{1}{\sqrt{\pi c^L}} \int_{-c^L}^{c^L} \sqrt{\frac{c^L \pm \zeta}{c^L \mp \zeta}}\, \tau^{*L}(\zeta)\, \mathrm{d}\zeta, \tag{5.4}$$

where $p^{*L} = -\sigma_y^{*L}$, $\tau^{*L} = -\tau_{xy}^{*L}$ due to the sign convention and c^L denotes the half-length of a straight crack. For closed cracks only (5.4) is relevant.

In essence, the method devised in Kachanov (1987) for open cracks is based on the following *Ansatz*:

> *The unknown tractions induced on the considered crack by the presence of other cracks can be approximated by tractions that would act on the considered crack if the other cracks were loaded by uniform average (normal and shear) tractions.*

It is claimed now that irrespective of whether interacting cracks are open or frictional, the central assumption of the Kachanov method remains valid, i.e. the unknown crack interaction stresses $\Delta\sigma_y^L$, $\Delta\tau_{xy}^L$ are induced only by uniform average tractions (as yet unknown) acting on the other cracks' faces. A far-reaching consequence of this assumption is that it yields a functional form for the unknown stresses $\Delta\sigma_y^L$, $\Delta\tau_{xy}^L$ since the problem of a single crack loaded by uniform tractions has analytical solution. Denote by P_{ij}^K and T_{ij}^K standard stress fields that are generated in the continuous material by the K-th crack loaded by uniform normal and shear tractions of *unit intensity*, respectively. These standard stress fields can be computed using a suitable Westergaard function (as it is done in this chapter) or can be found in textbooks on linear fracture mechanics. Hence, the crack interaction terms $\Delta\sigma_y^L$, $\Delta\tau_{xy}^L$ (generated in the continuous material) can be expressed in the following general form (Kachanov, 1987)

$$\Delta\sigma_y^L = -n_i^{(L)} \left[P_{ij}^K \langle\sigma_y^{*K}\rangle + T_{ij}^K \langle\tau_{xy}^{*K}\rangle\right] n_j^{(L)}, \tag{5.5}$$

$$\Delta\tau_{xy}^L = -n_i^{(L)} \left[P_{ij}^K \langle\sigma_y^{*K}\rangle + T_{ij}^K \langle\tau_{xy}^{*K}\rangle\right] m_j^{(L)}, \tag{5.6}$$

$$K, L = 1, \ldots, N; \quad (K \neq L).$$

In (5.5) and (5.6), the sum convention applies to the repeated indices K while it does not apply to the indices placed in parentheses i.e. (L); $\mathbf{n}^L$, $\mathbf{m}^L$ are the crack-attached normal and tangential unit vectors; the bracket $\langle\rangle$ denotes the average value of the bracketed quantity. The standard stress fields P_{ij}^K and T_{ij}^K are usually written assuming positive unit intensities of normal and shear tractions. However, in the considered case the average normal stress (internal pressure) $\langle\sigma_y^{*K}\rangle$ and the average shear stress $\langle\tau_{xy}^{*K}\rangle$ acting on the crack faces are subjected to the adopted sign convention. Hence, the minus signs in (5.5) and (5.6).

In (5.1) and (5.2), the actual stresses τ_{xy}, σ_y induced by the frictional-cohesive contact on the crack faces are interrelated through a law of dry friction. A simple Coulomb–Mohr law is adopted for this purpose:

$$\tau_{xy}^L = \quad \mp\tau_c \pm \mu\sigma_y^L, \tag{5.7}$$

where τ_c is the cohesion and μ is the coefficient of dry friction, both being positive constants. In Equation (5.7) and the equations to follow, the upper signs hold for cracks oriented at $0 < \varphi^L < \pi/2$ while the lower ones for $-\pi/2 < \varphi^L < 0$, Figure 5.1.

Making use of (5.1), (5.2) and (5.7), it follows that

$$\tau_{xy}^{*L} = \mp\tau_c \pm \mu\sigma_y^{\infty L} - \tau_{xy}^{\infty L} \pm \mu\,\Delta\sigma_y^L - \Delta\tau_{xy}^L, \tag{5.8}$$

$$K, L = 1, 2, \ldots, N.$$

If Equation (5.8) with $\Delta\sigma_y^L$ and $\Delta\tau_{xy}^L$ given by (5.5) and (5.6) is to hold for the averages $\langle\sigma_y^{*K}\rangle$, $\langle\tau_{xy}^{*K}\rangle$ on an arbitrary crack, it also has to hold for $\langle\sigma_y^{*L}\rangle$, $\langle\tau_{xy}^{*L}\rangle$ on the L-th crack itself (idea of self-consistency). Applying this idea to Equation (5.8), i.e. averaging it, leads to

$$\langle\tau_{xy}^{*L}\rangle = \mp\tau_c \pm \mu\sigma_y^{\infty L} - \tau_{xy}^{\infty L} \pm \mu\,\langle\Delta\sigma_y^L\rangle - \langle\Delta\tau_{xy}^L\rangle, \tag{5.9}$$

where:

$$\langle \Delta\sigma_y^L \rangle \;=\; -\Lambda_{11}^{KL}\,\langle \sigma_y^{*K} \rangle - \Lambda_{12}^{KL}\,\langle \tau_{xy}^{*K} \rangle, \tag{5.10}$$

$$\langle \Delta\tau_{xy}^L \rangle \;=\; -\Lambda_{21}^{KL}\,\langle \sigma_y^{*K} \rangle - \Lambda_{22}^{KL}\,\langle \tau_{xy}^{*K} \rangle, \tag{5.11}$$

In (5.10) and (5.11) Λ_{ij}^{KL} are the Kachanov (1987) transmission factors (interaction matrices) defined as follows

$$\left.\begin{aligned} \Lambda_{11}^{KL} &= n_i^{(L)}\langle P_{ij}^K\rangle^{(L)} n_j^{(L)} \\ \Lambda_{12}^{KL} &= n_i^{(L)}\langle T_{ij}^K\rangle^{(L)} n_j^{(L)} \\ \Lambda_{21}^{KL} &= n_i^{(L)}\langle P_{ij}^K\rangle^{(L)} m_j^{(L)} \\ \Lambda_{22}^{KL} &= n_i^{(L)}\langle T_{ij}^K\rangle^{(L)} m_j^{(L)} \end{aligned}\right\} \qquad (K \neq L), \tag{5.12}$$

$$\Lambda_{ij}^{KL} = 0; \qquad\qquad (K = L). \tag{5.13}$$

For convenience, the notation of the transmission factors in (5.12)–(5.13) has been slightly changed (cf. Basista and Gross, 1998b) as compared with that in the original paper (Kachanov, 1987). For example, Λ_{21}^{KL} denotes the average shear stress (lower index 2) on crack L due to unit normal stress (lower index 1) on crack K. Incidentally, it seems that there is a misprint with regard to the formula (13b) in the original paper, as noticed in Basista (2000). Namely, in the limit case of $K = L$ (crack interaction with itself) it should be $\Lambda_{ij}^{KK} = 0$ as in (5.13) and not $\Lambda_{ij}^{KK} = \delta_{ij}$ as in Kachanov (1987). Note that to compute the transmission factors the standard stress fields generated by the uniformly loaded K-th crack have to be integrated along the line of L-th crack. For a given configuration of N cracks this is usually done by numerical integration.

For closed frictional cracks $\sigma_y^{*L} = 0$, thus the following system of N linear equations is obtained from (5.9)–(5.13) (Basista and Gross, 1998b)

$$\left(\delta^{KL} \pm \mu\,\Lambda_{12}^{KL} - \Lambda_{22}^{KL}\right)\langle \tau_{xy}^{*K}\rangle \;=\; \mp\tau_c \pm \mu\sigma_y^{\infty L} - \tau_{xy}^{\infty L}, \tag{5.14}$$

$$K, L = 1, 2, \ldots, N.$$

The right hand side of (5.14) specifies the remote loading conditions and the friction-cohesion resistance on each crack's faces. In other words, it represents the effective (net) shear stress that drives the crack sliding. The crack array geometry and the influence of friction on the transmission of shear stresses are reflected by the left hand side. The system of equations (5.14) with the transmission factors (5.12), (5.13) and a given load $(\sigma_y^{\infty L}, \tau_{xy}^{\infty L})$ on crack faces constitute the governing system of linear algebraic equations from which the average shear stresses $\langle \tau_{xy}^{*K} \rangle$ can be computed.

If the average values of shear stresses $\langle \tau_{xy}^{*K} \rangle$ are known, it is straightforward to compute the whole distribution of τ_{xy}^{*K}. From (5.8), when combined with (5.5) and (5.6), it follows that (Basista and Gross, 1998b)

$$\tau_{xy}^{*L} = \mp\tau_c \pm \mu\sigma_y^{\infty L} - \tau_{xy}^{\infty L} + n_i^{(L)} T_{ij}^K \langle \tau_{xy}^{*K} \rangle \left(\mp\mu\, n_j^{(L)} + m_j^{(L)} \right). \tag{5.15}$$

Finally, combining (5.15) and (5.4), the K_{II} factors for interacting frictional cracks read (Basista, 2000)

$$\begin{aligned} K_{II}^L(+c) &= \sqrt{\pi\, c^{(L)}} \left(\tau_{xy}^{\infty(L)} \pm \tau_c \mp \mu\sigma_y^{\infty(L)} \right) \\ &\quad + \frac{\langle \tau_{xy}^{*K} \rangle}{\sqrt{\pi\, c^{(L)}}}\, n_i^{(L)} \int_{-c^L}^{c^L} \sqrt{\frac{c^L+\zeta}{c^L-\zeta}}\, T_{ij}^K\, \mathrm{d}\zeta \left(\pm\mu n_j^{(L)} - m_j^{(L)} \right) \end{aligned} \tag{5.16}$$

$$\begin{aligned} K_{II}^L(-c) &= \sqrt{\pi\, c^{(L)}} \left(\tau_{xy}^{\infty(L)} \pm \tau_c \mp \mu\sigma_y^{\infty(L)} \right) \\ &\quad + \frac{\langle \tau_{xy}^{*K} \rangle}{\sqrt{\pi\, c^{(L)}}}\, n_i^{(L)} \int_{-c^L}^{c^L} \sqrt{\frac{c^L-\zeta}{c^L+\zeta}}\, T_{ij}^K\, \mathrm{d}\zeta \left(\pm\mu n_j^{(L)} - m_j^{(L)} \right) \end{aligned}$$

5.3. Test examples

To evaluate the predictive capability of the present model, the basic equations (5.14), (5.15) (5.16) have been implemented numerically. For this purpose, a source FORTRAN code has been formulated in Basista (2000) based on a similar code for open cracks (Wagner and Gross, 1988) The numerical algorithm is relatively simple except for the weighted integrals in (5.16) which required some special treatment. The following three test examples of an infinite, linear elastic plate under uniaxial compression with

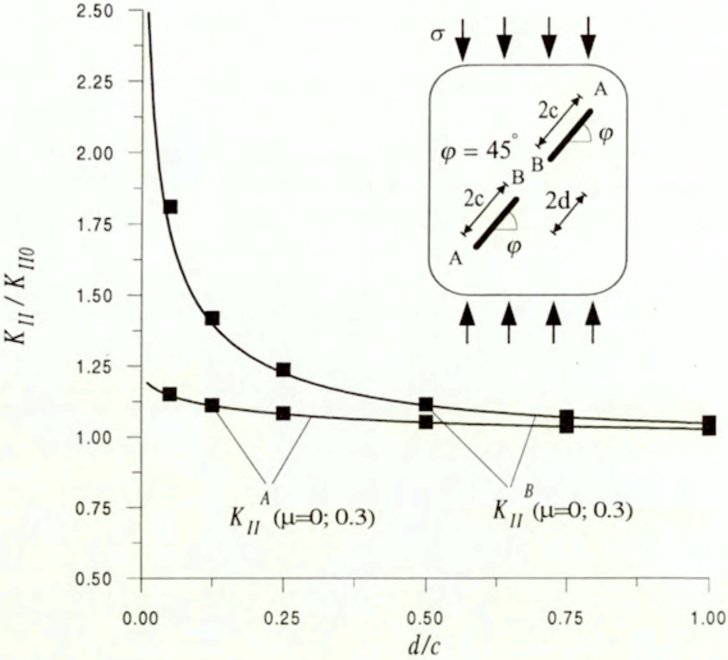

Figure 5.2. Two collinear cracks under uniaxial compression. Normalized K_{II} factors vs. relative distance of crack tips for $\mu = 0$; 0.3 and $\tau_c = 0$ (Basista, 2000). Solid lines depict present solution, squares – *BEM* solution.

- a pair of collinear inclined cracks (Figure 5.2, insert),
- a pair of symmetrically inclined cracks (Figure 5.3, insert),
- a pair of stacked cracks (Figure 5.5, insert),

have been solved using the developed code. In parallel, the same three test problems have been solved using the *BEM* source code (Lauterbach and Gross, 1998, 1999).

In Figures 5.2, 5.3, 5.4, 5.5 the present solutions are compared with the 'exact' numerical ones obtained by means of the *BEM*. For the selected test examples the normalized K_{II} factors vs. the relative distance of crack

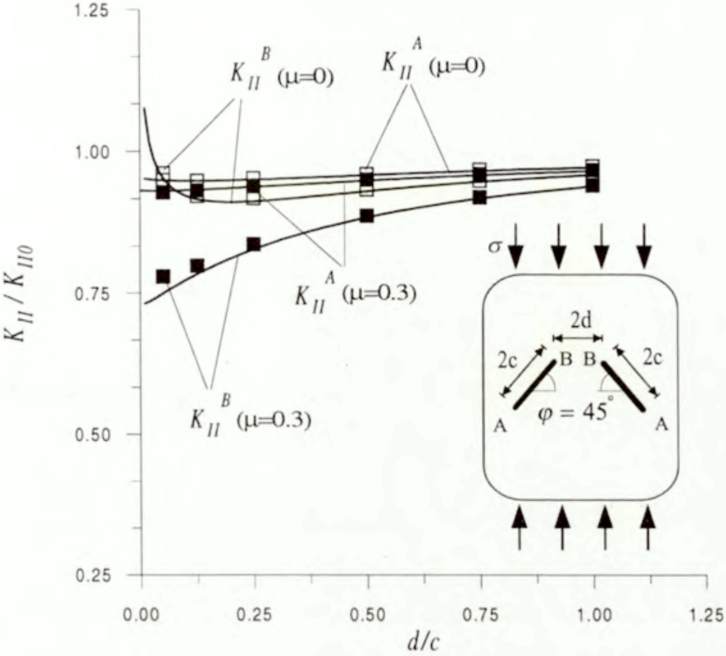

Figure 5.3. Two symmetrically inclined cracks under uniaxial compression. Normalized K_{II} factors vs. relative distance of crack tips (Basista, 2000). Solid curves – present solution, squares – *BEM* data for $\mu = 0$, $\mu = 0.3$ at $\tau_c = 0$.

tips d/c are plotted for frictionless ($\mu = 0$) and frictional contact ($\mu = 0.3$) on crack faces. The normalization factor K_{II0} is the stress intensity factor for the respective single crack under a given load with all other cracks absent. On the example of inclined cracks (see insert in Figure 5.3), an intermediate step of the method, namely the computed average shear stress $\langle \tau_{xy}^{*1} \rangle$ vs. d/c, is also illustrated and compared with the respective *BEM* data in Figure 5.4.

Typically of open cracks, collinear configurations induce amplification of stresses and stress intensity factors as cracks approach one another. In the case of frictional cracks, this effect is maintained as can be seen in Figure 5.2. On the other hand, the stacked crack configurations (Figures 5.3, 5.4, 5.5) promote shielding (for the most part) as d/c becomes smaller.

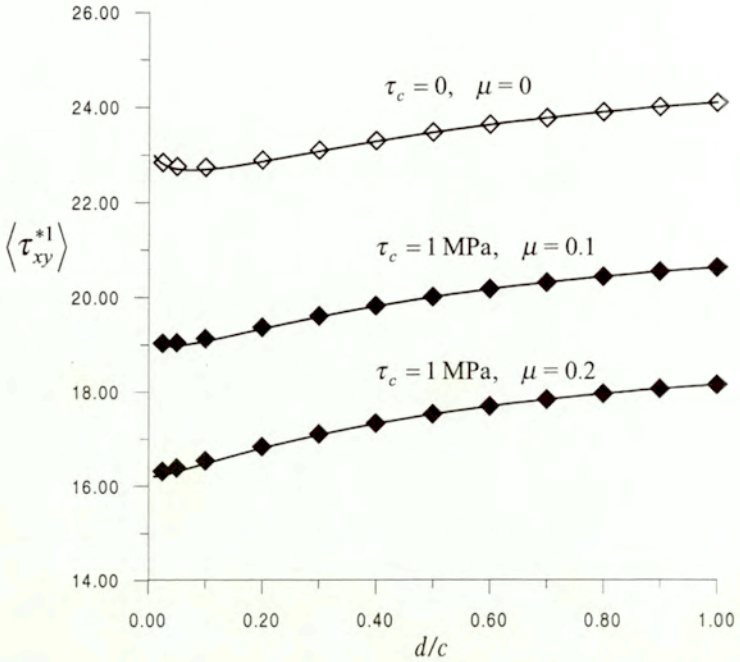

Figure 5.4. Average shear stress $\langle \tau_{xy}^{*1} \rangle$ as predicted by (5.14) vs. *BEM* data (diamonds) for inclined cracks of Figure 5.3 (Basista and Gross, 1998b).

All figures clearly show that accuracy of the extended Kachanov method is excellent even at very small distances between the crack tips. This could have been expected for aligned cracks since Kachanov's method had always worked fine for collinear crack arrays. However, stacked crack configurations are an acid test for the method. Surprisingly enough, for two parallel stacked cracks (Figure 5.5) the present results and the *BEM* data are practically indistinguishable with the exception of the outer tip at $\mu = 0.3$ and $d/c = 0.05$. But even there the error is merely 0.8%. The least accurate results are obtained in the case of inclined cracks for inner tips (labeled B in Figure 5.3) at $\mu = 0.3$ and $d/c = 0.05$. Nevertheless, the error in this case is less than 3% which is still very good for practical applications.

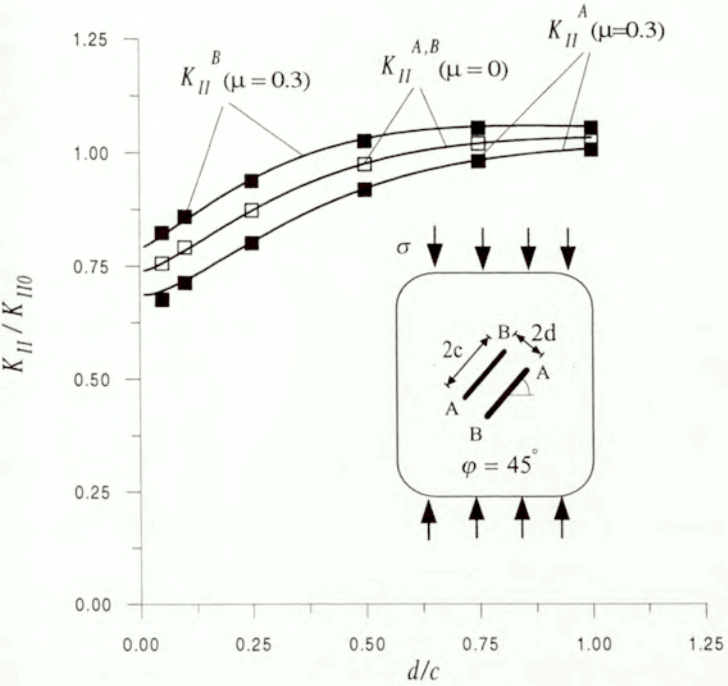

Figure 5.5. Two stacked cracks under uniaxial compression. Normalized K_{II} factors vs. relative distance of crack tips (Basista, 2000). Solid curves – present solution, squares – *BEM* data, for $\mu = 0$, $\mu = 0.3$ at $\tau_c = 0$.

5.4. Interaction of cracks loaded by splitting forces

For curvilinear winged cracks the crack–crack interaction problem can be solved only numerically (cf. Lauterbach and Gross, 1998). However, if the approximate model with straight wings and a pair of splitting forces (Figure 4.6b) is accepted, then the Kachanov method is again applicable (Basista and Gross, 2000). In fact, the problem reduces to the one shown in Figure 5.6 which is equivalent to the superposition of N subproblems each involving a single crack loaded by splitting forces F^L and unknown stresses σ_y^{*L} , τ_{xy}^{*L} , Figure 5.6b,c.

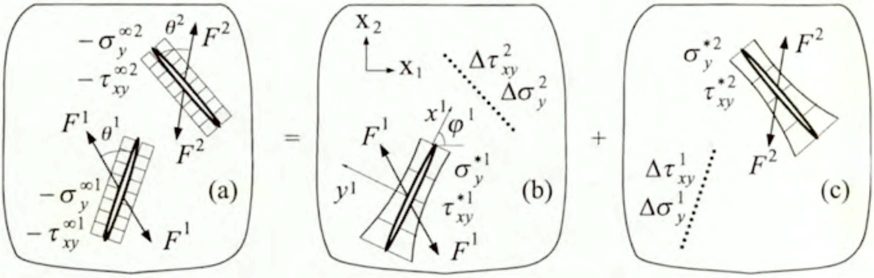

Figure 5.6. Superposition of stresses in force-driven model of sliding crack mechanism (Basista and Gross, 2000).

Formally, σ_y^{*L}, τ_{xy}^{*L} can be expressed as

$$\begin{aligned} \sigma_y^{*L} &= -(\sigma_y^{\infty L} + \Delta\sigma_y^L) = -(\sigma_y^{\infty L} + \Delta\sigma_y^{*L} + \Delta\sigma_y^{FL}), \\ \tau_{xy}^{*L} &= -(\tau_{xy}^{\infty L} + \Delta\tau_{xy}^L) = -(\tau_{xy}^{\infty L} + \Delta\tau_{xy}^{*L} + \Delta\tau_{xy}^{FL}), \end{aligned} \tag{5.17}$$

where $\Delta\sigma_y^{*L}$ and $\Delta\tau_{xy}^{*L}$ denote the unknown interaction terms due to σ_y^{*L} and τ_{xy}^{*L}, respectively. The terms $\Delta\sigma_y^{FL}$, $\Delta\tau_{xy}^{FL}$ are the known stresses induced along the line of the L-th crack by the concentrated forces F^K acting on the other cracks' faces. Note that superscript F in (5.17)–(5.19) stands for *force* and is not a crack label. Forces F^K are already determined from the frictional sliding on the preexisting cracks according to

$$F^K = 2c\,|\mp\tau_c \pm \mu\sigma_y^{\infty K} - \tau_{xy}^{\infty K}|.$$

All the Δ-terms can now be computed using the Kachanov method. However, at this stage of development a simplifying assumption is made with regard to $\Delta\sigma_y^{FL}$ and $\Delta\tau_{xy}^{FL}$ in order to profit from the already computed standard stresses and transmission factors. Namely, it is assumed that $\Delta\sigma_y^{FL}$, $\Delta\tau_{xy}^{FL}$ can be approximated by the stresses due to a constant normal loading p^K and constant shear loading q^K, where $p^K = -F^K \sin\theta^K/(2l^K)$, $q^K = \pm F^K \cos\theta^K/(2l^K)$ are simply the equivalent uniform distributions of F^K along the length of the K-th crack. Obviously, this assumption will become less accurate as the cracks get close to each other but it seemed interesting to check the limits of this simplification.

Consequently, after all the necessary algebraic steps of the method the average stresses can be computed from the following system of $2N$ linear equations (Basista and Gross, 2000)

$$\begin{gathered}\left(\delta_{ij}\delta^{KL} - \Lambda_{ij}^{KL}\right)\langle t_j^{*K}\rangle = -t_i^{\infty L} + \Lambda_{ij}^{KL} t_j^{FK} \\ i,j = 1,2; \qquad K,L = 1,2,\dots,N\end{gathered} \tag{5.18}$$

where:

$$\begin{aligned}\langle t_j^{*K}\rangle &= \left\{\langle\sigma_y^{*K}\rangle, \langle\tau_{xy}^{*K}\rangle\right\}, \\ t_j^{\infty L} &= \left\{\sigma_y^{\infty L}, \tau_{xy}^{\infty L}\right\}, \\ t_j^{F\,K} &= \left\{p^K, q^K\right\}.\end{aligned} \tag{5.19}$$

Hence, the crack face loading becomes (Basista and Gross, 2000)

$$\begin{aligned}\sigma_y^{*L} &= -\sigma_y^{\infty\,L} + n_i^{(L)}\left[P_{ij}^K\left(\langle\sigma_y^{*K}\rangle + p^K\right)\right. \\ &\qquad \left. + T_{ij}^K\left(\langle\tau_{xy}^{*K}\rangle + q^K\right)\right] n_j^{(L)}, \\ \tau_{xy}^{*L} &= -\tau_{xy}^{\infty\,L} + n_i^{(L)}\left[P_{ij}^K\left(\langle\sigma_y^{*K}\rangle + p^K\right)\right. \\ &\qquad \left. + T_{ij}^K\left(\langle\tau_{xy}^{*K}\rangle + q^K\right)\right] m_j^{(L)}.\end{aligned} \tag{5.20}$$

Finally, the stress intensity factors are given by (Basista and Gross, 2000)

$$\begin{aligned}K_I^L(\pm l) &= \frac{F^{(L)}\sin\theta^{(L)}}{\sqrt{\pi\, l^{(L)}}} \\ &\quad + \frac{1}{\sqrt{\pi\, l^{(L)}}}\int_{-l^{(L)}}^{l^{(L)}}\sqrt{\frac{l^{(L)}\pm\xi}{l^{(L)}\mp\xi}}\left(-\sigma_y^{*(L)}(\xi)\right)\mathrm{d}\xi, \\ K_{II}^L(\pm l) &= \frac{\pm F^{(L)}\cos\theta^{(L)}}{\sqrt{\pi\, l^{(L)}}} \\ &\quad + \frac{1}{\sqrt{\pi\, l^{(L)}}}\int_{-l^{(L)}}^{l^{(L)}}\sqrt{\frac{l^{(L)}\pm\xi}{l^{(L)}\mp\xi}}\left(-\tau_{xy}^{*(L)}(\xi)\right)\mathrm{d}\xi.\end{aligned} \tag{5.21}$$

In $(5.21)_2$ the ± sign in the first term on the right hand side refers to the crack orientation φ and not to crack tip $\pm l$ as it is the case otherwise.

Using the developed numerical code, the basic equations (5.18), (5.20), (5.21) have been solved in Basista and Gross (2000) for two test examples inserted in Figures 5.7, 5.9 and the solutions compared with the *BEM* results obtained using the Lauterbach and Gross (1998, 1999) numerical model. The present model works well for collinear cracks (Figures 5.7 and 5.8), especially with regard to K_I. In the case of slightly inclined stacked cracks (Figures 5.9 and 5.10) the accuracy is less satisfactory, and for $d/l \leq 0.2$ the present model ceases to be valid.

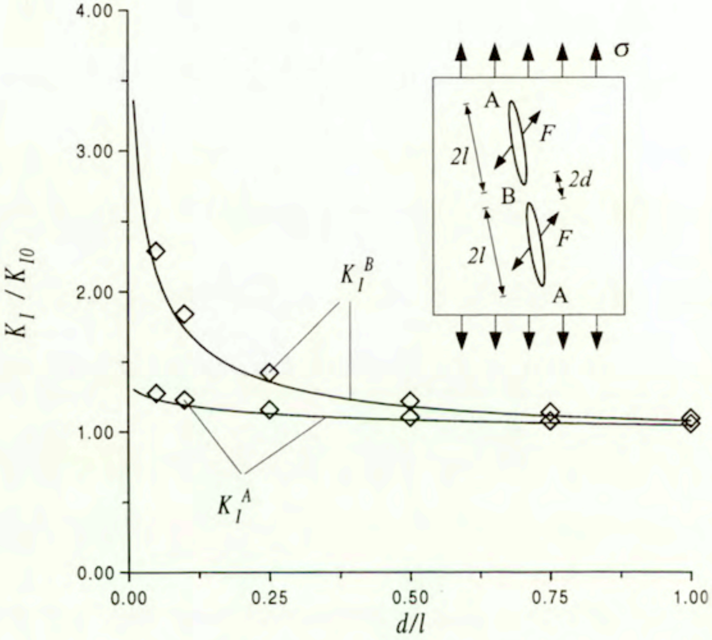

Figure 5.7. Normalized K_I factors for two collinear cracks with concentrated forces, $\varphi = -87°$, $\theta = 48°$ (Basista and Gross, 2000). Solid lines – present model, symbols – *BEM* solution.

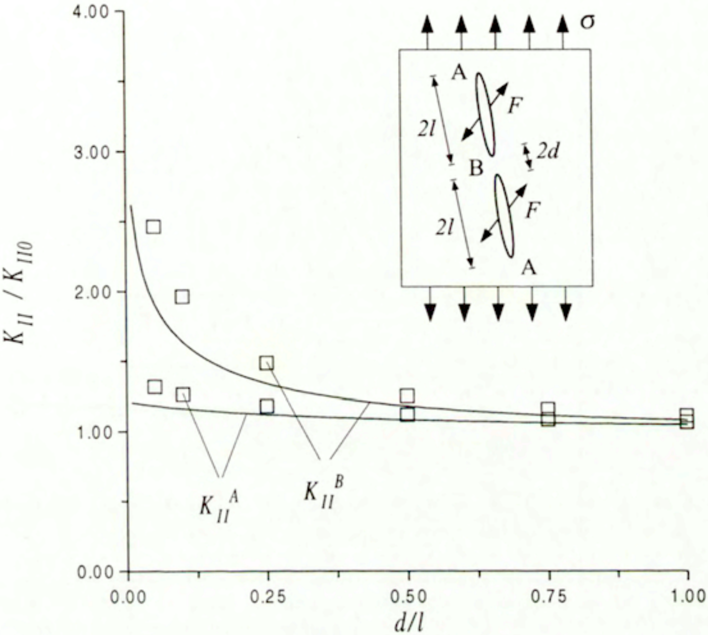

Figure 5.8. Normalized K_{II} factors for two collinear cracks with concentrated forces, $\varphi = -87°$, $\theta = 48°$ (Basista and Gross, 2000). Solid lines – present model, symbols – *BEM* solution.

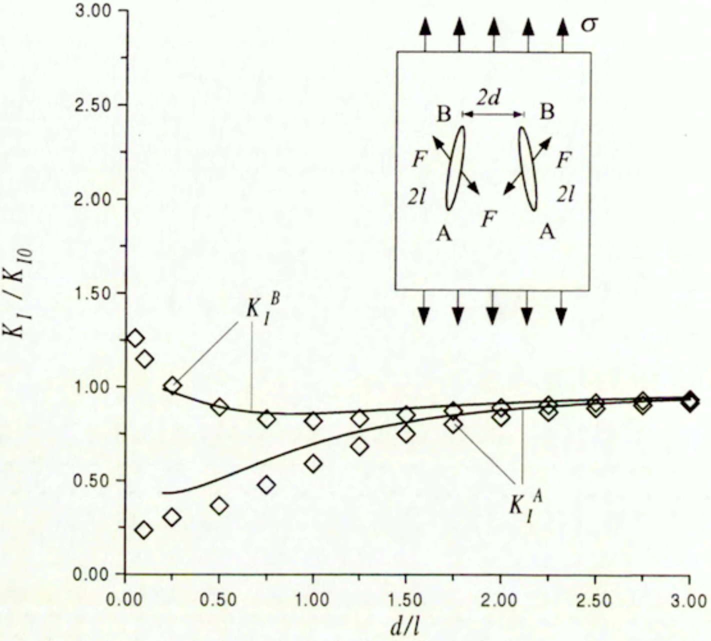

Figure 5.9. Normalized K_I factors for two inclined cracks with concentrated forces, $\varphi = \pm 87°$, $\theta = 48°$ (Basista and Gross, 2000). Solid lines – present model, symbols – *BEM* solution.

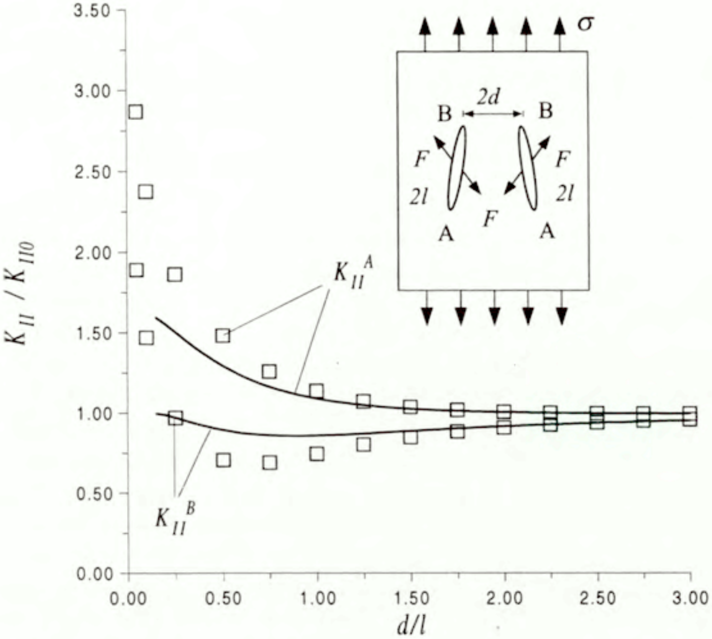

Figure 5.10. Normalized K_{II} factors for two inclined cracks with concentrated forces, $\varphi = \pm 87^\circ$, $\theta = 48^\circ$ (Basista and Gross, 2000). Solid lines – present model, symbols – *BEM* solution.

5.5. Conclusions

It has been shown in this chapter that the Kachanov method of crack interaction analysis can successfully be extended to the case of frictionally sliding Mode II cracks and to compression cracks with extra loading by concentrated splitting forces (mimicking the sliding crack model). Introducing the Coulomb–Mohr law for frictional contact on crack faces, the basic equations of the original model have been modified accordingly and implemented numerically. Similarly, the basic equations have been modified in the case of point-force loading. A number of test examples has been solved in a twofold manner: using the developed code (Basista, 2000; Basista and Gross, 2000) and the *BEM* program (Lauterbach and Gross, 1998, 1999). For frictional cracks, the agreement between the obtained results is remarkably good even at the crack tip distances as small as 0.05 of the crack length. As for loading by concentrated forces and remote compression, the agreement is satisfactory if the cracks are not closer to each other than $d/l = 0.2$. Clearly, this is partly due to the simplification made with regard to $\Delta\sigma_y^{FL}$, $\Delta\tau_{xy}^{FL}$ which can later be relaxed.

There are at least two reasons for the observed high accuracy of the extended Kachanov method when applied to frictional cracks. First of all, we have been dealing here with somewhat biased, though important, situations of straight cracks and distributed loading on crack faces. For such situations the Kachanov scheme is best suited. Secondly, the exact formulas for the SIFs (5.3), (5.4) involve the unknown crack-face tractions only in an integral sense. This is in tune with the basic assumption of the Kachanov method stating that it is the average tractions that contribute most to the SIFs. As for 3D crack configurations, it is known from the analysis of open cracks (Kachanov, 1993) that the method performs even better than in 2D cases.

Concluding this chapter, it seems quite legitimate to state that Kachanov's method of direct crack interaction analysis performs exceedingly well for frictional cracks under compression for non-process (frozen) patterns of straight cracks. However, if the interacting cracks start to grow, it is clear that their growth cannot be considered as self-similar. Hence, the key element of the method, being the standard stress fields for straight cracks, ceases to be valid. For the sliding cracks, this problem occurs from the very moment of the wing nucleation. It might be overcome, though, if the equivalent (force-driven or displacement driven) straight crack models are employed, as it has been done in Section 5.4. In the literature, the Kachanov method is applied to open cracks subjected to continuously distributed loadings. The computations of Section 5.4 have shown that the method can also handle interaction problems involving point-force loads of crack faces.

Chapter 6

Chemo-micromechanics of brittle solids exposed to aggressive ambient

Abstract. This chapter is concerned with a complex problem of damage in concrete induced by chemically aggressive ambient. On the example of external sulphate attack, a micromechanical damage model is formulated for plain concrete reacting with water-borne deleterious sulphates diffusing through concrete microstructure. The underlying physico-chemical processes like unsteady diffusion, double-decomposition reaction, expansion of reaction products, and microcracking are modeled on the microscale. The microscale models are then volume-averaged into a governing set of equations relating macrovariables of the considered problem. To illustrate efficiency of the derived model, expansions of the ASTM test specimens exposed to external sulphate attack are computed and compared with the experimental data of Ouyang et al. (1988).

6.1. Introduction

At first sight, the title above may suggest a topic that is peripheral to the backbone of this thesis. However, as it will become clear soon, it is very much in tune with the micromechanical damage modeling promoted so far. Anticipating considerations to come, this type of brittle damage differs from those investigated in the preceding chapters by the source of mechanical loading that generates microcracking – it is not an external loading agency but swelling of a chemical reaction product that cannot be accommodated by the material porosity. Even though the microcracking mechanism itself will turn out relatively simple, the time-dependent processes preceding the microcracking are quite involved necessitating a multidisciplinary modeling strategy. It should perhaps be added that the problems of chemo-damage (or more generally – environmental damage) in brittle structural materials are often addressed in engineering practice for their highly undesirable and costly consequences. For example, the significance of research in this area has recently been emphasized in Germany by launching in April 2001 a large, long-term, goverment-sponsored, scientific project on detrimental effects of aggressive environment on concrete and concrete structures.

In practical applications, the performance and durability of structural materials often depend to a large extent on the chemistry of the structure-ambient system. This is certainly true for phenomena such as corrosion, environment-assisted cracking of metals through a variety of embrittlement mechanisms, degradation of concrete and rocks in aggressive chemical environments. The underlying processes are, as a rule, highly complex involving a host of interrelated physico-chemical phenomena defying traditional modeling techniques. Indeed, the deleterious influence of the environment is, at the present time, dealt with on a purely empirical level. For a variety of obvious reasons this class of methods is far from satisfactory in dealing with an almost infinite spectrum of structure-ambient systems and processes.

Recent successes in micromechanical modeling, relating microstructure of a material to its macroresponse (Mura, 1987; Weng et al., 1990; Nemat-Nasser and Hori, 1993, 1999; Krajcinovic, 1996; etc.) provide a strong stimulus for application of the same methodology to the problem discussed in this chapter. The main objective here is to investigate the relation existing between the performance of a structure and the chemical composition of the material-ambient system. Gradual degradation of a concrete or mortar specimen exposed to **sulphate attack**, common to many environments, seems to be a particularly suitable example for the illustration of the proposed chemo-micromechanical modeling.

Concrete structures, although highly durable in general, may suffer corrosive damages if exposed to contact with aggressive environments. Among all types of chemical corrosion of Portland cement concretes, the sulphate attack has attracted the greatest attention of researchers mostly due to its frequent occurrence in engineering practice and severe consequences (Lea, 1970; Biczok, 1974; Soroka, 1980). The SO_4 ions are often present in the ground water in corrosive concentrations ($>$ 500 mg/liter). If a structure or foundation is permanently or temporarily immersed in the ground water the sulphate anions diffuse through the pores of concrete and trigger complex chemical reactions with the active components of hardened cement paste. The reactions products involve increase in volume which, if not accommodated by accessible pore space, causes microcracking and may eventually result in complete deterioration of a structure element.

The degradation of structural materials in active chemical environments may occur as a result of: (a) gradual decrease of toughness brought about by intrinsic dependence of the surface energy on the chemical potential (Rice, 1978), and/or (b) pressures developed by expansive reaction products (Mehta, 1983). In the case of sulphate attack, final failure is traceable to both of these effects. There exists an extensive literature documenting the chemistry and *in situ* observations of the sulphate corrosion. Over the years, some engineering means of protection have also been devised and are being commonly used at construction sites (Biczok, 1974). However, very little has been done as yet towards analytical modeling of this phenomenon, primarily due to complexity of the underlying physico-chemical processes.

The objective of this chapter is to formulate a comprehensive micromechanical theory modeling the damage in concrete caused by the external sulphate attack. Capturing the salient features and blurring unnecessary details, the primary concern is centered on relating the chemical composition of cement, the morphology of concrete, and the properties of the aggressive agent to the mechanical response of the affected specimen. Most of the experimental data related to the selected problem are geared towards phenomenological modeling. The paucity of data regarding some specific aspects of the problem was a hindrance in exact identification of some of material parameters necessary for computations. Consequently, the example worked out at the end of this chapter is added as an illustration of the power and efficiency of the proposed model in duplicating experimentally observed trends. A surprisingly close fit with experimental data was both pleasing and encouraging even though it was not sought.

6.2. Chemical reaction

The actual mechanism of sulphate corrosion has long been a matter of debate and disagreement among the cement chemists. It is now generally accepted that the destruction suffered by hardened concrete when exposed to sulphate bearing waters can be attributed to the formation of insoluble calcium sulphoaluminate $3CaO \cdot Al_2O_3 \cdot 3CaSO_4 \cdot 32H_2O$ (**ettringite**). However, the exact details of these reactions vary from source to source (cf. Hansen, 1968; Mather, 1968; Lea, 1970; Biczok, 1972; Mindess and Young, 1981). In this chapter, Hansen's (1968) model will be taken as a starting point but any other decomposition reaction suggested in the literature can be accommodated in the present framework without major changes.

The data of Odler and Gasser (1988) and Moukwa (1990) confirm the essential nature of the micromechanical changes associated with $\mathrm{MgSO_4}$ attack on cement paste. The expansion develops rather slowly since the pore space is sufficient to accommodate the initial growth of ettringite crystals. After protracted exposure, the remaining pore space becomes insufficient to contain the expansion of the needle-like ettringite crystals. Further growth of ettringite crystals exerts pressure on the surrounding cement paste and is considered to be the main cause of internal fracturing.

Following Hansen (1968), the chemical process taking place in the hardened cement paste inundated by a solution of magnesium sulphate can be specified as two sequential decomposition reactions:

$$\begin{array}{rccccccccc} & \mathrm{Ca(OH)_2} & + & \mathrm{MgSO_4} & + & \mathrm{2H_2O} & \rightarrow & \mathrm{CaSO_4\cdot 2H_2O} & + & \mathrm{Mg(OH)_2} \\ m: & 74.0 & + & 120.4 & + & 36 & \rightarrow & 172.1 & + & 58.3 \\ v: & 33.2 & + & 72.1 & + & 36 & \rightarrow & 74.1 & + & 24.5 \end{array} \tag{6.1}$$

$$\begin{array}{rccccccc} & \mathrm{3CaO\cdot Al_2O_3} & + & \mathrm{3(CaSO_4\cdot 2H_2O)} & + & \mathrm{26H_2O} & \rightarrow & \mathrm{3CaO\cdot Al_2O_3\cdot} \\ & & & & & & & \mathrm{\cdot\, 3CaSO_4\cdot 32H_2O} \\ m: & 270.2 & + & 3(172.1) & + & 26(18) & \rightarrow & 1254.5 \\ v: & 88.8 & + & 3(\ 74.1) & + & 26(18) & \rightarrow & 725.1 \end{array} \tag{6.2}$$

where the molar masses m (g/mol) and molar volumes v ($\mathrm{cm^3/mol}$) are listed below each chemical substance taking part in the reactions.

The first reaction (6.1) is a through-solution reaction since it proceeds in the aqueous medium filling the pores. Calcium hydroxide dissolved from the walls of pores reacts with the magnesium sulphate from the ambient solution to form gypsum ($\mathrm{CaSO_4\cdot 2H_2O}$) and magnesium oxide which precipitates from the solution. The difference in volume between gypsum (reaction product) and $\mathrm{Ca(OH)_2}$ (reactant) is readily accommodated by the original porosity of mortar and the additional space released by the dissolved $\mathrm{Ca(OH)_2}$. Simple computations performed by Hansen (1968) clearly indicate "that concrete cannot be caused to expand and crack by the simple mechanism of filling pores with solids by a trough-solution process".

The second reaction (6.2), involving tricalcium aluminate, newly formed gipsum, and water needed to form the ettringite, is often assumed to be of the solid-liquid or topochemical type. It occurs directly on the surface of $\mathrm{C_3A}$ crystal ($\mathrm{C = CaO}$, $\mathrm{A = Al_2O_3}$, according to the conventional cement industry nomenclature) and may generate large swelling pressures if the space available locally is not sufficient for undisturbed growth of the ettringite crystal. Comparing the volumes of reactants and products it follows that one volume of C_3A yields 8.2 volumes of solid ettringite. Consequently, such considerable expansion of the formed ettringite exerts pressure on the surrounding matrix which results in local tensile stresses of high magnitude. The local tensile stresses may, eventually, become sufficient to induce microcracking.

Hansen's model (6.1)–(6.2) is not the only one to be found in the literature. Mather (1968) proposes two alternatives: a single- and a double-decomposition (somewhat similar to Hansen's) reaction. Biczok (1972) introduces a change in (6.2) recognizing two alternative reactions depending on whether pH factor is below or above 12.5. Mindess and Young (1981) also agree with the first of the two reactions but allow for transformation of the ettringite to monosulphate in the case when all sulphates are consumed before the tricalcium aluminate is completely hydrated. According to Lea (1970) and Soroka (1980), the second of the two reactions involves C_4AH_{19}, where $C = CaO$, $A = Al_2O_3$, $H = H_2O$.

6.3. Kinetics of ettringite formation

The heterogeneous reactions (6.1) and (6.2) involve both a liquid and a solid phase. The kinetics of these reactions depends on the sequence of two processes. Firstly, the reactant particles must be brought into contact by diffusion of external sulphate-laden water through concrete. Subsequently, a chemical reaction between particles in contact may take place.

Several studies have addressed in the past the kinetics of ettringite formation (e.g. Plowman and Cabrera, 1984; Pommersheim and Chang, 1988; Brown and Lacroix, 1989). A short discussion of the model proposed by Pommersheim and Chang (1988), who considered a spherical C_3A grain exposed to a steady supply of sulphate ions, suffices for the present purposes. Let a spherical C_3A particle have an initial radius r_{a0} as sketched in Figure 6.1 (insert). As the reaction (6.2) progresses, a layer of ettringite forms on the outside of the shrinking (as yet unreacted) part of the C_3A grain. The reaction kinetics is, thus, contingent on the rate at which the sulphate ions diffuse through the thickening ettringite layer r_e shielding the unreacted part r_a of the C_3A grain. Since the hydration of C_3A in the

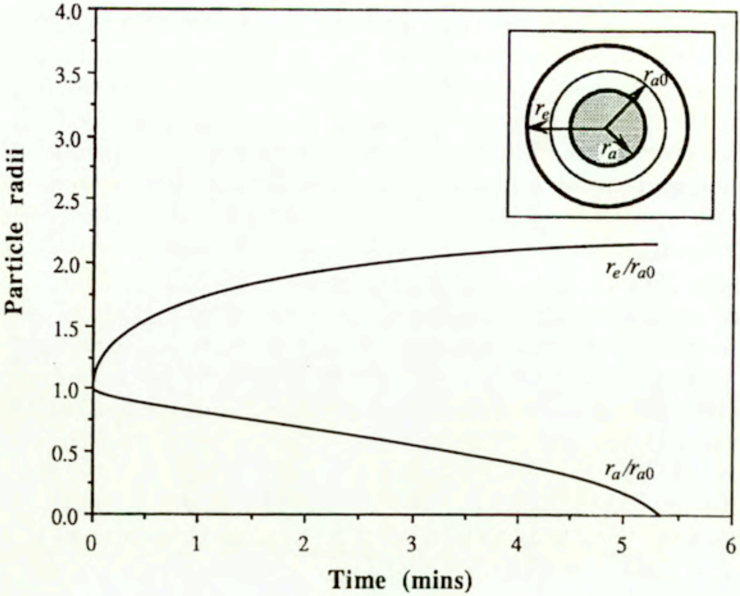

Figure 6.1. Hydration of C_3A particle and formation of ettringite crystal during hardening of cement paste (Krajcinovic, Basista, Mallick and Sumarac, 1992). Input data used in computations: sulphate concentration $c/c_0 = 1$, initial radius of C_3A particle $r_{a0} = 1\ \mu\text{m}$, diffusivity of ettringite $D_e = 0.5 \cdot 10^{-12}\ \text{m}^2/\text{s}$, ettringite porosity $\phi_e = 0.18$.

presence of gypsum is modeled as a steady diffusion process, therefore from Fick's first law and the stoichiometric analysis of (6.1)–(6.2) it follows that (Pommersheim and Chang, 1988)

$$\frac{\mathrm{d}r_a}{\mathrm{d}t} = -D_e\phi_e \frac{c r_e}{3r_a(r_e - r_a)\, d_a}\,, \tag{6.3}$$

$$\frac{\mathrm{d}r_e}{\mathrm{d}t} = (1-d)\left(\frac{r_a}{r_e}\right)^2 \frac{\mathrm{d}r_a}{\mathrm{d}t}\,, \tag{6.4}$$

where D_e is the diffusivity of ettringite, ϕ_e the porosity of the ettringite layer, c the actual molar concentration of sulphate; $d_a = 1/v_a$ and $d_e = 1/v_e$ are the molar density of C_3A and ettringite, respectively; $d = \frac{d_a}{(1-\phi_e)\, d_e}$.

From (6.1) and (6.2) we have $d_a = 11261.3\ \mathrm{mol/m^3}$, $d_e = 1379.1\ \mathrm{mol/m^3}$. Hence, for the assumed ettringite porosity $\phi_e = 0.18$ it follows that $d = 9.96$.

The analytical solution of Equations (6.3)–(6.4) with the initial condition $r_a = r_e = r_{a0}$ at $t = 0$ is given in Pommersheim and Chang (1988) in an implicit form. Krajcinovic, Basista, Mallick and Sumarac (1992) were able to get the explicit functional dependence of r_e and r_a on time using a standard numerical procedure for the solution of the ensuing sixth-order algebraic equation. These dependencies are shown in Figure 6.1 in a non-dimensional form.

As can be seen from Figure 6.1, the rate of ettringite production is rapid initially when the thickness of the ettringite layer is small. The process gets slower as time elapses since the particles of gypsum diffuse through an ever increasing layer of ettringite. This type of behavior is in agreement with the experimental results reported by Ogawa and Roy (1981).

The time t^R needed to fully convert a C_3A grain into ettringite can be derived from the solution of (6.3) and (6.4) upon setting $r_a \to 0$ (Krajcinovic, Basista, Mallick and Sumarac, 1992):

$$t^R = \frac{3\left(d - d^{\frac{2}{3}}\right) r_{a0}^2\, d_a}{2(d-1)\, D_e\, \phi_e\, c}\,. \tag{6.5}$$

It is instructive to plot the reaction time (6.5) in function of the relative sulphate concentration c/c_0, Figure 6.2. For the assumed numerical values $\phi_e = 0.18$, $D_e = 0.5 \cdot 10^{-12}\ \mathrm{m^2/s}$, and $r_{a0} = 1\ \mu\mathrm{m}$, even for the concentration as low as $c/c_0 = 0.1$, the full conversion of the C_3A core into the ettringite crystal does not exceed 1 hour. Consequently, since the sulphate-induced degradation of concrete is typically a process taking months, it seems reasonable to conclude that the actual rate-controlling mechanism is the diffusion of sulphate ions through the mortar matrix, the rate of ettringite production being of secondary importance.

The next step of the theory consists in the computation of ettringite-induced volumetric strains. Integration of (6.4) yields

$$\left(\frac{r_e}{r_{a0}}\right)^3 = (1-d)\left(\frac{r_a}{r_{a0}}\right)^3 + d. \tag{6.6}$$

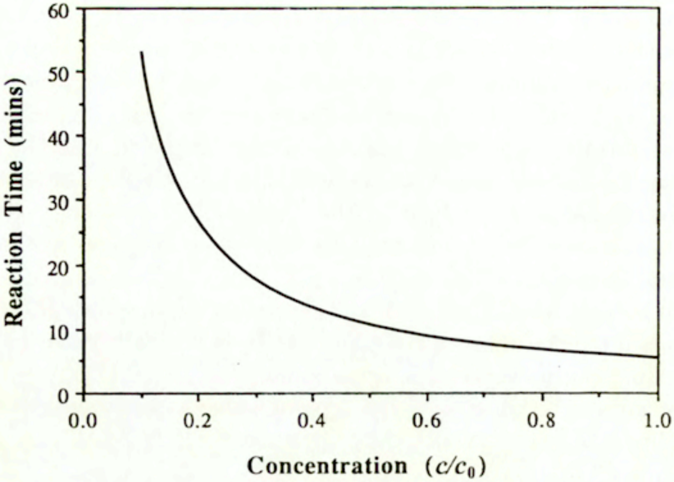

Figure 6.2. Reaction time t^R vs. concentration of sulphate c/c_0 (Krajcinovic, Basista, Mallick and Sumarac, 1992).

The volumetric strain due to expansion of a spherical ettringite particle reads

$$\varepsilon^v = \left(\frac{r_e}{r_{a0}}\right)^3 - 1, \tag{6.7}$$

which, when combined with (6.6), becomes (Krajcinovic, Basista, Mallick and Sumarac, 1992).

$$\varepsilon^v = (d-1)\left[1 - \left(\frac{r_a}{r_{a0}}\right)^3\right]. \tag{6.8}$$

The maximum expansion coincides with the completion of the reaction, i.e. at $r_a = 0$. Hence, from (6.8) it is

$$\varepsilon^v_{\max} = d - 1. \tag{6.9}$$

6.4. Diffusion with chemical reaction

In this study, a hardened concrete or mortar is assumed to be initially saturated by chemically inert water. At $t = 0$, the specimen is immersed in a pool of water containing a constant concentration c_0 of sulphate ions. The sulphate ions diffuse through the mortar driven by the concentration gradient. As they do so they encounter in their path calcium dioxide particles, react, form gypsum, and eventually ettringite as suggested by (6.1) and (6.2).

Spatial and temporal distribution of sulphate ions within the specimen is governed by a modification of Fick's second law (e.g. Finlayson, 1980)

$$\frac{\partial c}{\partial t} = \nabla \cdot (\mathbf{D}_{eff}\, \nabla c) + R(c), \tag{6.10}$$

where $c(\mathbf{x}, t)$ is the concentration of the diffusing substance, $\mathbf{D}_{eff}(\mathbf{x}, t)$ the effective diffusivity tensor, and $R(c)$ the rate of the reaction per unit volume (sink term). The reaction rate represents the time rate of change in the concentration of sulphate ions consumed in the chemical reaction with the active ingredients of the cement paste. A definite relation is found to exist between the number of molecules consumed in the reaction and the concentration of the solute. The simplest relation is based on the assumption that the number of molecules entering the reaction is linearly proportional to the concentration of the solute, i.e. $R(c) \propto (\mathrm{d}c/\mathrm{d}t)$. However, if the concentration of ettringite is known (or measurable) it is preferable to relate the sink term in (6.10) to the rate of ettringite production.

The material balance for the double-decomposition reaction (6.1)–(6.2) is

$$c^R = c_g^1 - c_g^0 \qquad \text{and} \qquad (c_g^1 - c_g^2)/3 = c_e - c_e^0\,, \tag{6.11}$$

where c^R is the molar concentration of $MgSO_4$ consumed in the first reaction to produce the concentration of gypsum c_g^1. In (6.11), the superscript 0 denotes the initial concentration while 1 and 2 denote the terminal concentrations produced in the course of reactions (6.1) and (6.2). The subscripts g and e refer to gypsum and ettringite, respectively. Since in the present case $c_g^0 = c_e^0 = c_g^2 = 0$, from (6.11) it follows that $c_g^1 = 3c_e$. Thus, the sink term in (6.10) is equal to the negative tripled rate of ettringite formation (Krajcinovic, Basista, Mallick and Sumarac, 1992):

$$R(c) = \frac{\mathrm{d}c^R}{\mathrm{d}t} = -3\frac{\mathrm{d}c_e}{\mathrm{d}t}. \tag{6.12}$$

As already discussed, the formation of ettringite during the hydration of cement was found to be controlled by diffusion. However, the mechanism by which ettringite is formed in the course of external sulphate attack on the hardened cement paste differs significantly from its formation during the hydration of cement. Before the sulphate ions can react with the C_3A particles remote from the main pores, they have to find their way to these particles through the network of micropores. Moreover, only a part of the C_3A grain is likely to be in immediate contact with the aggressive solution, and not all of the pores are suitable for the ettringite build-up (Hansen, 1968). Since a rigorous microstructural modeling of this process seems to be extremely complex and non-deterministic, it will simply be assumed that the rate of ettringite formation is proportional to the current amounts of the reactants (cf. Dawson, 1973; Krajcinovic, Basista and Sumarac, 1991b), i.e.

$$\frac{\mathrm{d}c_e}{\mathrm{d}t} = kcc_a = kc(c_a^0 - c_e), \tag{6.13}$$

where c is again the current molar concentration of the diffusing sulphate, c_a the current molar concentration of C_3A and c_a^0 the initial molar concentration of C_3A in the hardened cement paste. The assumption leading to expression (6.13) is corroborated by observations that the damage of mortar depends only on the concentration of sulphates and C_3A but not on the content of calcium hydroxide (Biczok, 1972). In (6.13), k is the rate constant of the double decomposition reaction (6.1)–(6.2) depending on the size, tortuosity and connectivity of the micropores. No experiments designed to determine the constant k in the case of external sulphate attack were reported in the literature. In the absence of precise data, k is herein a parameter to be determined from phenomenological rather than microstructural considerations.

Substitution of (6.13) into (6.12) and (6.10) leads to a partial differential equation (Krajcinovic, Basista, Mallick and Sumarac, 1992)

$$\frac{\partial c}{\partial t} = \nabla \cdot (\mathbf{D}_{\mathit{eff}}\, \nabla c) - 3kc(c_a^0 - c_e). \tag{6.14}$$

The associated boundary condition is that $c = c_0$ on the surfaces exposed to the water with constant concentration of sulphate ions. Initial condition is that $c = 0$ within the specimen at the beginning of the experiment $t = 0$.

If necessary, the concentrations of other active substances can be determined from the stoichiometric analysis once the concentration of sulphates

$c(\mathbf{x}, t)$ is computed solving the initial boundary value problem. Note that the double decomposition reaction can be terminated either by discontinuing the supply of the sulphates before all C_3A is consumed ($c = 0$), or when the entire supply of C_3A has been exhausted rendering the specimen chemically inert to further sulphate attack ($c_a^0 = c_e$).

6.5. Transport properties

As the solute diffuses through the specimen, chemical reactions and the attendant crystallization of the ettringite will take place in a large number of locations surrounding fluid conducting pores. The exact sizes, shapes, and locations of expanding ettringite crystals, which can exert substantial forces on the surrounding hardened cement paste, are generally not known. Consequently, it is not possible to consider every inclusion, superimpose the effects of all inclusions in the specimen, and compute the average of effective properties of the material. As the damage evolves through nucleation of new and growth of already existing microdefects, the macroresponse is affected primarily by the volume averages of defects. However, as the defect concentration increases beyond some threshold level, the microcracks interact and form large clusters which become an important, and finally dominant, factor influencing the macroresponse. The dependence of transport properties on the microdefects in two regimes is distinctly different. Thus, these two regimes must be studied independently.

6.5.1. Effective-medium regime

The problem of the determination of material properties is typically and efficiently resolved within the effective medium approximation framework discussed in great detail in Mura (1987), Aboudi (1991), Nemat-Nasser and Hori (1993). This approach has undeniable merits in modeling a part of the process preceding the critical phenomena but is, in its conventional form, of limited utility thereafter. Various effective media (continua) models such self-consistent, differential, double-embedded, etc. have been proposed in the past (cf. Nemat-Nasser and Hori, 1993). A study of the relative merits of these models is beyond the scope of this chapter. The most popular and most frequently used among the first-order effective media approximations is the so-called self-consistent method (SCM). The SCM is based on the assumptions that: (a) the mean stress field of each inclusion is identical and equal to the far-field stress, (b) external fields of each inclusion weakly depend on the exact configuration of other inclusions. Within this approximation, widely held to be adequate for low to moderate concentrations of inclusions, the analysis of the actual continuum containing many interacting inclusions is reduced to a much simpler problem of the superposition of analyses of a single inclusion embedded in an effective medium. The material parameters of the effective medium are determined using energy considerations.

Diffusivity

The diffusivity **D** is a structural parameter exhibiting strong dependence on the tortuosity of the fluid path through the solid (Dullien, 1979). In a virgin hardened cement paste the diffusivity depends on the pore structure, i.e. the distribution and connectivity of pores $\phi(r)$ having different radii r. Assuming the pores to be perfectly random with respect to their orientation and width, the virgin (undamaged) hardened cement paste may be considered to be of isotropic diffusivity. In the sequel, it will be assumed that the accessible porosity ϕ and isotropic diffusivity D_0 characterizing diffusion through the virgin hardened cement paste are known.

As the microcracks within the specimen nucleate and grow, the tortuosity of the fluid path decreases and the effective diffusivity increases. This problem has been discussed by many authors in the past on many levels of rigor and sophistication (e.g. Barenblatt et al., 1960; Salganik, 1974; Englman et al., 1983; Wilke et al., 1985; Bazant et al., 1987; Gueguen and Dienes, 1989).

The conventional continuum models, popular among analysts because of their computational efficiency, ignore the microscopic nature of the mixing process. In general, these models are based on volume averages of the involved field quantities and variables and are, therefore, applicable only in the initial stages of the process away from the critical phenomena. Even for this stage of the process, i.e. while the microcrack density within the solid is of moderate levels, it is often argued that the nature of the problem necessitates application of statistical models based on the studies of a random network of capillary sizes.

Salganik's (1974) model, developed within the SCM approximation, considers each inclusion to be of ellipsoidal shape, the concentration gradients within the inclusion $s_i^I = \partial c/\partial x_i$ are homogeneous whenever the far-field concentrations are homogeneous as well. In the case of randomly oriented penny-shaped microcracks of radius a, the effective diffusivity can be cast into a simple formula (Salganik, 1974)

$$D = D_0 \left(1 + \frac{32}{9}\, \omega \right), \tag{6.15}$$

where

$$\omega = N \langle a^3 \rangle \tag{6.16}$$

is the Walsh–Budiansky–O'Connell microcrack volume density parameter (micromechanical damage parameter). In (6.16), N is the number of microcracks per unit volume. The angular brackets denote volume averages taken over the RVE.

Elastic constants

In the case considered, the mortar matrix contain both ettringite inclusions and microcracks growing from the matrix-inclusion interfaces. The effect of the water inundating the specimen is neglected since the stresses do not "occur with significant rapidity to prevent communication of fluid between cracks" (Budiansky and O'Connell, 1976).

Comparison between overall specimen expansions (of up to 0.4%) and expansions of a single ettringite inclusion ($d = 9.96$) leads to an inescapable conclusion that the actual volume density of expanding inclusions is rather small. Even though self-consistent estimates for elastic moduli of a solid (mortar) containing a dilute suspension of spherical inclusions (ettringite crystals) are available (e.g. Christensen, 1991), it seems sufficient for the present purposes to invoke the much simpler mixture rule.[1] According to this rule, in the absence of microcracks, the effective elastic modulus of the mortar matrix with ettringite inclusions is

$$E_0 = (1 - f^I)\, E_{cp} + f^I E_e\,, \tag{6.17}$$

---

[1] This is probably the simplest averaging technique based on volume averaging for composite materials. For a two-phase RVE, the average of any quantity over the volume of the RVE is $\langle\cdot\rangle = (1-f)\,\langle\cdot\rangle_1 + f\,\langle\cdot\rangle_2$, where $\langle\cdot\rangle_\alpha$ stands for the volume average taken over the α-phase ($\alpha = 1, 2$) and f is the volume fraction of phase 2. This formula, and thus (6.17), follow directly from the definition of the volume average, i.e. $\langle\cdot\rangle = \frac{1}{2}\int_V (\cdot)\,\mathrm{d}V$.

where $f^I = \sum V^I/V$ is the total volume fraction of ettringite crystals in the mortar RVE, while the indices "*cp*" and "*e*" stand for cement paste and ettringite, respectively.

As a consequence of the large volumetric expansion of a single ettringite grain, the local stress concentration near the inclusions significantly exceeds the average macrostresses associated with the beam-column action of the specimen. Hence, the orientation of microcracks emanating from the interface will be perfectly random. Assuming further that all microcracks are penny-shaped, the self-consistent estimate for the overall elastic modulus E of the mortar matrix containing a dilute concentration of ettringite inclusions and microcracks is (Budiansky and O'Connell, 1976)

$$\frac{E}{E_0} = 1 - \frac{16}{45}\,\frac{(1-\nu^2)(10-3\nu)}{(2-\nu)}\,\omega, \tag{6.18}$$

and, implicitly, for the overall Poisson ratio ν

$$\omega = \frac{45}{16}\,\frac{(\nu_0-\nu)(2-\nu)}{(1-\nu^2)[10\nu_0-\nu(1+3\nu_0)]}\,, \tag{6.19}$$

where the damage parameter ω is again defined by expression (6.16) and the subscript "0" denotes the uncracked matrix (with etrringite crystals, though).

6.5.2. Percolation regime

Expressions (6.15) for the diffusivity and (6.18), (6.19) for the elastic parameters are valid only for dilute concentration of defects located far enough from each other to prevent their interaction. However, as the microcracks grow in size, the distance separating adjacent microcracks will decrease. As the defect clusters grow, they will invariably start dominating both the diffusivity and stiffness of the specimen. Since the location of inclusions and the ensuing shapes of the microcrack clusters are random, the determination of transport properties of the solid at this stage using traditional applied mechanics methods is not possible.

The behavior of systems in the stage characterized by the emergence of a defect cluster spanning an observed region exhibits certain universal aspects. The so-called percolation theory (see Chapter 8) represents an eminently suitable framework for studies of systems in the vicinity of the percolation threshold defined as emergence of a spanning cluster. The percolation models complement the effective continua models since the percolation threshold is defined as a critical density of microcracks $\omega = \omega_c$.

Diffusivity

Formula (6.15), suggesting linear dependence of diffusivity on microcrack density, is valid only if the microcracks are far apart. The diffusivity is enhanced solely by decreasing the tortuosity of the pore network. However, as soon as a cluster traversing the specimen forms, some of the liquid will be transported through it as well. The percolation threshold ω_c at which a spanning cluster, composed of randomly oriented penny-shaped microcracks of equal radii, connects two opposite surfaces of the sample has been determined by numerical simulations (Charlaix, 1986) as

$$\omega_c = N_c a^3 \approx 0.182, \tag{6.20}$$

where N_c is the critical number (per unit volume) of penny-shaped microcracks of radius a connected into an uninterrupted path through the specimen.

The scaling law for the diffusivity attributable to the spanning cluster is (Stauffer, 1985)

$$D_p \propto (\omega - \omega_c)^{\mu}, \tag{6.21}$$

where $\mu \approx 2$ is a universal exponent (dimensional invariant independent of microstructure, established by numerical simulation) for a three-dimensional case.

In order to account for the diffusion through the matrix containing non-intersecting penny-shaped microcracks and the conductance through the spanning cluster, it seems reasonable to postulate that a parallel connection between the two transport phenomena exists, i.e. that the overall diffusivity is (Krajcinovic, Basista, Mallick and Sumarac, 1992)

$$D = D_0 \left(1 + \frac{32}{9}\omega\right) + D_p\,, \tag{6.22}$$

where

$$D_p = D_0 \frac{(\omega - \omega_c)^2}{\omega_{ec} - \omega} \qquad \text{for} \quad \omega_c < \omega < \omega_{ec} \tag{6.23}$$

is the diffusivity through the spanning cluster, satisfying the conditions

$$D_p = 0 \quad \text{for} \quad \omega \leq \omega_c \qquad \text{and} \qquad D_p = \infty \quad \text{for} \quad \omega \geq \omega_{ec} \, . \tag{6.24}$$

Expressions (6.23)–(6.24) for diffusivity D_p acknowledge existence of two different universal classes of problems having different percolation thresholds (cf. Chapter 8): (a) $\omega = \omega_c$ (conduction percolation threshold) at which a spanning cluster traverses the volume creating a worm-hole in the material, and (b) $\omega = \omega_{ec}$ (elastic or rigidity percolation threshold) at which a cluster of cracks transects the volume. At the elastic percolation threshold the macrostiffness vanishes and it is, for simplicity, assumed that the diffusion becomes practically instantaneous.

Stiffness

Much as in the case of diffusivity, the SCM expressions for elastic moduli (6.18), (6.19) are, in principle, valid for dilute concentration of microcracks. The elastic percolation represents a different universal class necessitating additional numerical and experimental simulations to determine the elastic percolation threshold ω_{ec} at which the elastic modulus $E \to 0$, and the scaling law is $E \propto (\omega_{ec} - \omega)^f$ as $\omega \to \omega_{ec}$. Naturally, it would be more precise to state that the macrostiffness vanishes at $\omega = \omega_{ec}$ since volume averaging and, therefore, overall modulus E makes little sense when the crack cluster length exceeds the size of the RVE.

Numerical simulations (Sornette, 1988) indicate that

$$\omega_{ec} = \langle Na^3 \rangle_c \approx 0.712 \tag{6.25}$$

and

$$E \propto (\omega_{ec} - \omega)^{4.1} . \tag{6.26}$$

The effective-medium response in which E is a linear function of ω (6.18) and the response at impending percolation during which E is a strongly nonlinear function of ω (6.26), are separated by a crossover regime. The functional dependence $E(\omega)$ within the crossover regime requires significant numerical simulations which have still to be performed. However, it is interesting that a self-consistent estimate of the elastic percolation threshold is

$$\omega_{ec}^{SC} = \frac{9}{16} \approx 0.8\omega_{ec} \, . \tag{6.27}$$

Note that for an elastic solid with randomly distributed, open, penny-shaped microcracks the self-consistent estimate $\omega_{ec}^{SC} = 9/16$ at which the effective Young modulus E (6.18) vanishes is universal for all values of the initial Poisson ratio ν_0 (cf. Figure 5 in Budiansky and O'Connell, 1976). More importantly, the critical microcrack density $\omega_{ec}^{SC} = 9/16$ in (6.27) is exact since the effective Poisson ratio ν (6.19), being a decreasing function of ω, also vanishes at $\omega_{ec}^{SC} = 9/16$. The function $E(\omega)$ and its first four derivatives vanish at $\omega = \omega_{ec}$. Thus, the function $E(\omega)$ is so flat in the vicinity of ω_{ec} that $E(\omega_{ec}^{SC}) \approx 0.1E_0$. Consequently, the assumption that $E(\omega_{ec}^{SC}) \approx 0$ will be well within the overall accuracy. Indeed, the results of Lemieux et al. (1985) and Sahimi and Goddard (1986) indicate that the elastic percolation threshold of articulated lattices is surprisingly close to the value obtained from the effective medium theories, i.e. assuming that SCM is valid up to the point at which the elastic modulus E (6.18) vanishes. Experimental and numerical data supplied by Sieradzki and Li (1986), Benguigui (1986) lend further credence to this assumption, indicating that the actual magnitude of the elastic modulus at the critical microcrack density, (estimated using the SCM) is approximately 10% of its original value E_0. Finally, numerical simulations for lattices (Hansen et al., 1989; Krajcinovic and Basista, 1991) confirm the validity of the assumption that the SCM estimates of the elastic percolation threshold are quite accurate. In conclusion, consistent with the degree of approximations introduced by other simplifications, it seems reasonable to assume that the self-consistent estimate for the elastic modulus (6.18) is valid within the entire range $0 < \omega < 9/16$.

6.6. Stress–strain relationship

Central to the investigations of the durability of concrete structures is the determination of the macrostresses and macrostrains associated with the expansion of the reaction products and the ensuing damage evolution. On the microscale, chemical reactions (6.1)–(6.2) take place in small parts of the volume in the vicinity of pores with geometry conducive to the crystallization of ettringite. In general, the crystals will not form in subcapillary pores (Hansen, 1968). The expansion pressures cannot build up in the pores open to external surface, either. Consequently, the ettringite crystals capable of generating microcracks will nucleate only in a fraction of the overall pore network.

The present task consists in determining the compliance of the hardened cement paste containing an ensemble of expanding crystals and an ensemble of microcracks. At this point, it will be assumed that all expanding crystals are spherical in shape and all microcracks are penny-shaped. Consistent with the analysis in the preceding section, it will again be assumed that the defect concentration is low to moderate, rendering their direct interaction inconsequential. The incubation period, i.e. the time lag between the onset of the reaction and the onset of the specimen expansion (Ogawa and Roy, 1981), resulting from the initial unconstrained growth of the ettringite crystal within the pore, is short in comparison to the time needed for diffusion and will be neglected. It will also be assumed that relatively small pore pressures have no appreciable effect on the stress–strain relationship within the solid (e.g. Rice and Cleary, 1976).

6.6.1. Inhomogeneous inclusion

Consider first the stress and strain fields surrounding an inhomogeneous inclusion (expanding ettringite crystal) occupying domain Ω, embedded into a homogeneous and isotropic effective medium (cement paste containing a dilute concentration of randomly oriented defects). Assuming the inclusion to be spherical in shape, the free expansion strain attributable to the difference between volumes of reactants and reaction products is

$$\varepsilon_{ij}^{r} = \frac{1}{3}\varepsilon^{v}\delta_{ij} , \tag{6.28}$$

where ε^{v} is given by the expression (6.8) or (6.9), while δ_{ij} is the Kronecker symbol.

Denote the total eigenstrain within the inclusion by

$$\varepsilon_{ij}^{**} = \varepsilon_{ij}^{r} + \varepsilon_{ij}^{*} + \varepsilon_{ij}^{t} , \tag{6.29}$$

where ε_{ij}^{*} is the equivalent eigenstrain resulting from the disparity in elastic moduli between the matrix and inclusion; $\varepsilon_{ij}^{t} = \alpha T^{r}\delta_{ij}$ is the strain due to the thermal expansion associated with the heat released or consumed during the course of chemical reactions and crystal growth. As usual, α is the coefficient of thermal expansion (depending on ω) and T^{r} the temperature difference measured from some reference level (taken as $T^{r} = 0$). A similar reaction taking place during the hydration of cement in fresh cement paste is strongly exothermic, releasing substantial thermal energy of 1.45 J/g of the reaction product (cf. Mchedlow-Petrosian, 1988).

In the absence of mechanical tractions on external surfaces of the specimen, the expression for eigenstrain (6.29) can be derived as in Mura (1987) in the form

$$\varepsilon^{**}_{kk} = \frac{3(1-\nu)K^I}{(1+\nu)K^I-(4\nu-2)K}\,\varepsilon^r_{kk} + \alpha T^r = \beta\varepsilon^r_{kk} + \alpha T^r, \tag{6.30}$$

where the superscript I indicates reference to the inclusion while the non-indexed parameters characterize the surrounding effective continuum; K^I, K denote thus the bulk modulus of inclusion and effective continuum, respectively. All off-diagonal components of the strain tensor are equal to zero as a result of spherical symmetry. The inclusions grow in a degrading matrix containing a large number of microcracks, approximated by the effective continuum. Since the parameters of the effective continuum depend on the microcrack density ω, the eigenstrain (6.30) can be written as

$$\varepsilon^{**}_{kk} = \beta(\omega)\,\varepsilon^r_{kk} + \alpha T^r, \tag{6.31}$$

where the expressions for the bulk modulus $K(\omega)$ and the Poisson ratio $\nu(\omega)$ of the effective continuum (contained in β) can be obtained from (6.18), (6.19). Since the heat released during the exothermic reactions (6.1)–(6.2) is proportional to the mass of the reaction product (Mchedlow-Petrosian, 1988) expression (6.31) can finally be recast in a simple form

$$\varepsilon^{**}_{kk} = \beta(\omega, T^r)\,\varepsilon^r_{kk}\,. \tag{6.32}$$

However, since the heat diffuses through the cement paste faster than the sulphate ions, and since no reliable estimate of the heat released during reactions (6.1)–(6.2) is available, the thermal eigenstrain will be neglected at this stage of the model development. The uniform radial pressure within the expanding homogeneous, elastic inclusion must be proportional to the eigenstrain (6.32). Hence, from (6.9) and (6.32), the maximum pressure (coinciding with the completion of the reaction) exerted on the surrounding matrix is (Krajcinovic, Basista, Mallick and Sumarac, 1992)

$$p = K^I\varepsilon^{**}_{kk} = K_e\beta(\omega)\,(d-1), \tag{6.33}$$

where $K^I = K_e$ is the bulk modulus of inclusion (ettringite), while d is defined at (6.3)–(6.4).

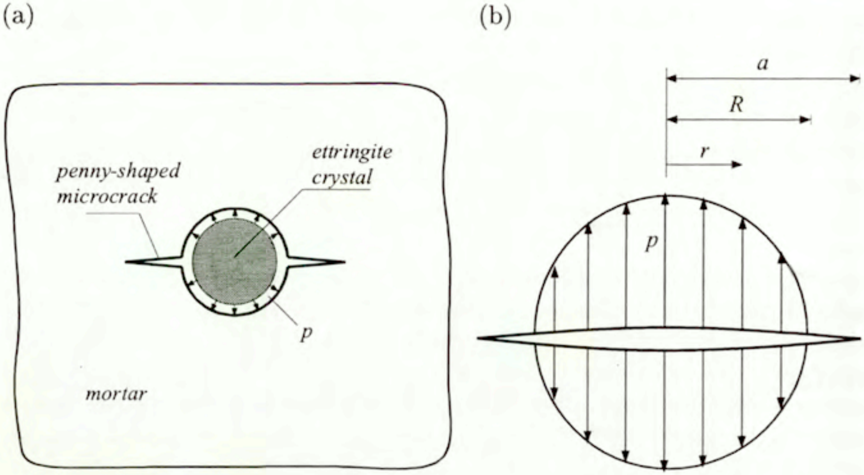

Figure 6.3. Two-dimensional visualizations of: (a) spherical ettringite crystal growing within a spherical pore, (b) continuous distribution of vertical ring load over penny-shaped microcrack.

The actual ettringite–pore interaction is simplified for the modeling purposes as shown in Figure 6.3a. Assuming that initially a very small notch exists at the inclusion-matrix interface, the stress intensity factor can be approximated as

$$K_I \approx \frac{pR^2}{\sqrt{\pi a^3}}\,, \tag{6.34}$$

where R is the pore radius, a the microcrack half-length, p is the swelling pressure. Since the SIF is not available for the three-dimensional case considered, expression (6.34) is derived using the solution for the ring load (Sneddon, 1946; Murakami, 1987) as the influence function (Figure 6.3b).

For a constant radius $R = r_{a0}$ of the C_3A inclusion, it follows from the Griffith criterion that

$$a = r_{a0}\,\sqrt[3]{\frac{p^2 r_{a0}}{\pi K_{Ic}^2}}\,, \tag{6.35}$$

where K_{Ic} is the fracture toughness of the hardened cement paste. As soon as the microcrack of radius a given by (6.35) opens, the pressure exerted by growing ettringite grain is released. Additional inclusion expansion is needed for further microcrack growth. From (6.34) it can be seen that the microcrack is stable because $\partial K_I/\partial a < 0$. Thus making use of (6.33), the terminal radius of a circular microcrack formed around a spherical C_3A grain of initial radius r_{a0} is (Krajcinovic, Basista, Mallick and Sumarac, 1992)

$$a = r_{a0}\sqrt[3]{\frac{[\beta(\omega)\,(1-d)K_e]^2 r_{a0}}{\pi K_{Ic}^2}}\,. \tag{6.36}$$

6.6.2. Stress–strain relationship on macroscale

Once the local stress and strain fields around an inhomogeneous inclusion have been determined, the magnitudes of the respective macrofields at each material point of the effective continuum can be computed through a homogenization process (i.e. by averaging these fields over the tributary RVE). Consider, to this end, a volume V containing a reasonably dilute concentration of spherical inclusions having a total volume of $V^I = f^I V$. The relation mapping the macrostresses $\boldsymbol{\sigma}$ on macrostrains $\boldsymbol{\varepsilon}$ can be written combining contributions of beam-column action and inhomogeneous inclusions:

$$\boldsymbol{\varepsilon} = \mathbf{S}(\omega) : \boldsymbol{\sigma} + \boldsymbol{\varepsilon}^I, \tag{6.37}$$

where $\mathbf{S}(\omega)$ is the effective compliance tensor reflecting recorded history, i.e. ettringite build-up and microcracking. Note that compressive stresses are viewed negative. Since the volume average of stress perturbations in the matrix (induced by ettringite crystal expansions) must by definition vanish, the second term on the right-hand side of (6.37) involves only summation of eigenstrains over all inclusions (Mura, 1987):

$$\boldsymbol{\varepsilon}^I = f^I \boldsymbol{\varepsilon}^{**}, \tag{6.38}$$

where f^I is the inclusion volume density and $\boldsymbol{\varepsilon}^{**}$ the eigenstrain given by (6.32).

Assuming perfectly random orientations of microcracks and random distribution of inclusions, the components of the effective compliance tensor $\mathbf{S}(\omega)$ can be computed using expressions (6.18), (6.19) for the effective Young modulus E and the Poisson ratio ν. Application of expression (6.37) requires, finally, formulation of a relation between the sulphate concentration $c(\mathbf{x}, t)$ obtained by solving (6.14) and the damage parameter $\omega(\mathbf{x}, t)$.

The microcrack radius a, given by (6.36), depends primarily on the initial radius of the C_3A grain.

As has already been shown, the actual reaction time is very short compared to the time of diffusion of sulphate ions through the mortar. Thus, on the diffusion time scale, the final microcrack length is attained instantaneously. Consequently, the rate of damage evolution is proportional to the rate at which C_3A particles are activated, the state of damage being defined by ω (6.16).

From the solution of the diffusion-reaction equation (6.14) it is possible to determine the molar concentration of the sulphate consumed to form etrringite crystals. Integrating the kinetic equation (6.13), we have (Krajcinovic, Basista, Mallick and Sumarac, 1992):

$$c^R(\mathbf{x}, t) = 3c_e(\mathbf{x}, t) = 3c_a^0 \left[1 - \exp\left(-k \int_0^1 c(\mathbf{x}, t)\,\mathrm{d}t\right)\right]. \qquad (6.39)$$

Thus, the number of C_3A grains (per unit volume V involved in the reaction with sulphate concentration (6.39) is (Krajcinovic, Basista, Mallick and Sumarac, 1992)

$$N_a = \frac{c^R}{\hat{m}_s} = \frac{c^R v_a}{4\pi r_{a0}^3}, \qquad (6.40)$$

where $\hat{m}_s$ is the mass of magnesium sulphate (in moles) needed to convert completely a single particle of tricalcium aluminate into ettringite, r_{a0} and v_a are again the initial radius and molar volume of the C_3A crystal.

Using relation (6.36) and the number of already reacted C_3A particles from (6.40) and (6.39), the damage parameter (6.16) can be cast into following implicit form (Krajcinovic, Basista, Mallick and Sumarac, 1992)

$$\omega = N_a a^3 = N_a \beta^2(\omega)\,(d-1)^2\,\frac{K_e^2 r_{a0}^4}{\pi K_{Ic}^2}. \qquad (6.41)$$

The final set of governing equations is obtained satisfying the equilibrium, compatibility and boundary conditions, depending on the particular problem.

6.7. Application

The ultimate test of any analytical model is its ability to reproduce experimentally measured data and to predict the response of a specimen or a structure. This task is in the present case hindered by unsatisfactory documentation of the published test results which generally lack precise data related to microstructural parameters (diffusivity, porosity, microcrack density, etc.).

In studies of chemically-assisted deterioration of concrete, it is a common experimental practice to perform tests on mortar instead of concrete specimens. The reason for that is that the considered deleterious corrosion processes proceed at much faster pace in mortar than in concrete, while their nature in both materials remains the same.

A set of data related to the expansion of mortar specimens exposed to a combined external attack of $MgSO_4$ and Na_2SO_4 has been provided by Ouyang et al. (1988) who performed experiments in accordance with ASTM C1012 recommendations. It was observed that the rate of mortar expansion during external sulphate attack is an increasing function of time (see also Lea, 1970).

The ASTM C490 prismatic test specimens (Figure 6.4) were placed in a mixed solution of 0.176 mol/l $MgSO_4$ and 0.176 mol/l Na_2SO_4. A tacit assumption is made that the action of magnesium sulphate and sodium sulphate on mortar are similar in the sense that both substances serve as sources for the aggressive ions SO_4^{2-}. In practice, magnesium sulphate is often more dangerous because it additionally decomposes hydrated calcium silicates (cf. Lea, 1970). On the other hand, it has been reported that sodium sulphate solution is more corrosive than magnesium sulphate solution if the calculated content of C_3A in the cement exceeds 9% (Biczok, 1972). In the light of this information, the assumption of equal average influence of both substances on concrete corrosion seems reasonable.

In order to determine the actual initial concentration of C_3A available for the reaction with aggressive ions diffusing through the test specimen, it is first necessary to estimate how much of C_3A anhydride remains in the cement paste after the hydration process. Denoting by f_g the amount of gypsum (mass fraction) usually added to Portland cement clinker to avoid rapid setting, the initial molar concentration of tricalcium aluminate is (Krajcinovic, Basista, Mallick and Sumarac, 1992)

$$c_a^0 = \frac{M_{cm}}{m_a V}\left(f_a - f_g \frac{m_a}{3m_g}\right), \tag{6.42}$$

where $f_a = (4.3\%,\ 7\%,\ 8.8\%,\ 12\%)$ is the mass fraction of C_3A in the cement as given in Ouyang et al. (1988). As before, m_a and m_g are the

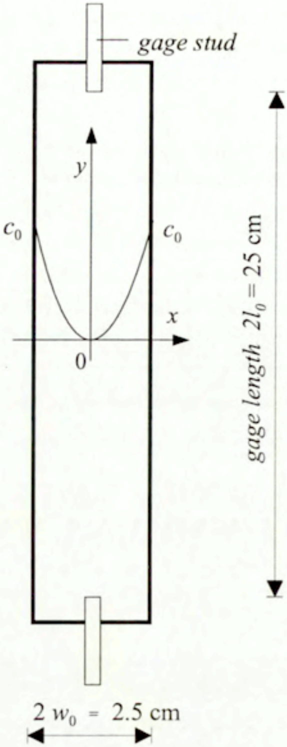

Figure 6.4. Cross section of ASTM test specimen for measurement of length change.

molar masses of C_3A and gypsum, M_{cm} is the mass of cement in $V = 1\ \mathrm{m}^3$ of mortar. The ratio $(m_a/3m_g)$ in (6.42) results from the mass balance of reaction (6.2).

6.7.1. Analytical one-dimensional model

Consider now the diffusion equation (6.14) with the diffusivity defined by (6.22)–(6.24). In an attempt to replicate the experimental trends, it seems sufficient to assume the diffusion to be one-dimensional (across the thickness only). Therefore, from (6.14) and (6.22) we have (Krajcinovic, Basista, Mallick and Sumarac, 1992)

$$\frac{\partial \tilde{c}}{\partial \tilde{t}} = \frac{\partial}{\partial \tilde{x}} \left\{ \left[\tilde{D}_0 \left(1 + \frac{32}{9}\omega \right) + D_p \right] \frac{\partial \tilde{c}}{\partial \tilde{x}} \right\} - 3k\tilde{c}(\tilde{c}_a^0 - \tilde{c}_e). \qquad (6.43)$$

In (6.43) and the equations to come, the following normalization is used:

$$\begin{aligned} &\tilde{x} = x/w_0\,, \qquad \tilde{c} = c/c_0\,, \qquad \tilde{c}_e = c_e/c_0\,, \\ &\tilde{c}^R = c^R/c_0\,, \qquad \tilde{t} = t/t_R\,, \qquad \tilde{D}_0 = \frac{D_0 t_R}{w_0^2}\,, \end{aligned} \qquad (6.44)$$

with reference time $t_R = 24$ h. The initial and the boundary conditions are (Figure 6.4)

$$\tilde{c}(\tilde{x},0) = 0, \qquad \tilde{c}(-1,\tilde{t}) = \tilde{c}(1,\tilde{t}) = 1, \qquad \frac{\partial \tilde{c}}{\partial x}(0,\tilde{t}) = 0. \qquad (6.45)$$

The governing equation (6.43) is highly nonlinear, rendering the analytical or approximate solutions not possible. Thus, it had to be solved numerically using finite difference method.

In the one-dimensional case considered, the σ–ε relation (6.37) acquires a simple form

$$\varepsilon = \frac{\sigma}{E} + f^I \varepsilon^{**}, \qquad (6.46)$$

where E is the elastic modulus of the damaged hardened cement paste containing both the ettringite inclusions and the microcracks. The f^I is again the volume fraction of the C_3A particles in $1\mathrm{m}^3$ of mortar, explicitly given as

$$f^I = \frac{4}{3} N_a \pi r_{a0}^3\,, \qquad (6.47)$$

where N_a is calculated form (6.40).

Since the stress components τ_{xy} and σ_x vanish, and $\sigma_y = \sigma \neq 0$ depends only on x (Figure 6.4), equilibrium is automatically satisfied. The compatibility conditions (in stresses) reduce to (Krajcinovic, Basista, Mallick and Sumarac, 1992)

$$\frac{\mathrm{d}^2}{\mathrm{d}\tilde{x}^2} \left[\sigma(\tilde{x},\tilde{t}) + E(\tilde{x},\tilde{t})\, f^I(\tilde{x},\tilde{t})\, \varepsilon^{**}(\tilde{x},\tilde{t}) \right] = 0. \qquad (6.48)$$

The approximate (averaged) boundary conditions at free edges ($y = \pm l_0$) are

$$\int_{-1}^{1} \sigma \, \mathrm{d}\tilde{x} = 0 \qquad \text{and} \qquad \int_{-1}^{1} \sigma \tilde{x} \, \mathrm{d}\tilde{x} = 0. \tag{6.49}$$

The latter condition is satisfied automatically as a result of the problem symmetry.

Solving (6.48) in conjunction with (6.49) and (6.46) leads to the following expression for the axial strain (Krajcinovic, Basista, Mallick and Sumarac, 1992):

$$\varepsilon(\tilde{x}, \tilde{t}) = \frac{1}{E(\tilde{x}, \tilde{t})} \int_{0}^{1} \varepsilon^{**}(\tilde{x}, \tilde{t}) \, E(\tilde{x}, \tilde{t}) \, f^{I}(\tilde{x}, \tilde{t}) \, \mathrm{d}\tilde{x}. \tag{6.50}$$

The coupled self-consistent estimates of the effective moduli E, ν are given by (6.18) and (6.19). However, the computations performed in Budiansky and O'Connell (1976) and depicted in their Figure 5 clearly show that for practical purposes (6.18) and (6.19) can be linearized in ω as

$$E \approx E_0 \left(1 - \frac{16}{9} \omega\right), \tag{6.51}$$

$$\nu \approx \nu_0 \left(1 - \frac{16}{9} \omega\right). \tag{6.52}$$

Approximation (6.51) of the effective Young modulus holds with a very good accuracy for a wide range of values of the effective Poisson ratio ν in (6.18).[1] Also, as can be deduced from Figure 5 in Budiansky and O'Connell (1976), expression (6.52) closely approximates the effective Poisson ratio ν (6.19) for those elastic materials whose Poisson ratio in undamaged state ν_0 is less than 0.3, e.g. for plain concrete.

Substituting (6.51) and (6.52) into the expression for eigenstrain (6.32), the parameter $\beta(\omega)$ becomes (Krajcinovic, Basista, Mallick and Sumarac, 1992)

$$\beta(\omega) = \frac{3\left[1 - \nu_0 \left(1 - \frac{16}{9}\omega\right)\right]}{2\frac{E_0}{E_e}\left(1 - \frac{16}{9}\omega\right)\left(1 - 2\nu_e\right) + \left[1 + \nu_0\left(1 - \frac{16}{9}\omega\right)\right]}. \tag{6.53}$$

---

[1] The exact SCM solution (6.18) can be rewritten as $(E/E_0) = 1 - k(\nu)\omega$. Computing $k(\nu)$, say, for $\nu = 0.3,\ 0.2,\ 0.1$ and comparing the obtained values with 9/16 as predicted by (6.51), the relative error is 2.6%, 0.3%, 1.1%, respectively.

The damage parameter ω can now be computed combining (6.41) and (6.53). The resulting cubic algebraic equation in terms of ω is omitted here for the sake of brevity.

So far, the microcracking due to the sulphate attack was attributed solely to the stress concentrations near the expanding ettringite crystals. The stresses resulting from the beam-column action of the specimen can be detrimental as well. Simple comparison of measured macrostrains (Ouyang et al., 1988) indicate that the number of expanding crystals N_a is relatively small. Consequently, the local stress fields in the vicinity of expanding crystals vastly exceed macrostresses σ. Thus, the damage attributed to the compressive stresses in regions bordered by external surfaces represents a second-order effect which will be neglected in computations. On the other hand, the tensile stresses acting on the inner core of the specimen are capable of activating the preexisting microcracks, always present in the bulk of concrete due to bleeding, shrinkage, etc. A wide spectrum of models for the tension-induced damage could be found in the available literature (e.g. Chapter 3 of this thesis; also Krajcinovic, 1989). However, in order to keep the present model tractable, elastic-perfectly brittle behavior will be assumed in tension. Incorporation of any model of tension-induced damage poses no serious problem to the present modeling algorithm and is only a matter of computational complexity.

In the pre-critical range ($\sigma < \sigma_{ut}$, $\varepsilon < \varepsilon_{ut}$), the axial expansion can be computed from formula (6.50) after solving the diffusion-reaction equation (6.14). Combining (6.50) with (6.32), (6.39)–(6.41), (6.47), and (6.53) leads to the following formula for strain (Krajcinovic, Basista, Mallick and Sumarac, 1992):

$$\varepsilon(\tilde{x}{=}0) = \frac{v_a(d-1)\,c_0}{3E(0,\tilde{t})} \int_0^1 E(\tilde{x},\tilde{t})\,\tilde{c}^R(\tilde{x},\tilde{t})\,\beta(\tilde{x},\tilde{t})\,\mathrm{d}\tilde{x}. \tag{6.54}$$

In the post-critical range ($\varepsilon > \varepsilon_{ut}$), the elastic solution (6.54) ceases to be valid. The simplest approach to determine the expansion in that range would consist in assuming that the stresses vanish after the tensile stresses reach the critical value σ_{ut} , i.e. when the macrocracks appear. Therefore, the expansion of the specimen is equal to the volume average of the unconstrained expansions of the ettringite crystals in the heavily damaged matrix (Krajcinovic, Basista, Mallick and Sumarac, 1992):

$$\varepsilon(\tilde{x}{=}0) = f^I \varepsilon^{**} = \frac{1}{3} c_F^R (d-1) v_a \,, \tag{6.55}$$

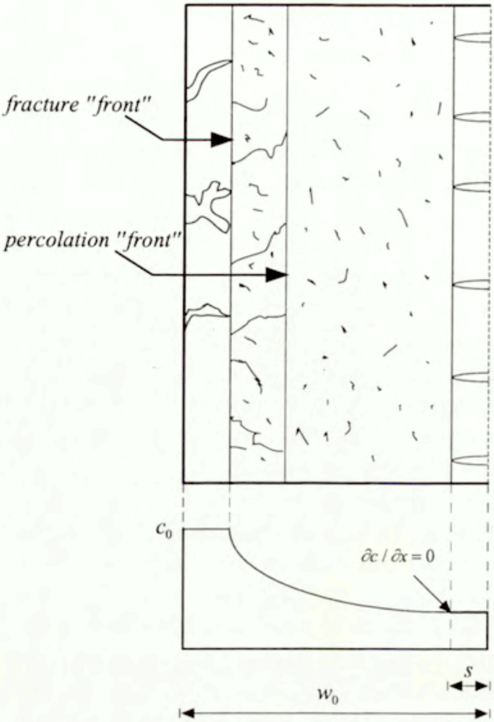

Figure 6.5. Schematic picture of damage evolution due to sulphate attack in mortar specimen.

where c_F^R is the moles of sulphate per unit volume used to produce ettringite in the fractured zone s (Figure 6.5). The total axial strain in the specimen (strain-controlled case) is obtained by superimposing (6.54) and (6.55). It should be stressed that the appearance of macrocracks in the tensile zone changes the boundary condition $(6.45)_3$ as follows (Krajcinovic, Basista, Mallick and Sumarac, 1992)

$$\frac{\partial \tilde{c}}{\partial \tilde{x}} = 0 \quad \text{at} \quad \tilde{x} = \pm(1 - \tilde{s}) \quad \text{for} \quad t > t_{cr}\,, \tag{6.56}$$

where $\tilde{s} = s/w_0$ (Figure 6.5) and t_{cr} denotes the time at which the macrocracks appear.

With gradual increase in the microcrack density, the elastic modulus (6.51) decreases. At one point, the elastic modulus may vanish, i.e. the material becomes damaged to the extent that it loses its load-carrying capacity and disintegrates into separate fragments. Consistent with the assumption that local stresses around expanding inclusions are dominant, the zone in which the material gets fragmented is contiguous to the external surface (Figure 6.5). Such a behavior (spalling[1]) is commonly observed in structural elements exposed to aggressive waters (e.g. Biczok, 1972). Spalling is modeled by introducing a fracture front (cf. Kachanov, 1986) separating the heavily damaged (spalled) zone from the material which can still carry the loads. The fracture front is preceded by a percolation front, i.e. a surface behind which the microcracks form the first continuous paths. Formulation of rigorous criteria for the propagation of fracture and percolation fronts is a complicated task. For the present analysis, the position of the percolation front will be identified with the plane in which $\omega_c = 0.182$ (6.20), while the fracture front (elastic percolation) is identified by $\omega_{ec}^{SC} = \frac{9}{16}$, (6.51), when the secant elastic modulus vanishes.

The emergence of the percolation and/or the fracture front(s) has a dramatic impact on the effective diffusivity (6.22). In particular, in the volume behind the fracture front it was assumed that $D_{\mathit{eff}} \to \infty$ as ω approaches the critical value 9/16. Consequently, the concentration of sulphate in the zone swept by the fracture front has the constant value $c = c_0$.

Identification of parameters

The following numerical values of the material parameters have been used in the computations: diffusivity of undamaged mortar $D_0 = 0.75 \cdot 10^{-12}$ m^2/s (Biczok, 1972), accessible porosity of mortar $\phi = 0.1$, porosity of ettringite $\phi_e = 0.18$ (Pommersheim and Chang, 1988), initial concentration of sulphate $c_0 = 352$ mol/m^3, initial radius of C_3A particle $r_{a0} = 1$ μm (Plowman and Cabrera, 1984), mass fraction of gypsum added to Portland cement $f_g = 6\%$ (Pommersheim and Chang, 1988). The parameter d defined in (6.4) equals 9.96.

Lacking precise experimental data, reasonable values have been assigned to the remaining parameters: Young's modulus of mortar $E_0 = 13$ GPa, Young's modulus of ettringite $E_e = E_0/5$, Poisson's ratio of mortar $\nu_0 = 0.3$,

---

[1] not to be confused with dynamic spalling

Poisson's ratio of ettringite $\nu_e = 0.2$, ultimate compressive stress of mortar $\sigma_{uc} = 40$ MPa, fracture toughness of mortar $K_{Ic} = 0.2\ \mathrm{MN/m^{3/2}}$.

The estimate of the rate constant k in the kinetic equation (6.13) is based on the premise that no substantial degradation of mortar occurs in specimens with C_3A content less than 5.5%. Therefore, the specimen with 4.3% C_3A in Ouyang et al. (1988), Figure 6.6, has been used for this purpose leading to $k = 1.35 \cdot 10^{-5}\ \mathrm{m^3/mol/s}$.

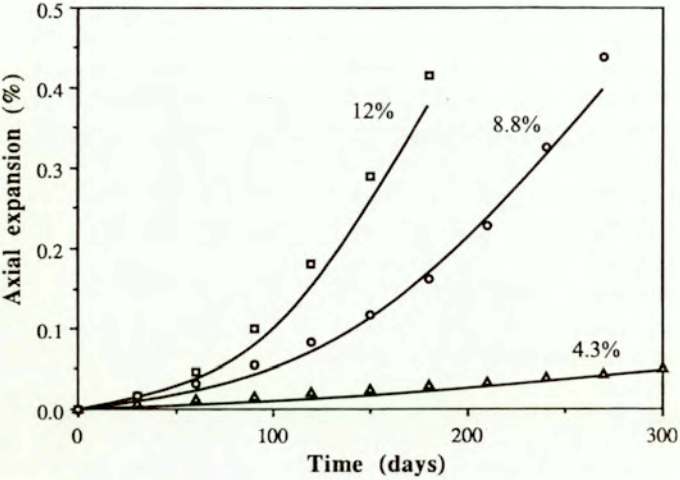

Figure 6.6. Axial expansion of mortar test bars due to external sulphate attack for different C_3A contents (solid lines) vs. experimental data (symbols) of Ouyang et al. (1988).

Results of computations

The graph depicted in Figure 6.6. represents the actual objective of this chapter, i.e. a test of the ability of the proposed model to relate the macrostructural expansion to the chemical composition of the mortar. The experimental results of Ouyang et al. (1988) are reproduced with satisfactory accuracy. The model clearly distinguishes between mortars with a small concentration of tricalcium aluminate and those rich in tricalcium aluminate which disintegrate when subjected to water-borne sulphates for a prolonged time. The mortar expansions for 8.8% and 12% of C_3A consist of two regimes: pre-critical (6.54) and post-critical (6.55). The transition takes place after 120 and 90 days, respectively. It is worth emphasizing that the approximation used to estimate the strains in the post-critical regime yields good results. The actual diffusion process in the experiment conducted by Ouyang et al. (1988) is three-dimensional. Therefore, the one-dimensional analysis carried out here for computational simplicity should be viewed as a lower bound for the expansions of mortar specimens.

Figure 6.7 illustrates the effect of damage accumulation on the profile of sulphate concentration within the specimen. The first (upper) plateau in the curve $t = 240$ days results form the fracture front attributed to severe sulphate corrosion. The second (lower) plateau occurs due to stress-induced tensile fracture in the middle portion of the specimen.

The variation of stresses and elastic modulus along the specimen cross section is depicted in Figure 6.8a,b for the case of 4.3% C_3A content. In this particular case the ultimate rupture strain has not been reached. The Young modulus undergoes a negligible reduction in magnitude as expected for sulphate-resistant mortars.

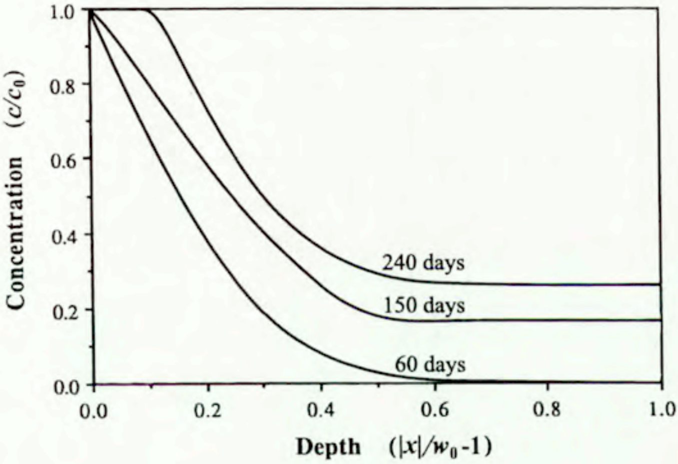

Figure 6.7. Concentration profiles within specimen containing 8.8% C_3A.

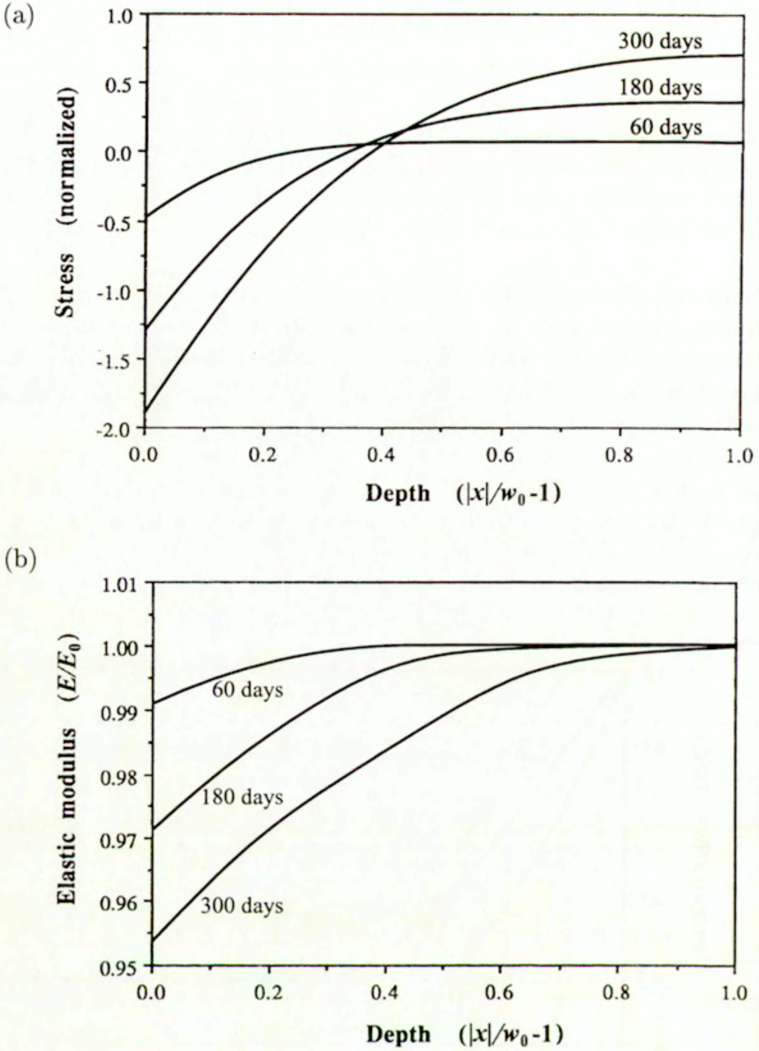

Figure 6.8. (a) Distribution of normalized stress σ/σ_{ut} along specimen thickness (4.3% C_3A); (b) Reduction of normalized Young's modulus (4.3% C_3A).

6.8. Summary and conclusions

The principal objective of the proposed model was to establish a direct relation between the chemical composition of the solid-ambient system and its response and/or durability. This objective has been reached by formulating an initial boundary value problem for the spatial and temporal degradation of a mortar prismatic bar exposed to external sulphate attack. The initial boundary-value problem couples unsteady diffusion, chemical reaction, and mechanical response. The coupling is both direct (i.e. sink term in the diffusion equation) and indirect through the transport properties (diffusivity and degrading stiffness). All material parameters, except for k, have been identified directly from the documented data. The rate constant of the chemical reaction k has been determined phenomenologically from the expansion of mortars with low concentration of C_3A. Once the parameter k had been determined by fitting the curve for the 4.3% concentration of C_3A, the formulated model has been able to predict the response for the other concentrations with remarkable ease and satisfactory accuracy.

A string of simplifying assumptions has been introduced to enhance tractability of the model. Some of these simplifications are necessary in view of the random geometry on the microscale and paucity of specific experimental data. Each simplification is supported by a physically justifiable argument. If desired, most of these assumptions can be eliminated. However, an attendant increase in computational complexity is then to be expected.

One of the major advantages in micromechanical models is that they can readily be modified and extended to related problems. Various other chemical processes such as alkali-aggregate and cation exchange reactions, formation of calcium salts, carbonic acid attack, etc., causing degradation of concrete structures are just some of the examples that readily come to mind. Similarly, humidity, frost, and corrosion actions on metals belong to the same group of environment-assisted damage processes. In each particular case, the modeling strategy will be similar even though the details will change according to the dominant mechanism of microstructural changes.

In conclusion, the proposed model clearly shows that an ambitious task of combining physical and chemical processes and their influence on the microstructure of a solid and its macroresponse is well within our present reach. Further developments in this direction must, however, include an experimental program oriented at more precise determination of micromechanical material parameters.

Chapter 7

Phenomenological brittle damage model inspired by micromechanics

Abstract. This chapter suggests a phenomenological damage description for brittle response of solids. Motivated by the key works of Kestin and Rice (1970) and Rice (1971, 1975), where a general thermodynamic framework with internal variables is presented for modeling inelastic material behavior, the proposed model carries over those results to brittle deformation processes and combines them with the micromechanics of damage in rock-like materials. The inelastic change of the compliance is identified as the "macroflux" and the dyad $\frac{1}{2}(\boldsymbol{\sigma} \otimes \boldsymbol{\sigma})$, with $\boldsymbol{\sigma}$ being the macroscopic stress tensor, as the affinity. The choice of the flux is consistent with the original Kachanov (1958) damage model and is derivable from its micromechanical counterpart promoted in Budiansky and O'Connell (1976). It is shown that for microcracks obeying the requirement of local dependence, a macroscopic damage potential can be obtained superimposing all micropotentials for individual microcracks (Griffith condition for each microcrack) and that the macroflux is then derivable using the normality property. At the present stage of development, the examples of uniaxial tension and compression of concrete specimens are added merely as an illustration of the outlined theory.

7.1. Introductory remarks

Micromechanical models possess that remarkable ability of relating random and heterogeneous microstructure of a material to the macrobehavior of a specimen. As such, they are much in tune with current research interests being developed in applied mechanics and materials science, where bridging the scales is one of the most pursued topics. However, as for practical engineering applications, rigorous micromechanical analyses of inhomogeneous stress and strain fields for arbitrary 3D microcrack patterns including kinking, forking, crack arrests, crack clustering, etc. may turn out to be a formidable task despite the steadily increasing computer power and more efficient numerical algorithms (cf. Basista, Krajcinovic and Sumarac, 1991, 1992). Consequently, it is not quite surprising that phenomenological damage models are not abandoned. To the contrary, phenomenological and micromechanical models coexist in the open literature or, what is more consequential in terms of modeling, the latter often serves as an inspiration for the former. The research effort in the field of phenomenological damage modeling is typical of any branch that is still under development: while older and more established models are being implemented numerically to solve particular initial boundary-value problems, new or improved models are still appearing, although at much lower pace than in the seventies or the eighties. More elaborate discussions on the phenomenological damage models can be found, for example, in Kachanov (1986), Lemaitre and Chaboche (1985), Lemaitre (1996), Litewka (1985), Litewka and Hult (1989), Talreja (1985), Najar (1987), Kachanov jr. (1992, 1993), Sobczyk and Spencer (1992), Woo and Li (1993), Krajcinovic (1996), Murakami (1988), Murakami and Kamiya (1997), Murakami et al. (1998), Skrzypek and Ganczarski (1999), Skrzypek et al. (1999), Chaboche (1999), Doliński (1999), Seweryn and Mróz (1995), Mróz and Seweryn (1999), or in some earlier works by Murzewski (1957, 1992) and Eimer (1978).

The purpose of this chapter is to show in a systematic manner how a workable phenomenological damage model for brittle solids can be derived, and how the micromechanics of the underlying microcracking processes can be helpful in its construction. The attention will be restricted to open microcracks and perfectly brittle deformations. During ductile deformations other energy dissipating mechanisms must be included as well. Also, frictional losses associated with the sliding of rough microcrack surfaces over each other may be essential when a brittle material is exposed to compressive tractions (cf. Chapter 4). At this point, however, it seems reasonable to start with a simple model for brittle response during which the energy lost on friction can be neglected in comparison with the energy needed for microcrack growth. Consistently with the preceding chapters, it will be assumed that during a homogeneous deformation a solid passes through continuous sequence of the constrained equilibrium states.

7.2. Thermodynamic considerations

Consider again the macrobehavior of the RVE of a rock-like material undergoing infinitesimal strains in the course of a perfectly brittle (no plastic strains) and isothermal deformation process. According to Rice (1975, 1978), the irreversible change in the Gibbs energy associated with the advance of open microcracks (without forking or branching) within the RVE is equal to the work done on the separation of the adjacent layers of atoms minus the gain in the surface energy of the newly created internal surfaces:

$$\begin{aligned} \mathrm{d}^i\Psi &= \Psi(\boldsymbol{\sigma}, H + \mathrm{d}H) - \Psi(\boldsymbol{\sigma}, H) \\ &= \sum_n \int_{L_n} [(G - 2\gamma)\,\mathrm{d}l]\,\mathrm{d}L = \sum_n f_n\,\mathrm{d}\xi_n\,. \end{aligned} \tag{7.1}$$

Here, the notation follows that of Chapter 4, i.e. $\boldsymbol{\sigma}$ is the macroscopic stress tensor, H is the history recording parameter, G is the elastic energy release rate, γ is the surface energy, $\mathrm{d}l(L)$ is the local advance of a point on the crack front L in the direction of its outward normal, f_n are the generalized thermodynamic forces conjugated to the incremental internal variables $\mathrm{d}\xi_n$. The summation in (7.1) extends over $n = 1, \ldots, N$ microcracks that are active.

In Rice's (1978) theory, the term $G - 2\gamma$ is the thermodynamic force consisting of the driving component G (energy which must be delivered to the crack tip to trigger crack growth) and the resistive component 2γ. In his derivation of (7.1), it has explicitly been admitted that crack growth may be a reversible process, hence crack healing is not excluded by thermodynamics. Indeed, from the condition of non-negative entropy production rate (II law of thermodynamics), it can be shown that $(G - 2\gamma)\dot{l} \geq 0$.[1] This inequality requires that for the onset of crack extension ($\dot{l} > 0$) it must hold $G - 2\gamma \geq 0$. On the other hand, for $G - 2\gamma < 0$ the crack healing ($\dot{l} < 0$) may follow from this inequality. Leaving aside the crack healing problem, it seems that the most interesting result of Rice's (1978) thermodynamic analysis is that the Griffith criterion for crack growth (i.e. $G \geq 2\gamma$) is just a direct consequence of the II law.

In real rock-like materials, the microcracking process can hardly be considered reversible, thus the surface energy 2γ should be viewed as an unrecoverable energy. In these circumstances, it is necessary to reexamine the problem of the thermodynamic force conjugated to l. Intuitively, it is not difficult to infer that the thermodynamic force in question will simply be G. Nevertheless, a systematic thermodynamic verification of this conjecture seems advisable. The derivation to be presented below follows the general lines and notation of Rice (1978), the main difference being that γ is not a part of the Helmholtz free energy but is dissipated as the crack extends.

---

[1] plane strain is assumed for simplicity

Let a crack of the length $2l$ grow quasi-statically under the action of external forces in a linear-elastic, homogeneous material in plain strain at constant temperature. From the I law of thermodynamics, expressed for a quasi-static process, we have

$$\dot{Q} + \dot{W} = \dot{U}, \tag{7.2}$$

where Q is the heat adsorbed by the solid from a heat reservoir, $W = \int P\,\mathrm{d}\Delta$ is the work of applied forces P on the load-point displacements Δ, $U = U(\Delta, l, T)$ is the internal energy; all energy terms in (7.2) and on are expressed per unit thickness of the solid. As in Rice (1978), the crack length l is regarded as an internal state variable.

The II law of thermodynamics requires that

$$\dot{S} = \Lambda + \frac{\dot{Q}}{T}, \qquad \Lambda \geq 0 \tag{7.3}$$

where $S(\Delta, l, T)$ is the entropy, T is the (absolute) temperature, Λ is the entropy production rate; for reversible processes, $\Lambda = 0$. Combining (7.2) and (7.3) gives

$$T\Lambda = T\dot{S} - \dot{Q} = T\dot{S} + P\dot{\Delta} - \dot{U} \geq 0. \tag{7.4}$$

Introducing the Helmholtz free energy (per unit thickness) $\Phi(\Delta, l, T) = U - TS$, inequality (7.4) takes the form (at $\dot{T} = 0$)

$$T\Lambda = P\dot{\Delta} - \dot{\Phi}(\Delta, l, T) = P\dot{\Delta} - \frac{\partial \Phi}{\partial \Delta}\dot{\Delta} - \frac{\partial \Phi}{\partial l}\dot{l} \geq 0. \tag{7.5}$$

In contrast to Equation (12) in Rice (1978), assume as acknowledged above that $2\gamma l$ does not contribute to the free energy Φ. Therefore,

$$\Phi = W_e(\Delta, l), \tag{7.6}$$

where $W_e(\Delta, l)$ is the isothermal elastic strain energy having the following properties

$$\left.\frac{\partial W_e(\Delta, l)}{\partial \Delta}\right|_{l\ \mathrm{fixed}} = P; \qquad -\left.\frac{\partial W_e(\Delta, l)}{\partial l}\right|_{\Delta\ \mathrm{fixed}} = G. \tag{7.7}$$

In view of (7.6) and (7.7), the entropy production rate (7.5) becomes

$$T\Lambda = G\dot{l} \geq 0. \tag{7.8}$$

Consequently, for brittle deformations in isothermal conditions with γ irreversibly spent on new surface creation, the generalized thermodynamic force conjugated to l is the elastic energy release rate G, as expected. Note that according to (7.8) crack healing ($\dot{l} < 0$) is now not permitted. This argument, addressed briefly in Basista and Gross (1998a), has been tacitly used in Chapter 4 when arriving at formulas (4.29)–(4.31). Also, the Griffith condition is not an intrinsic condition anymore deducible from the II law of thermodynamics, as it was the case for reversible γ in Rice (1978).

A similar problem has been considered in Neimitz (1999) for a more general case of elasto-plastic cracking materials. In his analysis, the energy is dissipated on the new surface creation as well as on plastic zone formation in the vicinity of the crack tip. Accordingly, the generalized thermodynamic force consists of two terms: one is responsible of all inelastic phenomena such as dislocation motion, voids and microcracks nucleation and growth occurring in the crack process zone, while the other one (shown to be G) is responsible for new surface creation.

It might be of some interest to establish a link between the incremental internal variables in (7.1) and the well known Walsh–Budiansky–O'Connell crack density parameter. For this purpose, consider the self-similar growth of a single circular microcrack of the radius l. From (7.1), the rate at which the Gibbs energy density $\psi = (1/V)\Psi$ is irreversibly changed due to the formation of a new free surface within the RVE can be expressed as (Basista, 1999)

$$\mathrm{d}^i\psi = \frac{1}{V}\int_L (G\,\mathrm{d}l)\,\mathrm{d}L = \frac{1}{V}\,G\,\mathrm{d}A = \frac{G}{l}\,\frac{2\pi\,l^2}{V}\,\mathrm{d}l = \frac{1}{V}\,f\,\mathrm{d}\xi, \qquad (7.9)$$

where $L = 2\pi l$ is the microcrack perimeter, $\mathrm{d}A = L\,\mathrm{d}l$ the increment of microcrack surface area. From (7.9) it follows that

$$f = \frac{G}{l} \qquad \text{and} \qquad \mathrm{d}\xi = 2\pi l^2 \mathrm{d}l. \qquad (7.10)$$

Consequently,

$$\mathrm{d}\omega \propto \frac{1}{V}\,\mathrm{d}\xi, \qquad (7.11)$$

where $\omega = \frac{1}{V}\,l^3$ is the familiar crack density parameter introduced by Bristow (1960) and then widely used, e.g. Walsh (1965), Budiansky and O'Connell (1976), etc.

On the macroscale, for the considered class of problems the Gibbs energy density allows decomposition (e.g. Krajcinovic, Basista and Sumarac, 1991a):

$$\psi(\boldsymbol{\sigma}, H) = \psi^0(\boldsymbol{\sigma}) + \Delta\psi(\boldsymbol{\sigma}, H) = \frac{1}{2}\boldsymbol{\sigma} : \mathbf{S}^0 : \boldsymbol{\sigma} + \frac{1}{2}\boldsymbol{\sigma} \, : \mathbf{S}^i : \boldsymbol{\sigma}, \tag{7.12}$$

where, consistently with the notation of (4.14), ψ^0 represents the elastic energy density of the intact homogeneous matrix, and $\Delta\psi$ a perturbation in the elastic energy density caused by the presence of microcracks within the RVE. Under the prescribed conditions (small stretching of the crystal lattice) both terms are homogeneous quadratic functions of macro (average) stresses. In (7.12), $\mathbf{S}^0$ denotes the compliance tensor of the matrix material and $\mathbf{S}^i$ the compliance attributable to the presence of microcracks. The expression for the strain can now be written as

$$\boldsymbol{\varepsilon} = \frac{\partial\psi}{\partial\boldsymbol{\sigma}} = (\mathbf{S}^0 + \mathbf{S}^i) : \boldsymbol{\sigma} = \mathbf{S} : \boldsymbol{\sigma}, \tag{7.13}$$

where $\mathbf{S}$ is the effective elastic compliance of the damaged material.

When the history recording parameter H changes, i.e. at least one of the microcracks grows in size ($\mathrm{d}l > 0$), the strain increment is (e.g. Basista, Krajcinovic and Sumarac, 1991)

$$\mathrm{d}\boldsymbol{\varepsilon} = \mathbf{S} \, : \mathrm{d}\boldsymbol{\sigma} + \mathrm{d}\mathbf{S}^i : \boldsymbol{\sigma} = \mathrm{d}^e\boldsymbol{\varepsilon} + \mathrm{d}^i\boldsymbol{\varepsilon}, \tag{7.14}$$

where, obviously, $\mathrm{d}\mathbf{S} = \mathrm{d}\mathbf{S}^i$ and the specific notation $\mathrm{d}^e\boldsymbol{\varepsilon}$ and $\mathrm{d}^i\boldsymbol{\varepsilon}$ follows that of Rice (1975). Explicitly, $\mathrm{d}^e\boldsymbol{\varepsilon} = \mathbf{S} : \mathrm{d}\boldsymbol{\sigma}$ denotes the elastic part of the strain increment representing the increase in strain due to the increase in stress, whereas $\mathrm{d}^i\boldsymbol{\varepsilon} = \mathrm{d}\mathbf{S}^i : \boldsymbol{\sigma}$ is the inelastic part of the strain increment (with plastic strains neglected) attributable to the change in compliance induced by the damage evolution. These two terms can symbolically be defined as

$$\begin{aligned} \mathrm{d}^e\boldsymbol{\varepsilon} &= \boldsymbol{\varepsilon}(\boldsymbol{\sigma} + \mathrm{d}\boldsymbol{\sigma}, H) - \boldsymbol{\varepsilon}(\boldsymbol{\sigma}, H), \\ \mathrm{d}^i\boldsymbol{\varepsilon} &= \boldsymbol{\varepsilon}(\boldsymbol{\sigma}, H + \mathrm{d}H) - \boldsymbol{\varepsilon}(\boldsymbol{\sigma}, H). \end{aligned} \tag{7.15}$$

In unloading ($\mathrm{d}H = 0$, i.e. all microcracks retain their accumulated size), the stress–strain relationship is linear. Consequently,

$$\mathrm{d}\boldsymbol{\varepsilon} = (\mathbf{S}^0 + \mathbf{S}^i) : \mathrm{d}\boldsymbol{\sigma} = \mathbf{S} : \mathrm{d}\boldsymbol{\sigma} = \mathrm{d}^e\boldsymbol{\varepsilon}, \tag{7.16}$$

such that the residual strain vanishes when $\boldsymbol{\sigma}$ is reduced to zero.

It should be noted that the total (effective) compliance in (7.13) depends on the already accumulated history. Hence, the initial and the unloading segments of the stress–strain curve will not be parallel if H changed during the deformation process. The slope of the initial segment of the loading curve is defined by $\mathbf{S}^0$ while the slope of the unloading segment by $(\mathbf{S}^0 + \mathbf{S}^i)$ reflecting the reduced stiffness of the solid attributed to the existing internal surfaces.

Alternatively to (7.9), $\mathrm{d}^i\psi$ can be written in terms of macroscopic variables as

$$\mathrm{d}^i\psi = \frac{1}{2}\boldsymbol{\sigma} : \mathrm{d}\mathbf{S} : \boldsymbol{\sigma} = \frac{1}{2}\boldsymbol{\sigma} : \mathrm{d}^i\boldsymbol{\varepsilon}. \tag{7.17}$$

Equating microscopic expression (7.9) for the density of energy needed to create an increment of a new surface with its macroscopic counterpart (7.17), gives

$$\frac{1}{V}\sum_n \int\limits_{L_n} (G\,\mathrm{d}l)\,\mathrm{d}L = \frac{1}{2}\boldsymbol{\sigma} : \mathrm{d}\mathbf{S} : \boldsymbol{\sigma}. \tag{7.18}$$

According to linear elastic fracture mechanics, the local representation for G can be given as a homogeneous function of the second order in the crack-tip stress intensity factors, thus as a quadratic function in the macroscopic homogeneous stress $\boldsymbol{\sigma}$. Hence, the following identity is always valid

$$\boldsymbol{\sigma} : \frac{\partial^2 G}{\partial\boldsymbol{\sigma}\,\partial\boldsymbol{\sigma}} : \boldsymbol{\sigma} = 2G(\boldsymbol{\sigma}, H). \tag{7.19}$$

Combining the two preceding equations leads to (Basista, 1999)

$$\boldsymbol{\sigma} : \mathrm{d}\mathbf{S} : \boldsymbol{\sigma} = \frac{1}{V}\sum_n \int\limits_{L_n} \left(\boldsymbol{\sigma} : \frac{\partial^2 G}{\partial\boldsymbol{\sigma}\,\partial\boldsymbol{\sigma}} : \boldsymbol{\sigma}\,\mathrm{d}l\right)\,\mathrm{d}L. \tag{7.20}$$

Consequently, it follows from (7.20) (see also Rice, 1975) that

$$\mathrm{d}\mathbf{S} = \frac{1}{V}\sum_n \int_{L_n} \left(\frac{\partial^2 G}{\partial\boldsymbol{\sigma}\,\partial\boldsymbol{\sigma}}\,\mathrm{d}l\right)\mathrm{d}L. \tag{7.21}$$

Similarly,

$$\mathrm{d}^i\boldsymbol{\varepsilon} = \frac{1}{V}\sum_n \int_{L_n} \left(\frac{\partial G}{\partial\boldsymbol{\sigma}}\,\mathrm{d}l\right)\mathrm{d}L. \tag{7.22}$$

Conceptually rigorous, these formulas are computationally efficient only for simple microcrack patterns and geometries for which the respective stress intensity factors (i.e. G) are available. For example, the components of the compliance tensor can be determined from (7.21) for penny-shaped microcracks in isotropic or transversely isotropic solids or for rectilinear slits in general anisotropic plates (Sumarac and Krajcinovic, 1987). Obviously, the expressions for the SIFs for an ensemble of N interacting microcracks of arbitrary shape, orientation and position within the RVE cannot in general be determined in analytical form. Moreover, the advance of the microcrack front $\mathrm{d}l(L)$ is a complex function of the coordinates along the microcrack perimeter L depending on the local stresses and the matrix microstructure. This state may be even more exacerbated by the change of microcrack status from passive to active and vice versa, as the loads are incremented and the history recorded.

The presented derivation of expressions (7.21) and (7.22) is based on energy considerations. Dual to this is the derivation employing the Eshelby inclusion method (e.g. Mura, 1987) and the ensuing expressions for eigenstrains. This approach in conjunction with the effective continua and effective field techniques has been used by many authors in the past when determining the effective elastic properties of solids with microdefects, e.g. Vavakin and Salganik (1973), Budiansky–O'Connell (1976), Cleary et al. (1980), Horii and Nemat-Nasser (1983), Mura (1987), Krajcinovic and Sumarac (1987), Christensen (1990), Benveniste et al. (1991), Ju (1991). Detailed accounts of these methods with applications to practical crack problems can be found in the books by Nemat-Nasser and Hori (1993), Kachanov (1993), Krajcinovic (1996).

7.3. "Macrofluxes" and affinities

One of the crucial issues when constructing a phenomenological damage model is the selection of macrofluxes and their affinities. Not infrequently, this task is accomplished in a fairly arbitrary manner without any reference to the underlying physics. Needless to say, the chances for ultimate success of a phenomenological model are significantly enhanced if the macrovariables are in some way derivable from their microscopic counterparts. The transition from the micro- to macroresponse is often referred to as homogenization, even though in a great majority of cases it involves just the volume (or area) averaging. From the practical standpoint, it is important to describe irreversible changes of the thermodynamic state by a minimum of macrofluxes which represent the average of micromechanical fluxes taken over the RVE on the observed material point.

The density of energy dissipated on damage growth can formally be expressed as

$$\mathrm{d}^i\psi = \mathbf{Q} \cdot \mathrm{d}\mathbf{q}, \tag{7.23}$$

where $\mathbf{Q}$ and $\mathrm{d}\mathbf{q}$ are the conjugated affinities and macrofluxes. Hence, comparing (7.23) and (7.17), the affinities and the macrofluxes can be selected as in Krajcinovic, Basista and Sumarac (1991a)

$$\mathbf{Q} = \frac{1}{2}(\boldsymbol{\sigma} \otimes \boldsymbol{\sigma}), \qquad \mathrm{d}\mathbf{q} = \mathrm{d}\mathbf{S}. \tag{7.24}$$

The change of the compliance is readily measurable locally, satisfying one of the principal requirements for the selection of internal variables. Moreover, the rate of change of the compliance is related to the rate of loss of primary bonds in the solid. Thus, since the area of microcracks is obviously related to the number of ruptured bonds in the material, it seems reasonable to measure the increase in the microcrack density by the change in the compliance. This is consistent with the original Kachanov damage model (Kachanov, 1958; Lemaitre and Chaboche, 1985) and is in tune with the work of Ortiz (1985) where the damage variable was defined directly as the elastic compliance tensor itself. Due to unilateral constraints placed on the displacement field by the microcracks, it is feasible to identify only the positive change of the compliance as the macroflux. If the state of stress changes in unloading from tension to compression, the compliance can decrease stepwise without any loss of energy to its original undamaged magnitude. In other words, tension-induced damage may not be felt by the material when stressed in compression.

7.4. Kinetics of damage growth

Having defined the macrofluxes and conjugated thermodynamic forces, the next step consists in specification of the kinetic law. The selection of a computationally efficient and physically justifiable kinetic law relating fluxes and affinities is a sensitive aspect of any model. In general, there are but two alternatives. It is either necessary to prescribe evolution laws for every flux independently or to introduce a flow (damage) potential from which the fluxes are derivable. In the past both methods have been used rather arbitrarily in order to replicate a limited set of experimental data. While the first approach was favored by many authors in the past (see Krajcinovic, 1984), the latter seems to be more promising in view of the fact that the fourth rank tensor $(7.24)_2$ has many components. The objective of this section is to derive the damage macropotential from the micropotentials and to ascertain conditions under which this transition is both feasible and justifiable. The present analysis follows the general theoretical framework for inelastic constitutive relations (Rice, 1971, 1975) while specifying it for brittle damage with the fluxes and affinities defined as in (7.24).

The total increment of the Gibbs energy density associated with the transition from one equilibrium state $(\boldsymbol{\sigma}, H)$ to a neighboring equilibrium state $(\boldsymbol{\sigma} + \mathrm{d}\boldsymbol{\sigma},\ H + \mathrm{d}H)$ is

$$d\psi = \mathbf{S} : \mathrm{d}\mathbf{Q} + \frac{1}{V_0} \sum_n f_n \mathrm{d}\xi_n \,, \tag{7.25}$$

where $\mathbf{S} : \mathrm{d}\mathbf{Q} = \boldsymbol{\varepsilon} : \mathrm{d}\boldsymbol{\sigma}$ is the work increment of surface forces, while the second term embodies the work increments on the internal variables. From (7.25) it follows that

$$\mathbf{S} = \left.\frac{\partial \psi}{\partial \mathbf{Q}}\right|_{\xi=\mathrm{const}} \qquad \text{and} \qquad f_n = V_0 \left.\frac{\partial \psi}{\partial \xi_n}\right|_{\sigma=const} . \tag{7.26}$$

Equating cross derivatives of (7.26) gives

$$\frac{\partial \mathbf{S}}{\partial \xi_n} = \frac{1}{V_0} \frac{\partial f_n}{\partial \mathbf{Q}} \,, \tag{7.27}$$

which is an analog of the Maxwell relation in Rice (1971) expressed here in terms of the effective compliance tensor **S** and its affinity **Q**, (7.24). Consequently, the inelastic change in compliance is given by (Krajcinovic, Basista and Sumarac, 1991a)

$$\mathrm{d}^i\mathbf{S} = \sum_n \frac{\partial \mathbf{S}}{\partial \xi_n} \mathrm{d}\xi_n = \frac{1}{V_0} \sum_n \frac{\partial f_n}{\partial \mathbf{Q}} \mathrm{d}\xi_n \,. \tag{7.28}$$

Assume now that the property of local dependence (Kestin and Rice, 1970) holds. In the present context it means that the rate of change of the surface area of a particular microcrack $\dot{\xi}_n$ depends on the macroscopic stresses σ_{ij} *only* through its own energy release rate f_n:

$$\dot{\xi}_n = \dot{\xi}_n(f_n, H). \tag{7.29}$$

Consequently, $\sum_n \dot{\xi}_n(f_n, H)\,\mathrm{d}f_n$ is trivially an exact differential of a scalar function $\tilde{\Omega}(f_n, H)$ since each term in the sum involves only one variable (Kestin and Rice, 1970). Taking the volume average of $\tilde{\Omega}$, and recognizing that f_n are quadratic functions of the macroscopic stress, we have (cf. Rice, 1971)

$$\Omega(\mathbf{Q}, H) = \frac{1}{V_0}\,\tilde{\Omega} = \frac{1}{V_0}\sum_n \int_0^{f_n(\mathbf{Q},H)} \dot{\xi}_n(f_n, H)\,\mathrm{d}f_n\,, \tag{7.30}$$

where integration is performed at fixed H. Differentiating Ω with respect to the macroaffinity yields

$$\frac{\partial\Omega}{\partial\mathbf{Q}} = \frac{1}{V_0}\sum_n \dot{\xi}_n\,\frac{\partial f_n}{\partial\mathbf{Q}}\,. \tag{7.31}$$

Comparing (7.31) and (7.28) it follows that $\Omega(\mathbf{Q}, H)$ is a damage potential from which the flux $\dot{\mathbf{S}}$ (rate of change of compliance) can be determined as (Krajcinovic, Basista and Sumarac, 1991a)

$$\dot{\mathbf{S}} = \frac{\partial\Omega(\mathbf{Q}, H)}{\partial\mathbf{Q}}\,. \tag{7.32}$$

Finally, the strain rates can be computed from the rate analog of (7.14).

Remarkably, the considered class of microcrack growth equations (7.29) implies a normality structure for macroscopic constitutive damage models. Moreover, it can be seen from (7.30) that the macroscopic damage potential $\Omega(\mathbf{Q}, H)$ is just the volume average of micropotentials for each microcrack within the RVE if the local kinetic relations of the type (7.29) are known. Also, it is important to notice that the macroscopic potential (7.30) has been derived here from the micropotentials rather than a priori postulated as was often the case in the literature. However, as admitted by Rice (1971), kinetic equations (7.29) are pertinent to a specific class of inelastic processes. The macropotential may exist for a wider class of kinetic relations provided that the micropotentials exist (Raniecki, 2001). The damage potential (7.30) and the normality rule (7.32) do not hold when the microcrack growth is dependent directly on the macroscopic stress. This happens, for example, in compression where the energy losses associated with frictional sliding are included. On the other hand, the existence of the damage potential (7.30) and the attendant normality property (7.32) seems to be valid for interacting microcracks too, as long as they remain open. The influence of other microcracks on the growth of a particular microcrack is reflected in the expression for G for that microcrack and ξs for all other microcracks (Rice, 1971). The expression for G may be very complex or even unavailable in closed analytical form. Nevertheless, it is still G, i.e. the thermodynamic force for that microcrack, that governs its growth. Hence, the basic prerequisite for the normality rule is satisfied. It cannot be ruled out, though, that due to interaction effects open microcracks may close and then slide with friction. Also, when microcracks start to form main clusters, the existence of the RVE may become questionable and the proposed framework may become inappropriate. In conclusion, it will be prudent enough to state that the macropotential exists for open microcracks at modest microcrack densities (cf. assumptions in effective-media approximations).

In order to establish links with the original derivation in Rice (1971, 1975), the above considerations have been carried out within the general formalism for time-dependent inelastic behavior. The actual concern of this chapter is with time-independent behavior. As such, brittle deformation of damaged elastic solids may be considered as a limiting case of the above formulation. Thus, normality of the rate $\dot{\mathbf{S}}$ to the flow potential surfaces (7.32) reduces now to normality of the inelastic increments of compliance $\mathrm{d}^i\mathbf{S}$ to the current damage surface provided that the constraints imposed on the microcrack kinetics (7.29) are satisfied.

Alternatively, as remarked in Rice (1971), the time-independent behavior may be discussed directly rather than as a limiting case of the time dependent theory. To this end, the expression for inelastic strains involving the term $\partial\Omega/\partial\mathbf{Q}$ will be replaced by the fundamental micro-to-macro transition relation (4.6) where it is assumed that the stress state during inelastic deformation must lie on the damage surface. The kinetic equations for the internal microstructural variables are then derivable from the consistency relations. In fact, this approach has effectively been used in Chapter 4 to formulate a micromechanical damage model of brittle deformation in compression.

According to (7.30) the macropotential can be derived as the volume average of micropotentials (Griffith criterion for each individual microcrack) within the RVE. The completion of this task presumes that a large databank defining the microcrack morphology is available and is, in general, contingent on a string of simplifying assumptions. Consequently, a substantial computational effort is required to determine the macropotential rigorously. For purely practical purposes, a simpler expression is often desirable to facilitate large scale computations typical of engineering applications. The balance of this section will be devoted to a simple formulation of damage surface and its kinetics in tension and compression with the respective micromechanics used as a general guidance.

7.5. Damage surface

The damage surface is understood herein as a piece-wise smooth, simply connected and convex surface enveloping the locus of all points in the space of affinities which can be reached without change in the recorded history. The notion of the damage surface has been used before by many authors, among others Dougill (1976), Dragon and Mróz (1979), Krajcinovic and Fonseka (1981), Yazdani and Schreyer (1988), Lubarda and Krajcinovic (1995). The existence of the damage surface is not only the matter of conjecture. Experimental identification of the damage surface was, indeed, accomplished by Holcomb (1983) and Holcomb and Costin (1986) using the acoustic emission technique. The conventional concepts of loading and unloading (central to the use of damage surface) were further corroborated by Holcomb and Costin (1986) by measuring the so-called Kaiser effect. According to Kaiser (1950), in any loading process that followed unloading no acoustic emissions occurred until the damage surface was again reached. Owing to the unilateral nature of the constraints imposed by a microcrack on the displacement field, it is reasonable to consider tension and compression independently. Also, at this stage of development it seems justified to restrict considerations to two-dimensional problems.

The macrofluxes are determined as in classical plasticity using the normality property (e.g. Martin, 1975):

$$\dot{q}_i = B(\mathbf{Q}, H)\,\frac{\partial\Omega}{\partial Q_i}\,\frac{\partial\Omega}{\partial Q_j}\,\dot{Q}_j\,, \tag{7.33}$$

where

$$B = -\left(\frac{\partial\Omega}{\partial q_k}\,\frac{\partial\Omega}{\partial Q_k}\right)^{-1} \tag{7.34}$$

is a non-negative scalar-valued hardening parameter. Expressions (7.33) and (7.34) imply that the flux is codirectional with the outer normal to the damage surface at the loading point. In the case when the frictional losses of energy become significant, the normality rule is typically relaxed (Rudnicki and Rice, 1975). Merely for completeness, we recall the definitions of loading and unloading. The flux is nonzero only if the loading point is on the damage surface and heading out:

$$\Omega = 0 \qquad \text{and} \qquad \frac{\partial \Omega}{\partial Q_j}\,\dot{Q}_j > 0. \tag{7.35}$$

In contrast, the flux vanishes (history is not recorded) if the loading point is either within the damage surface, or on the damage surface but heading inwards:

$$\begin{aligned} &\Omega < 0 \qquad \text{or} \\ &\Omega = 0 \qquad \text{and} \qquad \frac{\partial \Omega}{\partial Q_j}\,\dot{Q}_j < 0. \end{aligned} \tag{7.36}$$

The convexity property and the vertex problem can be analyzed analogously as in the classical theory of plasticity (for details see Rice, 1975).

(A) TENSION

Consider a single rectilinear slit of length $2l_0$ embedded in an infinite, homogeneous and isotropic elastic plate (Figure 7.1). The Griffith criterion can in this case be written in the form

$$\frac{\pi l_0}{E_0}(\sigma_1^2 \cos^2\theta + \sigma_2^2 \sin^2\theta) - 2\gamma = 0. \tag{7.37}$$

Geometrically, this condition is represented by a family of straight lines in the space of affinities $Q_1 = \frac{1}{2}\sigma_1^2$, $Q_2 = \frac{1}{2}\sigma_2^2$ with the angle θ and the microcrack length $2l_0$ considered as parameters (Krajcinovic, Basista and Sumarac, 1991a). Assuming for simplicity that all slits contained in the RVE are of equal length $2l_0$, and that θ is a random parameter, the conditions (7.37) form a fan of straight lines centered in the isotropic point $Q_1 = Q_2$ (Figure 7.2).

For an arbitrary stress path, the first microcrack to become critical is the one that is perpendicular to the larger of the two principal stresses. The magnitude of the other principal stress has no influence on the onset of the nonlinear behavior but can, obviously, become important as the external

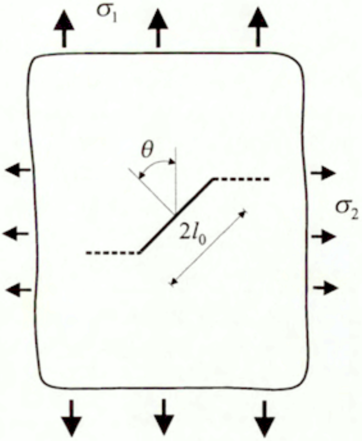

Figure 7.1. Single microcrack under biaxial tension $\sigma_1 > \sigma_2$.

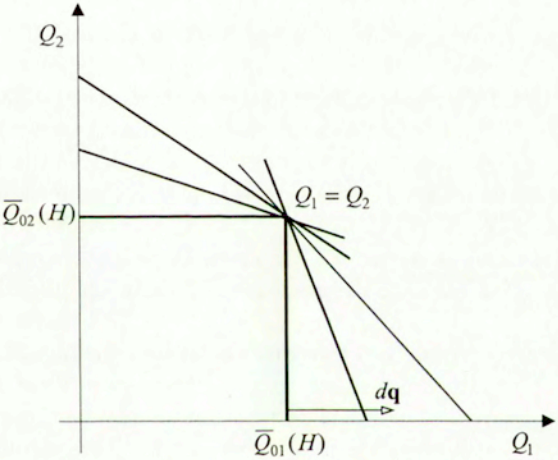

Figure 7.2. Damage surface for biaxial tension (Krajcinovic, Basista and Sumarac, 1991a).

tractions are further increased. The shear stress will play a corrective role kinking the slit in the direction normal to the larger of the two tensile stresses (dashed lines in Figure 7.1), Lawn and Wilshaw (1975).

Thus, in the case when $\sigma_1 > \sigma_2$ it seems justified to assume that, at least in the beginning, only $\mathrm{d}S_{1111} > 0$, while all other components of the compliance tensor remain unaltered. The point $Q_1 = Q_2$ corresponds to the isotropic damage evolution since the condition (7.37) is satisfied for all slits simultaneously. Consequently, for biaxial tension it seems reasonable to assume, as a simplest solution, a damage surface consisting of two perpendicular straight lines intersecting at the isotropic point (Krajcinovic, Basista and Sumarac, 1991a):

$$\begin{aligned} \Omega_1(Q_1\,,\,H) &= Q_1 - \bar{Q}_{01}(H) = 0, \\ \Omega_2(Q_2\,,\,H) &= Q_2 - \bar{Q}_{02}(H) = 0. \end{aligned} \tag{7.38}$$

The initial position of the two lines (7.38) comprising the damage surface represents the inner envelope of the family of straight lines defined by (7.37), Figure 7.2. In (7.38), the parameter $\bar{Q}_{0i}(H)$ characterizes the point at which the microcracking commences. It depends on the already accumulated history i.e. distribution, number and size of the existing slits in the RVE and is path dependent. In fact, owing to the unilateral nature of the constraints, the onset of microcracking depends on the sign of stresses as well.

Once the initial damage surface is determined as in (7.38), the fluxes (i.e. increments of the components of the compliance tensor) can be computed from (7.33). However, it is first necessary to define the kinetics of the damage surface, i.e. to specify the term $\bar{Q}_{0i}(H)$ characterizing the current position of the surface. This, in turn, makes it possible to compute the hardening parameter B from (7.34). From the Griffith condition $\mathrm{d}l > 0$ if $G - 2\gamma \geq 0$. Moreover, the crack propagates in an unstable (runaway) fashion if $\partial G/\partial l > 0$. Consequently, once a crack in a homogeneous tensile stress field becomes critical, its growth cannot be arrested. However, in the case of real brittle materials and microcracks the assumption of material homogeneity is not a realistic one. The internal energy barriers such as grain boundaries may arrest a sufficiently short crack. This situation is tacitly admitted when postulating existence of the R-curves. In other words, in real materials the growth of a single microcrack is a function of the energy release rate and the material structure. Experimental determination of the R-curves presents a nontrivial and often controversial enterprise. Even for well specified microcracks and the specimen geometry, the R-curve all too often tends to be a specimen rather than a material property. In the case of a solid weakened by a large number of interacting microcracks of various sizes, orientations and often irregular geometries, the evolution of damage is a very complex process. To determine the evolution of damage it is necessary to define the sequence in which the microcracks become unstable and the spatial distribution of the energy barriers within the volume (Krajcinovic and Sumarac, 1987; Sumarac and Krajcinovic, 1987). As it grows, a microcrack kinks along the path of minimum values of $\gamma(\mathbf{x})$ overcoming the sequence of successively higher energy barriers randomly distributed on its path. Hence, $\bar{Q}_0(\mathbf{q})$ must be a monotonically increasing function of stresses (similar to R-curve) satisfying the following conditions (Krajcinovic, Basista and Sumarac, 1991a)

$$\bar{Q}_0(q{=}0) = Q_0 = \frac{1}{2}\sigma_0^2\,, \tag{7.39}$$

and

$$\left.\frac{\mathrm{d}\bar{Q}_0}{\mathrm{d}q}\right|_{q=q_u} = 0, \tag{7.40}$$

where σ_0 is the stress level at the onset of nonlinear response. The condition (7.40) reflects the localization of damage (coalescence of neighboring microcracks into a macrocrack) assumed to occur at the apex of the stress–strain curve. This condition is derivable from (7.13) when expressed in the space of affinities ($2Q = \sigma^2$), and upon setting $(\mathrm{d}\sigma/\mathrm{d}\varepsilon) = 0$. Guided by the experimental evidence from carefully conducted strain-controlled tests (Evans and Marathe, 1968; Brühwiler et al., 1986), it is assumed that for brittle materials rounded peaks in the stress–strain curves emerge both in compression and tension alike (cf. Chapter 3). Note that the effective secant compliance remains finite at the onset of localization.

Using the conditions (7.39) and (7.40), the position of the damage surface in the uniaxial tension ($\sigma_1 = \sigma > 0$, $\sigma_2 = 0$) can simply be written as

$$\bar{Q}_0(q) = Q_{0t} + \frac{Q_{ut} - Q_{0t}}{q_{ut}^2}\,(2q_{ut} - q)q, \tag{7.41}$$

where $Q_{ut} = \frac{1}{2}\sigma_{ut}^2$ is the square of the direct tensile strength of the specimen. In order to reduce the number of material parameters, it will be assumed in the sequel that the ultimate stress exceeds the stress at the onset of microcracking by the factor of 2, i.e. $\sigma_{ut} = 2\sigma_{0t}$, which is reasonable for concrete. The proposed form of damage surface (7.38) in conjunction with (7.41) results in a damage evolution that is slow in the beginning and grows more rapidly as the incipient failure stress is approached.

Once the damage surface is defined, the macroflux is readily determined from the expressions (7.33), (7.34) and (7.41) in the form

$$q = \left(\frac{\varepsilon_{ut}}{\sigma_{ut}} - \frac{1}{E_0}\right)\left(1 - \sqrt{\frac{\sigma_{ut}^2 - \sigma^2}{\sigma_{ut}^2 - \sigma_{0t}^2}}\right), \tag{7.42}$$

where ε_{ut} is the strain corresponding to the ultimate stress σ_{ut} . The final form of the axial stress–strain relation in the ascending part of the curve is then

$$\begin{aligned} \varepsilon &= \left(\frac{1}{E_0} + q\right)\sigma \\ &= \sigma\left[\frac{1}{E_0} + \left(\frac{\varepsilon_{ut}}{\sigma_{ut}} - \frac{1}{E_0}\right)\left(1 - \sqrt{\frac{\sigma_{ut}^2 - \sigma^2}{\sigma_{ut}^2 - \sigma_{0t}^2}}\right)\tilde{H}(\sigma - \sigma_{0t})\right], \end{aligned} \tag{7.43}$$

where $\tilde{H}(\cdot)$ denotes the Heaviside function. All other components of the strain and compliance tensor remain unaffected. In the case of biaxial tension the damage evolution in two principal directions is uncoupled and can, therefore, be computed in form of the expression (7.43). In Figure 7.3, the stress–strain relation (7.43) is plotted and compared with the experimental data of Brühwiler et al. (1986) measured on plain concrete specimens subjected to direct tension.

The damage model proposed in this subsection is based on the often revoked assumption that under tension microcracks develop perpendicularly to the maximum principal stress direction. As remarked in Section 3.4, this assumption was verified experimentally many times and is commonly accepted even for heterogeneous brittle solids like concrete and rocks. A direct consequence of it is that an initially isotropic specimen becomes anisotropic (transversely isotropic in the uniaxial case) as the deformation proceeds. In the uniaxial example (Figure 7.3) this is reflected by the decreasing axial stiffness of concrete specimen whereas the other elastic constants retain their

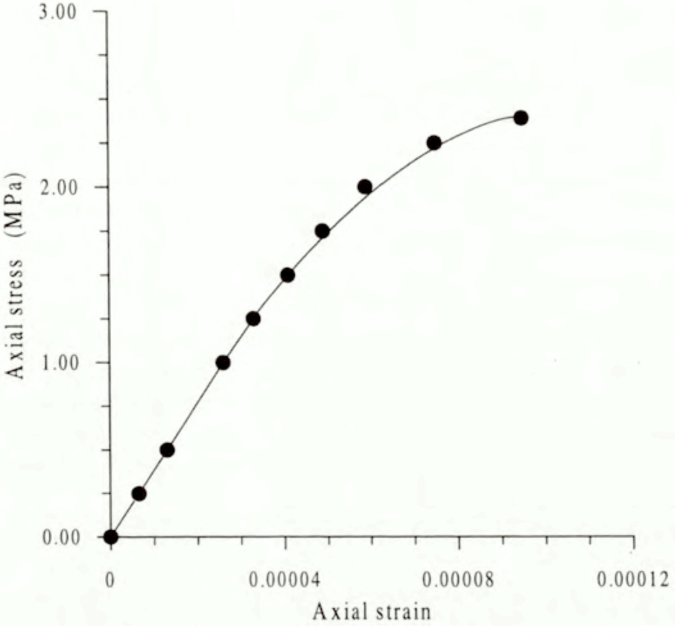

Figure 7.3. Uniaxial tension: theoretical stress–strain curve (7.43) vs. experimental data (dots) of Brühwiler et al. (1986) for plain concrete (Krajcinovic, Basista and Sumarac, 1991a).

original values. Recently, Murakami and Kamiya (1997) developed a phenomenological damage model for concrete incorporating the above experimental observation by means of a second-order damage tensor (Murakami and Ohno, 1981; Vakulenko and Kachanov, 1971; Kachanov, 1980). The curves depicted in Figure 5 in Murakami and Kamiya (1997) clearly show that only the axial component of the damage tensor experiences substantial growth while the lateral ones are practically negligible.

(B) COMPRESSION

The determination of the microcrack growth in a brittle specimen subjected to compression dominated stress field presents a more controversial issue. A popular model of damage evolution leading ultimately to splitting failure is that of sliding microcrack (cf. Chapter 4). This model suggests that the frictional sliding on the preexisting microcracks creates a wedging effect which in turn opens tension wing microcracks by kinking in the direction of maximum compression. A substantial computational effort is needed to determine the stress intensity factors of kinked microcracks. However, as has been mentioned in Chapter 4, numerous approximate expressions for the SIFs were suggested in the literature, among them the formulas by Horii and Nemat-Nasser (1986) which are relatively simple and accurate, and are well suited for the problem at hand. Since these results are used here only as a guidance, and since they are not very sensitive within the range ($30^\circ < \varphi < 60^\circ$), it seems appropriate to select a representative slit inclined at an angle $\varphi = 45^\circ$. Furthermore, ignoring finer details of the kinked path, it will be assumed that the wings are straight and parallel to the direction of maximum compression. More importantly, it will be assumed that the slanted microcrack (Figure 4.2) can be replaced by a Mode I straight microcrack parallel to σ_1 (cf. Figure 4.6b).

It should be kept in mind that considerations to follow are restricted only to brittle regime. Since the brittle-to-ductile transition (cf. Horii and Nemat-Nasser, 1986) is not included, the stress ratio σ_2/σ_1 will always be kept sufficiently small to avoid plastic flow near the tips of the preexisting flaws. The experiments on polycrystalline rock samples (Mogi, 1966) have shown that above the value of $\sigma_2/\sigma_1 \approx 0.2$ a change from brittle to ductile deformation is observed. Consequently, the present model will be confined to stress states for which $|\sigma_2| \ll |\sigma_1|$. Note that considerations of this subsection are merely intended as a plausible illustration of the proposed theory and should not be viewed as a complete phenomenological damage model for brittle materials under compression.

Introducing the above simplifications, the approximate expressions for SIFs (4.36) become (Basista, 1999)

$$K_I = \sigma_2' \sqrt{\pi l}, \qquad K_{II} = 0, \tag{7.44}$$

where

$$\sigma_2' = -\beta(l, c)\, \tau_{eff} + \sigma_2 \tag{7.45}$$

is the fictitious normal stress acting on the representative straight microcrack selected in such a manner that its energy release rate equals that of the actual kinked microcrack. The effective shear stress (4.26) acting on the preexisting slit (with $\varphi = 45°$ and $\tau_c = 0$) equals

$$2\tau_{\mathit{eff}} = (1-\mu)\sigma_1 - (1+\mu)\sigma_2\,. \tag{7.46}$$

The parameter $\beta(l, c)$ is derived to be

$$\beta(l,c) = \frac{\sqrt{2}}{\pi\sqrt{\tilde{l}(\tilde{l}+\tilde{l}^{*})}}\,, \tag{7.47}$$

where, as introduced in Chapter 4, $\tilde{l} = l/c$, $\tilde{l}^{*} = l^{*}/c$. The numerical value of the nucleus length $\tilde{l}^{*}$ can be estimated matching K_I at the kink initiation given by $(4.36)_1$ with the expression $K_I = \frac{3}{4}\sqrt{\pi c}\,\tau_{\mathit{eff}}\,(\sin\frac{\theta}{2} + \sin\frac{3\theta}{2})$ in Cotterell and Rice (1980). In the present case ($\theta = 45°$), it follows that $\tilde{l}^{*} = 0.21$. Obviously, the ratio β changes as the kinked part of the sliding microcrack grows. However, since the micromechanics of sliding microcrack is used here only as a guidance, it will be assumed that an average (constant) value of $\langle\beta\rangle$ be used in the sequel. Making use of expressions (7.44) to (7.47), the original problem of the sliding microcrack subjected to the actual macrostresses σ_1 and σ_2 is replaced by a problem of a representative Mode I microcrack subjected to the fictitious stress σ_2'. Consequently, using the transformation (7.45) the problem of a microcrack in the compression dominated field can be treated much in the same manner as a microcrack in a tensile field. The tensile fictitious stress σ_2' and the lateral compliance S_{22} are only of interest while all other components of $\mathbf{S}$ remain virtually unchanged. The inelastic part of an increment of the Gibbs energy is now given by

$$\mathrm{d}^i\psi = \frac{1}{2}(\sigma_2')^2\,\mathrm{d}S_{22}\,. \tag{7.48}$$

Moreover, it follows that

$$\mathrm{d}^i\boldsymbol{\varepsilon} = \mathrm{d}\mathbf{S} : \boldsymbol{\sigma}' \qquad \text{and} \qquad \mathbf{Q} = \frac{1}{2}(\boldsymbol{\sigma}' \otimes \boldsymbol{\sigma}') \tag{7.49}$$

instead of $(7.24)_1$. The damage surface can be then represented as

$$\begin{aligned}\Omega(\mathbf{Q}, H) &= Q_2 - \bar{Q}_0(H)\\ &= Q_2 - \left[Q_{0c} + \frac{Q_{uc} - Q_{0c}}{q_{uc}^2}\,(2q_{uc} - q_2)q_2\right] = 0\,,\end{aligned} \tag{7.50}$$

where $\mathbf{q} = \mathbf{S}^i$ and the subscripts $0c$, uc refer to the onset of wing growth and to the apex of the stress–strain curve, respectively.

In the uniaxial compression ($\sigma_1 = \sigma < 0$, $\sigma_2 = 0$), the fictitious stress (7.45) is given by

$$\sigma_2' = -\frac{1}{2}\langle\beta\rangle(1-\mu)\sigma \tag{7.51}$$

and the affinity $(7.49)_2$ reads

$$Q_2 = \frac{1}{4}\langle\beta\rangle^2(1-\mu)^2\sigma^2. \tag{7.52}$$

The inelastic component of the lateral compliance $q_2 = S_{22}^i$ is derived using the normality property (7.33), (7.34) in conjunction with (7.50). After simple integration, the final outcome reads

$$q_2 = q_{uc}\left(1 - \sqrt{1 - \frac{Q_2 - Q_{0c}}{Q_{uc} - Q_{0c}}}\right), \tag{7.53}$$

where

$$q_{uc} = \frac{\varepsilon_{uc}}{\sigma_{uc}} - \frac{1}{E_0}$$

is the inelastic component of S_{22} at the apex.

As mentioned above, using the transformation (7.45) a microcrack in the compressive field may equivalently be treated as subjected to the fictitious tensile stresses. Thus, it is reasonable to postulate that the affinities actually triggering the microcrack growth are the same in both cases, i.e.

$$Q_{0c} = Q_{0t} \qquad (\text{at} \;\; q = 0, \;\; \text{onset of kinking}). \tag{7.54}$$

In accordance with the experimental observations (e.g. Evans and Marathe, 1968), it is also assumed that $\sigma_{0t}/\sigma_{ut} = 0.5$, $\sigma_{0c}/\sigma_{uc} = 0.5$, $\mu = 0.5$ (typical of concrete). Consequently, from (7.54) and (7.52) it follows that

$$\frac{|\sigma_{uc}|}{\sigma_{ut}} = \frac{\sqrt{2}}{\langle\beta\rangle(1-\mu)}\,. \tag{7.55}$$

The compressive to tensile strength ratio attains the expected value for concrete $|\sigma_{uc}|/\sigma_{ut} \approx 10$ if the average length of the wing microcrack $\langle\tilde{l}\rangle$ computed from (7.55) and (7.47) equals 1.5. According to available data from the model experiments by Horii and Nemat-Nasser (1986) this value seems to be quite reasonable.

The stress–strain relations in the uniaxial compression are given by

$$\begin{aligned}
\varepsilon_1 &= \frac{\sigma}{E_0}\,, \\
\varepsilon_2 &= -\frac{\nu_0}{E_0}\,\sigma + q_2\sigma_2' \\
&= -\frac{\nu_0}{E_0}\,\sigma + \left(\frac{\varepsilon_{uc}}{\sigma_{uc}} - \frac{1}{E_0}\right)\left(1 - \sqrt{\frac{\sigma_{uc}^2 - \sigma^2}{\sigma_{uc}^2 - \sigma_{0c}^2}}\right)\bar{B}\sigma\,\tilde{H}(\sigma - \sigma_{0c}),
\end{aligned} \tag{7.56}$$

where $\bar{B} = \frac{1}{2}\langle\beta\rangle(1-\mu)$ is the material constant estimated to be $\bar{B} = 0.07$, and $\tilde{H}$ is the Heaviside function.

7.6. Summary and conclusions

The proposed framework for the development of a phenomenological damage model is consistent with the micromechanics of brittle deformation processes in addition to satisfying the requisite requirements of thermodynamics. The inelastic change of the compliance is identified as the macroflux and the dyad $\frac{1}{2}(\boldsymbol{\sigma} \otimes \boldsymbol{\sigma})$, with $\boldsymbol{\sigma}$ being the macroscopic stress tensor, as the affinity. The choice of the flux is in tune with the original damage model (Kachanov, 1958; Lemaitre and Chaboche, 1985) and is derivable from its micromechanical counterpart suggested by Budiansky and O'Connell (1976). Moreover, the suggested flux is readily measurable using methods of nondestructive testing on macroscopic specimens.

The kinetics of damage evolution has been defined similarly as in the conventional theory of plasticity. The conditions under which the potential exists have been discussed. In contrast to the theory of plasticity, the damage theory is not symmetric with respect to the sign of stresses.

A separate comment seems in order with respect to the proposed brittle damage model in compression. From (7.56) it can be inferred that the model, based on Mode I idealization of the winged microcrack and neglecting the frictional sliding contribution to the overall strain, cannot account for the nonlinear axial strains. While this is plausible for compact rocks such as granite where the axial strains are almost linear elastic (cf. Figure 4.8a), it certainly is not suitable for plain concrete under compression where the inelastic strains are significant and, more importantly, are of the same order of magnitude in axial and lateral direction (cf. Brühwiler et al., 1986; Murakami and Kamiya, 1997). Note that including $K_{II} \neq 0$ in (7.44) would not make this situation any better since, as judged from the experience gained in Chapter 4, the sliding contribution to the inelastic axial strain is too small to match the corresponding values reported for concrete. This is not quite unexpected since concrete is a porous material. For porous brittle materials alternative deformational micromechanisms such as pore collapse (Wang and Kemeny, 1993) or pore-squeezing (Figure 4.1a) should rather be used when constructing the damage surface.

At this stage of development, the model is confined to problems dominated by tension microcracks. The energy dissipated on frictional sliding has been neglected compared to the energy needed for creation of new internal surfaces within the material. Hence, it has been possible to use the normality property of the damage surface and significantly simplify the analysis. If, however, friction is to be accounted for, the normality rule has to be relaxed since the micromechanical fluxes will then depend on the macroscopic stresses not only via their own conjugated thermodynamic forces. Also, the secant compliance tensor will lose its diagonal symmetry making the selection of the macroflux as $d\mathbf{q} = d\mathbf{S}$ and the conjugated macroaffinity as $\mathbf{Q} = \frac{1}{2}(\boldsymbol{\sigma} \otimes \boldsymbol{\sigma})$ inappropriate.

Chapter 8

Lattice modeling of brittle damage

Abstract. In this chapter, brittle damage and fracture processes are analyzed using methods of the physics of critical phenomena rephrased for the class of problems considered in this thesis. Succinctly stated, this is an alternative modeling strategy applicable to random systems and processes in the vicinity of the critical point. In the present context, a randomly deteriorating solid is typically represented by a large lattice with an initial disorder imposed on selected properties of the lattice elements. On the examples of (1) percolation model, (2) rupture of central-force lattices, it is shown how the lattice models are interrelated with the damage mechanics models. The percolation model is applied to verify the accuracy of the effective media techniques when estimating the effective elastic constants of damaged solids. The numerical simulations on central-force lattices of the stress–strain behavior under tension (Hansen et al., 1989) are compared with the corresponding analytical estimates furnished by the parallel bar model (widely used in the damage mechanics literature). Finally, several interesting conclusions are drawn from the performed analysis regarding the accuracy of the effective media models (e.g. SCM, differential method, etc.), universality of damage variables, and microcrack interactions in tension.

8.1. Preliminaries

Quite independently of the continuum mechanics community, brittle damage-fracture processes have also been investigated by statistical physicists who use an entirely different modeling methodology. Instead of analyzing stress fields at the crack tips (fracture mechanics) or introducing a priori a damage variable into a continuum constitutive description (damage mechanics), they simulate a continuous brittle matter by means of discrete (regular or random) lattices which are subjected to certain type of disorder. The essential feature of the representation of a solid by a discrete graph is that it provides an opportunity to model the inhomogeneity of the microstructure by assigning appropriate statistical properties to the lattice bonds. Two major types of disorder are usually distinguished in the relevant literature: quenched and annealed. The quenched disorder denotes an initial disorder introduced, for example, into the elastic constants or rupture thresholds of individual lattice elements while the ensuing analysis of the system's fracture process is entirely deterministic. In the annealed disorder, the initial disorder may be absent but the analysis of the breaking process is stochastic.

Of several theoretical techniques available for dealing with highly disordered systems, the percolation model seems to be particularly appealing. The intellectual advantage of the percolation model consists in its almost game-like mathematical structure and a transparent and intuitively satisfying description for spatially random processes. The percolation disorder is bi-modal in the sense that a defect either occupies the considered site (or bond) of the lattice with the probability p or is absent there with the probability $1 - p$. As the bonds start to break under external tensile loading, the spatial patterns of defects (clusters) and their sequence of appearance are believed to mimic a real breaking process. The central questions posed in percolation and other statistical theories of disordered solids, are:

- What is the critical defect concentration p_c (*percolation threshold*) at which an infinite cluster appears spanning the opposite sides of a lattice system?

- How do different processes and transport properties of a material behave in the vicinity of the percolation thresholds (*scaling laws*)?

- Is there any universal law that is common to all initial defect distributions?

- Does the maximum stress and the total number of ruptured bonds at overall failure follow any universal law?

A deeper insight into the lattice modeling of disordered systems can be gained by consulting the excellent monographs by Zallen (1983), Stauffer (1985), Herrmann and Roux (1990), Sahimi (1994), Sornette (2000). Some specific conclusions concerning the links between the lattice models and the continuum damage mechanics have been formulated among others in Basista and Krajcinovic (1991), Krajcinovic and Basista (1991), Krajcinovic et al. (1994), Krajcinovic (1996), Delaplace et al. (1996), Basista (1997). The monograph by Krajcinovic (1996) provides also an exhaustive list of original papers on modeling of brittle fracture via statistical physics.

8.2. Percolation model

This subsection will be focused only on those aspects of the percolation theory that may be of importance in modeling brittle damage and fracture. When examining the existing literature on the applications of percolation theory to brittle fracture and confronting it with the damage mechanics findings, several interesting observations can be made. For example, a crack density parameter identical to that of Walsh–Budiansky–O'Connell (i.e. $\omega = N\langle l^3 \rangle / V$) also appears in the percolation models. However, its genesis is quite different, stemming from purely geometrical considerations. It was shown by Scher and Zallen (1970) that the critical volume (area) fraction of spherical (or circular) non-overlapping voids at percolation is a *dimensional invariant* independent of the lattice type. To illustrate this statement, consider a simple case of circular voids whose centers are randomly located on the nodes of a regular, very large, two-dimensional lattice. The critical void area fraction f_c (critical porosity, critical lacunity) can be determined directly using the site percolation model as

$$f_c = v p_c^s \,, \tag{8.1}$$

where p_c^s is the site percolation threshold, v is the filling (packing) factor for the considered lattice. The percolation threshold p_c^s denotes the critical fraction of lattice sites occupied by voids at the moment when an infinite void cluster transects a two-dimensional system. This situation corresponds to the specimen's failure in the strain controlled test. Consequently, equality (8.1) can be rewritten as

$$f_c = (N A_{\mathrm{void}})_c \,. \tag{8.2}$$

According to Scher and Zallen (1970), the critical porosity f_c is a *universal constant* equal to 0.45±0.03 irrespective of the lattice type, Table 8.1. This value persists to hold for all periodic two-dimensional lattices for which percolation data are available. A similar universality was also confirmed for the bond percolation model (Zallen, 1983) as shown by the last column in Table 8.1. As a consequence, this important result of Scher and Zallen implies that the critical value of the Walsh–Budiansky–O'Connell crack density parameter is a universal constant independent of the material microstructure. On the other hand, it should be emphasized that percolation thresholds p_c^s or p_c^b themselves are by no means dimensional invariants (see

Table 8.1. Percolation thresholds and dimensional invariants for site and bond percolation on selected lattices. Filling factors given for non-overlapping circles (2D lattices) and spheres (3D lattices); after Zallen (1983).

1	2	3	4	5	6	7
Lattice type	**Coordination number** z	**Percolation threshold (bond)** p_c^b	**Percolation threshold (site)** p_c^s	**Filling factor** ν	**Critical porosity** $\nu p_c^s = f_c$	**Critical connectivity** zp_c^b
Triangular (2D)	6	0.3473	0.5	0.9069	0.45	2.08
Square (2D)	4	0.5	0.593	0.7854	0.47	2.00
Honeycomb (2D)	3	0.6257	0.698	0.6046	0.42	1.96
Face centered (3D)	12	0.119	0.198	0.7405	0.147	1.43
Body centered (3D)	8	0.179	0.245	0.6802	0.167	1.43
Cubic (3D)	6	0.247	0.311	0.5236	0.163	1.48

columns 3 and 4 in Table 8.1). The universality of f_c for lattices became afterwards a milestone for the development of the continuum percolation.

In the case of overlapping (intersecting, permeable, or soft-core) circular voids the problem belongs to the class of *continuum percolation* and becomes somewhat more complicated. It is first necessary to determine the probability of overlapping of the neighboring voids. The percolation threshold will then coincide with the appearance of an infinite cluster of overlapping voids whose centers need not to occupy nodes of a regular lattice. Obviously, two voids of equal radii r will overlap if the distance between their centers is smaller than $2r$. Shante and Kirkpatrick (1971) have shown that the probability that a randomly selected point does not belong to a circular void is equal to e^{-n}, where n is the mean number of circular voids within a distance r from that point. At percolation, the critical value of n becomes

$n_c = zp_c^s/4$, where z is the coordination (or connectivity) number denoting the number of closest nodes. The critical fractional area of voids in a 2D case is (Balberg, 1987)

$$f_c = 1 - e^{-B_c/4}, \tag{8.3}$$

where B_c is the average critical number of circle centers within a given circle (*mean number of object intersections*). In a three-dimensional case, the critical fractional volume for permeable spherical voids becomes (Balberg, 1987)

$$f_c = 1 - e^{-B_c/8}. \tag{8.4}$$

Similarly as the critical porosity (8.2) for hard-core voids, the critical values of B_c (hencef_c in (8.3) and (8.4)), manifest a universal behavior for soft-core voids. This universality was demonstrated by Pike and Seager (1974) in an extensive program of numerical simulations.

The geometrical interpretation of the universal parameter B_c is quite instructive. Balberg et al. (1984) have found that

$$\begin{aligned} &B_c \approx N_c\langle A_{ex}\rangle \qquad &&\text{(in two dimensions),}\\ &B_c \approx N_c\langle V_{ex}\rangle \qquad &&\text{(in three dimensions),} \end{aligned} \tag{8.5}$$

where N_c is the critical number of defects per unit volume or area at percolation, V_{ex} is the so-called excluded volume of an object, and $\langle V_{ex}\rangle$ is the average of V_{ex} over all orientations of existing objects.

The *excluded volume* V_{ex} (or excluded area A_{ex} in 2D) of an object (A) is enveloped by the locus of points formed by the centers of all surrounding, geometrically similar objects (B) which just touch the object (A) without intersecting it. In other words, if the center of an adjacent object (D) is within the excluded volume of a similar object (A), two objects will penetrate each other. For the circular voids of equal radii shown in Figure 8.1 the excluded area is simply $A_{ex} = \langle A_{ex}\rangle = 4\pi r^2$. As pointed out by Balberg (1987), the advantage of this concept is that it accounts for the interaction between two objects. It associates a volume to objects which have no volume of their own (e.g. slits) and is simply related through (8.5) to the average number of bonds per site at percolation B_c, which is an invariant for a given object shape.

In the case of intersecting *slits*, the average number of intersections B_c is, indeed, a dimensional invariant but the critical crack density parameter

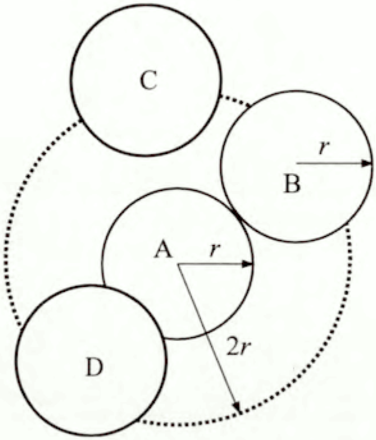

Figure 8.1. Geometrical concept of excluded area.

$N_c r^2$ is not (Robinson, 1984). As for uniformly distributed disks of constant radius r and vanishing thickness (penny-shaped cracks), the critical crack density is $\omega_c = N_c r^3 = 0.182$, whereas the crack intersections density at percolation equals $B_c = N_c \langle V_{ex} \rangle = \pi^2 N_c r^3 = 1.80$, Charlaix (1986).

Note that percolation means here emergence of an infinite cluster (borehole) penetrating a three-dimensional specimen from one side to the other. The corresponding critical point is called the *conductivity percolation threshold* (cf. Subsection 6.5.2). It shall not be confused with the second percolation threshold, called the *elastic percolation threshold*, at which the specimen loses its integrity while the secant elastic modulus drops to zero. Obviously, in a two-dimensional system both thresholds coincide. However, in the considered 3D case, the elastic percolation threshold, leading to fragmentation of the specimen, should occur at a substantially larger density of penny-shaped cracks than the conductivity threshold.

The percolation studies confirm, at least for non-intersecting defects, the utility of the Walsh–Budiansky–O'Connell crack density parameter in damage modeling. Although the starting points of the continuum and percolation models of brittle damage were quite distinct, both classes of models ended up with virtually the same parameter quantifying the evolving material deterioration. For non-intersecting defects, the critical value of this parameter has even been proven to be a dimensional invariant. Consequently, it may be concluded that for non-overlapping spherical or circular voids the strain-controlled rupture always happens at a constant value of the Walsh–Budiansky–O'Connell damage parameter. A further conclusion that can be drawn from the above analysis is that for spherical or circular non-overlapping voids, the Walsh–Budiansky–O'Connell parameter is apparently proportional to the volume (area) fraction of defects, i.e. to the porosity. However, this interpretation may be misleading since the same damage parameter $\omega = N\langle r^2\rangle$ is also derived for slits, while $\omega = N\langle r^3\rangle$ for penny-shaped cracks, where any relation to material porosity is irrelevant (Basista, 1999).

There is another aspect of the percolation theory that might be consequential for the continuum mechanics descriptions of the effective properties of heterogeneous elastic solids. The mere fact that a spanning cluster emerges at a finite (critical) microdefect concentration furnishes a simple validity check for the effective media/field methods at large microdefect concentrations. To substantiate this statement, consider a dilution process of a plate made of perfectly elastic, isotropic and homogeneous material weakened by a large number of randomly distributed, non-overlapping, circular voids (plane stress case). Incidentally, this is a classical problem analyzed by the effective media/field models and the percolation theory alike. The expressions for the Young modulus estimated, for example, by the dilute distribution method (DD), the self-consistent method (SCM), and the differential scheme (DS) can be found almost in any book on micromechanics (e.g. Nemat-Nasser and Hori, 1993) and are given by

$$\frac{E^{DD}}{E_0} = \frac{1}{1+3f}\,, \qquad \frac{E^{SCM}}{E_0} = 1-3f\,, \qquad \frac{E^{DS}}{E_0} = (1-f)^3, \tag{8.6}$$

where E_0 is the Young modulus of the undamaged material, $f = \sum_N (A_{\text{void}}/A) = \pi N\langle r^2\rangle$ is the area fraction of voids, N being the number of voids per unit area. On the other hand, since this is a two-dimensional site percolation problem, the critical value of the void density is $f_c = (NA_{\text{void}})_c \approx 0.45$, Table 8.1. The variation of the elastic modulus vs. void fraction has also been investigated experimentally in Vavakin and Salganik (1975), Benguigui (1984, 1986a), Sieradzki and Li (1986) and others. The data provided by Benguigui (1984, 1986a) are best suited to check the accuracy of the expressions (8.6). The Benguigui's experiments were careful, force-controlled, elastic tension tests conducted on thin metallic sheets (Al, Cu) with non-overlapping holes punched randomly on the sites of a square lattice. The applied loading device allowed measurements very close to the percolation limit (95% p_c^s). However, since the reported data were referred to the void number fraction ϕ, they had to be multiplied by the filling factor ($\nu = 0.7854$ for square lattice) in order to be comparable with the effective media results (8.6), (Krajcinovic, Mallick, Basista and Sumarac, 1992). In Figure 8.2, the theoretical estimations by the effective media methods (8.6) are depicted and confronted with the experimental results of Benguigui (1986a). Incidentally, Benguigui (1986b) performed similar tests for circular holes allowed to overlap (continuum percolation). These tests confirmed with a very good accuracy that the critical area fraction of voids in 2D is (Shante and Kirkpatrick, 1971; Pike and Seager, 1974; Balberg, 1987)

$$\phi_c = 1 - \exp(-N_c \langle A_{ex} \rangle / 4) \approx 0.68. \tag{8.7}$$

The scaling laws for the elastic modulus in the lattice (L) and continuum (C) percolation have the following forms

$$E \propto (f_c - f)^{T_L}, \qquad E \propto (\phi_c - \phi)^{T_C}, \tag{8.8}$$

where $(f_c - f)$ and $(\phi_c - \phi)$ are the lattice and continuum *proximity parameters*, respectively. The measured values for T_L and T_C (Benguigui, 1986a,b) fully agree with the theoretical numbers $T_L = 3.3 \pm 0.5$, $T_C = T_L + 3/2$ (Halperin et al., 1985).

As remarked in Basista (1999), several interesting conclusions can be drawn when examining Figure 8.2. For example, the Benguigui (1986a) test data closely match the analytical result for the site percolation according to which the critical porosity on two-dimensional periodic lattices equals $f_c = 0.45 \pm 0.03$. As for the effective media results yielded by the three methods presented in this figure, substantial differences have to be admitted even at small void densities. Moreover, only the self-consistent model predicts that the elastic modulus vanishes at a finite porosity $f_c^{SCM} = 0.33$. This is consistent with the existence of the critical porosity $f_c^s = 0.45$, although f_c^{SCM} clearly underestimates f_c^s. Leaving aside the discussion whether this is an accidental thus meaningless behavior, or a built-in property of the self-consistent model, the fact is that the dilute distribution model and the differential scheme do not recognize that the percolation threshold actu-

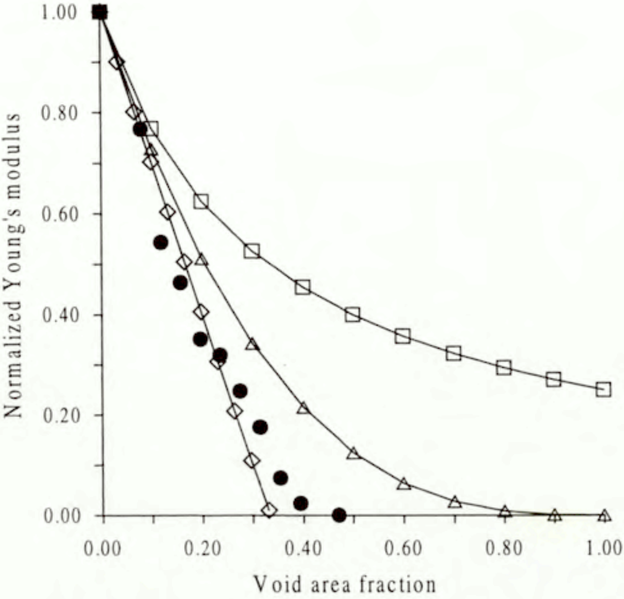

Figure 8.2. Effective elastic modulus E/E_0 for thin metal sheet with circular non-overlapping voids. Squares, triangles and diamonds represent DD, DS, and SCM predictions (8.6), respectively. Experimental data by Benguigui (1986a) marked by circles (Krajcinovic, Mallick, Basista and Sumarac, 1992; Basista, 1999).

ally exists (Basista, Krajcinovic and Sumarac, 1992). Evidently, the bottom line here is the answer to the question whether the defect density can be unlimitedly increased or, in other words, whether the existence of the representative volume element (thus volume averaging) can be justified at very high defect concentrations. The answer offered by the percolation theory is that the defects will eventually self-organize and join the largest defect cluster making the specimen statistically non-homogeneous. This sets limits to the applicability of the effective medium/field theories provided that defects are not constrained in their random nucleation (Basista, 1999). Note that the effective continua models and the percolation models are applicable in different regimes and may be deemed complementary. The difficult region between those two, called the *crossover* regime, is currently under intensive studies by applied mechanicians as well as statistical physicists. In terms of continuum mechanics, the crossover regime could be identified, roughly speaking, with the softening portion of the stress–strain curve.

Despite unquestionable successes of the percolation theory in describing phenomena that approach the critical state, a certain amount of caution seems in order when using it to model brittle fracture processes. In a static case, the percolation model is *not* a suitable model to represent the damage-fracture process of brittle solids. It is commonly known that microcracks in brittle solids start to grow from the preexisting flaws. The longest and most favorably oriented microcrack, i.e. the one located perpendicularly to the maximum tensile stress direction, is the first to grow when its elastic strain energy release rate reaches the critical value. This, however, does not have much in common with a simple bi-modal type of disorder of the percolation model. Also, the existing percolation models are almost exclusively confined to tensile loading conditions whereas for brittle solids the compressive stress states are of primary importance (Basista, 1999).

On the other hand, the percolation model seems to be more suitable for the description of dynamic fracture processes (cf. Basista, 1997). Short duration times and high intensity of stress impulses amplify the random character of the microcrack nucleation and proliferation. In particular, brittle spall damage, which by its very nature involves random nucleation of defects under the action of tensile stress waves, offers a promising and yet unexplored field of possible applications of the percolation theory. Some initial efforts in this direction can be found in Dienes (1982) and Tonks (1996).

8.3. Central-force lattices

Random nucleation processes are well captured by the percolation model. If, however, a damage process is dominated by the growth of microdefects (as it is the case in brittle solids) more sophisticated types of disorder have to be employed when modeling elastic rupture. For example, one could think of a continuous distribution function of the rupture strengths or stiffnesses of the lattice bonds. In statistical physics, these types of disorder are conveniently studied on regular lattice systems which are expected to mimic heterogeneous elastic continua. Typically, three main classes of such lattices are distinguished:

- *fuse lattices* – electrical networks of random fuses (scalar equivalent of the vector problem of elastic rupture),
- *central-force lattices* (trusses) – consisting of elastic bonds (springs) that can freely rotate around their end points and carry axial forces only,
- *beam lattices* – whose elastic bonds carry axial forces, transverse forces, and bending moments.

In the recent past, an extensive research effort has been undertaken by the statistical physicists to investigate elastic rupture problem using fuse lattices (e.g. de Arcangelis et al., 1985; Duxbury et al., 1987; de Arcangelis and Herrmann, 1989; Hansen et al., 1991), central-force lattices (Feng and Sen, 1984; Beale and Srolovitz, 1988; Hansen et al., 1989), and beam lattices (Feng et al., 1984; Herrmann et al., 1989). Limited by the space, attention will be focused here on the central-force lattices.

More than a decade ago Hansen et al. (1989) published an important study devoted to the rupture of central-force lattices. Inspired by that paper, Krajcinovic and Basista (1991) presented some interesting links between the numerical simulations on central-force networks, and the analytical predictions of a simple parallel-bar model used in damage mechanics. Hansen et al. (1989) considered a regular, two-dimensional triangular lattice (Figure 8.3a) consisting of nodes joined by elastic-brittle springs of identical elastic constants set to be unity by definition. The quenched disorder was introduced in the bond rupture thresholds f_c. Note that in quenched disorder the disorder is introduced before the breaking process starts and is not changed thereafter. Moreover, the algorithm that is used to model the breakdown process is deterministic. In contrast, in the annealed disorder, there is no disorder within the network at the beginning of the breakdown process but disorder is introduced through a stochastic nature of the algorithm used to determine the sequence of bonds' breaking. In the considered work of Hansen et al. (1989), the quenched disorder has the form of a uniform distribution of the rupture thresholds, Figure 8.4a, which means that f_c can take any value between 0 and 1 with equal probability. Somewhat unrealistically for brittle solids, it was assumed that the bond rupture thresholds in tension and compression are equal, $f_+ = f_- = f_c$. The bottom and top rows of the lattice are attached to rigid bars in order to assure uniformity of the applied displacement Λ. The boundary conditions in the horizontal direction are periodic and the whole problem is treated within

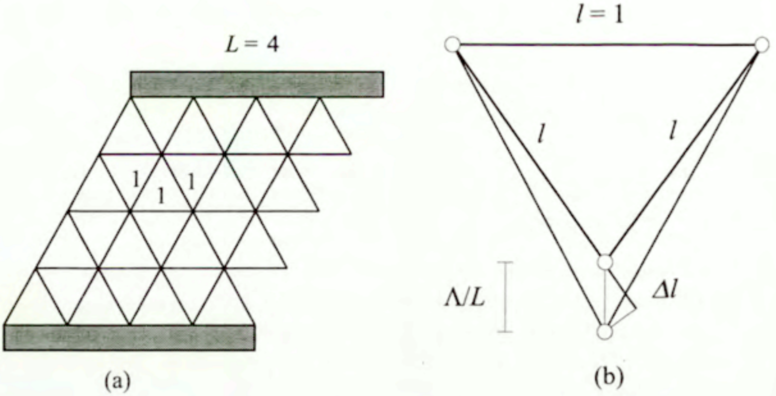

Figure 8.3. (a) Central-force triangular lattice with rigid bars (after Hansen et al., 1989). (b) Estimation of strain in a bond (Basista, 1999).

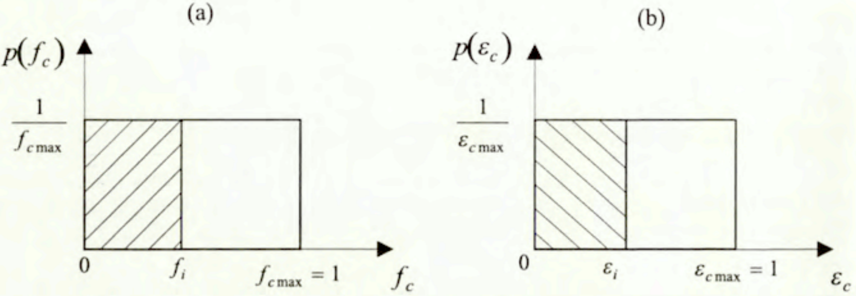

Figure 8.4. Probability density function for bond rupture thresholds: (a) in terms of forces (Hansen et al., 1989), (b) in terms of strains (Basista, 1999).

the limits of small deformations. Having introduced the quenched disorder in the bond rupture strengths, the forces in the bonds are computed using the conventional (deterministic) truss analysis for each increment of the elongation imposed on the rigid bars. Four lattice sizes $L = 4,\ 8,\ 16,\ 24$ were considered to ascertain the size effect. It should be mentioned that all quantities appearing in the sequel are non-dimensional. This is due to the specific length scale introduced in Hansen et al. (1989) for displacements motivated by linearity of the considered problem. The forces in bonds were scaled using the scale of the rupture thresholds distribution, i.e. they assumed (non-dimensional) values between 0 and 1. Having determined the forces, the displacements of bonds were also known since bonds' elastic moduli were arbitrarily set to 1. The length scale for the lattice sizes was different from that for displacements: L was scaled by the bond length l which was assumed to be 1 (Figure 8.3a).

If the force in a bond exceeded its rupture threshold, the bond was removed from the lattice, the forces in the extant bonds were recomputed and checked against the rupture criterion again, the next broken bond was then removed, and so on until the elastic modulus of the whole lattice dropped to zero. The computations were performed for each simulation (physical realization) which differed from the others by the spatial distribution of bonds with different rupture strengths. Hansen et al. (1989) generated 10000 4×4, 1000 8×8, 300 16×16, and 30 24×24 lattices over which the results were averaged. Whenever possible, the original notation of Hansen et al. (1989) will be preserved throughout this section. It is therefore advisable to recall the basic symbols:

- L is the lattice size (number of rows),
- f_c is the bond rupture threshold,
- Λ, Λ_c is the total external displacement (subscript c indicates that "bond break was observed").
- F, F_c is the total external force,
- f_j is the local force in a bond,
- N is the total number of diagonal (force carrying) bonds,
- n is the number of broken bonds,
- $F_{\max}$ is the maximum force recorded during a numerical simulation,
- $n_{\max}$ is the number of bonds broken at the maximum force,
- $\langle\cdot\rangle$ denotes an averaged quantity,
- K is the elastic modulus of the pristine lattice (set to 1 in Hansen et al., 1989).

In order to make the main results of Hansen et al. (1989) traceable, the following *mean-field* analysis (not contained in the original paper) will now be performed. Consider a single lattice element, Figure 8.3b and apply the external elongation Λ to the rigid bars. The strain in a stretched bond is given by

$$\varepsilon_i = \frac{\Delta l_i}{l_i} = \frac{\Lambda}{L}\frac{\sqrt{3}}{2}\,, \tag{8.9}$$

where, as already mentioned, the bond length l is set to 1. Since the overall displacement is a stretch and the boundary conditions are periodic, only the diagonal bonds carry the forces thus are susceptible to rupture (Hansen et al., 1989). It can be shown that the total number of diagonal bonds is $N = 2L^2$. Choosing the number of ruptured bonds n as the history-recording parameter, a physically appealing damage measure is the following scalar (cf. Basista, 1999)

$$D = \frac{n}{N} = \frac{n}{2L^2}\,. \tag{8.10}$$

On the other hand, the damage parameter (8.10) can be interpreted statistically as the cumulative probability function $P(f_i)$ of the assumed probability density function $p(f_c)$ for the bond rupture thresholds:

$$D = \int_0^{f_i} p(f_c)\,\mathrm{d}f_c = P(f_c < f_i), \tag{8.11}$$

where the rupture threshold of the weakest bond is 0. Damage is thus defined as the probability that the force in a bond f_i exceeds its rupture threshold f_c. For the assumed uniform distribution of rupture thresholds (Figure 8.4a) the damage parameter (8.11) takes the form (cf. Basista, 1999)

$$\begin{gathered} D = \int_0^{f_i} \frac{1}{f_{c\,\max}}\,\mathrm{d}f_c = \frac{f_i}{f_{c\,\max}} = f_i\,, \\ \text{or} \\ D = \int_0^{\varepsilon_i} \frac{1}{\varepsilon_{c\,\max}}\,\mathrm{d}\varepsilon_c = \frac{\varepsilon_i}{\varepsilon_{c\,\max}} = \varepsilon_i\,, \end{gathered} \tag{8.12}$$

where the latter of these formulas is expressed in terms of strains (cf. Figure 8.4b). Comparing the two definitions of D, i.e. $(8.12)_2$ and (8.10), we get

$$n = 2L^2\varepsilon_i\,, \tag{8.13}$$

which is identical to the relation (4) in Hansen et al. (1989). Moreover, when Equation (8.13) is combined with (8.9), an important linear equation (3) of the original paper Hansen et al. (1989) is recovered:

$$\Lambda(n) = \frac{1}{\sqrt{3}}\,\frac{n}{L}\,. \tag{8.14}$$

Finally, dividing both sides of (8.14) by L, a linear proportionality between the damage $D = n/(2L^2)$ and the overall strain $\varepsilon = \Lambda/L$ is revealed. Remarkably, this linear regime was clearly confirmed by the respective numerical simulations in Hansen et al. (1989).

The primary objective in Hansen et al. (1989), though, was to establish a universal (size-independent) relation between the overall (average) force $\langle F_c(n)\rangle$ and the total elongation $\langle \Lambda_c(n)\rangle$, with the number of broken bonds n being the control variable. As a first step, the data $\langle F_c\rangle$ vs. n up to the apex were fitted according to the following parabola (Hansen et al., 1989)

$$\langle F_c(n)\rangle = \left(1 - \alpha\frac{n}{L^2}\right)\langle \Lambda_c(n)\rangle. \tag{8.15}$$

Equivalently, one can say that a linear correction $(1 - \alpha n/L^2)$ was sought to the lattice elastic modulus (set to be 1 by definition). The authors hoped to find a value for the parameter α that is constant for all lattice sizes. However, it turned out that the best fit of the form (8.15) was obtained for $\alpha = 1.0$, $\alpha = 1.25$, $\alpha = 1.5$, $\alpha = 1.65$ corresponding to $L = 4$, $L = 8$, $L = 16$, $L = 24$, respectively. In conclusion, the linear *Ansatz* (8.15) proved insufficient to capture the degradation of the elastic modulus without a scale effect. Hence, a universal relation was sought in the space of different variables assuming the following functional dependence (Hansen et al., 1989)

$$\langle F_c(n)\rangle = L^{\beta}\,\Phi\left(\langle \Lambda_c(n)\rangle\,L^{-\gamma}\right), \tag{8.16}$$

where β, γ are unknown exponents and Φ is a universal function independent of the lattice size. In other words, Φ may be considered a universal function if the force-displacement data obtained from the numerical simulations for different lattice sizes, can be collapsed on a single master curve plotted in the reduced variables $\left\{\langle F_c(n)\rangle/L^{\beta}\right\}$ vs. $\{\langle \Lambda_c(n)\rangle/L^{\gamma}\}$. The authors found out that for $\beta = \gamma = \frac{3}{4}$ the trial function (8.16) fitted the simulation data exceedingly well. The only exception was the size $L = 4$, which was disregarded for being "obviously too small to give any reliable estimates" (Hansen et al., 1989). The parabolic fit (8.15) when combined with the mean-field estimate (8.14) gives

$$F_c(\Lambda_c) = \left(1 - \frac{\alpha\sqrt{3}}{L}\,\Lambda_c\right)\Lambda_c\,, \tag{8.17}$$

where the averaging symbols have been omitted. The functional form of α is dictated by the rescaling relation (8.16) as (Hansen et al., 1989)

$$\alpha \propto L^{1-\beta}, \tag{8.18}$$

with $\beta = \frac{3}{4}$. In addition to the central-force model, similar rescaling was obtained for the fuse model (de Arcangelis and Herrmann, 1989) and for the elastic beam model (Herrmann et al., 1989). Quite surprisingly, the value of $\beta = \frac{3}{4}$ seems to be universal for all three models. In the post-peak regime, statistical fluctuations were very strong, thus it was not possible to find a universal exponent for all $\left\{F_c(n)/L^\beta\right\}$ vs. $\left\{\Lambda_c(n)/L^\beta\right\}$ curves. Consequently, in that regime the overall behavior of the lattice systems was *multifractal.*

So far, we have highlighted the main points of the important paper by Hansen et al. (1989) on rupture of central-force lattices. The same problem was later revisited in Krajcinovic and Basista (1991), Basista and Krajcinovic (1991), Basista (1999). The remaining part of this section closely follows the analysis and recapitulates the original results published in that series of papers.

When examining the data in Hansen et al. (1989), it has been noticed in Krajcinovic and Basista (1991) that the proportionality (8.18) can actually be expressed in the following exact form

$$\alpha = \beta L^{1-\beta}, \tag{8.19}$$

where the proportionality factor and the universal exponent coincide having the constant value of $\beta = \frac{3}{4}$. This simple observation has far-reaching consequences. Each scaling law in Hansen et al. (1989) can now be expressed in a closed analytical form, Table 8.2.

Inserting the equality (8.19) in the assumed force–displacement relation (8.17) yields (Krajcinovic and Basista, 1991; Basista, 1999)

$$F_c = K\left[1 - \tilde{D}(L,\Lambda_c)\right]\Lambda_c = \bar{K}\Lambda_c\,, \tag{8.20}$$

Table 8.2. Central-force lattice: closed-form expressions obtained in Krajcinovic and Basista (1991) for scaling laws in Hansen et al. (1989).

Hansen et al. (1989)	Krajcinovic and Basista (1991)
$\Lambda_{c\,\max} \propto L^\beta$	$\Lambda_{c\,\max} = \frac{1}{2\beta\sqrt{3}}\,L^\beta$
$n_{c\,\max} \propto L^{\beta+1}$	$n_{c\,\max} = \frac{1}{2\beta}\,L^{\beta+1}$
$F_{c\,\max} \propto L^\beta$	$F_{c\,\max} = \frac{1}{2}\,K\Lambda_{c\,\max}$

where $\bar{K} = K(1-\tilde{D})$ is the effective elastic modulus. Recall that the elastic modulus of an undiluted lattice K is set to 1 by definition. The damage parameter emerging in (8.20) is linearly proportional to the displacement Λ_c (or strain, $\varepsilon = \Lambda_c/L$) and is a function of the lattice size, namely (Krajcinovic and Basista, 1991)

$$\tilde{D}(L) = \sqrt{3}\beta\,\Lambda_c\,L^{-\beta} = \sqrt{3}\beta\,\varepsilon\,L^{1-\beta} = 2\beta\,D\,L^{1-\beta}. \tag{8.21}$$

In contrast, the effective elastic modulus (secant stiffness) $\bar{K} = F_c/\Lambda_c$ is independent of the lattice size. The last of the equalities (8.21) shows how the rescaled damage parameter $\tilde{D}$ is related to the density of ruptured bonds D, (8.10). Except for the scale effect, both parameters manifest linear dependence on the overall displacement. The damage parameter $\tilde{D}$ can also be rewritten as a function of the externally applied force (Krajcinovic and Basista, 1991):

$$\tilde{D}(L,F) = \frac{1}{2} - \frac{1}{2}\sqrt{1 - 4\sqrt{3}\,\beta\,L^{-\beta}\,\frac{F}{K}}\,. \tag{8.22}$$

It follows from (8.22) that in the virgin unstressed state $\tilde{D}(F{=}0) = 0$, while at the apex of the force-displacement curve $\tilde{D}_{\max}(F_{c\,\max}) = \frac{1}{2}$.

The parameter α, number $n_{c\,\max}$, density of ruptured bonds $n_{c\,\max}/N$, displacement $\Lambda_{c\,\max}$, force $F_{c\,\max}$ and damage $\tilde{D}_{\max}$ at the apex of the force–displacement curve have been computed from the above analytical expressions in Krajcinovic and Basista (1991) and are arranged in Table 8.3. The corresponding numerical data read off from Figure 6 in Hansen et al. (1989) are added in parentheses. As suggested in Hansen et al. (1989) the numerical data for $L = 4$ are disregarded.

Table 8.3. Central-force lattice: numerical data from Hansen et al. (1989) (in parentheses) vs. analytical results of Krajcinovic and Basista (1991).

L	α	$n_{c\,\max}$	$n_{c\,\max}/N$	$\Lambda_{c\,\max}$	$F_{c\,\max}$	$\tilde{D}_{\max}$
4	1.06 (1.00)	9 (–)	0.280	1.09 (–)	0.54 (–)	1/2 (0.500)
8	1.26 (1.25)	25 (26)	0.195	1.83 (1.91)	0.92 (0.94)	1/2 (0.521)
16	1.50 (1.50)	85 (81)	0.166	3.08 (3.00)	1.54 (1.56)	1/2 (0.487)
24	1.66 (1.65)	173 (168)	0.155	4.17 (4.13)	2.09 (2.15)	1/2 (0.495)

Before drawing any conclusion from Table 8.3, it is instructive to recall the simplest form of a disordered system, i.e. a *parallel bar model* (fiber bundle with global sharing rule), Figure 8.5. The parallel bar model has been known since the early work of Daniels (1945) and often used afterwards in damage mechanics (e.g. Janson and Hult, 1977; Krajcinovic, 1979; Krajcinovic and Silva, 1982; Krajcinovic et al., 1993) and statistical physics (Phoenix and Taylor, 1973; Sornette, 1989) to describe failure processes. It is a bundle of N loose bars (links) of equal stiffness k carrying the external tensile load F. Since the links are loose there are tensile forces within the system but no shear forces. The rigid bars (buses) located at both ends of the system enforce equal elongation of all links. The initial stiffness of the whole system is $K = Nk$. Each link is linear elastic and breaks when the tensile force in the link exceeds its rupture strength f_c. When a bond rup-

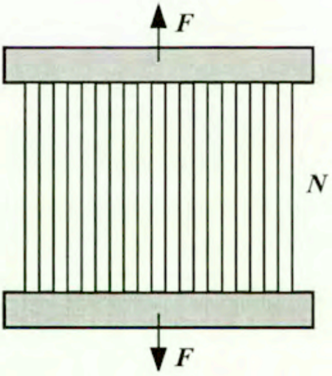

Figure 8.5. Parallel bar model.

tures its force is released and has to be taken over (quasi-statically) by the remaining bonds. The distribution of link rupture strengths is prescribed in advance (quenched disorder) by the probability density function $p(f_c)$. The position of a link in the bundle is inconsequential since all extant links equally participate in carrying the load (mean-field approximation). It should be emphasized that the parallel bar model rules out any spatial interactions. Also, the fiber bursting (cf. Hemmer and Hansen, 1992) is not considered here. Hence, the macroresponse of the system depends solely on the fraction of ruptured links (n/N). The scale effect is not accounted and, since there is no length parameter, the model is local. The process of damage and final rupture is attributed to the disorder in the rupture thresholds of material constituents. The model is not capable of accounting for the stress concentrations (hot spots) nor the interplay between the weak links and hot spots.

For such a system, the equilibrium of forces yields

$$F = (N-n)f = N\left(1-\frac{n}{N}\right)\frac{K}{N}\,\Lambda = K(1-D)\,\Lambda = \bar{K}\Lambda, \qquad (8.23)$$

where Λ is the elongation, while the force–displacement relation for an extant link is $f = k\Lambda = (K/N)\Lambda$. Similarly as before, $D = (n/N)$ is the damage parameter (fraction of ruptured links) and $\bar{K}$ is the current secant effective elastic modulus (stiffness) of the system. Obviously, n takes different values at the same levels of F in the parallel bar model and the central force lattice.

If the number of links is very large (rigorously speaking – infinite), the equilibrium Equation (8.23) can be cast into an integral form (Krajcinovic, 1996)

$$\begin{aligned} F &= N\int_{f}^{f_{\max}} f\,p(f_c)\,\mathrm{d}f_c = k\Lambda\left[N\int_{ku}^{f_{\max}} p(f_c)\,\mathrm{d}f_c\right] \\ &= K(1-D)\Lambda, \end{aligned} \qquad (8.24)$$

where the term in brackets represents the number of non-ruptured links. Note that a dual interpretation of the damage parameter D is used in (8.24). On one hand it is defined as the fraction of ruptured links $(D = n/N)$, on the other – as the cumulative probability function $P(f_i)$ of the assumed probability density function of the link rupture strengths (cf. (8.11)). For the uniform strength distribution (Figure 8.4), the force-displacement curve predicted by the parallel bar model takes the form of a quadratic parabola (e.g. Krajcinovic and Silva, 1982):

$$F = K\left(1 - \frac{k\Lambda}{f_{c\,\max}}\right)\Lambda, \tag{8.25}$$

where, consistently with the earlier notation, $f_{c\,\max}$ is the rupture strength of the strongest link. The damage parameter $D = k\Lambda/f_{c\,\max}$ is linearly proportional to the elongation of the system. A similar dependence was observed for the central-force lattice, Equation (8.14). It is easy to see that at the apex of the force-displacement parabola (8.25), it holds again

$$F_{c\,\max} = \frac{1}{2}\,K\Lambda_{c\,\max}\,. \tag{8.26}$$

Comparing the last cell in Table 8.2 (see also three last columns in Table 8.3) with (8.26) it can be seen that for the same distributions of bond rupture thresholds the central-force lattice and the parallel bar system manifest *identical* response at the apex (Krajcinovic and Basista, 1991). This is rather an unexpected result since the central-force lattice accounts in a natural manner for defect interactions, whereas the parallel bar model totally ignores any defect interaction. Also, the size effect that is included in the central-force model disappears for the secant elastic modulus. In the parallel bar model the size effect is absent by definition.

On the basis of the presented analysis, several conclusions have been formulated in Krajcinovic and Basista (1991), Basista (1999). These conclusions can be expressed as follows:

1. The secant elastic modulus (or more generally the secant effective elastic stiffness tensor) seems to be the proper choice for a damage parameter. The following facts strongly support this choice:
    - it was possible in Hansen et al. (1989) to collapse all the force-displacement simulation data in the pre-peak regime on a single master curve for all the lattice sizes considered,
    - at the apex it holds $\bar{K}_{c\,\max} = \frac{1}{2}\,K$ (or $\tilde{D}_{\max} = \frac{1}{2}$) irrespective of the lattice size ($L = 4,\ 8,\ 16,\ 24$),
    - at the apex it also holds $\bar{K}_{c\,\max} = \frac{1}{2}\,K$ (or $\tilde{D}_{\max} = \frac{1}{2}$) irrespective of the lattice type, i.e. central-force lattice vs. parallel bar system; this conclusion should be checked for other network models.

2. The fraction of broken bonds (density of microcracks) (8.10) is a poorer damage parameter since it manifests a size effect, cf. Delaplace et al. (1996).

3. The lattice response under *tension* within the hardening regime is weakly affected by the defect interactions. The defect interactions, if present, should be profound at the apex and beyond it. The $(F_{c\,\max} - \Lambda_{c\,\max})$ equations, that have been proved identical for the central-force lattice and parallel bar system at the apex, indicate rather the opposite.

4. The mean-field assumption used in Hansen et al. (1989) in the analysis of the central-force lattice turned out to be correct. Consequently, it suffices to consider only the volume averages of microstructural disorder while higher statistical moments seem unnecessary when modeling the tensile lattice response.

Note that conclusion 1 obtained from the rupture analysis of disordered systems corroborates the ideas addressed earlier in the CDM literature suggesting that damage be properly quantified by the changes of the elastic stiffness (cf. Lemaitre and Chaboche, 1978; Ortiz, 1985).

Chapter 9

Conclusions and future research

This multi-aspect study has addressed a number of damage problems in brittle engineering materials with special emphasis on rocks and plain concrete. Throughout the thesis, the dominant and recurring theme has been the formulation of workable constitutive models relating the macroscopic material response induced by quasi-static mechanical loading (or chemical attack) to the underlying physical (or physico-chemical) processes within the material microstructure. To enhance the text clarity, each of Chapters 2, 3, 4, 5, 6, 7, 8 has been preceded by a brief abstract stating the chapter's main objective. Also, Chapters 3, 4, 5, 6, 7, 8 have ended with partial conclusions summarizing the obtained original results and emphasizing their prospective impact on the current modeling practice. More general conclusions ensuing from the presented research follow below.

It is commonly agreed upon that the development of damage mechanics started with the pioneering work of L.M. Kachanov (1958). Since then, this branch of contemporary solid mechanics has passed through a series of relative ups and downs. After the infancy period in the late fifties and early sixties, where the basic ideas of continuum damage were articulated by Kachanov and further elaborated by Rabotnov, the field went through a period of apparent dormancy only to experience a rapid progress in the mid seventies and the eighties. At that time, extensive research efforts were directed towards continuum description of creep and fatigue related damage phenomena (e.g. Chrzanowski, 1976). The names of Lemaitre, Hult, Murakami and Krajcinovic were probably among the most quoted ones in the context of the CDM. Various international symposia on continuum damage mechanics were held and an advanced course on CDM was even organized in 1987 at the CISM in Udine, Italy. All that could have been seen as signs of the strength of a new discipline. However, it was only partly true. The other part was that the CDM models have concentrated on solving particular engineering problems (in which voids and microcracks played the central role) and left aside the more physical understanding of what damage actually is. A typical recipe for the formulation of a workable damage model was: (1) select a convenient damage variable, (2) assume a damage evolution law, (3) fit everything into the theory of tensor function representations and the thermodynamics with internal variables, implement numerically the obtained equations using available FEM codes. As rightfully noted by Krajcinovic (1995), the negligence of micromechanical basis has often resulted in arbitrary selections of the damage variables and lead to constitutive equations plagued by numerous adjustable constants of vague physical interpretation. Some of those ambiguities have later been cleared up by the micromechanical damage models which borrowed a lot of their scientific ground from the fracture mechanics.

In principle, an internal (damage) variable can be selected arbitrarily as long as it does not violate the laws of thermodynamics. On the other hand, to minimize the number of material parameters involved, it is absolutely necessary to endow the selected internal variable with a clear physical meaning (Kestin and Bataille, 1978). Complying with this requirement, a damage variable should be "observable, identifiable and measurable" (Krajcinovic and Mastilovic, 1995). From the micromechanical studies of Chapters 3 and 4, it can be concluded that a suitable damage parameter on the microscale is the Walsh–Budiansky–O'Connell microcrack density parameter, $\omega = N\langle a^3\rangle/V$. On the atomic level, damage is uniquely measured by the fraction of ruptured atomic bonds. These physically appealing damage measures require robust experimental techniques and sophisticated laboratory equipment to yield reliable data. In engineering practice, theses measures are seldom observable and directly measurable. Therefore, having in mind the accepted definition of damage (cf. Chapter 1) according to which damage represents the effect of microcracks on the macroscopic material behavior, it seemed quite rational to recommend that damage be macroscopically quantified by the changes in the elastic stiffness (or compliance) tensor. This idea is not entirely new; it was suggested in an early paper by Lemaitre and Chaboche (1978) and explicitly used by Ortiz (1985). However, new are the results of studies on central-force lattices performed in Chapter 8 which have strengthened this concept by showing that the effective (secant) elastic modulus is a universal parameter independent of the lattice size and type. The major advantages furnished by the effective stiffness selected as the damage parameter are:

- The statistics of microcracks within a material with regard to their number, shape, orientation and location are generally not known.

Hence, from the pragmatic viewpoint the effective stiffness S_{ijkl} seems to be an identifiable continuum damage parameter.

- The effective stiffness is readily measurable in the laboratory or *in situ* on structures. For example, it can be acquired either directly from the changes of the slope of the unloading path in the stress–strain curves, or indirectly by relating it to the decrease in the natural material frequencies in vibration tests.
- The effective stiffness is the key constituent of micromechanical and phenomenological damage models for brittle materials. For other damage variables (e.g. Walsh–Budiansky–O'Connell microcrack density parameter, Kachanov second-order microcrack density tensor) the effective stiffness has to be computed first (cf. Horii and Nemat-Nasser, 1983). If the effective stiffness itself is taken as the damage variable this cumbersome computational step becomes redundant.
- The second order tensor representations of damage cannot be measured in tests and must be, therefore, inferred from measurements of the effective stiffness (Krajcinovic and Mastilovic, 1995)
- In elastic percolation studies, the effective stiffness is an order parameter manifesting universal behavior in the vicinity of the percolation threshold. As already mentioned, its lattice-size independence, weak sensitivity to microcrack interactions (in tension) and to details of the microcrack distribution confirms its usefulness in quantifying the internal material deterioration (Krajcinovic and Basista, 1991).

All these arguments point to the effective stiffness as possibly the only logical choice for the macroscopic damage variable. However, this is not always true in terms of failure. To illustrate this statement consider a classical example of the uniaxial tension of an RVE containing: (a) two collinear equal microcracks and (b) the same microcracks stacked one over the other. The effective elastic modulus in the direction perpendicular to the microcracks is identical in both configurations. The same cannot be said, though, about the RVE propensity to fail. Obviously, configuration (a) is much more susceptible to rupture due to the stress amplification effect than configuration (b) for which the K_I is actually reduced by presence of the other microcrack. This example brings us to the conclusion that the effective stiffness tensor is a suitable representation of damage when the microcrack interaction effects are absent (or weak). In other words, the effective stiffness is a proper macroscopic damage measure as long as the Walsh–Budiansky–O'Connell microcrack density parameter is a proper microscopic characteristic of damage. Obviously, this ceases to be valid at large microcrack densities resulting in microcrack clustering since volume averaging becomes then meaningless. Another limit to the applicability of the above damage measures is set by the band-width of microcrack sizes. If the initial damage involves a wide spectrum of microcrack sizes then damage accumulation effect may not occur. Instead, a longest and most favorably oriented microcrack may cause spontaneous failure under long range tensile strain (the so-called extrinsic failure; Krajcinovic, 1996). The rock-like materials, however, are seldom subjected to tensile loads in their natural environments or by design. Under compressive loading, the damage accumulation is a sound experimental fact, thus S_{ijkl} or $\omega = N\langle a^3\rangle/V$ are legitimate damage measures.

The Rice thermodynamic framework with microstructural internal parameters has effectively been applied in Chapter 4 to formulate the macroscopic stress–strain relations for brittle rocks in compression based on the sliding microcrack mechanism. The key element of the proposed model is the correct expression for the Gibbs potential. Once it has been done, the derivation of the inelastic strain increments due to frictional sliding and wing microcracking is only a matter of a proper flux identification and carefully performed differentiation operations. In this sense, the proposed model can be seen as an alternative, if not advantageous, algorithm as compared with the kinematical one for which the respective crack opening displacement tensor (or effective secant compliance tensor) is the basic ingredient spanning the micro- and macroscale. The microcrack interaction being not considered, the model predictions (volume-averaged over the RVE) have yielded reasonable results when confronted with the test data (Figure 4.8). However, an open question still remains how to incorporate the microcrack interactions into the Rice formalism and what are the limits of such incorporation.

The percolation theory when used to brittle damage and failure problems is contingent to certain limitations as well. Since the percolation-type disorder is bi-modal, it is a suitable modeling tool for damage phenomena dominated by random and uncorrelated microdefect nucleation. Consequently, it has been used in Chapter 8 to verify the validity of the effective-media estimates of the elastic modulus for a plate with randomly located circular holes – a classical site percolation problem. It would be inappropriate to use it in cases dominated by microdefect growth since the requirement of randomness is then not preserved. Physically, the percolation model is well suited for compression problems with significant confining pressures inhibiting the growth of the nucleated microcracks (e.g. deformation of brittle rocks in crustal conditions). Also, spall damage falls within the same class of problems since high intensities and short duration times of tensile rarefaction waves favor random microcrack nucleation. Referring to the results depicted in Figure 8.2, it has been concluded in Chapter 8 that the SCM is the only method among the considered ones that predicts a vanishing elastic modulus at a finite value of the porosity. This observation has been interpreted that SCM model correctly predicts the existence of the percolation threshold, although the actual value of the critical porosity $f_c^{SCM}(E = 0) = 0.33$ underestimates the exact one by ca. 27%. A similar conclusion but without any reference to percolation was suggested in Budiansky–O'Connell (1976). On the other hand, some authors consider the occurrence of the critical porosity f_c^{SCM} to be rather a deficiency of the method than a merit. That criticism is based on the assumption that elastic modulus should decrease smoothly with increasing porosity and vanish only when $f_c \to 1$, Figure 8.2. It also means that statistical homogeneity of the material is kept preserved in the effective continua models until the specimen is entirely filled up with holes which, in fact, excludes the hole clustering. Which conclusion is correct it remains yet to be seen but claiming that randomly diluted material will not generate hole clusters seems to be too restrictive and contradicting the basic results of the percolation theory.

Micromechanical modeling combined with the percolation theory has successfully been applied to corrosive type of damage in concrete-like materials brought about by chemically aggressive substances diffusing through the material microstructure and reacting with the hardened cement paste (cf. Chapter 6). This type of micromechanical modeling is quite complex since it involves several coupled physico-chemical processes, some of them proceeding at very different time rates, what makes the numerical computations rather unwieldy. Therefore, like in other workable micromechanical models, a string of simplifying assumptions has had to be introduced in order to make the proposed model manageable. In return, the model has handled the difficult problem of external sulphate attack on concrete with relative ease giving predictions that agree fairly well with the test data (Figure 6.6).

Future research

The bulk of the author's research work presented in this thesis has been concerned with the microcracks embedded in a homogeneous elastic matrix. This is an important but a first step in constructing a rational damage theory of brittle deformation. Except for Chapter 8, where particular damage simulations on disordered lattices have been discussed, the statistics of the material microstructure has not been considered. Distributions of weak planes, energy barriers and local stresses within a material sample are statistical in nature and are prone to evolve as the deformation process continues. Consequently, if a damage model aspires to be realistic, it will eventually have to take all these effects into account. This need is well matched by the progress in experimental techniques allowing for a steadily improving reconstruction of the damaged material structure from the test data. However, as long as the data acquisition is not feasible or incomplete, computational micromechanics or computer simulations combined with the methods of statistical physics will have to suffice for some time.

Another aspect of the brittle damage that requires careful scrutiny is the softening regime in the stress–strain diagrams. Physically, it is related to the localization of microcracks into a dominant cluster (fault or shear band). The fault contributes overwhelmingly to the overall specimen displacements while the rest of the material remains elastic or may even experience elastic unloading. The material ceases to be statistically homogeneous rendering the RVE concept invalid.

A potentially interesting but difficult topic is the brittle-ductile transition. Except for the preliminary effort in Horii and Nemat-Nasser (1986), little else has been done in the theoretical modeling of this phenomenon. There seems to be an urgent need to investigate this problem since crustal rocks are often exposed to large confinements which make them behave in a ductile manner.

The size effect in brittle materials is a well-known phenomenon that has been studied experimentally and theoretically for over 40 years now (e.g. Leonhardt and Walter, 1962; Bazant, 1984; Elices and Planas, 1992). However, the results of those studies are all too seldom employed in the existing damage models. Since the size (and shape) effects cannot be ignored in concrete structures, formulation of damage models with account for the size effect seems to be an appealing research area.

As for phenomenological damage models, only those based on the underlying micromechanics have a good chance for success. The current trend in this type of modeling is to include the problems of frictional sliding and microcrack closure in the constitutive framework (cf. Halm and Dragon, 1998).

Apart from the cognitive aspect, the ultimate goal of micromechanical, phenomenological and lattice damage descriptions should be in providing models that are applicable to failure analysis of engineering structures. Speaking more generally, it seems that the future of damage mechanics will depend on its role in estimations of structural failure.

Finally, a comment on experimental challenges in the context of brittle damage mechanics. Despite the continuous progress in the experimental characterization of damage, there are numerous issues awaiting resolution. First of all, unambiguous identification of microcrack number, shapes, sizes and orientation within the specimen poses a serious experimental problem. Usually, it is being done from the observation of thin sections of a damaged specimen. Acoustic emissions measurements combined with digital image processing are very helpful furnishing reliable (yet quantitative) information regarding the location, type of nucleating microcracks and their evolution patters. Also, it is necessary to develop experimental techniques capable of distinguishing closed microcracks (passive damage) within a heterogeneous material texture. Most of the analytical or numerical models in damage mechanics refer to the RVE without giving much thought to its size or even existence. Although conceptually relatively clear, the RVE determination from tests is a demanding task for experimentalists.

References

Aboudi, J. (1991). *Mechanics of Composite Materials – a Unified Micromechanical Approach*, Elsevier, Amsterdam.

Ashby, M.F. (1979). Micromechanics of fracture in static and cyclic failure, in: *Fracture Mechanics*, R.A. Smith (Ed.), Pergamon Press, Oxford, 1–27.

Ashby, M.F. and Hallam, S.D. (1986). The failure of brittle solids containing small cracks under compressive stress states, *Acta Metall.*, **34**, 497–510.

ASTM C1012 (1987). Standard test method for: Length change of hydraulic-cement mortars exposed to a sulphate solution, *Annual Book of ASTM Standards*, 04.01.

ASTM C490 (1986). Standard specification for: Apparatus for use in measurement of length change of hardened cement paste, mortar and concrete, *Annual Book of ASTM Standards*, 04.01.

Atkinson, B.K. and Meredith, P.G. (1987). Experimental fracture mechanics data for rocks and minerals, in: *Fracture Mechanics of Rock*, B.K. Atkinson (Ed.), Academic Press, London, 477–525.

Balberg, I. (1987). Recent developments in continuum percolation, *Phil. Mag.* **B56**, 991–1003.

Balberg, I., Anderson, C.H., Alexander, S. and Wagner, N. (1984). Excluded volume and its relation to the onset of percolation, *Phys. Rev. B*, **30**, 3933–3943.

Barenblatt, G.I., Zheltov, Iu.P. and Kochina, I.N. (1960). Basic concepts in the theory of seepage of homogeneous liquids in fissured rocks, *Prikl. Mat. i Mekh.*, **24**, 852–864.

Basista, M. (1984). Continuum Damage Mechanics – a review of existing theories, *IFTR Reports*, 40 (in Polish).

Basista, M. (1988). Damage mechanics: experimental background, *Eng. Trans.*, **36**, 707–737.

Basista, M. (1993). On micromechanical modeling of deformation of compact rock in compression, *Eng. Trans.*, **41**, 395–417.

Basista, M. (1997) Modeling of spall damage in brittle solids, *Eng. Trans.*, **45**, 501–527.

Basista, M (1999). Micromechanical, phenomenological, and lattice modeling of brittle damage, in: *Modeling of Damage and Fracture Processes in Engineering Materials*, M. Basista and W.K. Nowacki (Eds.), IPPT PAN, Warszawa, 236–298.

Basista, M. (2000). On interactions of frictional cracks, *Arch. Mech.*, **52**, 329–340.

Basista, M. and Gross, D. (1985). One-dimensional constitutive model of microcracked elastic solid, *Arch. Mech.*, **37**, 587–601.

Basista, M. and Gross, D. (1989). A note on brittle damage description, *Mech. Res. Comm.*, **16**, 147–154.

Basista, M. and Gross, D. (1997). Internal variable representation of microcrack induced inelasticity in brittle materials, *Int. J. Damage Mechanics*, **6**, 300–316.

Basista, M. and Gross, D. (1998a) The sliding crack model of brittle deformation: an internal variable approach, *Int. J. Solids Structures*, **35**, 487-509.

Basista, M. and Gross, D. (1998b) The sliding crack model revisited, in: *Damage Mechanics in Engineering Materials*, G.Z. Voyiadjis, J.W. Ju and J.L. Chaboche (Eds.), Elsevier Science, 125–143.

Basista, M. and Gross, D. (2000). A note on crack interactions in compression, *Int. J. Fracture*, **102**, L67–L72.

Basista, M. and Krajcinovic D. (1991). Brittle deformation of disordered solids, *Composites Eng.*, **1**, 103–112.

Basista, M., Krajcinovic, D. and Sumarac D. (1991) Analytical modeling of the brittle deformation of solids, in: *Damage Mechanics in Engineering Materials*, J.W. Ju, D. Krajcinovic, H. Schreyer (Eds.), ASME Publ., AMD-**109**, MD-**24**, New York, 27–40.

Basista, M., Krajcinovic, D. and Sumarac D. (1992). Micromechanics, phenomenology and statistics of brittle deformation, in: *Computational Plasticity – Fundamentals and Applications*, D.R.J. Owen, E. Oñate, E. Hinton (Eds.), Pineridge Press, Swansea, UK., 1479–1490.

Bazant, Z.P. (1984). Size effect in blunt fracture: concrete, rock, metal, *J. Engng Mech. ASCE*, **110**, 518–535.

Bazant, Z.P, Bittnar, Z., Jirasek, M. and Mazars, J. (1994). *Fracture and Damage in Quasi-brittle Structures*, E & FN Spon, London.

Bazant, Z.P., Sener, S. and Kim, J.K. (1987). Effect of cracking on drying permeability and diffusivity of concrete, *ACI Mater. J.*, **84-M35**, 351–357.

Beale, P.D. and Srolovitz, D.J. (1988). Elastic fracture in random materials, *Phys. Rev. B*, **37**, 5500–5507.

Benguigui, L. (1984). Experimental study of the elastic properties of a percolating system, *Phys. Rev. Lett.*, **53**, 2028–2030.

Benguigui, L. (1986a). Elasticity and fracture near a percolation threshold in two dimensions, in: *Fragmentation, Form and Flow in Fractured Media*, R. Englman and Z. Jaeger, eds., *Annals Israel Phys. Soc.*, **8**, 288–293.

Benguigui, L. (1986b). Lattice and continuum percolation transport exponents: Experiments in two-dimensions, *Phys. Rev. B*, **34**, 8176–8179.

Bensoussan, A., Lions, J.L. and Ramos, R.R. (1978). *Asymptotic Analysis for Periodic Structures*, North Holland, New York.

Benveniste, Y., Dvorak, G.J. and Chen, T. (1991). On diagonal and elastic symmetry of the approximate effective stiffness tensor of heterogeneous media, *J. Mech. Phys. Solids*, **39**, 927–946.

Benveniste, Y., Dvorak, G.J., Zarzour, J. and Wung, E.C.J. (1989). On interacting cracks and complex crack configurations in linear elastic media, *Int. J. Solids* Structures, **25**, 1279–1293.

Bettin, A. and Gross, D. (1990). Crack propagation in materials with local inhomogeneities under thermal load, in: *Thermal Effects in Fracture of Multiphase Materials*, K.P. Herrrmann and Z.S. Olesiak (Eds.), Lecture Notes in Engineering, Springer Verlag, **59**, 85–93.

Biczok, I. (1972). *Concrete Corrosion Concrete Protection*, Akademiai Kiado, Budapest.

Bieniawski, Z.T. (1967). Mechanism of brittle fracture of rock, *Int. J. Rock Mech. Min. S*ci. **4**, 407–423.

Brace, W.F. and Bombolakis, E.G. (1963). A note on brittle crack growth in compression, *J. Geophys. Res.*, **68**, 3709–3713.

Brace, W.F., Paulding, B.W. and Scholz, C. (1966). Dilatancy in the fracture of crystalline rocks, *J. Geophys. Res.*, **71**, 3939–3953.

Bristow, J.R. (1960). Microcracks and the static and dynamic elastic constants of annealed and heavily cold-worked metals, *British J. Appl. Phys.*, **11**, 81–85.

Broek, D. (1974). *Elementary Engineering Fracture Mechanics*, Noordhoff, Leyden.

Brown, P.W. and LaCroix, P. (1989). The kinetics of ettringite formation, *Cem. Concr. Res.*, **19**, 879–884.

Brühwiler, E., Flückinger, D. and Rösli, H. (1986). Versuche über den Einfluss höher Dehngeschwindigkeiten und Vorbelastungsgeschichten auf die Festigkeit und das Verformungsverhalten von Beton, *Versuchsbericht*, Eidgenössiche Technische Hochschule, Zürich.

Budiansky, B. and O'Connell, R.J. (1976). Elastic moduli of cracked solid, *Int. J. Solids Struct*ures, **12**, 81–97.

Cannon, N.P., Schulson, E.M., Smith, T.R. and Frost, H.J. (1990). Wing cracks and brittle compressive fracture, *Acta Metall. Mater.*, **38**, 1955–1962.

Chaboche, J.L. (1988). Continuum damage mechanics. Part I and II, *J. Appl. Mech.*, **55**, 59–72.

Chaboche, J.L. (1999). Thermodynamically founded CDM models for creep and other conditions, in: *Creep and Damage in Materials and Structures*, H. Altenbach and J. Skrzypek (Eds.), Springer, Vienna.

Charlaix, E. (1986). Percolation thresholds of a random array of discs: A numerical simulation, *J. Phys. A*, **19**, L533–L536.

Chen, W. F. (1982). *Plasticity of Concrete*, McGraw–Hill, New York.

Chen, Y.Z. (1984). General case of multiple crack problems in an infinite plate, *Eng. Fracture Mech.*, **20**, 591–597.

Christensen, R.M. (1990). A critical evaluation for a class of micro-mechanics models, *J. Mech. Phys. Solids*, **38**, 379–404.

Christensen, R.M. (1991). *Mechanics of Composite Materials.* Krieger, Malabar, FL.

Chrzanowski, M. (1976). Use of the damage concept in describing creep-fatigue interaction under prescribed stress, *Int. J. Mech. Sci.*, **18**, 69–73.

Cleary, M.P., Chen, I.W. and Lee, S.M. (1980). Self-consistent techniques for heterogeneous media, *J. Eng. Mech. Div. ASCE*, **106**, 861–887.

Coon, M.D. and Evans, R.J. (1972). Incremental constitutive laws and their associated failure criteria with application to plain concrete, *Int. J. Solids Structures*, **8**, 1169–1183.

Costin, L.S. (1983). A microcrack model for the deformation and failure of brittle rock, *J. Geophys. Res.*, **88**, 9485–9492.

Cotterell, B. and Rice, J.R. (1980). Slightly curved or kinked cracks, *Int. J. Fract.*, **16**, 155–169.

Cox, S.J.D. and Paterson, L. (1990). Damage development during rupture of heterogeneous brittle materials: a numerical study, in: *Deformation Mechanisms, Rheology and Tectonics*, R.J. Knipe and E.H. Rutter (Eds.), Geol. Soc. Lond. Spec. Publ.

Daniels, H.E. (1945). The statistical theory of the strength of bundles of threads, *Proc. Roy. Soc. London. A*, **183**, 405–435.

Davison, L. and Stevens, A.L. (1973). Thermomechanical constitution of spalling elastic bodies, *J. Appl. Phys.*, **44**, 668–674.

Dawson, B.E. (1973). *Kinetics and Mechanisms of Reactions.* Methuen Educational Ltd., London.

de Arcangelis, L. and Herrmann, H.J. (1989). Scaling and multiscaling laws in random fuse networks, *Phys. Rev. B*, **39**, 2678–2681.

de Arcangelis, L., Redner S. and Herrmann, H.J. (1985). A random fuse model for breaking process, *J. Physique Lett.*, **46**, L585–L590.

Delaplace, A., Pijaudier-Cabot, G. and Roux, S. (1996). Progressive damage in discrete models and consequences on continuum modelling, *J. Mech. Phys. Solids*, **44**, 99–136.

Deng, H. and Nemat-Nasser, S. (1992). Dynamic damage evolution in brittle solids, *Mech. Mater.*, **14**, 83–103.

Deng, H. and Nemat-Nasser, S. (1994). Microcrack interaction and shear fault failure, *Int. J. Damage Mech.*, **3**, 3–37.

Dienes, J.K. (1982). Permeability, percolation, and statistical crack mechanics, in: *Issues on Rock Mechanics*, R.E. Goodman and F.E. Heuze (Eds.), Proc. 23rd Symp. on Rock Mech., Berkeley, CA.

Doliński, K. (1999). Fatigue damage and reliability assessment of cemented hip prosthesis, *J. Theor. Appl. Mech.*, **37**, 505–518.

Dougill, J.W. (1976). On stable progressively fracturing solids, *ZAMP*, **27**, 423–437.

Dragon, A. and Mróz, Z. (1979). A continuum model for plastic-brittle behavior rock and concrete, *Int. J. Eng. Sci.*, **17**, 121–137.

Dullien, F.A.L. (1979). *Porous Media. Fluid Transport and Pore Structure*, Academic Press, New York.

Duxbury, P.M., Leath, P.L. and Beale, P.D. (1987). Breakdown properties of quenched random systems: The random-fuse network, *Phys. Rev. B*, **36**, 367–380.

Dyskin, A.V., Germanovich, L.N., Jewell, R.J., Joer, H., Krasinski, J.S., Lee, K.K., Roegiers, J.-C., Sahouryeh, E. And Ustinov, K.B. (1995). Some experimental results on three-dimensional crack propagation in compression, in: *Mechanics of Jointed and Faulted Rock*, Rossmanith (ed.), Balkema Rotterdam, 91–96.

Eimer, Cz. (1978). Elasticity of cracked medium, *Arch. Mech.*, **30**, 827–836.

Elices, M. and Planas, J. (1992). Size effect in concrete structures: R-curve approach, in: *Application of Fracture Mechanics to Reinforced Concrete*, A. Carpinteri (Ed.), Elsevier Applied Science, Torino, Italy, 169–200.

Englman, R., Gur, Y. and Jaeger, Z. (1983). Fluid flow through a crack network in rocks, *J. Appl. Mech.*, **50**, 707–711.

Erdogan, F. And Sih, G.C. (1963). On the crack extension in plates under plane loading and transverse shear, *J. Basic Eng.*, **85**, 519–527.

Evans, R.H. and Marathe, M.S. (1968). Microcracking and stress–strain curves for concrete in tension, *Matériaux et Constructions*, **1**, 61–64.

Fanella, D. and Krajcinovic, D. (1988). A micromechanical model for concrete in compression, *Eng. Fract. Mech.*, **29**, 49–66.

Feng, S. and Sen, P.N. (1984). Percolation on elastic networks: New exponents and threshold, *Phys. Rev. Lett.*, **52**, 216–280.

Feng, S., Sen, P.N., Halperin, B.I. and Lobb, C.J. (1984). Percolation on two-dimensional elastic networks with rotationally invariant bond-bending forces, *Phys. Rev. B*, **30**, 5386–5389.

Feng, X.Q. and Yu, S.W. (1995). Micromechanical modelling of tensile response of elastic-brittle materials, *Int. J. Solids Structures*, **32**, 3359–3372.

Finlayson, B.A. (1980). *Nonlinear Analysis in Chemical Engineering*, McGraw–Hill, New York.

Forster, F. and Scheil, E. (1936). Akustische Untersuchung der Bildung von Martensitnadeln, *Z. Metallkunde*, **29**, 245.

Gambin, B. and Telega, J.J. (2000). Effective properties of elastic solids with randomly distributed microcracks, *Mech. Res. Comm.*, **27**, 697–706.

Germanovich, L.N., Carter, B.J., Ingraffea, A.R., Dyskin, A.V. and Lee, K.K. (1996). Mechanics of 3-D crack growth under compressive loads, in: *Rock Mechanics*, Aubertin, Hassani and Mitri (Eds.), Balkema, Rotterdam, 1151–1160.

Goodman, R.E. (1963). Subaudible noise during compression of rocks, *Geol. Soc. Amer. Bull.*, **74**, 487–490.

Griggs, D.T., Turner, F.J. and Heard, H.C. (1960). Deformation of rocks at 500° to 800°C, in: *Rock Deformation. Geol. Soc. A. Mem.*, **79**, 39–104.

Gross, D. (1982). Spannungsintensitaetsfaktoren von Risssystemen, *Ing. Archiv*, **51**, 301–310.

Gross, D. (1996). *Bruchmechanik*, Springer, Berlin–Heidelberg.

Gross, D., Becker, W. and Basista, M. (1990). A simple mesostructural model for damage-induced inelasticity of brittle materials, in: *Yielding, Damage, and Failure of Anisotropic Solids*, J.P. Boehler (Ed.), Mechanical Eng. Publ., London, 681–692.

Gueguen, Y. and Dienes, J. (1989). Transport properties of rocks from statistics and percolation, *Math. Geol.*, **21**, 1–13.

Halm, D. and Dragon, A. (1998). Anisotropic model of damage and frictional sliding for brittle materials, *Eur. J. Mechanics A/Solids*, **17**, 439–460.

Halperin, B.I., Feng, S. and Sen, P.N. (1985). Differences between lattice and continuum percolation transport exponents, *Phys. Rev. Lett.*, **54**, 2391–2394.

Hansen, A., Hinrichsen, E.L. and Roux, S. (1991). Scale-invariant disorder in fracture and related breakdown phenomena, *Phys. Rev. B*, **43**, 665–678.

Hansen, A., Roux, S. and Herrmann H.J. (1989). Rupture of central-force lattices, *J. Physique*, **50**, 733–744.

Hansen, W.C. (1968). The chemistry of sulphate-resisting portland cement, in: *Performance of Concrete*, E.G. Swenson (Ed.), University of Toronto Press, 18–55.

Hayakawa, K. and Murakami, S. (1998). Space of damage conjugate force and damage potential of elastic-plastic-damage materials, in: *Damage Mechanics in Engineering Materials*, G.Z. Voyiadjis, J.W. Ju and J.L. Chaboche (Eds.), Elsevier Science, 27–44.

Hemmer, P.C. and Hansen, A. (1992). The distribution of simultaneous fiber failures in fiber bundles, *J. Appl. Mech.*, **59**, 909–914.

Herrmann H.J., Hansen, A. and Roux, S. and (1989). Fracture of disordered, elastic lattices in two dimensions, *Phys. Rev. B*, **39**, 637–648.

Herrmann, H. J. and Roux, S. (1990). *Statistical Models for the Fracture of Disordered Media*, North-Holland.

Hill, R. and Rice, J.R. (1973). Elastic potentials and the structure of inelastic constitutive laws, *SIAM J. Appl. Math.*, **25**, 448–461.

Holcomb, D.J. (1983). Using acoustic emissions to determine in-situ stress: problems and promise, in: *Geomechanics – AMD, ASME Publ.*, S. Nemat-Nasser, ed., **57**, 11, New York.

Holcomb, D.J. and Costin, L.S. (1986). Detecting damage surfaces in brittle materials using acoustic emissions, *J. Appl. Mech.*, **53**, 536–544.

Horii, H. and Nemat-Nasser, S. (1983). Overall moduli of solids with microcracks: load induced anisotropy, *J. Mech. Phys. Solids*, **31**, 155–171.

Horii, H. and Nemat-Nasser, S. (1985a). Compression-induced microcrack growth in brittle solids: axial splitting and shear failure, *J. Geophys. Res.*, **90**, 3105–3125.

Horii, H. and Nemat-Nasser, S. (1985b). Elastic fields of interacting inhomogeneities, *Int. J. Solids Structures*, **21**, 731–745

Horii, H. and Nemat-Nasser, S. (1986). Brittle failure in compression: splitting, faulting and brittle-ductile transition, *Phil. Trans. Roy. Soc. London*, **319**, 337–374.

Ingraffea, A.R. (1987). Theory of crack initiation and propagation in rock, in: *Fracture Mechanics of Rock*, B.K. Atkinson (Ed.), Academic Press, London, 71–110.

Irwin, G.R. (1957). Analysis of stresses and strains near the end of a crack traversing a plate, *J. Appl. Mech.*, **24**, 361–365.

Jaeger, J.C. and Cook, N.G.W. (1976). *Fundamentals of Rock Mechanics*, Chapman and Hall, London.

Janson, J. and Hult, J. (1977). Fracture mechanics and damage mechanics – a combined approach, *J. Méc. Appl.*, **1**, 69–84.

Ju, J.W. (1991). On two-dimensional self-consistent micromechanical damage models for brittle solids, *Int. J. Solids Structures*, **27**, 227–258.

Ju, J.W. and Tseng, K.H. (1995). An improved two-dimensional micromechanical theory for brittle solids with randomly located interacting microcracks, *Int. J. Damage Mech.*, **4**, 23–57.

Kachanov, L.M. (1958). On the time to rupture in creep conditions, *Izv. AN SSSR, Otd. Tekhn Nauk*, **8**, 26–31.

Kachanov, L.M. (1976). *Introduction to Continuum Damage Mechanics*, Nijhoff, Dordrecht.

Kachanov, M. (1980). Continuum model of medium with cracks, *J. Eng. Mech. Div. ASCE*, **106**, 1039–1051.

Kachanov, M. (1982). A microcrack model of rock inelasticity, Part I: Frictional sliding on microcracks, *Mech. Mater*, **1**, 19–27.

Kachanov, M. (1987). Elastic solids with many cracks – a simple method of analysis, *Int. J. Solids Structures*, **23**, 23–43.

Kachanov, M. (1992). Effective elastic properties of cracked solids. Critical review of some basic concepts, *Appl. Mech. Rev.*, **45**, 304–335.

Kachanov, M. (1993). Elastic solids with many cracks and related problems, in: *Advances in Applied Mechanics*, J. Hutchinson and T. Wu (Eds.), **30**, 259–445, Academic Press, New York, NY.

Kaiser, J. (1950). An investigation into the occurrence of noises in tensile tests or a study of acoustic phenomena in tensile tests, *PhD thesis*, Technische Hochschule München, Germany

Kasperkiewicz, J. (1983). Modelling of inhomogeneity in certain cement-based composites, *Int. J. Cement Composites and Lightweight Concrete*, **5**, 41–48.

Kemeny, J.M. and Cook, N.G.W. (1991). Micromechanics of deformation in rocks, in: *Toughening Mechanisms in Quasi-Brittle Materials*, S. P. Shah, ed., Kluwer, 155–188.

Kendall, K. (1978). Complexities of compression failure, *Proc. R. Soc. London A.* **361**, 245–263.

Kestin, J. (1992). Local equilibrium formalism applied to mechanics of solids, *Int. J. Solids Structures*, **29**, 1827–1836.

Kestin, J. and Bataille, J. (1978). Irreversible thermodynamics of continua and internal variables, in: *Continuum Models of Discrete Systems*, J.W. Provan (Ed.), Univ. of Waterloo Press, Waterloo, Canada.

Kestin, J. and Rice, J.R. (1970). Paradoxes in the application of thermodynamics to strained solids, in: *Critical Review of Thermodynamics*, E. B. Stuart et al., eds., Mono Book Corp., Baltimore, 275–298.

Knott, J.F. (1973). *Fundamentals of Fracture Mechanics*, Butterworth, London.

Krajcinovic D. and Basista, M. (1991b). Rupture of central–force lattices revisited, *J. Physique I*, **1**, 241–245.

Krajcinovic D., Basista, M. and Sumarac D. (1991a). Micromechanically inspired phenomenological damage model, *J. Appl. Mech.*, **58**, 305–310.

Krajcinovic D., Basista, M. and Sumarac D. (1991b). Micromechanics of brittle composites exposed to chemically aggressive ambients, in: *Microcracking Induced Damage in Composites*, G. Dvorak and C. Lagoudas (Eds.), ASME Publ., AMD-**109**, MD-**22**, New York, 101–112.

Krajcinovic D., Basista, M. and Sumarac D. (1994). Basic principles of damage mechanics, in: *Damage Mechanics of Composite Materials*, R. Talreja (Ed.), Elsevier, 1–51.

Krajcinovic D., Basista, M., Mallick K. and Sumarac D. (1992). Chemo-micromechanics of brittle solids, *J. Mech. Phys. Solids*, **40**, 965–990.

Krajcinovic D., Mallick K., Basista, M. and Sumarac D. (1992). Elastic moduli of perforated plates in the neighborhood of critical state, *Int. J. Solids Structures*, **29**, 1837–1847.

Krajcinovic, D. (1979). Distributed damage theory of beams in pure bending, *J. Appl. Mech.*, **46**, 592–596.

Krajcinovic, D. (1984). Continuum damage mechanics, *Appl. Mech. Rev.*, **37**, 397–402.

Krajcinovic, D. (1989). Damage mechanics, *Mech. Mater.*, **8**, 117–197.

Krajcinovic, D. (1995). Continuum damage mechanics: when and how?, *Int. J. Damage Mech.*, **4**, 217–229.

Krajcinovic, D. (1996). *Damage Mechanics*, Elsevier, Amsterdam.

Krajcinovic, D. (2000). Damage mechanics: accomplishments, trends and needs, *Int. J. Solids Structures*, **37**, 267–277.

Krajcinovic, D. and Fanella, D. (1986). A micromechanical damage model for concrete, *Eng. Fract. Mech.*, **25**, 585–596.

Krajcinovic, D. and Fonseka, G.V. (1981). The continuous damage theory of brittle materials. Parts I and II, *J. Appl. Mech.*, **48**, 809–824.

Krajcinovic, D. and Mastilovic, S. (1995). Some fundamental issues of damage mechanics, *Mech. Mater.*, **21**, 217–230.

Krajcinovic, D. and Silva, M. A. G. (1982). Statistical aspects of the continuous damage theory, *Int. J. Solids Structures*, **18**, 551–562.

Krajcinovic, D. and Sumarac, D. (1987). Micromechanics of damage processes, in: *Continuum Damage Mechanics: Theory and Application*, D. Krajcinovic and J. Lemaitre (Eds.), Springer, Vienna.

Krajcinovic, D. and Sumarac, D. (1989). A mesomechanical model for brittle deformation processes, *J. Appl. Mech.*, **56**, 51–62.

Krajcinovic, D. and Vujosevic, M. (1998). Strain localization – short to long correlation length transition. *Int. J. Solids Structures*, **35**, 4147–4166.

Krajcinovic, D., Lubarda, V. and Sumarac, D. (1993). Fundamental aspects of brittle cooperative phenomena – Effective continua models, *Mech. Mater.*, **15**, 99–115.

Labuz, J.F. and Bridell, J.M. (1993). Reducing frictional constraint in compression testing through lubrication, *Int. J. Rock Mech. Min. Sci.& Geomech. Abstr.*, **30**, 451–455.

Labuz, J.F. and Carvalho, F.C.S. (1998). Micromechanisms in failure of rock-like materials, Paper presented at the *32. Solid Mechanics Conference SolMec'98*, Zakopane, Poland.

Lauterbach, B. (2001). Zur mikrorissinduzierten Schädigung spröder Materialien, *PhD Thesis*, Institute of Mechanics, Darmstadt University of Technology, Germany.

Lauterbach, B. and Gross, D. (1998). Crack growth in brittle solids under compression, *Mech. Mater.*, **29**, 81–92.

Lauterbach, B. and Gross, D. (1999). Analysis of microcrack interaction in brittle solids, in: *Fracture and Damage Mechanics*, M.H. Aliabadi (Ed.), University of London, UK, 213–222.

Lawn, B.R. and Wilshaw, T.R. (1975). *Fracture of Brittle Solids*, Cambridge University Press, Cambridge, UK.

Lawn. B.R, Marshall, D.B (1998). Nonlinear stress–strain curves for solids containing closed cracks with friction, *J. Mech. Phys. Solids*, **46**, 85–113.

Lea, F.M. (1970). *The Chemistry of Cement and Concrete.* Edward Arnold, London.

Lehner, F. and Kachanov, M. (1996). On modelling of "winged" cracks forming under compression, *Int. J. Fract.*, **77**, R69–R75.

Lemaitre, J. (1996). *A Course on Damage Mechanics*, Springer, Berlin–Heidelberg.

Lemaitre, J. and Chaboche, J.L. (1978). Aspect phénoménologique de la rupture per endommagement, *J. Méc. Appl.*, **2**, 317–365.

Lemaitre, J. and Chaboche, J.L. (1985). *Mécanique des Materiaux Solides*, Dunod, Paris.

Lemieux, M.A., Bretton, P. and Tremblay, A.M.S. (1985). Unified approach to numerical transfer matrix methods for disordered systems: Application to mixed crystals and to elasticity percolation, *J. Phys. Lett.*, **46**, L1–L7.

Leonhardt, F. And Walter, R. (1962). Beiträge zur Behandlung der Schubprobleme in Stahlbetonbau. *Beton- und Stahlbetonbau* (Berlin), March, 56–64, and June, 141–149.

Lewiński, T. and Telega, J.J. (2000). *Plates, Laminates and Shells. Asymptotic Analysis and Homogenization*, Series on Advances in Mathematics for Applied Sciences, **52**, World Scientific, Singapore.

Litewka, A. (1985). Effective material constants for orthotropically damaged elastic solid, *Arch. Mech.*, **37**, 631–642.

Litewka, A. and Hult, J. (1989). One parameter CDM model for creep rupture prediction, *Eur. J. Mech., A/Solids*, **8**, 185–200.

Lockner, D. (1993) The role of acoustic emission in the study of rock fracture, *Int. J. Rock Mech. Min. Sci. & Geomech. Abstr.*, **30**, 883–899.

Lubarda, V. and Krajcinovic, D. (1993). Damage tensors and the crack density distribution, *Int. J. Solids Structures*, **30**, 2859–2877.

Lubarda, V. and Krajcinovic, D. (1995). Constitutive structure of the rate theory of damage in brittle elastic solids, *Appl. Math. Comp.*, **67**, 81–101.

Mai, Y.W. (1991). Failure characterisation of fibre-reinforced cement composites with *R*-curve characteristics, in: *Toughening Mechanisms in Quasi-Brittle Materials*, S.P. Shah (Ed.), Kluwer Publ., New York, 489–527.

Mai, Y.W. and Cotterell, B. (1982). Slow crack growth and fracture instability in cement composites, *Int. J. Cement Composites*, **4**, 33–37.

Martin, J.B. (1975). *Plasticity. Fundamentals and General Results.* MIT Press, Cambridge, MA.

Matczyński, M. and Sokołowski, M. (1982). Interaction of cracks in elastic media, *Arch. Mech.*, **34**, 89–104.

Mather, B. (1968). Field and laboratory studies of the sulphate resistance of concrete, in: *Performance of Concrete*, E.G. Swenson (Ed.), University of Toronto Press, 66–76.

Mauge, C. and Kachanov, M. (1994). Effective elastic properties of an anisotropic material with arbitrary oriented interacting cracks, *J. Mech. Phys. Solids*, **42**, 561–584.

Mchedlow-Petrosjan, O.P. (1988). *The Chemistry of Inorganic Structural Materials*, 2nd edition, Stroi-Izdat, Moscow.

Mehta, P.K. (1983). Mechanism of sulphate attack on portland cement concrete – another look, *Cem. Concr. Res.*, **13**, 401–406.

Meredith, P.G. (1989). Comparative fracture toughness testing of rocks, in: *Fracture Toughness and Fracture Energy. Test Methods for Concrete and Rock.* Tohoku Univ. Sendai, Japan, 211–223.

Meredith, P.G., Ayling, M.R., Murrell, S.A.F. and Sammonds, P.R. (1991). Cracking, damage and fracture in stressed rock: a holistic approach, in: *Toughening Mechanisms in Quasi-Brittle Materials*, S.P. Shah (Ed.), Kluwer, The Netherlands, 67–89.

Mindess, S. and Young, J.F. (1981). *Concrete*, Prentince Hall, Englewood Clifs, N.J.

Mogi, K. (1962). Study of the elastic shocks caused by the fracture of a heterogeneous material and its relation to earthquake phenomena, *Bull. Earthquake Res. Inst.*, **40**, 125–173.

Mogi, K. (1966). Pressure dependence of rock strength and transition form brittle to ductile flow, *Bull. Earth. Res. Inst.*, **44**, 215–232.

Moss, W.C. and Gupta, Y.M. (1982). A constitutive model describing dilatancy and cracking in brittle rock, *J. Geophys. Res.*, **87**, 2985–2998.

Moukwa, M. (1990). Characteristics of the attack of cement paste by $MgSO_4$ and $MgCl_2$ from the pore structure measurements, *Cem. Concr. Res.*, **20**, 148–158.

Mróz, Z. and Seweryn, A. (1999) Multiaxial damage and fatigue conditions, in: *Modeling of Damage and Fracture Processes in Engineering Materials*, M. Basista and W.K. Nowacki (Eds.), IPPT PAN, Warszawa, 117–180.

Mura, T. (1987). *Micromechanics of Defects in Solids*, Martinus Nijhoff Publ., The Hague, The Netherlands.

Murakami, S. (1988). Mechanical modelling of material damage, *J. Appl. Mech.*, **55**, 280–286.

Murakami, S., Hayakawa, K. and Liu, Y. (1998). Damage evolution and damage surface of elastic-plastic-damage materials under multiaxial loading, *Int. J. Damage Mech.*, **7**, 103–128.

Murakami, S. and Kamiya, K. (1997). Constitutive and damage evolution equations of elastic-brittle materials based on irreversible thermodynamics, *Int. J. Solids Structures*, **39**, 473–486.

Murakami, S. and Ohno, N. (1981). A continuum theory of creep and creep damage, in: *Creep in Structures*, A.R.S. Ponter and D.R. Hayhurst, (Eds.), 422–444, Springer Verlag, Berlin.

Murakami, Y. (1987). *Stress Intensity Factors Handbook*, Pergamon Press, New York.

Murzewski, J. (1957). Une théorie statistique du corps fragile quasi-homogene, *IX-e Congrés International de Mécanique Apliquée*, Actes, **V**, 313–320, Univ. De Bruxelles.

Murzewski, J. (1992). Brittle and ductile damage of stochastically homogeneous solids, *Int. J. Damage Mech.*, **1**, 276–289.

Najar, J. (1987). Continuous damage of brittle solids, in: *Continuum Damage Mechanics. Theory and Applications*, D. Krajcinovic and J. Lemaitre (Eds.), Springer, Vienna, 233–294.

Neimitz, A. (1999). Analysis of stable and unstable crack growth, in: *Modeling of Damage and Fracture Processes in Engineering Materials*, M. Basista and W.K. Nowacki (Eds.), IPPT PAN. Warszawa, 57–89.

Nemat-Nasser, S. and Horii, H. (1982). Compression-induced nonplanar crack extension with application to splitting, exfoliation and rockburst, *J. Geophys. Res.* **87**, 6805–6821.

Nemat-Nasser, S. and Hori, M. (1993). *Micromechanics: Overall Properties of Heterogeneous Materials*, Elsevier, Amsterdam.

Nemat-Nasser, S. and Hori, M. (1999). *Micromechanics: Overall Properties of Heterogeneous Materials*, Elsevier, Amsterdam, The Netherlands.

Nemat-Nasser, S. and Obata, M. (1988). A microcrack model of dilatancy in brittle materials, *J. Appl. Mech.*, **55**, 24–35.

Neville, A.M. (2000). *Właściwości Betonu*, Wydanie IV, Polski Cement, Kraków.

Obert, L. (1941). Use of subaudible noise for the prediction of rock bursts, *Rep. RI 3555, US Bureau of Mines*, Washington, DC.

Odler, I. and Gasser, M. (1988). *J. Am. Ceram. Soc.*, **71**, 1015–1026.

Ogawa, K. and Roy, D.M. (1981). C_4A_3S hydration, ettringite formation, and its expansion mechanism: I. Expansion; ettringite stability, *Cem. Concr. Res.*, **11**, 741–750.

Ortiz, M. (1985). A constitutive theory for the inelastic behavior of concrete, *Mech. Mater.*, **4**, 67–93.

Ostoja-Starzewski, M. (1994). Micromechanics as a basis of continuum random fields, *Appl. Mech. Rev.*, **47**, S221–S230.

Ouyang, Ch., Mobasher, B. and Shah, S.P. (1990). An R-curve approach for fracture of quasi-brittle materials, *Eng. Fract. Mech*, **37**, 901–913.

Ouyang, C., Nanni, A. and Chang, W.F. (1988). Internal and external sources of sulphate ions in portland cement mortar: two types of chemical attack, *Cem. Concr. Res.*, **18**, 699–709.

Peng, S. and Johnson, J.M. (1972). Crack growth and faulting in cylindrical specimens of Chelmsford granite. *Int. J. Rock Mech. Min. Sci.*, **9**, 37–86.

Perzyna, P. (1986). Internal state variable description of dynamic fracture of ductile solids, *Int. J. Solids Structures*, **22**, 797–818.

Phoenix, S.L. and Taylor, H.M. (1973). The asymptotic strength distribution of a general fibre bundle, *Adv. Appl. Prob.*, **5**, 200–216.

Pike, G.E. and Seager, C.H. (1974). Percolation and conductivity: A computer study, *Phys. Rev. B*, **10**, 1421–1446.

Plowman, C. and Cabrera, J.G. (1984). Mechanism and kinetics of hydration of C_3A and C_4AF extracted from cement, *Cem. Concr. Res.*, **14**, 238–248.

Pommersheim, J. and Chang, J. (1988). Kinetics of hydration of tricalcium aluminate in the presence of gypsum, *Cem. Concr. Res.*, **18**, 911–922.

Ponte-Castañeda, P. and Suquet, P. (1998). Nonlinear composites, in: *Advances in Applied Mechanics*, **34**, 171–302.

Raniecki, B. (2001). *Private communication.*

Rice, J.R. (1968). Mathematical analysis in the mechanics of fracture, in: *Fracture – An Advanced Treatise*, H. Liebowitz (Ed.), **II**, 192–308.

Rice, J.R. (1971). Inelastic constitutive relations for solids: an internal-variable theory and its application to metal plasticity, *J. Mech. Phys. Solids*, **19**, 433–455.

Rice, J.R. (1975). Continuum mechanics and thermodynamics of plasticity in relation to microscale deformation mechanisms, in: *Constitutive Equations in Plasticity*, A.S. Argon (Ed.), The MIT Press, Cambridge, MA, 23–79.

Rice, J.R. (1976). The localization of plastic deformation, in: *Proceedings 14th IUTAM Congress*, W.T. Koiter (Ed.), North-Holland Publ. Co., 207–220.

Rice, J.R. (1978). Thermodynamics of the quasi-static growth of Griffith cracks, *J. Mech. Phys. Solids*, **26**, 61–78.

Rice, J.R. and Cleary, M.P. (1976). Some basic stress diffusion solutions for fluid saturated elastic porous medium with compressible constituents, *Rev. Geophys. Space Phys.*, **14**, 227–241.

Robinson, P.C. (1984). Numerical calculations of critical densities for lines and planes, *J. Phys. A*, **17**, 2823–2830.

Rudnicki, J.W. and Rice, J.R. (1975). Conditions for the localization of deformation in pressure-sensitive dilatant materials, *J. Mech. Phys. Solids*, **23**, 371–394.

Sadowski, T. (1994). Modelling of semi-brittle MgO ceramic behaviour under compression, *Mech. Mater.*, **18**, 1–16.

Sahimi, M. (1994). *Applications of Percolation Theory*, Taylor & Francis Publ. London, UK.

Sahimi, M. and Goddard, J.D. (1986). Elastic percolation models for cohesive mechanical failure in heterogeneous systems, *Phys. Rev. B*, **33**, 7848–7851.

Salganik, R.L. (1974). Transport processes in bodies with a large number of cracks, *Mech. Solids (Inzhenerno-Fizicheskii Zhurnal)*, **27**, 1534–1538.

Sammis, C.G. and Ashby, M.F. (1986). The failure of brittle porous solids under compressive stress states. *Acta Metall.*, **34**, 511–526.

Sanchez-Palencia, E. (1981). *Non-homogeneous media and Vibration Theory*, Lecture Notes in Physics, No. 127, Springer, Berlin.

Scher, H. and Zallen, R. (1970). Critical density in percolation processes, *J. Chem. Phys.*, **53**, 3759–3761.

Schmidt, R.A. and Lutz, T.J. (1979). K_{Ic} and J_{Ic} of Westerly granite – effects of thickness and in-lane dimensions, in: *Fracture Mechanics Applied to Brittle Materials*, ASTM Spec. Techn. Publ. STP **678**, 166–182.

Scholz, C.H. (1968). Microfracturing and the inelastic deformation of rock in compression, *J. Geophys. Res.*, **73**, 1417–1432.

Scholz, C.H. and Kranz, R. (1974). Notes on dilatancy recovery, *J. Geophys. Res.*, **79**, 2132–2135.

Scott, I.G. (1991). Basic acoustic emission, in: *Nondestructive testing Monographs and Tracts*, **6**, 246 pages, Gordon and Breach, Newark, NJ.

Seaman, L., Curran, D.R. and Shockey, D.A. (1976). *Computational models for ductile and brittle fracture, J. Appl. Phys.*, **47**, 4814–4826.

Seweryn, A. and Mróz, Z. (1995). A non-local stress failure condition for structural elements under multiaxial loading, *Eng. Fract. Mech.*, **51**, 955–973.

Shante, V.K.S. and Kirkpatrick, S. (1971). An introduction to percolation theory, *Adv. Phys.*, **20**, 325–357.

Shockey, D.A., Curran, D.R., Seaman, L., Rosenberg, J.T. and Petersen, C.F. (1974). Fragmentation of rock under dynamic loads, *Int. J. Rock Mech. Sci. & Geomech. Abstr.*, **11**, 303–317.

Sieradzki, K. and Li, R. (1986). Fracture behavior of a solid with random porosity, *Phys. Rev. Lett.*, **56**, 2509–2512

Sih, G.C. (1973). *Handbook of Stress Intensity Factors*, Lehigh Univ.

Skrzypek, J. and Ganczarski; A. (1999). *Modeling of Material Damage and Failure of Structures*, Springer, Berlin–Heidelberg.

Skrzypek, J., Kuna-Ciskał, H. and Ganczarski, A. (1999). Continuum damage mechanics modeling of creep-damage and elastic-damage-fracture in materials and structures, in: *Modeling of Damage and Fracture Processes in Engineering Materials*, M. Basista and W.K. Nowacki (Eds.), IPPT PAN, Warszawa, 181–235.

Sobczyk, K. and Spencer B.F. (1992). *Random Fatigue. From Data to Theory*, Academic Press, San Diego.

Sornette, D. (1988). Critical transport and failure in continuum crack percolation, *J. Phys. France*, **49**, 1365–1377.

Sornette, D. (1989). Elasticity and failure of a set of elements loaded in parallel, *J. Phys. A*, **22**, L243–L250.

Sornette, D. (2000). *Critical Phenomena in Natural Sciences*, Springer, Heidelberg.

Soroka, I. (1980). *Portland Cement Paste and Concrete*. Chemical, New York.

Stauffer, D. (1985). *Introduciton to Percolation Theory*, Taylor & Francis, London, UK.

Steif, P. S. (1984). Crack extension under compressive loading, *Eng. Fract. Mech.*, **20**, 463–473.

Steinbrech, R.W., Dickerson, R.M. and Kleist, G. (1991). Characterisation of the fracture behavior of ceramics through analysis of crack propagation studies, in: *Toughening Mechanisms in Quasi-Brittle Materials*, S.P. Shah (Ed.), Kluwer Publ., New York, 353–375.

Sumarac, D. (1987). Self-consistent model for the brittle response of solids, *PhD Thesis*, Civil Eng., Mechanics and Metallurgy Dept., University of Illinois at Chicago Circle, Chicago IL.

Sumarac, D. and Krajcinovic, D. (1987). A self-consistent model for microcrack weakened solids, *Mech. Mater.*, **6**, 39–52.

Swoboda, G. and Yang, Q. (1999). An energy-based damage model of geomaterials – II. Deduction of damage evolution laws, *Int. J. Solids Structures*, **36**, 1735–1755.

Tada, H., Paris, P. and Irwin, G. (1985). *The Stress Analysis of Cracks Handbook.* Paris Productions Inc., St. Louis, MO.

Talreja, R. (1985). A continuum mechanics characterization of damage in composite materials, *Proc. Roy. Soc. London A* **399**, 195–216.

Tapponier, P. and Brace, W.F. (1976). Development of stress-induced microcracks in Westerly granite, *Int. J. Rock Mech. Min. Sci. Geomech. Abstr.*, **13**, 103–112.

Tonks, D.L. (1996). Disorder, percolation and wave propagation effects in ductile fracture, in: *High-Pressure Shock Compression of Solids II*, L. Davison, D.E. Grady and M. Shahinpoor (Eds.), Springer.

Torelli, L. and Scheidegger, A.E. (1972). Three-dimensional branching-type models of flow through porous media, *J. Hydrol.*, **15**, 23–37.

Vakulenko, A.A. and Kachanov, M. (1971). Continuum theory of cracked media, *Izv. AN SSSR, Mekh. Tverdogo Tela*, **4**, 159–166.

Vavakin, A.S. and Salganik, R.L. (1975). Effective characteristics of nonhomogeneous media and with isolated nonhomogeneities, *Izv AN SSSR, Mekh. Tverdogo Tela*, **10**, 65–75.

Wagner, Ch. and Gross, D. (1988). Untersuchungen zur Wechselwirkung zwischen Defekten und einem Einzelriss, *DFG-Report*, Gr 596/15-1, Institute of Mechanics, Darmstadt University of Technology.

Walsh, J.B. (1965). The effect of cracks on uniaxial compression of rocks, *J. Geophys. Res.*, **70**, 399–411.

Wang, P.T. (1977). Complete stress–strain curves of concrete and its effects on ductility of reinforced concrete members, *PhD Thesis*, University of Illinois at Chicago Circle.

Wang, R. and Kemeny, J.M. (1993). Micromechanical modeling of tuffaceous rock for application in nuclear waste storage, *Int. J. Rock Mech. Min. Sci. & Geomech. Abstr.*, **30**, 1351–1357.

Weng, J.G., Taya, M. and Abe, H., Eds. (1990). *Micromechanics and Inhomogeneity*, Springer, New York.

Wilke, S.E, Guyon, E. and de Marsily, G. (1985). Water penetration through fractured rocks: test of three-dimensional percolation description, *Math. Geol.*, **17**, 17–27.

Willam, K. and Iordache, M.-M. (1994). Fundamental aspects of failure modes in brittle solids, in: *Fracture and Damage in Quasi-brittle Structures*, E & FN Spon, London, 53–67.

Woo, C.W. and Li, D.L. (1993). A universal physically consistent definition of material damage, *Int. J. Solids Structures*, **30**, 2097–2108.

Yazdani, S. and Schreyer, H.L. (1988). An anisotropic damage model with dilatation for concrete, *Mech. Mater.*, **7**, 231–244.

Zaitsev, Yu. (1982). *Modelling of Deformation and Strength Using Fracture Mechanics Methods* (in Russian), Stroiizdat, Moscow.

Zaitsev, Yu. (1985). Inelastic properties of solids with random cracks, in: *Mechanics of Geomaterials*, Z. Bazant (Ed.), Wiley.

Zallen, R. (1983). *The Physics of Amorphous Solids*, J. Wiley & Sons, New York, NY.

Zhang, A., Wagner, Ch.F., and Dresen, G. (1996). Acoustic emission, microstructure, and damage model of dry and wet sandstone stressed to failure, *J. Geophys. Res.*, **101**, 17507–17524.

Zhao, Y., Huang, J., and Wang, R. (1993). Real-time SEM observations of the microfracturing process in rock during a compression test, *Int. J. Rock Mech. Min. Sci. & Geomech. Abstr.*, **30**, 643–652.

Zoback, M.D. and Byerlee, J.D. (1975). The effect of cyclic differential stress on dilatancy in Westerly granite under uniaxial and triaxial conditions, *J. Geophys. Res.*, **80**, 1526–1530.

Mikromechaniczne i sieciowe modele kruchego uszkodzenia

Streszczenie

Niniejsza praca jest wieloaspektowym studium procesów uszkodzenia w skałach i betonie w zakresie deformacji kruchych. Czynnikami wywołującymi wzrost uszkodzenia są tu quasi-statyczne obciążenia rozciągające, ściskające oraz chemicznie agresywne środowisko. Rozważa się izotermiczne procesy deformacji przy założeniu małych odkształceń i pominięciu efektów plastycznych. Zasadniczym celem pracy jest sformułowanie równań konstytutywnych dla powyższych materiałów, przyjmując za punkt wyjścia udokumentowane doświadczalnie mechanizmy rozwoju uszkodzeń na poziomie mikroskopowym. Modele teoretyczne zostały w pracy podzielone na mikromechaniczne, fenomenologiczne i sieciowe. Odnoszą się one wprawdzie do tych samych zjawisk fizycznych, ale różni je przyjęta metodologia i zakres stosowalności, co uzasadnia taki podział. Zgodnie z tytułem, większa część pracy poświęcona jest mikromechanicznym i sieciowym modelom kruchego uszkodzenia. Model fenomenologiczny przedstawiony w Rozdziale 7 jest przykładem wykorzystania informacji z poziomu mikro do zbudowania modelu makroskopowego, ale nie stanowi jeszcze zamkniętej teorii. Wyprzedzając wnioski końcowe można dodać, że wymienione trzy grupy modeli nie są wobec siebie konkurencyjne, ale wzajemnie się uzupełniają. Praca zawiera przykłady zastosowań proponowanych modeli i porównania z wynikami doświadczeń. Rozdziały 1 i 2 mają charakter opisowy, Rozdziały 3, 4, 5, 6, 7, 8 stanowią oryginalną, badawczą część pracy. Rozdział 9 zawiera podsumowanie, wnioski i sugestie dalszych badań. Zamknięciem pracy jest spis literatury cytowanej w tekście. Niniejsza praca podsumowuje kilkunastoletni okres aktywności badawczej autora w dziedzinie mechaniki uszkodzenia materiałów kruchych.

Najważniejsze definicje, założenia i zakres pracy

W Rozdziale 1 przedstawiono najważniejsze definicje i założenia mechaniki uszkodzenia oraz zakres i cele szczegółowe pracy. Wskazano główne różnice między kruchym uszkodzeniem a zniszczeniem oraz kruchym uszkodzeniem a plastycznością w przypadku materiałów skałopodobnych. Zwrócono uwagę, że powszechnie używane określenie „mechanika uszkodzenia" (*Damage Mechanics*, DM) nie powinien być utożsamiany z chronologicznie wcześniejszym określeniem „kontynualna mechanika uszkodzenia" (*Continuum Damage Mechanics*, CDM). Pierwszy z nich odnosi się bowiem do znacznie szerszej klasy modeli obejmującej, poza CDM, również modele mikromechaniczne i modele fizyki statystycznej (*lattice models*). Przedstawiono zwięzłą charakterystykę tych trzech klas modeli w kontekście kruchych deformacji, wskazując ograniczenia każdej z klas, ale i ich walory oraz wzajemną komplementarność. Wśród ogólnych założeń pracy (założenia szczegółowe pojawią się przy omawianiu kolejnych rozdziałów) należy wymienić: liniowo-sprężysty i izotropowy model materiału matrycy, obecność mikroszczelin w materiale przed przyłożeniem obciążenia, umiarkowane ciśnienia boczne (stąd brak efektów plastycznych przy ściskaniu), pominięcie wpływu temperatury, ograniczenie analizy do przypadków dwuwymiarowych.

Podstawy doświadczalne

W Rozdziale 2 oraz na początku Rozdziałów 3, 4, 6 zebrano najważniejsze obserwacje doświadczalne, które stanowiły motywację do sformułowania modeli teoretycznych w tej pracy. Przypomniano, że polikrystaliczne skały i beton charakteryzują się złożonym i nieliniowym zachowaniem pod działaniem obciążeń mechanicznych. Na przykład, w testach ściskania próbek skalnych obserwuje się: odejście od liniowości w relacji odkształcenie–naprężenie i stopniową zmianę stałych sprężystych materiału, silny wpływ ciśnienia bocznego na wytrzymałość graniczną oraz na typ zniszczenia próbki, dodatnią dylatancję, tzn. nieliniowy wzrost objętości próbki wskutek rozwoju mikroszczelin, anizotropię deformacyjną wynikająca z kierunkowego procesu wzrostu mikroszczelin, pętle histerezy w cyklach obciążenie–odciążenie, odkształcenia trwałe po całkowitym odciążeniu, występowanie stanów po-krytycznych w testach sterowanych przemieszczeniem (krzywa osłabienia). Autorzy doświadczeń są zgodni co do tego, że w rozważanych materiałach przy małych i umiarkowanych ciśnieniach bocznych odejście od liniowości w wykresie σ–ε następuje pod wpływem wzrostu liczby i wielkości mikropęknięć w czasie obciążenia. Przyjmuje się dalej, że mikroszczeliny obserwowane w procesie deformacji rozwijają się z mikrodefektów, które są obecne w strukturze materiału jeszcze przed przyłożeniem obciążenia, a wynikają z naturalnych (lub technologicznych) procesów powstawania tych materiałów. Te wstępne mikrodefekty stają się koncentratorami naprężeń w procesie obciążenia. Wzrost mikropęknięć może odbywać się w wyniku działania jednego lub kilku mikromechanizmów uszkodzenia (por. Rysunek 4.1), takich jak mechanizm pustki lub inkluzji w polu naprężeń ściskających, mechanizm wypychania ziaren, mechanizm zginania wydłużonych ziaren, mechanizm punktu potrójnego, mechanizm szczeliny poślizgowej (Rysunek 4.2), czy mechanizm miażdżenia pustki. W skałach niskoporowatych, np. w granicie, dominujący może być mechanizm mikroszczeliny poślizgowej (*sliding microcrack* lub *winged microcrack*), podczas gdy w betonach i skałach o dużej porowatości (piaskowce, marmury) przeważać będą mechanizmy związane z deformacją pustek, tzn. mechanizm ściskania lub miażdżenia pustki. Podczas jednoosiowego ściskania bez udziału ciśnienia bocznego mikroszczeliny pojawiają się w omawianych materiałach głównie na płaszczyznach równoległych do kierunku maksymalnego naprężenia ściskającego. Mikroszczeliny te wzrastają i łączą się tworząc w zaawansowanym etapie procesu deformacji szczeliny makroskopowe. Zniszczenie końcowe w postaci rozłupania próbki (*splitting*) jest przypisywane niestatecznej propagacji najczęściej jednej makroszczeliny biegnącej wzdłuż kierunku maksymalnego ściskania (Rysunek 2.1a). Zniszczenie w tym przypadku ma raczej gwałtowny charakter, a odkształcenia niesprężyste w momencie zniszczenia są względnie małe. Jeśli natomiast ciśnienie boczne jest obecne w próbie ściskania, to proces deformacji jest bardziej złożony, gdyż może wystąpić przejście od kruchego do ciągliwego typu deformacji. Krzywa σ–ε jest wówczas wyraźnie odchylona od prostej Hooke'a, a wielkości odkształceń sprężystych i niesprężystych przy maksymalnym obciążeniu są porównywalne. Zniszczenie końcowe (*shear band* lub *faulting*) jest wynikiem lokalizacji deformacji rozumianej jako interakcja i łączenie się wielu mikroszczelin, które wzrastając w sposób stabilny współdziałają ze sobą, by wreszcie utworzyć dominującą makroszczelinę nachyloną do kierunku maksymalnego ściskania (Rysunek 2.1b). W przypadku dużych ciśnień nie tworzy się pojedyncza powierzchnia zniszczenia, ale obserwuje się pseudo-ciągliwy typ zniszczenia przy obecności dużych deformacji i wielu równomiernie rozrzuconych mikroszczelin (Rysunek 2.1c). Mechanizmy uszkodzenia i zniszczenia skał w stanach rozciągania są dużo prostsze niż przy ściskaniu. W testach sterowanych przemieszczeniem rozwój uszkodzenia polega na stopniowej aktywacji istniejących mikroszczelin, których rozmiar i położenie pozwala na osiągnięcie warunku Griffitha przy danych poziomach obciążenia. Taka mikroszczelina wzrasta w sposób niestateczny aż do momentu, w którym zostaje zatrzymana przez przeszkodę o wyższej odporności na pękanie (np. ziarno kruszywa w betonie). Przy dalszym wzroście obciążenia, kolejne mikroszczeliny ulegają aktywacji powodując, że (pominąwszy skalę naprężeń) wykres σ–ε ma jakościowo podobny przebieg jak w testach ściskania (Rysunek 3.2). Ostateczne zniszczenie rozciąganej próbki następuje, gdy jedna z zatrzymanych uprzednio szczelin zacznie ponownie wzrastać w sposób niestateczny, a jej wzrost nie zostanie zablokowany przez heterogeniczną strukturę materiału. Należy przy tym dodać, ze w testach sterowanych siłą w zasadzie nie rejestruje się krzywoliniowej części wykresu σ–ε, a zniszczenie próbki następuje raptownie przy osiągnięciu przez najbardziej niebezpieczną mikroszczelinę krytycznej wartości współczynnika intensywności naprężeń. W Rozdziale 2 podano również podstawowe informacje na temat zastosowania metody emisji akustycznej do badania detekcji i ewolucji mikroszczelin oraz omówiono zjawisko podkrytycznego wzrostu mikroszczelin, które odgrywa ważną rolę w procesach deformacji skał w ich naturalnym środowisku, czyli w skorupie ziemskiej. Podstawy eksperymentalne korozji siarczanowej betonu, której model matematyczny przedstawiono w Rozdziale 6, zostaną omówione w dalszej części streszczenia.

Mikromechaniczny model uszkodzenia przy rozciąganiu

W Rozdziale 3 przedstawiono model uszkodzenia materiałów kruchych poddanych działaniu jednorodnych naprężeń rozciągających. Na podstawie analizy pojedynczej mikroszczeliny położonej prostopadle do kierunku jednoosiowego rozciągania, określono zmianę gęstości energii komplementarnej Gibbsa wywołanej obecnością mikroszczeliny. Stosując formalizm termodynamiczny z parametrami wewnętrznymi (np. Rice, 1971) wyprowadzono w systematyczny sposób przyrostowe równania konstytutywne. Następnie zaproponowano równanie wzrostu długości mikroszczeliny (3.5)–(3.6) oparte na klasycznym kryterium Griffitha i koncepcji krzywej R, wykorzystując przesłanki doświadczalne do aproksymacji kształtu tej krzywej. Wprowadzając zaproponowane równanie wzrostu mikroszczeliny do równania konstytutywnego otrzymano nieliniowe, przyrostowe równanie $\mathrm{d}\varepsilon$–$\mathrm{d}\sigma$, (3.14). Rozważono mikroszczeliny bez interakcji oraz najprostsze układy mikroszczelin z uwzględnieniem interakcji. Wykonano implementację numeryczną uzyskanych równań, przedstawiono ich graficzną ilustrację (por. Rysunek 3.5, 3.8, 3.10) oraz dyskusję otrzymanych krzywych dla kilku przykładowych konfiguracji mikroszczelin. Uogólniając zbudowany model na stany płaskie (Rysunek 3.11), wyprowadzono wzór (3.30) określający gęstość energii Gibbsa dla reprezentatywnego elementu objętościowego (RVE) zawierającego N prostoliniowych mikroszczelin w modzie mieszanym I-II. Integralną częścią tego wzoru jest symetryczny tensor uszkodzenia II-rzędu $\boldsymbol{\omega}$, który pojawiał się wcześniej w pracach innych autorów (np. Kachanov, 1980; Murakami i Ohno, 1981) jako postulat, w prezentowanym zaś modelu wynika w sposób naturalny ze struktury potencjału sprężystego. Znając gęstość energii Gibbsa, otrzymano w standardowy sposób przyrostowe równania $\mathrm{d}\boldsymbol{\varepsilon}$–$\mathrm{d}\boldsymbol{\sigma}$, (3.31), (3.32). W odniesieniu do kinetyki wzrostu uszkodzeń przyjęto fizycznie uzasadnione założenie, że mikroszczeliny wtórne powstają w wierzchołkach mikroszczelin pierwotnych i wzrastają w kierunku prostopadłym do kierunku maksymalnego głównego naprężenia rozciągającego, tworząc zagięcie (*kink*) w stosunku do kierunku mikroszczeliny pierwotnej. Rzeczywista mikroszczelina zagięta jest następnie zastępowana fikcyjną mikroszczeliną prostoliniową, która doznaje obrotu i zmiany długości (Rysunek 3.12). Warunek wzrostu długości mikroszczeliny fikcyjnej (3.33) sformułowano dla projekcji tej mikroszczeliny na kierunek normalny do maksymalnego głównego rozciągania. Zmianę orientacji tej mikroszczeliny określa równanie (3.35) uzupełnione o zależności geometryczne (3.36).

Mikromechaniczny model uszkodzenia oraz interakcja mikroszczelin przy ściskaniu

Rozdziały 4 i 5 poświęcono mikromechanicznemu opisowi uszkodzenia w skałach pod działaniem obciążeń ściskających. Spośród wielu możliwych mechanizmów deformacji wybrano mechanizm mikroszczeliny poślizgowej (Rysunek 4.2), gdyż ujmuje on stosunkowo najwięcej faktów doświadczalnych obserwowanych w testach ściskania skał. Model konstytutywny sformułowano w ramach formalizmu termodynamicznego z mikrostrukturalnymi parametrami wewnętrznymi (Rice, 1971, 1975). Dokonano interpretacji tego formalizmu w przypadku mikroszczelin poślizgowych. Rozważono szczegółowo dwie fazy deformacji: (1) fazę poślizgów tarciowych na powierzchniach mikroszczelin pierwotnych PP' (Rysunek 4.2) bez zmiany ich długości i przed powstaniem mikroszczelin wtórnych $PQ, P'Q'$ (tzw. skrzydeł), (2) fazę pełnej aktywności mechanizmu, tzn. wzrostu krzywoliniowych mikroszczelin wtórnych wywołanego poślizgami na powierzchniach mikroszczelinach pierwotnych w obecności ciśnienia bocznego σ_2. Algorytm postępowania przy budowaniu modelu obejmował następujące kroki: (a) sformułowanie równań aktywacji poślizgów (4.28), (4.45) wynikających z zasady superpozycji naprężeń, równań równowagi i warunku tarcia Coulomba–Mohra; (b) określenie zmian gęstości energii komplementarnej Gibbsa wywołanych obecnością mikroszczelin pierwotnych (faza 1 — równanie 4.18) i mikroszczelin poślizgowych (faza 2 — równanie 4.29); (c) identyfikacja infinitezymalnych przyrostów parametrów wewnętrznych (uogólnionych przemieszczeń termodynamicznych) i sprzężonych z nimi sił termodynamicznych na poziomie mikroskali, (4.21), (4.31); (d) zastosowanie uproszczonych modeli mikroszczeliny poślizgowej (Rysunek 4.6a,b) umożliwiających oszacowanie współczynników intensywności naprężeń, (4.35)–(4.36); (e) wyprowadzenie przyrostowych, makroskopowych równań $\mathrm{d}\varepsilon_{ij}$–$\mathrm{d}\sigma_{ij}$, (4.37)–(4.43) przy wykorzystaniu fundamentalnej zależności Rice'a (4.6); (f) specyfikacja równań kinetyki dla mikroskopowych parametrów wewnętrznych, (4.45)–(4.47); (g) implementacja numeryczna otrzymanych równań. W pracy przeanalizowano zarówno proces obciążenia, jak i odciążenia. Z uwagi na specyfikę modelu mikroszczeliny poślizgowej jako mechanizmu deformacji (np. możliwość dyssypacji energii podczas redukcji obciążenia zewnętrznego), przyjęto w podrozdziale 4.6, że odciążenie ma miejsce w każdym przypadku, gdy efektywne (średnie) naprężenie styczne na powierzchniach mikroszczeliny pierwotnej ulega zmniejszeniu, tzn. gdy $\mathrm{d}|\tau_{\mathit{eff}}| < 0$. Termin „odciążenie" jest wobec tego rozumiany jako odciążenie mikroszczeliny poślizgowej, które można osiągnąć przez redukcję obciążenia zewnętrznego, albo przez zmianę drogi obciążania. Rozważono szczegółowo przypadki odciążenia, wyprowadzając właściwe równania $\mathrm{d}\varepsilon_{ij}$–$\mathrm{d}\sigma_{ij}$ i równania kinetyki uszkodzeń. W podrozdziale 4.7 przedstawiono zastosowanie zbudowanego modelu do opisu deformacji próbek granitowych w stanie jednoosiowego ściskania. Na Rysunku 4.8 otrzymane krzywe teoretyczne porównano z wynikami doświadczeń (Zoback i Byerlee, 1975) notując dobrą zgodność. Rysunek 4.9 został zaczerpnięty z pracy doktorskiej B. Lauterbach (TU Darmstadt, RFN), gdyż potwierdza słuszność równań wyprowadzonych w Rozdziale 4 niniejszej pracy. Rysunek ten przedstawia porównanie wyników numerycznych uzyskanych przez autorkę przy pomocy metody elementów brzegowych (*BEM*) i metody elementów skończonych (*FEM*) oraz wyników doświadczalnych w stanie dwuosiowego ściskania (Zoback i Byerlee, 1975). Należy dodać, że cytowane wyniki *FEM* to bezpośrednia implementacja numeryczna (pakiet *FEAP*) równań z podrozdziałów 4.5 i 4.6 niniejszej pracy, zaś wyniki *BEM* autorka uzyskała dla modelu mikroszczeliny poślizgowej bez uproszczeń (por. Rysunek 4.2) przy pomocy własnego programu źródłowego. Godna uwagi jest zgodność wyników dostarczonych przez oba modele teoretyczne.

Rozdział 5 dotyczy modelowania interakcji mikroszczelin poślizgowych pod działaniem naprężeń ściskających. Motywacją do podjęcia tego tematu były fakty doświadczalne wskazujące na decydującą rolę interakcji mikroszczelin w procesie kruchego zniszczenia materiałów skałopodobnych. W szczególności, zadaniem badawczym postawionym w tym rozdziale było wyznaczenie współczynników intensywności naprężeń dla dowolnej liczby prostoliniowych, zamkniętych mikroszczelin z tarciem i kohezją na powierzchni kontaktu (tzw. faza 1 w modelu mikroszczeliny poślizgowej). W następnej kolejności należało wyznaczyć współczynniki intensywności naprężeń w wierzchołkach mikroszczelin wtórnych (faza 2). Dokładne rozwiązanie pełnego problemu interakcji mikroszczelin poślizgowych z krzywoliniowymi „skrzydłami" jest możliwe jedynie numerycznie. W literaturze przedmiotu istnieje jednak wiele metod przybliżonych, które są zadowalająco dokładne i szybkie w porównaniu z metodami *stricte* numerycznymi. Spośród wielu znanych, przybliżonych metod bezpośredniej analizy interakcji szczelin wybrano analityczno-numeryczną metodę Kachanova jr. (1987) z uwagi na jej dwa walory: dużą dokładność i prostotę. Metoda Kachanova była do tej pory z powodzeniem stosowana w literaturze do szczelin otwartych. Oryginalnym wkładem Rozdziału 5 jest rozszerzenie tej metody na przypadek mikroszczelin tarciowych oraz jej adaptacja do mikroszczelin poślizgowych, reprezentowanych przez model uproszczony z parą sił skupionych (Rysunek 4.6b). W metodzie Kachanova zakłada się, że decydujący wpływ na wielkość współczynników intensywności naprężeń dla danej szczeliny mają naprężenia średnie (normalne i styczne) działające na pozostałe szczeliny, zaś fluktuacje tych naprężeń są w zagadnieniach interakcji — drugorzędne. Założenie to pozwala na wykorzystanie tzw. standardowych pól naprężenia, które można wyznaczyć analitycznie posiłkując się funkcją naprężenia Westergaarda dla szczelin prostoliniowych. Uśredniając otrzymane równania (5.8) możliwe jest następnie wyznaczenie średnich naprężeń normalnych i stycznych na brzegach danej szczeliny, po obliczeniu tzw. współczynników transmisji naprężeń (5.12). Obecność tarcia i kohezji na powierzchniach kontaktu mikroszczelin (5.7) zmienia podstawowe równania metody Kachanova — układ równań liniowych do wyznaczenia naprężeń średnich ma teraz postać (5.14), a rzeczywisty rozkład naprężeń określają równania (5.15). Współczynniki intensywności naprężeń przyjmują zmodyfikowaną formę (5.16). Dokonano implementacji numerycznej układów równań (5.14), (5.15), (5.16), budując źródłowy program CRACK2D.FOR. Po przetestowaniu kodu numerycznego, rozwiązano kilka przykładów interakcji mikroszczelin, a wyniki porównano z rozwiązaniami dokładnymi uzyskanymi metodą elementów brzegowych przy wykorzystaniu programu zbudowanego w Instytucie Mechaniki Politechniki w Darmstadt. Stwierdzono bardzo dobrą zgodność wartości współczynników intensywności naprężeń obliczonych przy pomocy programu CRACK2D.FOR z wartościami obliczonymi metodą elementów brzegowych (por. Rysunki 5.2, 5.3, 5.4, 5.5). W dalszej części Rozdziału 5 przedstawiono adaptację metody Kachanova do przypadku dowolnej liczby mikroszczelin otwartych poddanych działaniu zewnętrznego pola naprężeń ściskających oraz pary sił skupionych przyłożonych do brzegów mikroszczelin. Wyprowadzono podstawowe równania (5.18)–(5.21), przeprowadzono ich implementację numeryczną i rozwiązano testowe problemy interakcji mikroszczelin, porównując otrzymane wartości K_I i K_{II} z wartościami obliczonymi metodą elementów brzegowych (Rysunki 5.7–5.10). Dokładność uzyskanych wyników jest zadowalająca, jednak dla konfiguracji z Rysunku 5.9 przy odległościach $d/l < 0.2$ metoda przestaje funkcjonować. W konkluzji tego rozdziału stwierdzono, że metoda Kachanova daje doskonałe wyniki w przypadku „zamrożonego" układu prostoliniowych, zamkniętych mikroszczelin doznających poślizgów z uwzględnieniem tarcia i kohezji. Jeśli jednak w grę wchodzi ewolucja mikroszczelin, to podstawowe elementy metody, tzn. standardowe pola naprężeń i współczynniki transmisji naprężeń nie dają się zastosować, gdyż wzrost mikroszczelin nie jest wtedy samopodobny (*self-similar*).

Uszkodzenie betonu pod działaniem chemicznie agresywnego środowiska

W Rozdziale 6 zbadano ważny praktycznie problem rozwoju mikroszczelin w konstrukcjach betonowych wskutek reakcji chemicznych między aktywnymi składnikami stwardniałego betonu i agresywnym otoczeniem, np. zasiarczoną wodą gruntową (agresja siarczanowa, por. Neville, 2000). Na pierwszy rzut oka problem ten zdaje się wykraczać poza główną oś pracy, czyli modelowanie uszkodzenia w materiałach skałopodobnych poddanych rozciąganiu lub ściskaniu. Jednakże dokładniejsza analiza tego rozdziału szybko przekonuje, że mamy do czynienia z klasycznym mikromechanicznym modelem kruchego uszkodzenia wywołanego lokalnymi naprężeniami rozciągającymi. Obecność tych naprężeń nie jest wynikiem zewnętrznego obciążenia, ale wzrostu objętości produktów reakcji chemicznej w stosunku do objętości substratów. Agresja siarczanowa stwardniałego betonu wykonanego z cementu portlandzkiego jest sekwencją sprzężonych procesów fizyko-chemicznych. Najpierw, jony siarczanowe $SO_4^=$ z obecnego w wodzie gruntowej siarczanu magnezu lub sodu wnikają do wnętrza elementów konstrukcji poprzez sieć porów w wyniku dyfuzji wywołanej różnicą koncentracji. Następnie, dochodzi do kontaktu i reakcji jonów $SO_4^=$ z kryształami glinianu trójwapniowego (C_3A), które nie uległy hydratacji w procesie wiązania cementu. Reakcja ta, ujęta wzorami (6.1)–(6.2), jest reakcją heterogeniczną. W swej drugiej części (6.2) ma ona charakter topochemiczny, tzn. zachodzi wprost na powierzchni kryształu C_3A, a nie w roztworze i prowadzi do powstania uwodnionego siarczanoglinianu wapniowego (ettringitu). Objętość molowa ettringitu jest ponad 8 razy większa od objętości molowej C_3A. Pory nie są w stanie przyjąć tak dużego przyrostu objętości. Powstają lokalne ciśnienia, a w konsekwencji mikropęknięcia struktury betonu w konstrukcji. Pojawienie się nowych mikroszczelin wpływa na wzrost porowatości, co z kolei przyspiesza dyfuzję siarczanów, a w konsekwencji wzmaga reakcję podwójnego rozkładu. Cały proces staje się samonapędzający. Beton doznaje coraz większych wydłużeń, które przy braku zabezpieczeń antykorozyjnych mogą prowadzić do całkowitego zniszczenia zaatakowanego elementu konstrukcji. Należy dodać, że procesy korozji siarczanowej są powolne (mogące trwać latami), natomiast sama prędkość powstawania ettringitu, wynikająca z kinetyki reakcji, jest o kilka rzędów wielkości większa. W omawianym rozdziale zaproponowano mikromechaniczny model opisu powyższych procesów. Wynikiem końcowym tego modelu miało być określenie wielkości makroskopowych odkształceń betonu wywołanych atakiem siarczanowym. Podstawowe elementy zbudowanego modelu to: (a) równanie dyfuzji z członem reakcyjnym, (6.10); (b) reakcja podwójnej wymiany (6.1)–(6.2) i jej analiza stechiometryczna (6.11)–(6.12); (c) kinetyka reakcji powstawania ettringitu, (6.3)–(6.5) i (6.13); (d) analiza własności transportowych skorodowanego betonu w zakresie małych i dużych koncentracji mikroszczelin, podrozdział 6.5; (e) wyznaczenie lokalnych pól naprężeń i odkształceń wokół inkluzji ettringitu, (6.28)–(6.33); (f) model mikropękania wskutek wzrostu kryształu ettringitu, (6.34)–(6.36) oraz model perkolacyjny w zaawansowanej fazie degradacji materiału; (g) sformułowanie makroskopowych relacji naprężenie–odkształcenie uwzględniających obecność inkluzji ettringitu i ewolucję uszkodzenia, (6.37)–(6.41). W podrozdziale 6.7 rozważono szczegółowo przypadek jednowymiarowy, przedstawiając specyfikację wszystkich równań modelu. Otrzymane równania zastosowano do obliczenia osiowych wydłużeń próbek w testach zalecanych przez ASTM i porównano z wynikami takich testów uzyskanych w pracy Ouyang i in. (1988) notując dobra zgodność, Rysunek 6.6.

Fenomenologiczny model uszkodzenia materiałów kruchych

Rozdział 7 zawiera propozycję fenomenologicznego opisu uszkodzenia skał i betonu przy wykorzystaniu podstawowych informacji, których dostarcza mikromechanika procesów kruchego uszkodzenia. Ograniczono się do procesów deformacji, w których dominują mikroszczeliny otwarte (*Mode I*), a dyssypacja energii związana z tarciem i odkształceniami plastycznymi może być pominięta. Stosując formalizm termodynamiczny z parametrami wewnętrznymi wg Rice'a (1971, 1975, 1978), sformułowano mikroskopowe i makroskopowe równania zmiany gęstości energii Gibbsa wywołanej pojawieniem się mikroszczelin, (7.9), (7.17). Na tej podstawie otrzymano równania zmiany tensorów podatności i odkształceń niesprężystych, (7.21), (7.22). Podkreślono, że skuteczność tych równań zależy od tego, czy dla rozważanego problemu możliwe jest wyznaczenie (analityczne bądź numeryczne) współczynników intensywności naprężeń dla wszystkich mikroszczelin wewnątrz *RVE*. Analizując makroskopowe równanie zmiany gęstości energii Gibbsa, zaproponowano (por. (7.24)), aby w fenomenologicznych modelach kruchego uszkodzenia, tensor podatności $\mathbf{S}$ uznać za makroskopowy parametr wewnętrzny, z którym sprzężona jest siła termodynamiczna $\mathbf{Q} = \frac{1}{2}(\boldsymbol{\sigma} \otimes \boldsymbol{\sigma})$, gdzie $\boldsymbol{\sigma}$ oznacza tensor naprężenia. Następnym krokiem było sformułowanie równań kinetyki uszkodzenia. Do tego celu zastosowano podejście Rice'a (1971), sformułowane pierwotnie dla plastyczności metali, adaptując je do procesów kruchego uszkodzenia. Ograniczono się do klasy takich związków kinetycznych, w których prędkości zmian parametrów wewnętrznych zależą od makroskopowego naprężenia jedynie poprzez ich własne sprzężone siły termodynamiczne (por. Kestin i Rice, 1970; Rice, 1971, 1975). W kontekście kruchego uszkodzenia oznacza to, że prędkość zmian pola powierzchni danej mikroszczeliny zależy od makroskopowego naprężenia $\boldsymbol{\sigma}$ jedynie poprzez jej własną prędkość uwalniania energii sprężystej G. Na tej podstawie wyprowadzono równania (7.30)–(7.32), z których wynika, że dla rozważanej klasy problemów: (1) istnieje makroskopowy potencjał uszkodzenia Ω będący objętościowym uśrednieniem mikropotencjałów (np. warunków Griffitha dla wszystkich mikroszczelin w *RVE*) oraz (2) prędkość zmian tensora podatności można wyznaczyć z zasady normalności, $\dot{\mathbf{S}} = (\partial\Omega/\partial\mathbf{Q})$. W części aplikacyjnej (podrozdział 7.5) zaproponowano proste równania powierzchni uszkodzenia uwzględniające najważniejsze przesłanki mikromechaniczne w odniesieniu do ewolucji mikroszczelin w dwuwymiarowych stanach rozciągania i ściskania. Przedstawiono porównanie z eksperymentem oraz przeprowadzono krytyczną dyskusję przyjętych założeń w części dotyczącej uszkodzenia przy ściskaniu.

Procesy uszkodzenia i zniszczenia w ujęciu modeli sieciowych

Problemy uszkodzenia i zniszczenia materiałów nie są wyłączną domeną mechaniki. Leżą one również w centrum zainteresowania fizyki statystycznej zajmującej się tzw. zjawiskami krytycznymi (*critical phenomena*) w ośrodkach nieuporządkowanych (*disordered media*). Począwszy od lat siedemdziesiątych obserwuje się gwałtowny rozwój fizyki zjawisk krytycznych lecz dopiero od niedawna zauważalna jest pewna interakcja tej gałęzi fizyki i mechaniki. W Rozdziale 8 podjęto próbę zastosowania metod fizyki zjawisk krytycznych do opisu procesów uszkodzenia i zniszczenia w materiałach kruchych. Jednocześnie pokazano, że podejście interdyscyplinarne, w którym wyniki symulacji statystycznych są analizowane przez pryzmat kontynualnych modeli uszkodzenia, prowadzi do interesujących wniosków dotyczących wyboru parametrów uszkodzenia w modelach CDM oraz interakcji mikrodefektów. W ujęciu fizyki statystycznej, ciało poddane losowej deterioracji mikrostruktury może być reprezentowane przez dyskretną sieć (*lattice*, *network*) o dużych rozmiarach (ściśle mówiąc — nieskończoną), w której zadaje się wstępne nieuporządkowanie (*initial disorder*) w odniesieniu do wybranych własności elementów sieci. Sieci mogą być regularne lub losowe, zaś wstępne nieuporządkowanie może dotyczyć na przykład wytrzymałości elementów na zerwanie, stałych sprężystych, itd. W pracy rozważa się dwa modele losowego uszkadzania struktury: (1) model perkolacyjny (*percolation model*), oraz (2) model kratownicowy (*central-force lattice*) z jednorodnym rozkładem wytrzymałości elementów na zerwanie. Model perkolacyjny ma charakter bi-modalny, tzn. mikrodefekt pojawia się w wybranym elemencie sieci z prawdopodobieństwem p albo jest nieobecny w tym elemencie z prawdopodobieństwem $1 - p$, niezależnie od tego, co dzieje się z elementami sąsiednimi. Model perkolacyjny nie uwzględnia zatem interakcji mikrodefektów. W modelu kratownicowym, gdzie każde zerwanie elementu oznacza redystrybucję sił w pozostałych elementach, interakcja mikrodefektów jest uwzględniana w sposób naturalny. Wokół perkolacyjnego modelu nieuporządkowania powstała teoria perkolacji (*percolation theory*), która znalazła szerokie zastosowanie w wielu innych dziedzinach nauki. W zagadnieniach zniszczenia, teoria perkolacji szuka odpowiedzi na następujące pytania: (1) Jaka jest krytyczna koncentracja mikrodefektów p_c, zwana „progiem perkolacji" (*percolation threshold*), przy której pojawi się nieskończony agregat mikrodefektów (*infinite cluster*) łączący dwa przeciwległe brzegi sieci? (2) Jak przebiegają różne procesy i zachowują się własności transportowe w pobliżu progu perkolacji — jakie są ich „prawa skalujące" (*scaling laws*)? (3) Czy istnieją prawa skalujące, które byłyby uniwersalne dla wszystkich wstępnych rozkładów mikrodefektów? (4) Czy maksymalne naprężenie i całkowita liczba zerwanych elementów w momencie globalnego zniszczenia sieci podlegają jakimś uniwersalnym prawom zachowania? Jednym z najważniejszych wyników teorii perkolacji sieci regularnych jest wykazanie, że krytyczna wartość porowatości f_c jest wielkością uniwersalną, niezależną od rozkładu mikrodefektów, a zależną jedynie od liczby wymiarów problemu ($2D$ lub $3D$). Fakt ten został wykorzystany w podrozdziale 8.2 do krytycznej ewaluacji różnych metod tzw. ośrodków efektywnych (*effective media techniques*) wykorzystywanych przy szacowaniu zmian modułów sprężystych wraz z rosnącą porowatością materiału (Rysunek 8.2). Dla dwuwymiarowego ośrodka z losowo rozrzucanymi pustkami kołowymi (bez nakładania się), jedynie metoda wewnętrznie-zgodna (*self-consistent method, SCM*) przewiduje zerowanie się siecznego modułu sprężystości przy skończonej wartości porowatości $f_c^{SCM} = 0.33$. Należy dodać, że próg perkolacji dla tego zadania wynosi $f_c = 0.45 \pm 0.03$. Pozostałe metody (*dilute distribution, differential scheme*) w ogóle nie przewidują istnienia progu perkolacji. Oznacza to, że ignorują one zjawisko samoorganizacji mikrodefektów prowadzące do powstania nieskończonego agregatu pustek, czyli rozerwania próbki w zadaniu dwuwymiarowym, przy porowatości znacznie mniejszej od 1. Ponadto, analiza przeprowadzona w podrozdziale 8.2 potwierdza użyteczność mikroskopowego parametru gęstości mikrodefektów Walsh'a–Budiansky'ego–O'Connell'a w modelowaniu procesów kruchego uszkodzenia i zniszczenia. W dalszej części Rozdziału 8 skupiono się nad symulacją uszkodzenia i zniszczenia podczas rozciągania przy zastosowaniu sieci kratowych (*central-force lattices*). Inspiracją do podjęcia tego tematu badawczego była ważna publikacja francuskich fizyków statystycznych Hansen i in. (1989). Analizując wyniki obliczeń w pracy Hansen i in. (1989), udało się zauważyć, że istnieje ścisła zależność skalująca (8.19), która pozwala wyrazić wszystkie wyniki Hansena i in. (1989) w postaci zamkniętych wzorów (por. Tablice 8.2 i 8.3). Co więcej, na podstawie wyprowadzonej zależności (8.19) okazało się, że maksymalna wartość parametru uszkodzenia (8.22) bez względu na rozmiar sieci wynosi $\tilde{D}_{\max} = \frac{1}{2}$ (Tablica 8.3), zaś zależność siła–przemieszczenie (F_c–Λ_c) przyjmuje w punkcie maksimum postać $F_{c\,\max} = \frac{1}{2} K \Lambda_{c\,\max}$, gdzie $K = 1$ jest sztywnością sieci w stanie nieuszkodzonym. Oba wyniki są dość zaskakujące, gdyż przypisywano je dotąd modelowi tzw. „belek równoległych" (*parallel bar model* lub *fiber bundle*, Rysunek 8.5), który ignoruje zarówno interakcję mikrodefektów, jak i efekt skali. Powyższe związki pozwoliły sformułować kilka interesujących wniosków, z których najważniejsze to: (a) efektywny moduł sprężystości (lub ogólniej — tensor efektywnych stałych sprężystych) jest dobrym kandydatem na zmienną uszkodzenia, (b) liczba zerwanych elementów sieci jest gorszym wyborem w sensie zmiennej uszkodzenia, gdyż jest wrażliwa na efekt skali, (c) w stanach rozciągania wpływ interakcji mikrodefektów na globalne zachowanie się sieci jest pomijalny (do chwili osiągnięcia maksimum obciążenia).

Podsumowanie

W Rozdziale 9 dokonano podsumowania całej pracy, sformułowano wnioski ogólne (wnioski szczegółowe zawarto w poszczególnych rozdziałach) oraz przedstawiono rejestr problemów uszkodzenia materiałów kruchych, które wymagają dalszych badań. Spośród wniosków ogólnych można wymienić trzy najważniejsze. Po pierwsze, mikromechaniczne, fenomenologiczne i sieciowe modele kruchego uszkodzenia są wobec siebie komplementarne, a najbardziej skuteczne wydają się być modele interdyscyplinarne czerpiące z wyników i metodologii wszystkich trzech podejść. Po drugie, wyniki uzyskane w tej pracy potwierdzają tezę, że tensor podatności (lub sztywności) spełnia wymagania stawiane zmiennej uszkodzenia w zakresie kruchych deformacji i mikroszczelin otwartych. Po trzecie, nie kwestionując walorów poznawczych tej dziedziny, mechanika uszkodzenia będzie się dalej rozwijać, o ile będzie w stanie przewidywać zniszczenie konstrukcji. Oznacza to z jednej strony konieczność budowania teorii słusznych dla dużych gęstości mikrodefektów z uwzględnieniem możliwości ich agregacji (lokalizacji), z drugiej zaś — intensywną implementację numeryczną takich teorii i konfrontację z wynikami doświadczeń.